IntechOpen

Gas Sensors

Edited by Sher Bahadar Khan, Abdullah M. Asiri and Kalsoom Akhtar

Gas Sensors

Edited by Sher Bahadar Khan, Abdullah M. Asiri and Kalsoom Akhtar

Published in London, United Kingdom

IntechOpen

Supporting open minds since 2005

Gas Sensors
http://dx.doi.org/10.5772/intechopen.80141
Edited by Sher Bahadar Khan, Abdullah M. Asiri and Kalsoom Akhtar

Contributors
Rakesh Kumar Sonker, Saroj Radheyshyam, Rahul Johari, Bc Yadav, Mostafa BarzegarGerdroodbary, Fatma SARF, Ja-Yu Lu, Borwen You, Musarrat Jabeen, R Vasant Kumar, Mohamad Ayad, Nagy Torad, Nazar Shah, Majeed Gul, Murrawat Abbas, Muhammad Amin

© The Editor(s) and the Author(s) 2020
The rights of the editor(s) and the author(s) have been asserted in accordance with the Copyright, Designs and Patents Act 1988. All rights to the book as a whole are reserved by INTECHOPEN LIMITED. The book as a whole (compilation) cannot be reproduced, distributed or used for commercial or non-commercial purposes without INTECHOPEN LIMITED's written permission. Enquiries concerning the use of the book should be directed to INTECHOPEN LIMITED rights and permissions department (permissions@intechopen.com).
Violations are liable to prosecution under the governing Copyright Law.

CC BY

Individual chapters of this publication are distributed under the terms of the Creative Commons Attribution 3.0 Unported License which permits commercial use, distribution and reproduction of the individual chapters, provided the original author(s) and source publication are appropriately acknowledged. If so indicated, certain images may not be included under the Creative Commons license. In such cases users will need to obtain permission from the license holder to reproduce the material. More details and guidelines concerning content reuse and adaptation can be found at http://www.intechopen.com/copyright-policy.html.

Notice
Statements and opinions expressed in the chapters are these of the individual contributors and not necessarily those of the editors or publisher. No responsibility is accepted for the accuracy of information contained in the published chapters. The publisher assumes no responsibility for any damage or injury to persons or property arising out of the use of any materials, instructions, methods or ideas contained in the book.

First published in London, United Kingdom, 2020 by IntechOpen
IntechOpen is the global imprint of INTECHOPEN LIMITED, registered in England and Wales, registration number: 11086078, 7th floor, 10 Lower Thames Street, London, EC3R 6AF, United Kingdom
Printed in Croatia

British Library Cataloguing-in-Publication Data
A catalogue record for this book is available from the British Library

Additional hard and PDF copies can be obtained from orders@intechopen.com

Gas Sensors
Edited by Sher Bahadar Khan, Abdullah M. Asiri and Kalsoom Akhtar
p. cm.
Print ISBN 978-1-78985-159-5
Online ISBN 978-1-78985-160-1
eBook (PDF) ISBN 978-1-83880-501-2

We are IntechOpen, the world's leading publisher of Open Access books

Built by scientists, for scientists

4,700+
Open access books available

121,000+
International authors and editors

135M+
Downloads

Our authors are among the

151
Countries delivered to

Top 1%
most cited scientists

12.2%
Contributors from top 500 universities

WEB OF SCIENCE™

Selection of our books indexed in the Book Citation Index in Web of Science™ Core Collection (BKCI)

Interested in publishing with us?
Contact book.department@intechopen.com

Numbers displayed above are based on latest data collected.
For more information visit www.intechopen.com

Meet the editors

Prof. Dr. Sher Bahadar Khan received his PhD from HEJ, Karachi University, Pakistan. He then started his postdoctoral career in nanochemistry and nanotechnology and continued to work as a postdoctoral research fellow until February 2010 at Yonsei University, South Korea. In March 2010, he joined the Center for Advanced Materials and Nano-engineering, Department of Chemistry, Najran University, as an assistant professor and continued his work until August 2011. He then joined the Chemistry Department, King Abdulaziz University, Jeddah, Saudi Arabia, as an assistant professor in September 2011. Currently, he is a full professor in the Chemistry Department, King Abdulaziz University, and is performing research in nanochemistry and nanotechnology. He was honored with the top scientist award of KP Science & Technology in 2018. He was also honored with the Deanship of Scientific Research award at King Abdulaziz University for book, patent, and highly ranked scientific publications. He is the author of 320 research articles, 12 books, and six patents with almost 1000 ± 10 impact factors, 6665 citations, and a 45 h-index.

Prof. Abdullah Mohamed Asiri received his PhD from the University of Wales, College of Cardiff, UK, in 1995. He has been Head of the Chemistry Department at King Abdulaziz University since October 2009 and is the Founder and Director of the Center of Excellence for Advanced Materials Research. He is also a professor of organic photochemistry. His research interest covers color chemistry, synthesis of novel photochromic and thermochromic systems, synthesis of novel coloring matters and dyeing of textiles, materials chemistry, nanochemistry, nanotechnology, polymers, and plastics. He is the editor-in-chief of the King Abdulaziz University *Journal of Science* and is also a member of the editorial board of *Pigments and Resin Technology* (UK), *Organic Chemistry in Sight* (New Zealand), and *Recent Patents on Materials Science* (USA). He is the Vice-President of the Saudi Chemical Society (Western Province branch).

Dr. Kalsoom Akhtar received her PhD from the Chemistry Department, Ewha Women's University, Seoul, Korea. Dr. K. Akhtar is an assistant professor at the Chemistry Department, King Abdulaziz University, and is performing research in organic and nanochemistry, which comprises photocatalysis, organic synthesis, and metal oxide nanomaterials. She is the author of two books and 65 research papers.

Contents

Preface **XIII**

Chapter 1 **1**
Metal Oxide Gas Sensors by Nanostructures
by Fatma Sarf

Chapter 2 **19**
Application of Knudsen Force for Development of Modern Micro Gas Sensors
by Mostafa Barzegar Gerdroodbary

Chapter 3 **37**
Optical Gas Sensors Using Terahertz Waves in the Layered Media
by Borwen You and Ja-Yu Lu

Chapter 4 **57**
A Review on Preparation of ZnO Nanorods and Their Use in Ethanol Vapors Sensing
by Musarrat Jabeen, R. Vasant Kumar and Nisar Ali

Chapter 5 **81**
Design and Growth of Metal Oxide Film as Liquefied Petroleum Gas Sensors
by Rakesh Kumar Sonker, Saroj Radheyshyam Shabajeet, Rahul Johari and Balchandra Yadav

Chapter 6 **101**
Synthesis of Metal Oxide Semiconductor Nanostructures for Gas Sensors
by Nazar Abbas Shah, Majeed Gul, Murrawat Abbas and Muhammad Amin

Chapter 7 **125**
Gas Sensors Based on Conducting Polymers
by Nagy L. Torad and Mohamad M. Ayad

Preface

Gas sensors have become a highly researched area because they can detect and recognize different types of toxic gases and low concentrations of vapor compounds. This interest in gas sensing has attracted worldwide interest, because of several diverse applications. Nowadays, there are many tools and materials that can be employed to design a gas sensor system. However, improvements in gas sensing system performance have been substantially correlated with advances in nanotechnology. This book focuses on the fabrication and application of gas sensing systems. It covers the recent developments of different materials used to design gas sensors, such as conducting polymers, semiconductors, as well as layered and nanosized materials. The widespread applications of various gas sensors for the detection of gaseous compounds are also discussed. The book provides an overview of recent attributes of gas sensors and their applications to a broad audience, including beginners, graduate students, and specialists in both academic and industrial sectors. It contains seven chapters that describe the design, fabrication, different uses, applications, and attributes of gas sensors. The first chapter is related to metal oxide gas sensors such as ZnO and multiwalled carbon nanotubes as well as their composites. It describes the performance of fabricated sensors for sensing NO_2, NH_3, and CO gases. The second chapter discusses the design of microgas sensors using radiometric phenomena, which occurs due to the temperature difference in rarefied gases. The effects of primary factors and parameters are also described. The third chapter presents terahertz wave propagation in layered media based on waveguide and artificial material configurations to sense gas molecules, especially volatile organic compounds. Improvement in detection sensitivity and selectivity is also discussed with the aid of multilayer microporous polymer structures as a terahertz artificial material to adsorb vapor molecules. The fourth chapter is related to a review of the preparation of ZnO nanorods and their use in ethanol vapor sensing, where the efficiency of 1D ZnO nanostructures prepared by different techniques as a sensing material for gaseous compounds, especially ethanol, is discussed. Ethanol detection characteristics using a ZnO sensor reveals its efficiency in terms of electrical resistance, capacitance, and impedance. The fifth chapter describes the design and fabrication of films based on metal oxide materials for petroleum vaporous compounds. The sixth chapter discusses the synthesis and sensing mechanisms of different toxic chemicals using ZnO nanowire materials synthesized by thermal evaporation through a vapor transport method using a vapor liquid solid mechanism. The chapter also reveals the sensing performance of ZnO nanowires for CH_4 gas with high sensitivity. The seventh chapter describes the contribution of conducting polymers as effective sensing materials to enhance their sensitivity, selectivity, and stability to detect gaseous compounds.

Sher Bahadar Khan, Abdullah M. Asiri and Kalsoom Akhtar
King Abdulaziz University,
Saudi Arabia

Chapter 1

Metal Oxide Gas Sensors by Nanostructures

Fatma Sarf

Abstract

Recently, metal oxide gas sensors by nanostructures have stirred interest and have found their way in many applications due to their high sensitivity, material design compliance and high safety properties. Gas performance tests of n-type ZnO, Al-doped ZnO and ZnO/MWCNT structures toward different type gases from our previous studies have been reported. It is indicated that nanoparticle formations on the film surfaces, grain sizes, gas types and operating temperatures have a severe effect on the chemisorption/physisorption process. Low concentration detection, determination of grain size limit values and reducing operating temperature to room temperature are already obstacles on long-life sensitivity and long-term stability characters. Doping is an effective way to increase gas sensitivity with atomic surface arrangement and active gas adsorption sites, which are generated by doping atoms. However, C-based material/MO nanostructures are preferred than doped MO films with their working even at room temperature. Up to now, a lot of methods to improve the gas sensitivity has been proposed. With the help of the development of surface modification methods such as different types of doping and MO-C composite, sensitivity, which is the most important parameter of sensor performance, can also be stable as well as increasing later on.

Keywords: metal oxide, gas sensor, toxic gas, doping, multiwalled carbon nanotube

1. Introduction

Increased environmental pollution, numerous motor vehicles, factory wastes and urbanization factors have been the source of high increases in the release of toxic, explosive and flammable gases in the environment of developed countries. High rate of gas emissions has both a negative impact on human/animal health and it can also have bad consequences on the environment and natural resources from day by day.

With the start of the Industrial Revolution, the acceleration of coal and mine quarries caused a significant increase in deaths due to toxic gas. First, canaries were used in gas detectors in mines. The cost and difficulty of using different methods for determination of toxic gases have revealed the gas sensors. In 1815, British scientist H. Davy developed a gas meter called 'Davy's lamp' against methane gas [1]. In 1926, Johnson produced the first commercial catalytic, combustion gas sensor, and in 1929, the company they founded with Williams became the first company in Silicon Valley in electronics [2].

Gas sensors are used to detect combustible, explosive and toxic gases, when the measured gas concentration exceeds the threshold value they can give an alarm (sound, signal, etc.) that can be used as portable or fixed devices. The most important part of this device production is the sensor which determines 4S parameters (sensitivity, selectivity, stability, speed). Apart from them, recovery time, response time and power consumption are also other parameters. The sensor part records changes in the physical conditions or chemical components as signals (permeability, resistance, temperature, acoustic wave, capacitance, etc.) as a result of interaction between target gas and surface atoms (O^-, O^{2-}, H^+ and OH^-) by absorption/desorption of gas on the material surface at a specific operating temperature. Signal can correlate concentration of target gas [3].

The recent change in the OSHA Time Weighted Average (TWA) Permissible Exposure Limit (PEL) is 25, 35 and 1 ppm for NH_3, CO and NO_2 gases, respectively [4].

CO is a toxic colorless gas, environmental pollutant and kills by causing hypoxia with damaged hemoglobin cells in the blood. In general, the measurement of CO gas is realized by detection of percentage of carboxyhemoglobin in the blood. Another important issue is creation of residential and automotive environment so it is so necessary fast and sensitive detection. Difficulty in detecting very low levels and continuous CO formation in the air poses problems [5].

Odorless and toxic ammonia (NH_3) combustion, which is used in a large area as a fertilizer, refrigerant material and household cleaning product, is a major hazard. Using or producing ammonia besides any uncontrolled leaks by the infrastructures or its explosion causes health hazards. In addition, it is a chemical pollutant in the production of silicon type devices in clean room [6].

Nitrogen dioxide (NO_2) is a volatile and toxic gas. It has hazardous effects in environment as a secondary pollutant and its detection is so important. NO_2 gas generates fuel burning at high temperature and in nitrogen cycle, including acid rains. Under even very low concentrations (<10 ppm) it causes serious damages for human health such as throat discomfort, transient coughs, eye irritation, fatigue and nausea [7].

With nano-sized designed gas sensors, surface to volume ratio is increased for absorbed target gas as well as higher efficiency is obtained than traditional bulk-scale designed devices, because different atomic coordination and translational symmetry at the surface ensure electrical properties changing in semiconductors [8]. In particular, a dramatic increase using the nano-sized designed gas sensors have been observed in industrial areas such as pharmaceuticals, medical, automotive, building automation, space tools, wearable devices. The first study of the semiconductor material group was given by Brattain and Bardeen on germanium (Ge) in 1953 [9]. In the next study, in 1954, Heiland had a research report on the gas sensitivities of metal oxides, and also in 1962 Seiyama showed that ZnO structures were sensitive to reactive gases in the air [10]. In 1968, Taguchi-type sensors were introduced to market and metal oxide (SnO_2) gas sensors were moved to industrial level [11].

Nano-scale designed gas sensors are usually classified depending on measurement data as follows; (i) chemiresistors, (ii) thermal conductivity gas sensors, (iii) acoustic wave gas sensors, (iv) calorimetric gas sensors, (v) optical gas sensors (vi) electrochemical gas sensors and (vii) infrared absorption gas sensors [13, 14].

Chemiresistive gas sensor working principle can be explained simply as adsorption of electron with target gas on the surface can cause charge transfer (a change in charge carrier concentration) between target gas/material surface region (receptor function) so electrical properties can be (resistance or conductivity) increase or decrease. Easy measurement with two electrodes is a factor in their preference and supplying safety.

Today, using chemiresistive metal oxide (MO) semiconductors, real-time gas sensor has gained great importance both in the science/industrial world due to their high sensitivity to chemical environments, low price, simple implantation, safety and durable to high temperature/high pressure, indicating that compelling conditions. Companies such as FIS, Mics, UST, CityTech, Appliedensors and Newcosmos produce millions of MO gas sensor per year, especially the Figaro company which produces Taguchi type sensors [15].

Gas selectivity is a critical problem for metal oxide gas sensors. To increase the selectivity of metal oxide sensors, it is proposed to use a heating mode of a gas-sensing floor with rapid temperature modulation in the last studies.

Metal oxide semiconductor gas sensors are focused on different and new materials at room temperature with the increasing need for faster, more precise and easy gas sensing, as showed in **Figure 1**. Thus, the most important parameter mechanism is gas sensitivity, which still does not reveal the exact reasons (strongly related to surface reactions), can be detailed. Production techniques (spray pyrolysis, pulsed laser deposition, magnetron sputtering, spin coating, and chemical bath deposition) are undeniable facts because structure parameters, grain boundaries, point defects, surface morphology, porosity, etc. must be affected. Additionally, reducing (H_2, H_2S, etc.)/oxidizing (NH_3, NO_2, etc.) gas types and p- or n-type is also effective on the chemiresistive MO performance, as showed in **Figure 2**. Oxidizing or reducing gas is associated with electron affinity, which is compared to the work function of most metal oxide so in the case of oxidizing gas, the adsorbed gas molecules on the surface of the MO are anions.

The change in electrical resistance of semiconductors can be explained as follows; formation of the space-charge depletion zone on the surface and around the particle and the energy band bending. Surface energy barriers with variable heights and widths depend on the relationship between charging the surface states of the adsorbed species for conduction electrons. In gas sensors using n-type semiconductor oxide, it has been observed that the resistance of the oxide increases with the interaction of gases such as O_3 or NO_2, while the resistance decrease of the oxide occurs with interaction of gases such as CH_4 and CO, as showed in **Figure 2**.

It is discussed that resistive-type metal oxide semiconductors produced by nanostructures (especially thin films) in detail toward NH_3, NO_2 and CO gases. Additionally, effect of doping and nanocomposite forming with C-based material (especially carbon nanotubes) were studied.

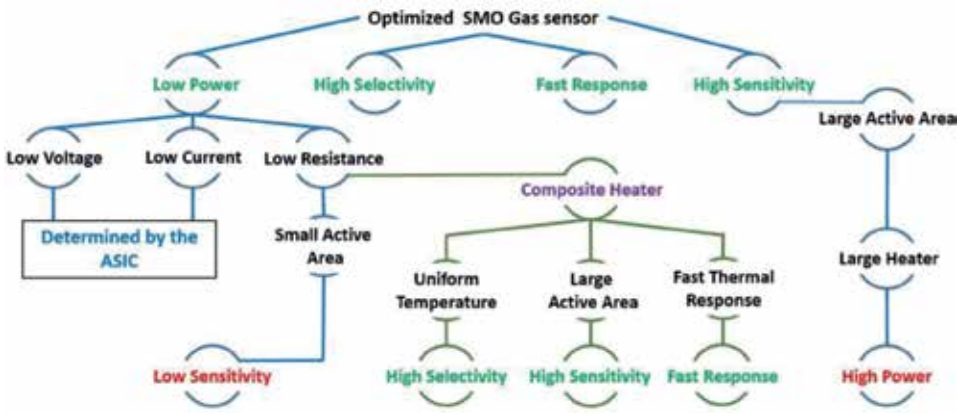

Figure 1.
Advantages and disadvantages of semiconductor metal oxides (reprinted from study of [12] with their permission).

Type of Sensitive Material	Type of Aimed Gas	Response(S)
n-type	oxidizing	R_g / R_a
	reducing	R_a / R_g
p-type	oxidizing	R_a / R_g
	reducing	R_g / R_a

Figure 2.
Sensitivity measurement of material type and target gas type (reprinted from study of [16] et al. with their permission).

2. Metal oxide (MO) gas sensors

Since 1962, the addition of the oxygen contained in the metal oxides to the reaction so increase of reactions and their stable chemical transduction properties which can reversibly convert chemical reactions on a surface make the metal oxides attractive for detect various harmful, toxic, and explosive gases. Development of gas sensors, which are almost 21% of the metal oxides used in the field, is rapidly increasing [17]. Because they have unique properties such as low cost, long lifetime, fast response time and relatively high sensitivity. However, some restrictions are detected in these structures such as background gas effect, poor selectivity and power consumption in high temperature conditions which could not be proper for especially wireless applications.

Basically, the main challenge is they operate only at elevated temperatures and consume more power with high operating temperatures. Physisorption and chemisorption are surface adsorption forms of oxygen. Physisorption to chemisorption needs activation energy with realized by increasing operating temperature. In addition, forming of oxygen species depends on the operating temperature substantially. Sun et al. reported that molecular species are more than atomic species below 150°C, this cause a decrease in gas sensitivity [18].

Another goal of gas sensitivity works is to ensure that electrical change in the gas environment occurs not only at grain boundaries but on the entire material surface. Since grain boundaries are smaller than MO particles, surface chemistry is more effective and the effect of grain boundaries on electrical change is not considered.

To achieve high performance from MO gas sensors, detailed knowledge of the gas sensing mechanism is essential. In general, it can be explained as follows; oxygen adsorption on the surface of sensing material, adsorbed oxygen species (extrinsic surface acceptor states) molecular (O_2^-) or atomic (O^-, O^{2-}), captured from the interior of the sensing material, resulting in a depletion layer on the surface due to oxygen species. Eventually observing a decrease in the conductivity/resistance [19]. In other words, oxygen ions on the surface of metal oxides are highly active interactions with the target gas molecule. When O_2 molecules adsorb from the surface of the MO, they break off electrons from the conductivity band (E_i) and trap electrons form on the surface, which come across in ion form. This causes band bending and electron depletion layer (space charge layer) formation. When the electron concentration in the conductivity band decreases, the conductivity decreases as well. At the same time, negatively charged traps in these different types of adsorbed oxygen cause downward bending of the band curve, which, compared to the flat state of the band, decreases conductivity. The thickness of the electron depletion layer is the width of the band bending region. The displacement of adsorbed oxygen with other molecules and the reaction of different oxygen ions with reduced gas changes conductivity.

Among metal oxide gas sensors single (ZnO, NiO, TiO_2, SnO_2, WO_3, etc.), binary and ternary samples have unique properties such as chemical stability, relatively low harmful for environment, abundant in nature and low cost. Wang et al. showed that metal oxides selected for real gas sensors can be separated according to their electronic structure [20];

a. d^0 transition metal oxides: In this group (WO_3, V_2O_5, TiO_2 and etc.), d^0 electronic configurations are preferred with their wide band gap energy and surface forms so it can measure easily.

b. pre-transition metal oxides: In this group (Al_2O_3, MgO and etc) are not preferred due to neither electrons nor holes forming so occurs very band gap energy, structural instability and difficulty of measure electrical conductivity.

c. post-transition metal oxides: They have d^{10} electronic configuration. ZnO, SnO_2 Ga_2O_3 and In_2O_3 are preferred in MO gas sensor applications. Because they are so proper for electron accumulation and chemisorption of donor-like species occurrence.

3. Thin film metal oxide gas sensors

In semiconductor gas sensor applications, advantages of thin film using are low resource waste, high surface/volume ratio, low power consumption, easy compliance with integrated circuits and easy alteration of electrical properties with changing film production parameters. Thin film technology allows the film properties to be changed by keeping the thickness parameter under considerable control. In this way, thin films are easily integrated into the device during the material production process. They can also be used as electronic circuit elements by acting as new materials when they are produced in multilayer.

Thin film metal oxides are used by the detection a lot of gas types such as Carbon-based (CO, CO_2, CH_4, C_2H_5OH, C_3H_8), nitrogen-based (NH_3, NO, NO_2), H_2, H_2S, ethanol, acetone, LPG and moisture.

The large number of grain boundaries in thin film polycrystalline MO's limits mobility, thus reducing carrier concentration and decreasing gas sensitivity. The presence of depletion layers in these grain boundaries is the most important factor that reduces mobility. Grain boundaries affect mobility due to their positioning to potential barriers with high intensity defect levels.

There have been a lot of ZnO thin film study to detect NO_2 gas sensing that have been reported with different morphologies nanowires, nanorods [21], nanoprisms [22] and nanospheres [23] in order to enhance surface area. In 2019, Duoc et al. synthesized ZnO nanowires and nanorods with using on-chip grown via hydrothermal method at room temperature NO_2 gas sensing [24]. The diameter of these structures severely affected gas sensing, indicating nanowires were more sensitive than nanorods. ZnO nanobarded fibers were synthesized by electrospinning and chemical bath deposition. These structures showed improved NO_2 detection performance for gas concentrations up to 30 ppb [25].

In our previous study, nanoflower shaped n-type ZnO films synthesized by chemical bath deposition and their 0.5 ppm NO_2 gas sensing was detected, showing in **Figures 3** and **4** [26]. Operating temperature was chosen at 200°C due to statical recovery kinetics were worse under this temperature. Oxygen vacancies (oxygen-deficient ZnO) acted as adsorption sites, electron donor sites and nucleation centers for small metal clusters. Reaction on the ZnO film surface was given by two

equations between exposing oxidizing type NO_2 molecules and oxygen species in the ZnO grain boundaries;

$$O_{2(ads.)} + 2e^- \leftrightarrow 2O^-_{(ads.)} \quad (1)$$

$$NO_2 + O^- \rightarrow NO_3 + e^- \quad (2)$$

With increasing annealing temperature and thereby decreased grain sizes caused an increase surface/volume ratio and NO_2 gas sensing, as expected for n-type ZnO. It was interesting that very high annealing temperature (>500°C) could lead to deterioration on the substrate/deposited layer interface, as showed in **Figure 3d**.

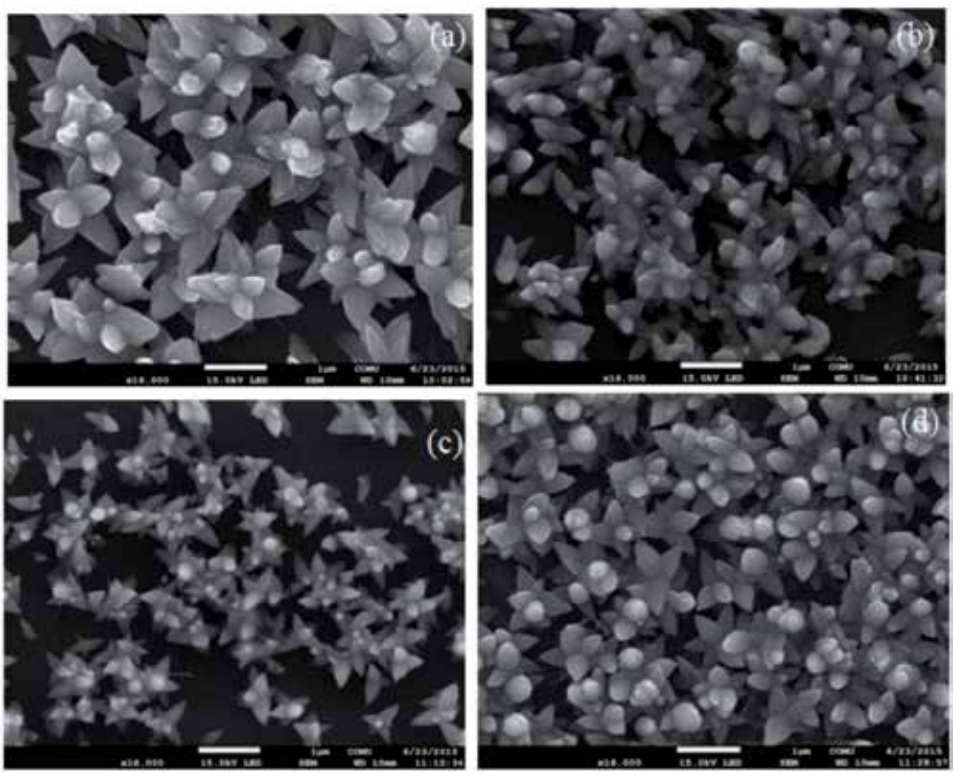

Figure 3.
SEM images of (a) ZnO and annealed ZnO films at (b) 450°C, (c) 500°C and (d) 550°C (reprinted from [26]).

4. Doping

To arrangement structural, morphological and gas sensing properties of MO nanomaterials, doping is an effective method with metallic ions (Al, Fe, Co, Cu, Ag and etc.). Defect sites and location of a host or doping ions determines grain size and electronic band of nanomaterials thereby sensing layer resistance. The substituted atoms can act as reactive sites for gas adsorption [27]. On the other word, surface impurities and defects with generating doping ions and thereby adsorption sites can cause extrinsic electronic states [28]. The reduction of the grain size to nanometers or to a scale comparable to the thickness of the charge depletion layer

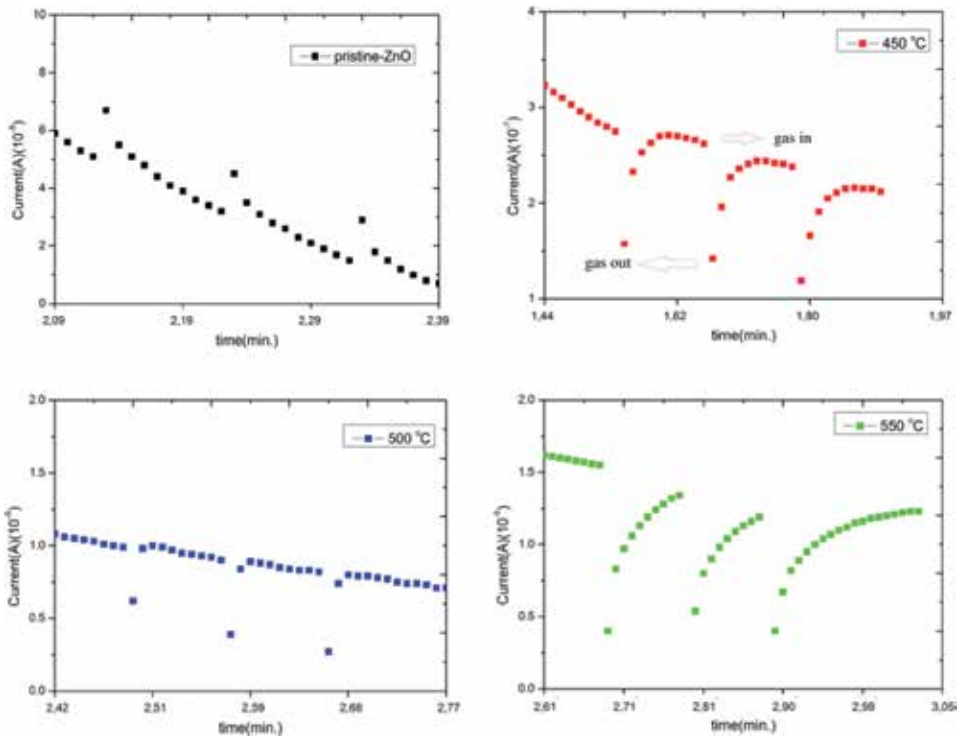

Figure 4.
0.5 ppm NO_2 gas sensitivity of ZnO thin films at 200°C (reprinted from [26]).

leads to a dramatic improvement in the gas sensitivity. It has been also found that the crystal structure of the grains affects the absorption of gases. Metal atom doping can also increase gas selectivity as reported by Govardhan and Grace [29].

Ionic radius difference plays a very important role between metal dopant and host metal (Zn, Sn, Fe, etc.) in gas sensing. Interstitial sites and oxygen vacancies are so critical in physisorption and chemisorption processes. To determine electronic traps in the doped structure deep level transient spectroscopy is an effective method.

However, heavily doped metal oxides (>10%) showed poor gas performance with high concentration defect regions, which is attributed to limitation on the Fermi level shift during interaction with the target gas [30].

The highest surface roughness values are 5% Al doping, and samples with this dopant have the highest NH_3 response times, explained by Aydın et al. [31]. Other Al:ZnO film studies were received by Dimitrov et al. [32] and Patil and Sondkar [33] toward CO gas.

In our previous study, Al-source effect was investigated on the NH_3 gas sensing and response time parameters as showed in **Figures 5–7** [34]. Alteration of surface particle type and dissolve depending on Al-source were caused by gas sensing parameters severely due to changing the energy-band gap structure, surface effective/contact area and NH_3 gas adsorption rate. Oxygen molecules that are adsorbed convert into oxygen species depending on temperature by capturing free electrons from the oxide. Then, depletion layers form in surface areas, leading to an increase in oxide resistance. According to Eq. (3), the electrons were released back to the conduction band, finally resulting in the decrease of the resistance.

$$2NH_3 + 3O^- \rightleftarrows N_2 + 3H_2O + 3e^- \quad (3)$$

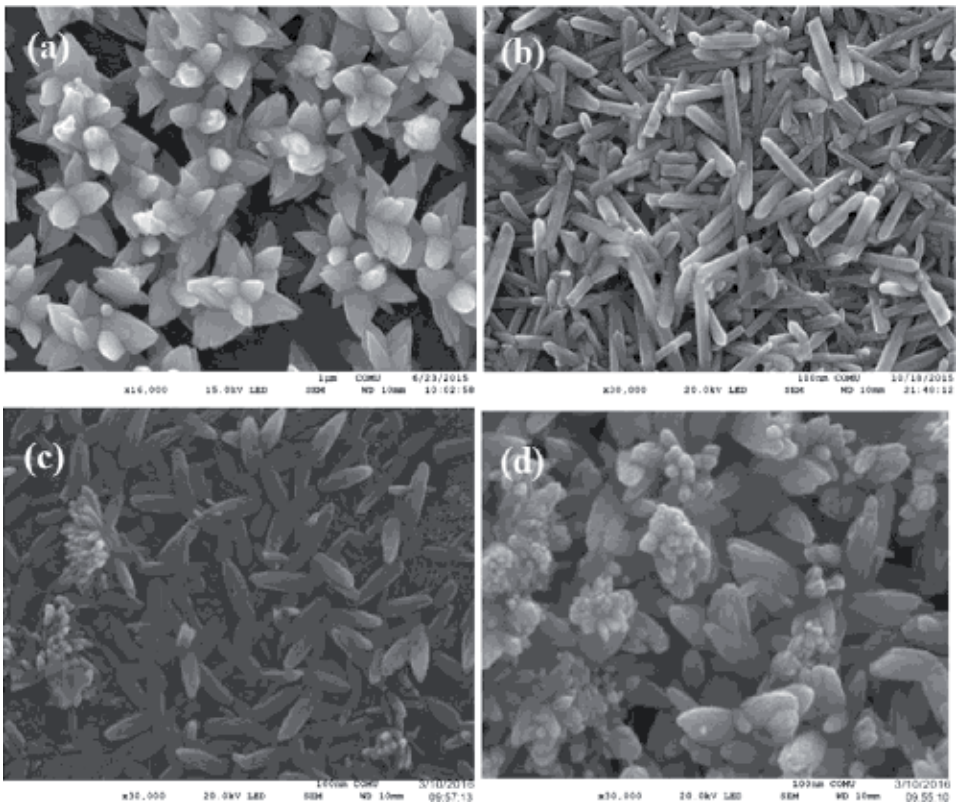

Figure 5.
SEM images of (a) pure ZnO and (b, c, and d) different Al:ZnO films depending on Al-source reprinted from [35].

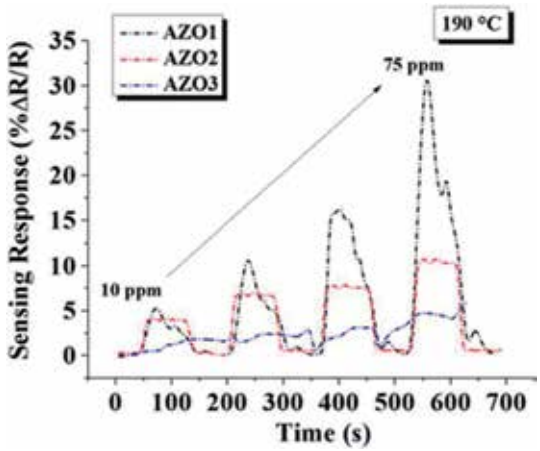

Figure 6.
NH_3 sensing response of Al:ZnO films as a function of time (reprinted from [34]).

As showed in **Figures 5** and **6**, nanorod formations (**Figure 5b**) had highest response times and gas sensing at low temperatures in powder Al-source used samples. Al-sources have high impact on gas sensing character due to changing film growth process and surface morphologies.

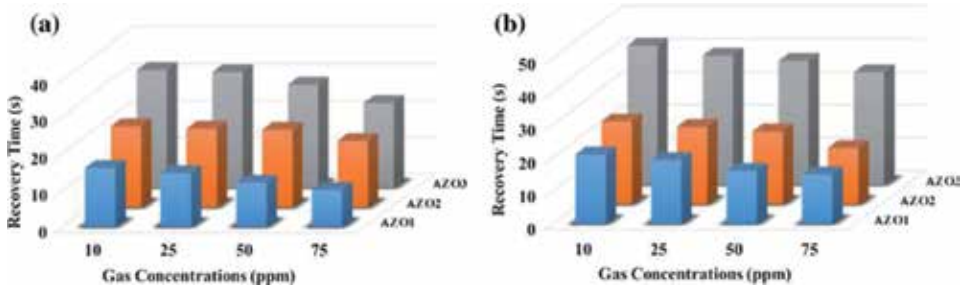

Figure 7.
(a) NH_3 gas response and (b) NH_3 gas recovery times of Al:ZnO films (reprinted from [34]).

5. MO/CNT nanocomposites

The exceptional and unique properties of carbon-based materials (carbon nanotubes, graphene, graphite, and plumbane) offer a great advantage for the production of improved composites, while their applications as a matrix element depends primarily on the relationship between the matrix and the other material. Gas sensor sensitivity of some MO-C-based nanostructures (MO: ZnO, SnO_2, TiO_2) is showed in **Table 1** and SWCNT-MO structure studies are so rare until now, interestingly. Because SWCNTs are much more expensive than MWCNTs and titanium oxide film production is usually expensive by physical methods. Defects forms such as atom vacancies, functional groups and stone wall defects on nanotubes can enhance the sensitivity toward different gases with metal oxide compositions. Additionally, as a matrix material supplies high quality of crystal lattice leading to a quite low electronic noise and they act as the Schottky barrier. These defect sites lower the activation energy barrier thus enabling chemisorptions of analytes on the surface of CNTs and make room temperature measurements possible [35].

In general, incorporation of C-based material into MO structure, n-type to p-type convert or p-n junction are observed so active sites available for gas adsorption and formation desired depletion layer [36].

Another improvement mechanism approach at room temperature proposed by Tai et al., indicating that supporting role of MO nanoparticles layer (first

	NO_2 gas sensing	NH_3 gas sensing	CO gas sensing	References
Graphene-ZnO	17.4 (100 ppm)	1.25 (10 ppm)	23.5 (1 ppm)	[36–38]
Graphene-SnO_2	2.45 (20 ppm)	1.9 (500 ppm)	9 (400 ppm)	[39–41]
Graphene-TiO_2	—	1.7 (10 ppm)	6.5 (100 ppm)	[42, 43]
MWCNT-ZnO	1.025 (10 ppm)	41 (10 ppm)	—	[44, 45]
MWCNT-SnO_2	2 (10 ppm)	1.06 (60 ppm)	0 (100 ppm)	[39, 46, 47]
MWCNT-TiO_2	—	2 (100 ppm)	7 (50 ppm)	[48, 49]
SWCNT-ZnO	6 (250 ppm)	—	0 (50 ppm)	[50, 51]
SWCNT-SnO_2	11.1 (10 ppm)	50 (100 ppm)	1.29 (50 ppm)	[52–54]
SWCNT-TiO_2	—	—	—	—

Table 1.
Comparison of some MO/C-based nanostructure gas sensors sensitivity (S%) toward NO_2, NH_3, and CO gases.

depletion layer from adsorption of ionized oxygen) as well as formed accumulation heterojunction at interface between MO and C-based material (second depletion layer) [37].

In a recent study, Lee et al. explained that improvement mechanism that was attributed the removal of oxygen-containing functional groups, the supply of electrons from the oxygen vacancies of ZnO material, and the formation of C-O-Zn bonds in ZnO-rGO membrane and operation under 100 ppm NO_2 at room temperature [55].

Among C-based materials, two types of carbon nanotubes (CNTs) (both single-walled [SWCNT] and multi-walled [MWCNT] carbon nanotubes) are so attractive in gas sensor support material studies due to their room temperature gas sensing, fast response and good reversibility properties. Hollow cores and inner/outside walls of CNTs supply large gas adsorption regions so they allow donating/withdrawing charge carrier mobilization [56]. Therefore, it causes a change in charge carrier concentration.

Multi-walled carbon nanotubes (MWCNTs) are nanoscale materials that comprise of several concentric single walled carbon nanotubes (SWCNTs) and exhibit diameters in the range of 5 and 30 nm [57]. Purification of MWCNTs (acid treatment, oxidation by heating, filtration, centrifugation, size-exclusive chromatography, etc.) is a preferred method to observation of no signal between target gas/CNT surface [58].

Sputter of nanoclusters of proper type atoms on surface provides catalysis process, enhancing gas sensing with functionalization of CNTs [59].

As reported to our previous study, MWCNT coating and MWCNT etching with HCl acid treatment effect was investigated on nanoflower ZnO seed layer against CO gas, showed in **Figures 8** and **9** [60]. The gas-sensing results had been shown that the response had been dramatically enhanced with the decoration of MWCNTs and rMWCNTs/ZnO sensor had exhibited the highest response to CO gas at 70°C. Consequently, it had been determined that gas sensing performance of the MWCNTs-decorated ZnO sensors had improved surface reactions with ZnO lattice. This may be attributed to the diffusion of the target gas through MWCNTs nanochannels.

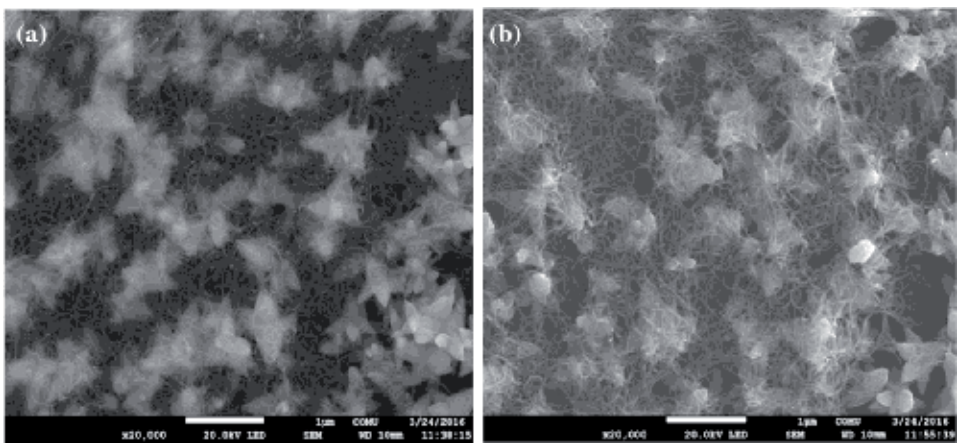

Figure 8.
SEM images of (a) ZnO/MWCNT and (b) ZnO/etched MWCNT films (reprinted from [60]).

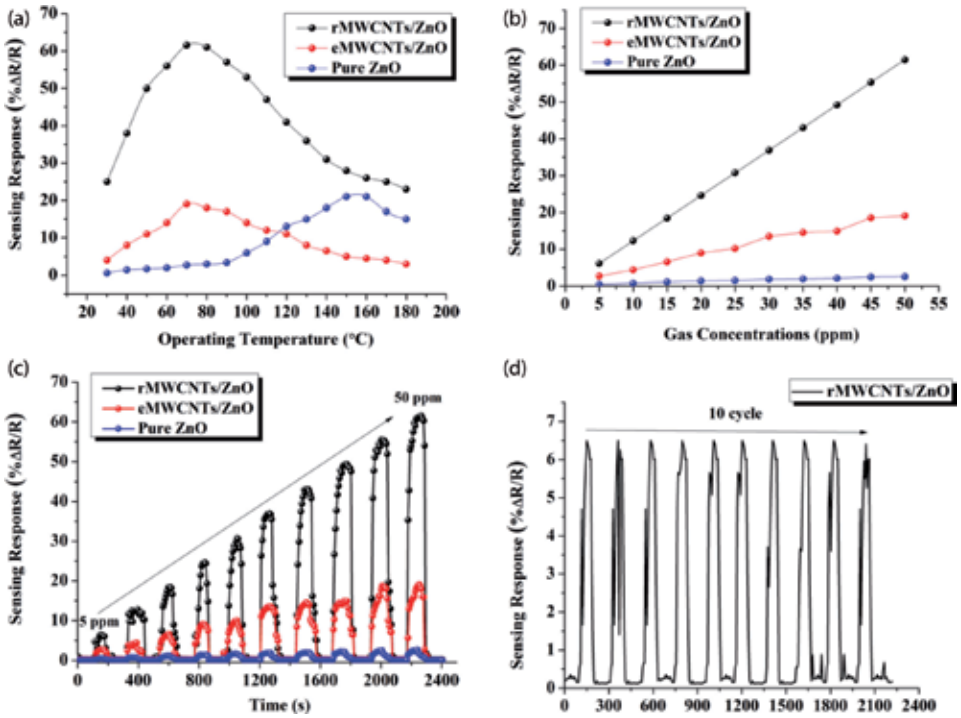

Figure 9.
Gas sensing parameters of ZnO/MWCNT film (reprinted from [60]).

6. Conclusion

In global, gas sensor market demands high performance on all 4S parameters (most common from ppb to ppm), miniaturization of weight, compatibility with other device components/wireless, flexibility for especially wearable devices and fabrication cost. It is expected to reach nearly 3 billion dollars in 2027. Recently, chemiresistive metal oxide semiconductor gas sensors are so interesting due to low cost, relatively high sensitivity and easy integration with CMOS compatible devices. The fact that the metal oxide gas sensor studies are very wide and there are quite a lot of publications in the literature about this topic. Hence some limitations are obligatory in this chapter.

Unlike other gas sensors in chemiresistive gas sensors, target gas concentration variation can be done in a quantitative way by direct measurement of electrical resistance. A change in the barrier height occurs between the particles due to the reducing or oxidizing of target gas. This detection largely depends on the grain size, depletion layer width and conduction characteristics of the nanostructures. Debye length must be compatible to the depletion layer.

Long-life sensitivity is still a key challenge. Today, the first and most common approach can be given as rapid decrease of material dimension (3D to 1D) and thus it has rapid expansion on the sensitive region but other factors (background gas, grain boundaries, granular forms, humidity and etc.) can be disregarded. Additionally, minimum particle size and enhanced/tunable surface reactivity at room temperature are main goals in a lot of studies. However, particle stability thereby gas sensing performance is not stable especially with particle size changing.

Gas transfer via micro-, meso-, and nano-porous sensing films with their assembled hierarchical, hollow, and yolk-shell forms has an enormous effect on interaction of target gas-oxygen species-nanoparticles.

In this study, metal oxide gas sensors by nanostructures were investigated comprehensively. ZnO nanoflower, Al:ZnO depending on Al-solution type and ZnO/MWCNT films were investigated toward different gases from our previous studies. Gas sensitivity was preferred main gas sensor parameter.

The results show that there is an interaction between the gas molecules and the sample surface based on the exchange of charges. While there is no gas in the environment, O_2 molecules adsorbed on the sample surface form an electron depletion zone. When the sample interacts with gas molecules, O_2 molecules also interact with the gas, and O_2 molecules begin to be dislocated from the surface. By separating O_2 molecules from the surface, electrons are released according to the property of the gas (reducing or oxidizing), or an electron is ionized from the sample. Thus, the change in electrical conductivity is observed. The detection rates and return mechanisms of the samples have also been fairly quick. Return times indicate that the main mechanism between the gases and the sample surface is physical adsorption. In physical adsorption, gas molecules are held in structurally formed cavities on the surfaces of the container in which they are located, interacting with the surface atoms Van der Waals. This phenomenon is reversible.

In MO and metal doping MO studies, film growth process must be under control to avoid agglomerative formations and un-expected ion positions in crystal structure, this causes gas adsorption process decreasing. Similar effect also occurs in C-based material/MO nanocomposites however having bonds of C-based materials and p- to n-type conversion/p-n junction have improvement effect on the gas sensitivity with expanded depletion region, indicating room temperature sensing.

On the other hand, in improvement studies of gas sensors, metal oxide gas sensors based on micro-hotplates fabricated with micro-electro-mechanical system (MEMS) technology that needs to be developed due to being restrictions on material and design. Uniform mesoporous structures are also desirable because they allow more sensing regions for gas diffusion. Additionally, metal organic frameworks (MOFs) with ultrahigh porosity have been also so attractive especially last years.

Considering the circumstances mentioned above, engineering control over the metal oxide structure and sensor design is so critical in order to obtain high stability as well as high gas sensitivity. Development of new metal oxide material compositions and their high stability/crystallinity will bring high performance gas sensors. New nanofabrication techniques and surface improved studies have contributed to development metal oxide gas sensors.

Acknowledgements

I would like to thank Emin Yakar and Sani Demiri for academic support. Also, I would like to thank Irmak Karaduman Er and Selim Acar for their help in the gas sensor performance measurements section.

Thank you to the Science and Technology Application and Research Center (ÇOBILTUM/ÇOMU) for supporting instrumental analysis.

DOI: http://dx.doi.org/10.5772/intechopen.88858

Author details

Fatma Sarf
Physics Department, Çanakkale Onsekiz Mart University, Çanakkale, Turkey

Address all correspondence to: fatmaozutok@comu.edu.tr

IntechOpen

© 2019 The Author(s). Licensee IntechOpen. This chapter is distributed under the terms of the Creative Commons Attribution License (http://creativecommons.org/licenses/by/3.0), which permits unrestricted use, distribution, and reproduction in any medium, provided the original work is properly cited.

References

[1] Thomas JM. Sir Humphry Davy and the coal miners of the world: A commentary on Davy (1816) an account of an invention for giving light in explosive mixtures of fire-damp in coal mines. Philosophical Transactions of the Royal Society A: Mathematical Physical and Engineering Sciences. 2015;**373**:20140288-20140299. DOI: 10.1098/rsta.2014.0288

[2] Liu X, Cheng S, Liu H, Hu S, Zhang D, Ning HA. Survey on gas sensing technology: Review. Sensors. 2012;**12**:9635-9665. DOI: 10.3390/s120709635

[3] Nazemi H, Joseph A, Park J, Emadi A. Advanced micro- and nano-gas sensor technology: A review. Sensors. 2019;**19**:1285-1308. DOI: 10.3390/s19061285

[4] Available from: https://www.osha.gov/dsg/annotated-pels/tablez-1.html

[5] Nandy T, Coutu RA Jr, Ababei C. Carbon monoxide sensing technologies for next-generation cyber-physical systems: Review. Sensors. 2018;**18**: 3443-3478. DOI: 10.3390/s18103443

[6] Gardner DE et al. Acute Exposure Guideline Levels for Selected Airborne Chemicals. Vol. 6. 2007. ISBN: 0-309-11214-1, 318 pages, 6 x 9. Available from: http://www.nap.edu/catalog/12018.html

[7] Bernstein JA et al. The health effects of nonindustrial indoor air pollution. The Journal of Allergy and Clinical Immunology. 2008;**121**:585-591. DOI: 10.1016/j.jaci.2007.10.045

[8] Veal TD, King PDC, McConville CF. Electronic properties of post-transition metal oxide semiconductor surfaces. Springer Series in Materials Science. 2012:127-145. DOI: 10.1007/978-1-4419-9931-3_6

[9] Neri G. First fifty years of chemoresistive gas sensors. Chem. 2015;**3**:1-20. DOI: 10.3390/chemosensors3010001

[10] Seiyama T, Kato A, Fujiishi K, Nagatani M. A New Detector for Gaseous Components Using Semiconductive Thin Films. Analytical Chemistry. 1962;**34**(11):1502-1503. DOI: 10.1021/ac60191a001

[11] Kumar R, Imam SA, Khan MR. A critical review of Taguchi gas sensor for the detection of VOC's. MASAUM Journal of Reviews and Surveys. 2009;**1**(2):177-183

[12] Lahlalia A, Neel OL, Shankar R, Selberherr S, Filipovic L. Improved sensing capability of integrated semiconducting metal oxide gas sensor devices. Sensors. 2019;**19**;14. DOI: 10.3390/s19020374

[13] Dey A. Semiconductor metal oxide gas sensors: A review. Materials Science and Engineering B. 2018;**229**:206-217. DOI: 10.1016/j.mseb.2017.12.036

[14] Özütok F. Obtaining of nanocomposites which metal oxide thin films with metal and/or CNT modification for sensor applications [PhD Thesis]. Turkey: Çanakkale Onsekiz Mart University; 2016. 90 p

[15] Yuan Z, Li R, Meng F, Zhang J, Zuo K, Han E. Approaches to enhancing gas sensing properties: A review. Sensors. 2019;**19**:25. DOI: 10.3390/s19071495

[16] Gao X, Zhang T. An overview: Facet-dependent metal oxide semiconductor gas sensors. Sensors and Actuators B: Chemical. 2018;**277**:604-633. DOI: 10.1016/j.snb.2018.08.129

[17] Cho M, Park I. Recent trends of light-enhanced metal oxide gas sensors: Review. Journal of Sensor Science and

Technology. 2016;**25**(2):103-109. DOI: 10.5369/JSST.2016.25.2.103

[18] etal S. Metal oxide nanostructures and their gas sensing properties: A review. Sensors. 2012;**12**:2610-2631. DOI: 10.3390/s120302610

[19] Shankar P, Rayappan JBB. Gas sensing mechanism of metal oxides: The role of ambient atmosphere, type of semiconductor and gases—A review. Science Letters Journal. 2015;**4**:126-133

[20] Wang C, Yin L, Zhang L, Xiang D, Gao R. Metal oxide gas sensors: Sensitivity and influencing factors. Sensors. 2010;**10**:2088-2106. DOI: 10.3390/s100302088

[21] Kumar R, Al-Dossary O, Kumar G, Umar A. Zinc oxide nanostructures for NO_2 gas–sensor applications: A review. Nano-Micro Letters. 2015;**7**(2):97-120. DOI: 10.1007/s40820-014-0023-3

[22] Shi L, Naik AJT, Goodall JBM, Tighe C, Gruar R, Binions R, et al. Highly sensitive ZnO nanorod- and nanoprism-based NO_2 gas sensors: Size and shape control using a continuous hydrothermal pilot plant. Langmuir. 2013;**29**:10603, 10.1021/la402339m-10609

[23] Dilonardo E, Penza M, Alvisi M, Di Franco C, Palmisano F, Torsi L, et al. Evaluation of gas-sensing properties of ZnO nanostructures electrochemically doped with Au nanophases. Beilstein Journal of Nanotechnology. 2016;**7**:22-31. DOI: 10.3762/bjnano.7.3

[24] Duoc VT, Le DTT, Hoa NC, Duy NV, Hung CM, Nguyen H, et al. New design of ZnO nanorod- and nanowire-based NO_2 room-temperature sensors prepared by hydrothermal method. Journal of Nanomaterials. 2019. DOI: 10.1155/2019/6821937

[25] Lee et al. ZnO nanobarbed fibers: Fabrication, sensing NO_2 gas, and their sensing mechanism. Applied Physics Letters. 2011;**98**:193114. DOI: 10.1063/1.3590202

[26] Özütok F, Demiri S. Nanoflower-like ZnO films prepared by modified chemical Bath deposition: Synthesis, optical properties and NO_2 gas sensing mechanism. Digest Journal of Nanomaterials and Biostructures. 2017;**12**(2):309-317

[27] Mariammal RN, Ramachandran K. Increasing the reactive sites of ZnO nanoparticles by Li doping for ethanol sensing. Materials Research Express. 2019;**6**:015024. DOI: 10.1088/2053-1591/aae559

[28] Varpula A, Novikov S, Haarahiltunen A, Kuivalainen P. Transient characterization techniques for resistive metal-oxide gas sensors. Sensors and Actuators B. 2011;**159**: 12-26. DOI: 10.1016/j.snb.2011.05.059

[29] Govardhan K, Grace AN. Metal/metal oxide doped semiconductor based metal oxide gas sensors—A review. Sensor Letters. 2016;**14**(8):741-750(10). DOI: 10.1166/sl.2016.3710

[30] Zhang D, Li C, Liu X, Han S, Tang T, Zhou C. Doping dependent NH_3 sensing of indium oxide nanowires. Applied Physics Letters. 2003;**83**: 1845-1847. DOI: 10.1063/1.1604194

[31] Aydın H, Yakuphanoğlu F, Aydın C. Al-doped ZnO as a multifunctional nanomaterial: Structural, morphological, optical and low-temperature gas sensing properties. Journal of Alloys and Compounds. 2019;**773**:802-811. DOI: 10.1016/j.jallcom.2018.09.327

[32] Dimitrov IG, Og Dikovska A, Atanasov PA, Stoyanchov TR, Vasilev T. Al doped ZnO thin films for gas sensor application. Journal of Physics Conference Series. 2008;**113**:012044. DOI: 10.1088/1742-6596/113/1/012044

[33] Patil NL, Sondkar SY. Synthesis of Al doped ZnO by sol-gel method for CO_2 gas sensing. International Journal on Recent Trends in Engineering & Technology. 2013;**9**(1):118-120. DOI: 01.IJRTET.9.1.32

[34] Özutok F, Karaduman I, Demırı S, Acar S. Influence of different aluminum sources on the NH_3 gas-sensing properties of ZnO thin films. Journal of Electronic Materials. 2018. DOI: 10.1007/s11664-018-6099-7

[35] Sattler KD. Carbon Nanomaterials Sourcebook: Graphene, Fullerenes, Nanotubes, and Nanodiamonds. Boca Raton, Florida, USA: CRC Press; 2016. p. 630

[36] Sun D, Luo Y, Debliquy M, Zhang C. Graphene-enhanced metal oxide gas sensors at room temperature: A review. Beilstein Journal of Nanotechnology. 2018;**9**:2832-2844. DOI: 10.3762/bjnano.9.264

[37] Li J, Liu X, Sun J. One step solvothermal synthesis of urchin-like ZnO nanorods/graphene hollow spheres and their NO_2 gas sensing properties. Ceramics International. 2016;**42**:2085-2090. DOI: 10.1016/j.ceramint.2015.09.134

[38] Tai H, Yuan Z, Zheng W, Ye Z, Liu C, Du X. ZnO nanoparticles/reduced graphene oxide bilayer thin films for improved NH_3-sensing performances at room temperature. Nanoscale Research Letters. 2016;**11**:130. DOI: 10.1186/s11671-016-1343-7

[39] Srivastava V, Jain K. At room temperature graphene/SnO_2 is better than MWCNT/SnO_2 as NO_2 gas sensor. Materials Letters. 2016;**169**:28-32. DOI: 10.1016/j.matlet.2015.12.115

[40] Chen Y, Zhang W, Wu Q. A highly sensitive room-temperature sensing material for NH_3:SnO_2-nanorods coupled by rGO. Sensors and Actuators B. 2017;**242**:1216-1226. DOI: 10.1016/j.snb.2016.09.096

[41] Shojaee M, Nasresfahani S, Sheikhi MH. Hydrothermally synthesized Pd-loaded SnO_2/partially reduced graphene oxide nanocomposite for effective detection of carbon monoxide at room temperature. Sensors and Actuators B. 2018;**254**:457-467

[42] Ye Z, Tai H, Guo R, Yuan Z, Liu C, Su Y, et al. Excellent ammonia sensing performance of gas sensor based on graphene/titanium dioxide hybrid with improved morphology. Applied Surface Science. 2017;**419**:84-90. DOI: 10.1016/j.apsusc.2017.03.251

[43] Bandı S, Hastak V, Peshwe DR, Srıvastav AK. In-situ TiO_2–rGO nanocomposites for CO gas sensing. Bulletin of Materials Science. 2018;**41**:115. DOI: 10.1007/s12034-018-1632-0

[44] Kwon YJ, Mirzaei A, Kang SY, Choi MS, Bang JH, Kim SS, et al. Synthesis, characterization and gas sensing properties of ZnO-decorated MWCNTs. Applied Surface Science. 2013;**413**:242-252. DOI: 10.1016/j.apsusc.2017.03.290

[45] Schütt F, Postica V, Adelung R, Lupan O. Single and networked ZnO–CNT hybrid tetrapods for selective room-temperature high-performance ammonia sensors. ACS Applied Materials & Interfaces. 2017;**9**: 23107-23118. DOI: 10.1021/acsami.7b03702

[46] Choi K, Park J, Park K, Kim HJ, Park H, Kim S. Low power micro-gas sensors using mixed SnO_2 nanoparticles and MWCNTs to detect NO_2, NH_3, and xylene gases for ubiquitous sensor network applications. Sensors and Actuators B. 2010;**150**:65-72

[47] Wei L, Shizhen H, Wenzhe C. An MWCNT-doped SnO_2 thin film NO_2

gas sensor by RF reactive magnetron sputtering. Journal of Semiconductors. 2010;**31**(2):024006-024006. DOI: 10.1088/1674-4926/31/2/024006

[48] Kaushik P, Eliáš M, Prášek J, Pytlíček Z, Zajíčková L. Titanium dioxide modified multi-walled carbon nanotubes as room temperature NH_3 gas sensors. IEEE. 2018; DOI: 10.1109/ICSENS.2018.8589876

[49] Lee J-S, Ha T-J, Hong M-H, Park C-S, Park H-H. The effect of multiwalled carbon nanotube doping on the CO gas sensitivity of TiO_2 xerogel composite film. Applied Surface Science. 2013;**269**:125-128

[50] Barthwal S, Singh B, Singh NB. ZnO-SWCNT nanocomposite as NO_2 gas sensor. Materials Today: Proceedings. 2018;**5**:15439-15444

[51] Hernández SC et al. Hybrid ZnO/SWNT nanostructures based gas sensor. Electroanalysis. 2012;**24**(7):1613-1620. DOI: 10.1002/elan.201200135

[52] Carpenter MA, Mathur S, Kolmakov A. Metal Oxide Nanomaterials for Chemical Sensors. Berlin, Germany: Springer Science & Business Media; 2012. 548 p

[53] Su HC, Zhang M, Bosze W, Myung NV. Tin dioxide functionalized single-walled carbon nanotube (SnO_2/SWNT)-based ammonia gas sensors and their sensing mechanism. Journal of the Electrochemical Society. 2014;**161**(14):B283-B290

[54] Yang A, Tao X, Wang R. Room temperature gas sensing properties of SnO_2/multiwall-carbon-nanotube composite nanofibers. Applied Physics Letters. 2007;**91**:133110

[55] Lee H, Heish Y, Lee C. High sensitivity detection of nitrogen oxide gas at room temperature using zinc oxide-reduced graphene oxide sensing membrane. Journal of Alloys and Compounds. 2019;**773**:950-954. DOI: 10.1016/j.jallcom.2018.09.290

[56] Castro EA. Nanoscience and Advancing Computational Methods in Chemistry: Research Progress. IGI Global; 2012. 321 p

[57] Gangu KK, Maddila S, Jonnalagadda SB. A review on novel composites of MWCNTs mediated semiconducting materials as photocatalysts in water treatment. The Science of the Total Environment. 2019;**646**:1398-1412. DOI: 10.1016/j.scitotenv. 2018.07.375

[58] Gao C, Guo Z, Liu J, Huang X. The new age of carbon nanotubes: An updated review of functionalized carbon nanotubes in electrochemical sensors. Nanoscale. 2012;**4**:1948. DOI: 10.1039/c2nr11757f

[59] Nguyen LQ, Phan PQ, Duong HN, Nguyen CD, Nguyen LH. Enhancement of NH_3 gas sensitivity at room temperature by carbon nanotube-based sensor coated with Co nanoparticles. Sensors. 2013;**13**:1754-1762. DOI: 10.3390/s130201754

[60] Özutok F, Karaduman I, Acar S, Demırı S. Enhancing the CO gas sensing properties of ZnO thin films with the decoration of MWCNTs. Journal of Materials Science: Materials in Electronics. 2018;**47**(5):2648-2657. DOI: 10.1007/s10854-018-0288-2

Chapter 2

Application of Knudsen Force for Development of Modern Micro Gas Sensors

Mostafa Barzegar Gerdroodbary

Abstract

Development of new simple gas sensor is highly significant due to its various industrial applications. In this chapter, comprehensive studies on the new micro gas sensor of Micro In-plane Knudsen Radiometric Actuator (MIKRA) are done to evaluate the performance of its technique on the detection of gas. This new micro gas sensor works by the radiometric phenomena, which occurs due to temperature difference in rarefied gas. In order to simulate this micro gas sensor, direct simulation Mont Carlo (DSMC) is recognized as a reliable method. This study highly focused on the main mechanisms of the flow feature and force generation in low-pressure domain. In order to study this micro gas sensor, comprehensive numerical results are thoroughly investigated and the effects of primary factors and parameters are revealed. In addition, the main details of computational approach for the simulation of this micro gas sensor are fully presented. Finally, the performance of this sensor in various operating conditions is explained and main findings are discussed.

Keywords: micro gas sensor, Knudsen force, rarefied gas, DSMC

1. Introduction

Gas sensors are widely used in various industrial applications for evaluation of the main elements inside the gas mixture. In addition, this device is significant for detection of dangerous gas such as CO_2, H_2 and ammonia. In addition, gas sensors are widely used for the evaluation of the main products of the combustion. Since this instrument is a main element in the various applications, considerable researches and studies have been performed to develop new techniques for the detection of the various gases. Indeed, the present gas sensor is highly expensive and spacious and these disadvantages of the current sensors have motivated the researchers to develop a simple and cheap method for the gas detection [1–6].

Various methods and techniques are applied for the gas sensors [7–10]. However, current sensors could not perform in the micro scale. Recently, scientists and researchers have investigated molecular force which is produced by the temperature difference on the solid body in high Knudsen numbers. Since this force occurs in high Knudsen numbers, it is known as Knudsen force.

Knudsen number (Eq. (1)) is mainly defined as the ratio of the mean free path of gas (λ) to specific length (L) as follows:

$$Kn = \frac{\lambda}{L} = \frac{\mu}{p_\infty L}\sqrt{\frac{2\,k_B T_\infty}{m}}. \quad (1)$$

In Eq. (1), the term of mean free path of gas (λ) is proportional to the temperature and viscosity. According to this equation, high Knudsen number is obtained by decreasing either the pressure of the domain or size of our model. Previous studies [8–16] clearly showed that the Knudsen force is highly proportional to the main characteristics of the gas inside the domain.

Actually, thermal stresses are produced by the non-uniformity of the temperature within rarefied gases and create bulk fluid flows that could employ forces on solid body [17, 18]. Ketsdever et al. [17] presented broad literature reviews to reveal the origin of the Knudsen thermal force. They widely considered the technical remark of source of the Knudsen thermal force and active factor on the rate of induced forced. According to their findings, operative factors such as pressure of domain and gas component as well as the thermal gradient magnitude play significant role on the value of the exerted force. These characteristics enable researchers to apply this for the measurement of gas type.

One of the effective methods to apply the Knudsen force is to reduce the size of the model and construct micro device [19]. Micro Knudsen gauge and microscale radiometric actuator are the main conventional devices that implement this technique for industrialized applications. Numerous studies have been directed to inspect and evaluate the key features of Knudsen force in these instruments [18]. Strongrich et al. [19] performed experimental work and numerical studies to calculate Knudsen force on a non-uniformly heated beam. They highly focused on this molecular force and finally offer their new micro gas sensor as Micro In-plane Knudsen Radiometric Actuator (MIKRA) as shown in **Figure 1**. This sensor could be used either detection of gas types or measurement of gauge pressure [20, 21]. One of the significant aspects of this micro gas sensor is the micro size of this device that enables it to work in the various operating condition. Since this device is highly significant, considerable works have been performed to evaluate this micro gas sensor [11–13]. In our these papers, the main characteristics of this sensor are investigated and the precision of measured Knudsen force for different gas mixtures, for instance, hydrogen, methane/helium, methane/SO_2, carbon dioxide, ammonia, and inert gas. These researches are conducted to reveal the performance and capability of this micro gas sensor in diverse operating conditions [14–18]. These works have

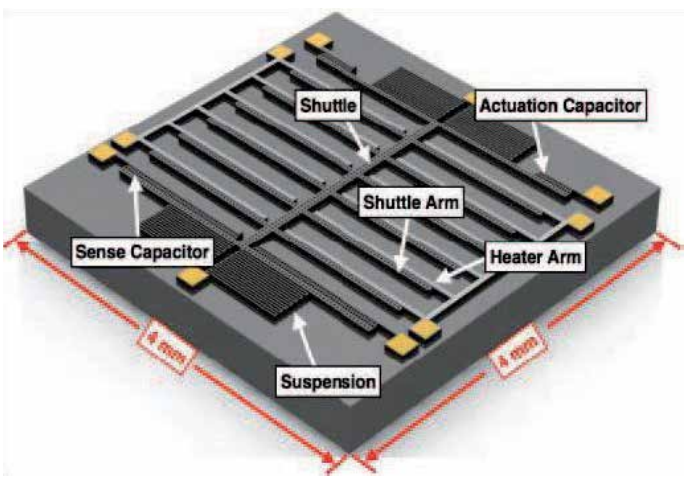

Figure 1.
Micro In-plane Knudsen Radiometric Actuator (MIKRA) [21].

tried to disclose the influence of temperature difference of cold and hot arm, the gap size, and pressure of domain on the value of the exerted force on the cold side.

The physics of the Knudsen force in the Knudsen gage are widely investigated by the researchers and scholars. Passian et al. [22–24] as pioneer research group initiated to reveal the main characteristic of the Knudsen force at the microscale. They mainly studied on a micro cantilever which includes two surfaces with dissimilar temperatures separated by a gap in rarefied domain. Theoretical and experimental studies have been conducted via a U-shaped silicon microcantilever to disclose the main parameters. The impact of thermal difference on the Knudsen forces in the transitional regime is examined by Lereu et al. [25]. The measurement of these forces at ordinary environment on test configurations made by surface micromachining of polysilicon are done by Sista and Bhattacharya [26]. Kaajakari and Lal [27] studied Knudsen forces produced within molecular flow regime to examine surface micromachined hinged structure assembly. Furthermore, negative thermophoretic force is studied by different scholars [28] and the influence of valuable factors on radiometric force is disclosed [29, 30].

In order to simulate the model, DSMC approach is a reliable technique for evaluation of the exerted Knudsen force in the rarefied domain. This method is highly popular and conventional for the simulation of the problems with low-pressure condition. Hence, numerous scholars and scientists [31–40] applied this for the simulation of scientific and engineering problems.

Recognition of the force value in the low-pressure domain is the primary challenge in this field. Indeed, scholars have performed various studies to obtain the reliable and comprehensive correlation which offers the main value of Knudsen force in various operating and geometrical conditions [41–46]. Following the above description and containing the historical perspective, the broadly established modern appreciative is such that the major force related to vane rotation is the force generated close to the edges of the vane, in a zone with the dimensions of a mean free path according to Einstein. At very low pressures, the mean free path is great and the entire area of the vane is involved in force generation. As the pressure rises and flow enters the transition regime, the mean free path shrinks and the effective force-producing area of the vane is reduced. At some pressure (where the free path is on the order of the vane thickness according to Einstein), a maximum is gotten and force generation thereafter initiates to weaken as thermal creep and then convective currents initiate to lead the flow. A brief visual summary of the expected force output of a Nichols radiometer vane in free-space is shown in **Figure 2**, where comparisons are made for several of the dominant theories of the previous century. Here, FM denotes free molecular, B&L denotes Brüche and Littwin experimental measurements and "Einstein" denotes his correlation.

For a Crookes type radiometer, Scandurra et al. [46] have offered a first expression for radiometric force that includes both pressure and shear components. For the normal force per unit area (pressure difference) on a thin vane, they offered

$$F_n = (2 - \alpha_E)\frac{15\,k}{32\sqrt{2}\,\pi\sigma^2}\,\Delta T l, \tag{2}$$

where α_E is the energy accommodation coefficient, k is the Boltzmann constant, $\pi\sigma^2$ is the total collision cross section of the gas molecule, and l is the vane perimeter. For the shear stress, the expression is

$$F_\tau = \alpha_E\frac{15\,k}{64\sqrt{2}\,\pi\,\sigma^2}\,\frac{\Delta T}{\lambda}(\tau l), \tag{3}$$

where τ is the vane thickness. One of the key assumptions of that work is constant pressure in the gas surrounding the heated vane.

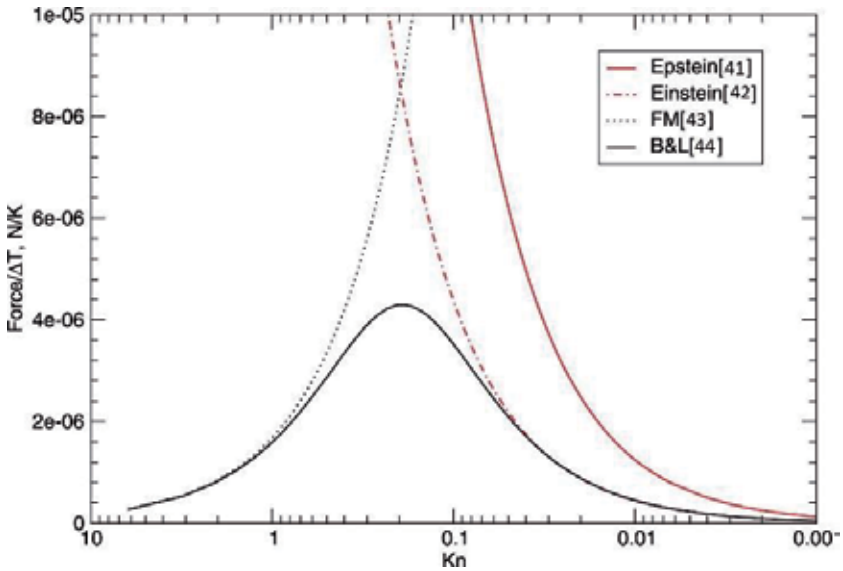

Figure 2.
Nichols radiometer: force prediction.

For a Crookes radiometer, practically, all earlier analytical estimates of the radiometric force, with the exception of the Brüche and Littwin bell-shaped correlation, were implicitly or explicitly assuming a collision-dominated flow, where the radiometer vane area is much larger than the gas mean free path. This is essentially a slip flow regime, where the impacts of the free molecular, area-related forces are relatively small. This explains that the proposed expressions depend on the perimeter of the radiometer vane, and not on its area. While this is a reasonable approach for many cases, where the velocity distribution function is close

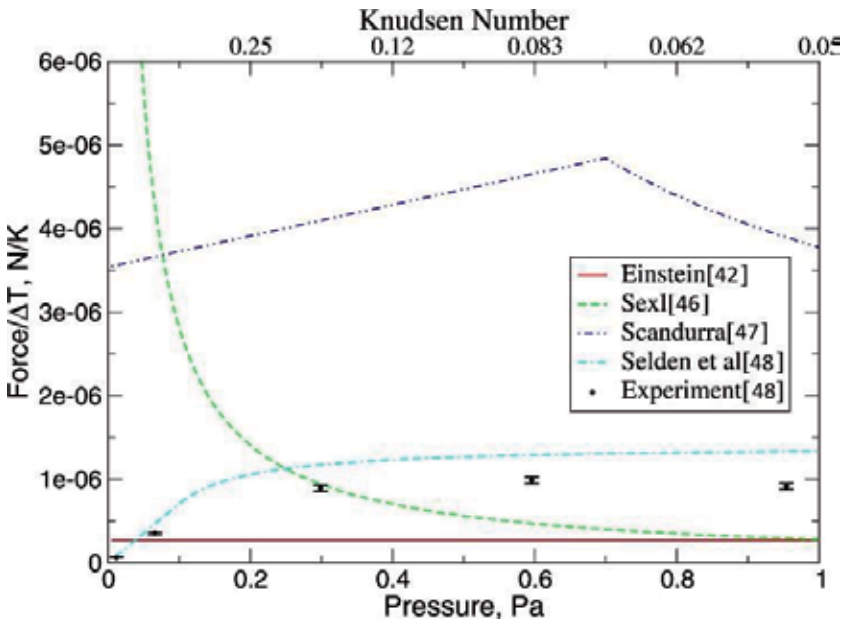

Figure 3.
Crookes radiometer: force prediction and comparison with experimental data.

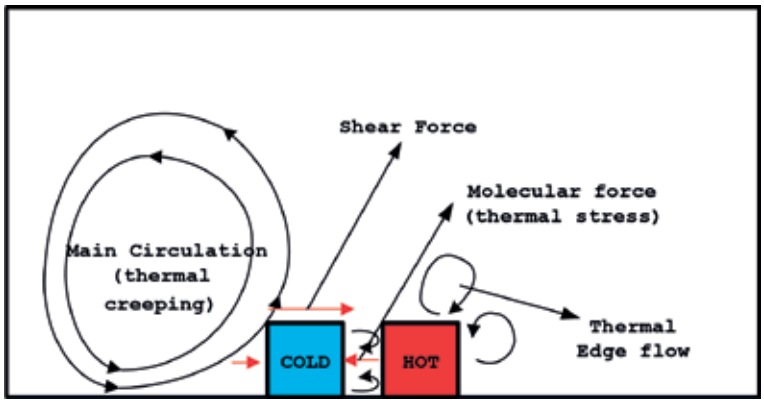

Figure 4.
Flow feature and main stream inside the MIKRA [10].

to equilibrium and the pressures at the centers of two sides of the radiometer are equilibrated, it is not obvious that such an approach is applicable to the regime where the flow is far from equilibrium, and both the area and the edge contribute to the radiometric forces.

The authors of Ref. [47] used an assumption similar to Einstein's, and calculated force with n = 1. They found that the radiometric force computed with this simple empirical expression gives surprisingly close agreement with experimental results, as shown in **Figure 3**. The assumption of n = 1 works very well, even though, the pressure imbalance occurs over a region of 10 mean free paths. The agreement is fairly good in the free molecular and nearly free molecular flows (pressures below or about 0.1 Pa, or Knudsen numbers above 0.5 that are characterized by a nearly linear increase in the radiometric force, and the area-related radiometric forces are dominant). Then, even though the empirical expression stems from the free molecular formula, the agreement is also quite reasonable in the transitional flow where the collisions start to reduce the radiometric force, and both area- and edge-related radiometric forces are important (Knudsen numbers between 0.5 and 0.05, where the maximum radiometric force is observed).

The recognition of the main effective term on this type of sensor is highly significant for the evaluation and performance analysis of this device. According to previous works, three main flow patterns are recognized in this model. As shown in **Figure 4**, the Molecular force Known as thermal stress is the main effective factor that produce the Knudsen force within the gap of two arms. The direction of this force is from hot to cold side. The second dominant term in this model is known as thermal creeping. This flow pattern is produce shear force on the top of cold arm and the direction of this flow is from cold to hot side. The least important flow pattern is thermal edge flow which occurs in the vicinity of the sharp edge with high temperature. In the following, comprehensive details of each factor will be explained.

In the following, the governing equations and the main technical approach for the simulation of this micro gas sensor is presented. In addition, the boundary condition of this model according to the real working condition is defined. Then, the results of various codes are compared to evaluate the performance of each methods. In the next step, the main flow feature inside the model is studied to define the impact of main parameters. Moreover, the effect of the pressure and temperature difference of the hot and cold arm is determined. Finally, the performance of this sensor in detection of gas mixture will be explained.

2. Numerical approach

2.1 Governing equations

In order to simulate the flow inside the rarified gas, Navier-Stokes equations are not valid and consequently, computational fluid dynamics (CFD) approaches is applicable. In fact, the continuity is not governed in low-pressure free molecular regime to near-continuum. Therefore, high order equation of Boltzmann equation should be solved to obtain the flow pattern in molecular regime. In followings, Boltzmann equation is presented.

$$\frac{\partial}{\partial t}(nf) + \mathbf{c}.\frac{\partial}{\partial \mathbf{r}}(nf) + \mathbf{F}.\frac{\partial}{\partial \mathbf{c}}(nf) = Q \tag{4}$$

where n, $\mathbf{c}$, and f are number density, molecular velocity, and velocity distribution function, respectively. In addition, $Q = \int_{-\infty}^{+\infty}\int_{0}^{4\pi} n^2\left(f^* f_1^* - f f_1\right) g\, \sigma\, d\Omega\, d^3 c_1$ is the collision integral which describes the change in the velocity distribution function due to intermolecular collisions.

Since solving the Boltzmann equation is hard, researchers try to find approaches that present similar results to that of Boltzmann equations. DSMC technique of Bird [48], as a particle method based on kinetic theory, is a reliable approach for simulation of rarefied gases. There are some software packages such as OpenFOAM and SPARTA in which DSMC method is developed for the simulation of the engineering problems. OpenFOAM is open-source code is proficient and flexible software for simulation of complex models [49].

2.2 Numerical procedure

In order to perform the DSMC simulations, some assumptions are made. For modeling of the collision, the variable hard sphere (VHS) collision model is used. Collision pairs are chosen based on the no time counter (NTC) method, in which the computational time is proportional to the number of simulator particles [36].

In this type of the sensor, the gap (distance between the heater and shuttle arms) is recognized as the characteristic length (L) and it is 20 μm. In this model, it is recommended to initiate 20 particles in each cell to minimize the statistical scatter.

2.3 Geometry and boundary condition

Figure 5 illustrates the generated grid and the boundary condition applied on the model. The size of the domain is 600 × 300 μm in x and y direction. There were 150 × 65 collision cells in the x and y directions, respectively. All surfaces were assumed to be fully diffuse.

The free domain condition is applied on the top of domain while the side of the domain is symmetry. Constant temperature is applied to the hot and cold arms. The pressure of the domain varied from 0.465 to 11.2 Torr, meaning the Knudsen number varied from 4.64 to 0.19, respectively. The bottom of the domain is at constant temperature (T = 298 K). The simulations are performed for single gas of nitrogen. In this research, two types of the temperature condition (real and constant temperature) are applied on the cold and hot arm. In constant type, it is assumed that the temperature of hot and cold arm is fixed with variation of pressure and effect of four constant temperature differences (310–300, 330–300, 350–300 and 400–300 K) is investigated. In the real temperature type,

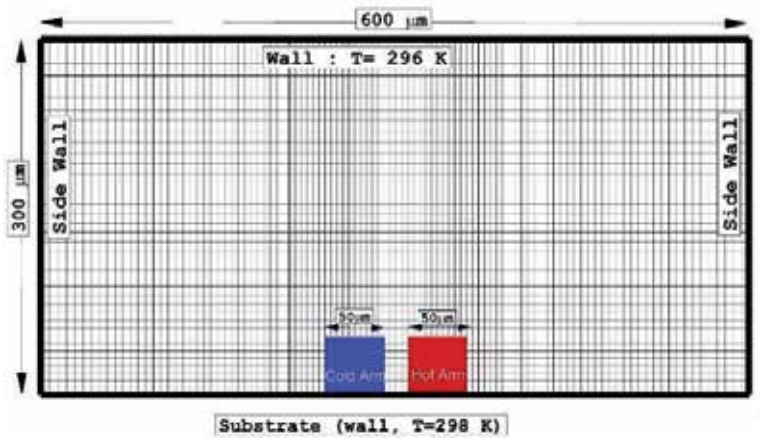

Figure 5.
The boundary condition and grid of the present model [12].

Pressure	Kn	Hot arm	Cold arm
(Pa)	—	(K)	(K)
62	4.48	353	303
155	1.8	350	303
387	0.72	347	303
966	0.29	325	302
1500	0.18	315	300

Table 1.
Temperature of the cold and hot arm (real temperature).

the temperature of the cold and hot arm varies with the pressure of the domain. In order to valid our results, the temperature variation of the cold and hot arm is obtained from experimental data of Strongrich et al. [21] and presented in **Table 1**.

3. Results and discussion

3.1 Verification

In order to evaluate the precision and correctness of the numerical results, it is highly significant to compare simulation with experimental data. As mentioned in the previous section, the results of the SPARTA and DSMC are compared with experimental data (**Figure 6**). The comparison of results of simulations with that of experimental data of Strongrich et al. [21] for various pressure conditions shows that applied assumptions and procedures is logic and reasonable. In addition, obtained results of the SPARTA-DSMC code [21] also confirm the correctness of our results. The evaluation displays a worthy agreement of our work with other techniques.

3.2 Analysis of flow structure

In order to realize the main mechanism of this new gas sensor, the flow feature and temperature distribution inside the micro gas sensor are illustrated in **Figure 7**

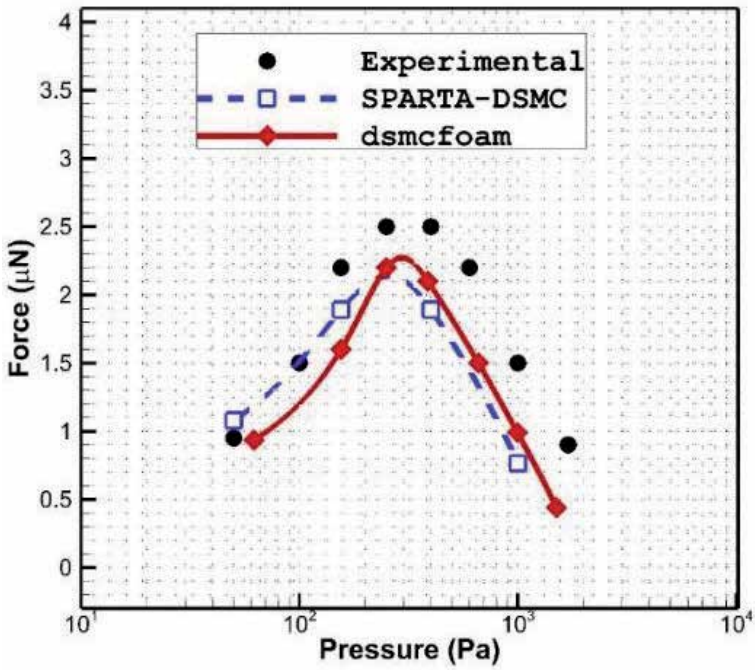

Figure 6.
Comparison of the obtained results (dsmcfoam) with experimental and numerical of Strongrich et al. [21].

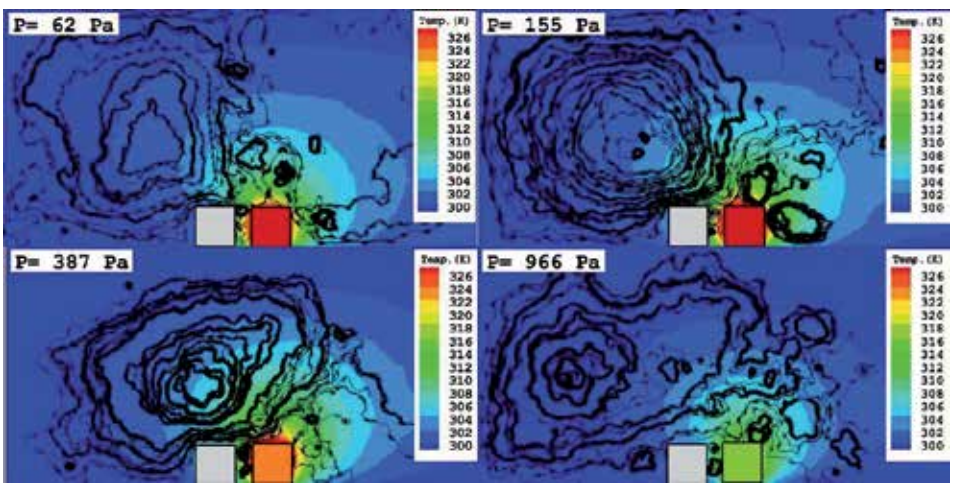

Figure 7.
Flow pattern and temperature distribution inside the MIKRA for different pressure conditions with real arm temperature [11].

when the real temperature is applied on the arms. As shown in the figures, the main characteristics of the flow feature significantly varies with change of the temperature. Since the main difference of flow structure inside the model is related to the temperature distribution, this study also considers the temperature distributions as well as flow pattern.

In low pressure (P = 62 Pa), one big circulation as well as a few small ones are noticed. As the pressure of the domain increases, three main circulations are observed in which two of them is on the top of the hot arm. The main circulation

fully covered the whole domain. It is significant to note that the temperature diffusion strengthen as the pressure of the domain is raised. In high pressure (P = 966 Pa), the temperature of the hot arm is not high enough and the number of the particles considerably increases. Due to these reasons, the diffusion of the temperature inside the domain highly declines. Therefore, the temperature gradient as the main source of the circulation reduces.

3.3 Effect of the temperature difference

As mentioned in the previous section, the effect of the temperature is significant in the performance of this type of micro gas sensor. In order to recognize the main effect of the temperature, constant temperature is applied for all pressure to investigate the effect of pressure (or number of particles) in the performance of the system. **Figure 4** compares the temperature contour along with streamline patterns for various operating pressures when the temperature of the hot and cold arm is fixed 350 and 300 K for all pressure domains, respectively. In this figure, hot arms are colored according to the temperature of particles in the vicinity of arms, while the temperature of the hot solid arm is 350 K. This coloring method improves the perceptibility of the temperature difference in various pressures.

As shown in **Figure 8**, the temperature diffusion to particles that exist in the vicinity of the hot arm increases by raising the pressure of the domain. Indeed, the number of the particles increases when the pressure is raised. Therefore, the particles interaction to hot surface increases in high pressure. The evaluation of the flow feature inside the micro gas sensor will reveal significant results. The main circulation inside domain occurs due to thermal creeping. As the pressure increases inside the model, the main circulation moves to the right side on the top of the gap. Contours clearly show that the strength of the circulation intensifies by growing the pressure till 387 Pa. Then, the circulation weakens inside the domain.

The temperature gradient alters meaningfully from the high pressure (P = 966 Pa) situation to rigorously rarefied (P = 62 Pa) case where noticeable kinks in the contour lines are perceived. These kinks are originated at the sharp angles on the top of the

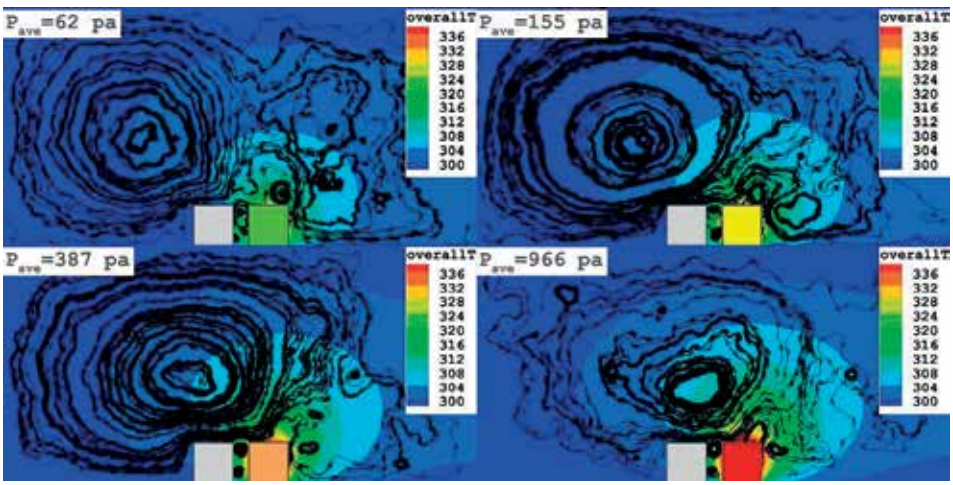

Figure 8.
Flow pattern and temperature distribution inside the MIKRA for different pressure conditions (T_{hot} = 350, T_{cold} = 300) [10].

arms. Dissimilar to the high-pressure conditions wherein intermolecular collisions promptly smooth out those kinks in the gap of the arms, the absence of adequate intermolecular collisions in the rarefied situations lets these kinks to diffuse much additional away from the hot arms as displayed in **Figure 7**. Therefore, the temperature of hot arm simply enters inside the domain and the noticeable temperature gradient observed in the vicinity of hot arm. In the next sections, it will be clarified how this temperature gradient influences on the induced flow field.

In order to recognize the main impact of the temperature in our problem, **Figure 9** illustrates the flow structure and temperature distribution inside the micro gas sensor in various temperature differences of 10, 30, 50, and 100 K at pressure of 387 Pa. Our findings reveal that the strength of the main circulation intensifies as the temperature difference of the hot and cold arm increases. It was predicted that this would occurs as the temperature gradient inside the model increases. One of important findings of this contour is the temperature penetration. In fact, temperature difference plays significant role on the particles direction. **Figure 10** shows the temperature distribution in the vicinity of the arms. The figure displays that the temperature gradient is intensive on the edges of the hot arm. In order to distinguish the induced flow pattern nearby of the edge, it is supposed that molecules within a mean free path away from

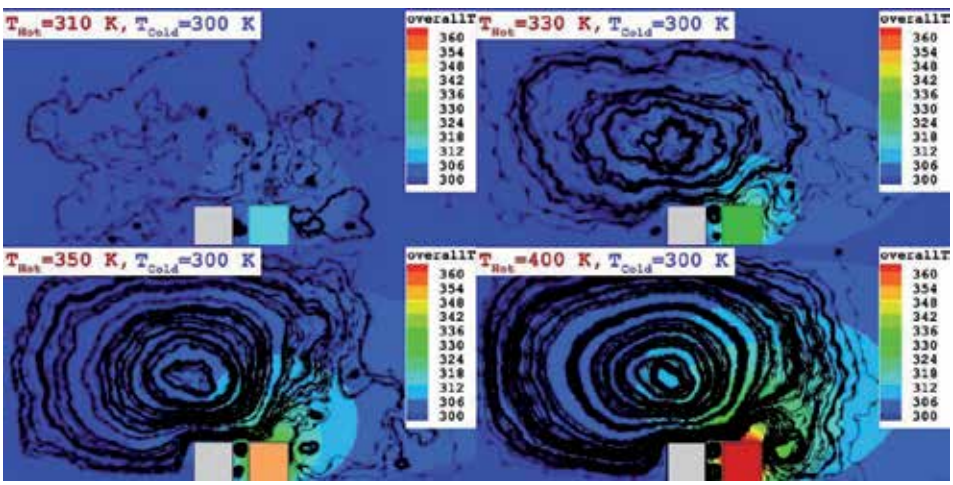

Figure 9.
Flow pattern and temperature distribution inside the MIKRA for different temperature differences (P = 387 Pa) [11].

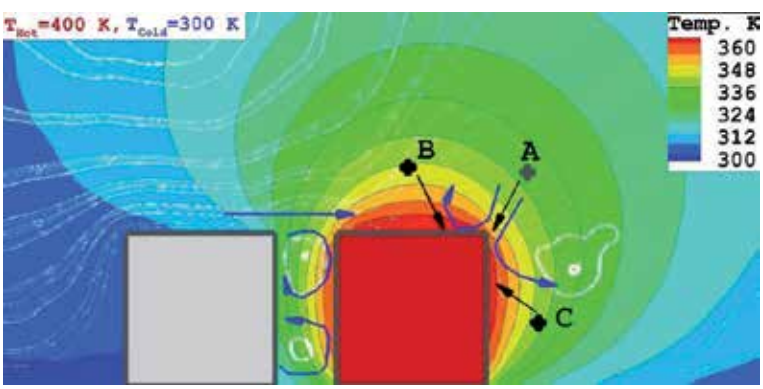

Figure 10.
Schematic illustration of the flow feature in the vicinity of the arms [11].

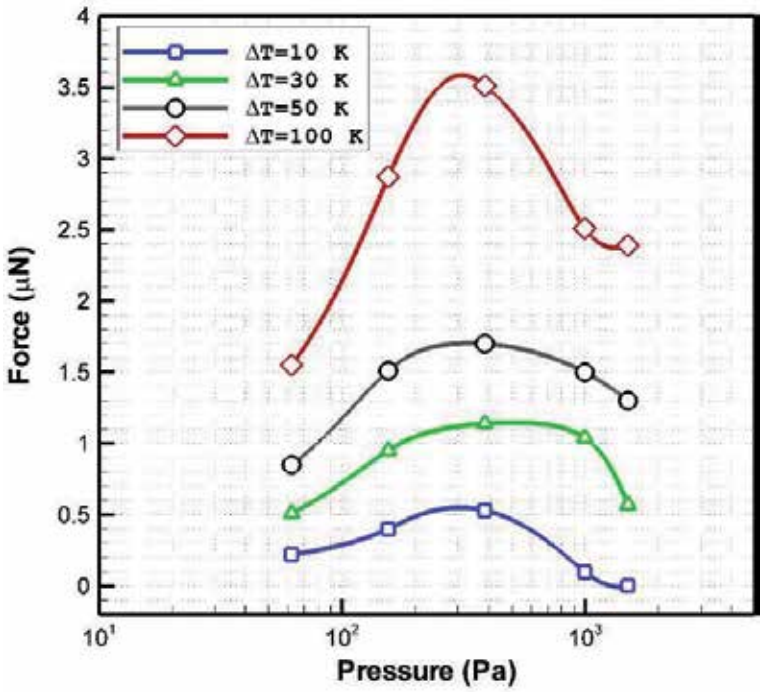

Figure 11.
Variation of the thermal Knudsen force in various temperature differences [11].

this area arrive at the surface without experiencing any intermolecular collision. As is shown in **Figure 6**, the temperature molecules coming from points B and C is high, while those from point A have low temperatures. Since the diffuse condition is applied as a function of the wall, the tangential velocity of the molecules after collision with the wall is related to the wall temperature. Hence, the tangential velocity of the cold molecules (A) highly increases while hot molecules (B and C) do not experience any change in their velocity. Therefore, the direction of cold molecules after collision is more dominant and they induce a vortex (blue lines) in the edge of the hot arm. Since the temperature of the cold arm is not varied, this flow is not observed on top of the cold arm.

Figure 11 plots the variation of the net force on the cold arm for various temperature differences of 10, 30, 50, and 100 K. Obtained results clearly demonstrate that main inflation occurs in the maximum Knudsen force.

In order to evaluate the primary factors on this micro gas sensor, the effect of force on the both sides of the cold arm is investigated. Since the exerted force should be normalized, Eq. (3) is applied to compare the change of the force as the ratio to exerted force when temperature difference is 10 K.

$$FR = 100 \times \left(\frac{F}{F_{\Delta T=10}}\right)_p. \tag{5}$$

Figure 12 illustrates the variation of the FR for various pressures of domain when the temperature of the hot arm is 30, 50, and 100 K. Comparison of the Knudsen force on both sides of the cold arm clearly reveals that FR declines on right side as the pressure of the domain is increased. This shows that the effect of molecular thermal force within gap is limited due to high interactions of molecules. On the other side, the Knudsen force on the left side of the increases with rising of the pressure of domain. This confirms that the influence of the thermal creeping on the

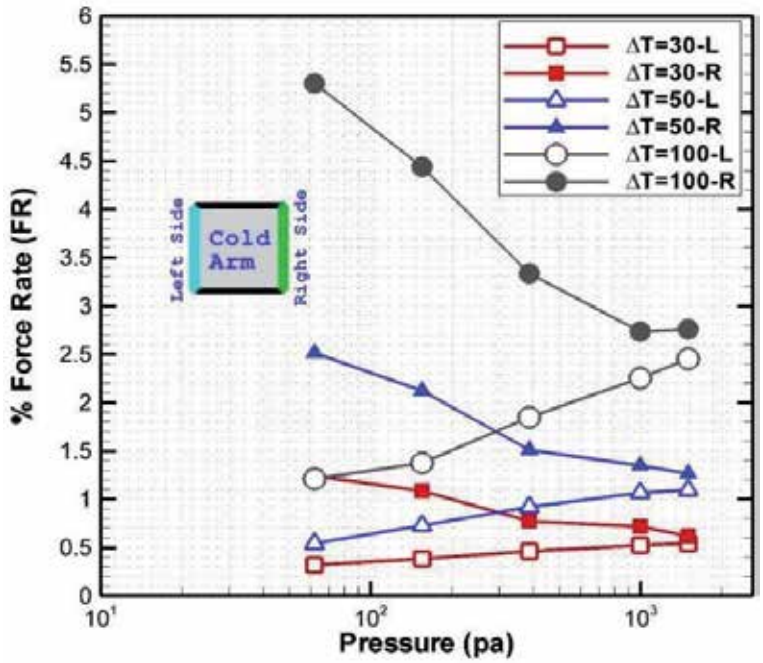

Figure 12.
Variation of the exerted force on hot and cold side [11].

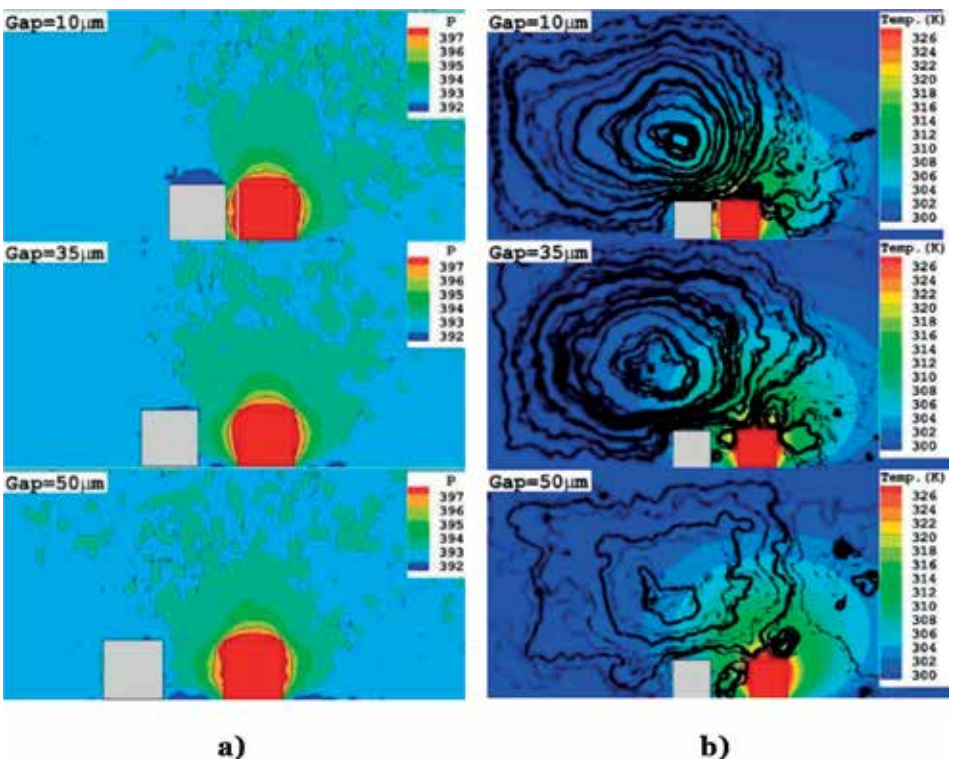

Figure 13.
Comparison of (a) normalized pressure (b) flow pattern and temperature distribution in various gap sizes [12].

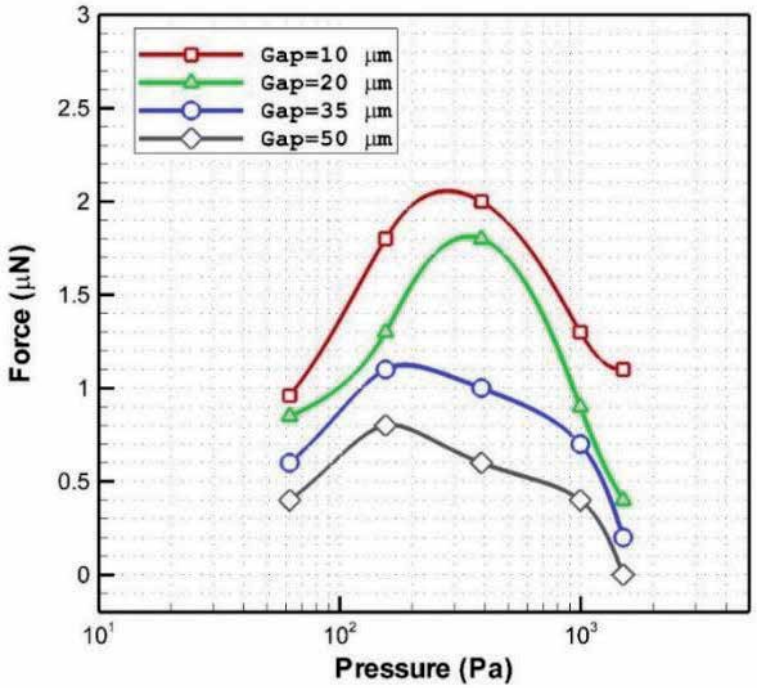

Figure 14.
Comparison of applied Knudsen force on the cold arm for various gap sizes [12].

left side is strengthened. Obtained results also indicate that the rate of FR augments with rising of the temperature difference of the hot and cold arm.

3.4 Effect of gap size

In order to determine the main characteristics of the each term, the pressure of the domain is normalized by the average pressure of domain as follows:

$$I = \frac{P}{P_{ave}}. \tag{6}$$

Since the gap size is crucial in the main characteristics of our problem, the impact of gap size on the normalized pressure and flow structure are depicted in **Figure 13a** and **b**, respectively. As the gap size increases in our model, the thermal creeping effect declines due to high gap of the hot and cold arm. Meanwhile, the number of small circulations increases inside the model.

Figure 14 illustrates the variation of the Knudsen thermal force on the cold arm. Our findings show that increasing the gap size declines the value of the exerted Knudsen force on the model. The variation of the Knudsen force on cold arm presents significant note about the value of the Knudsen number. Since the gap size is known as the specific length (l) in our model, change of this size significantly influence on the value and pressure of the maximum Knudsen force. In low gap size (10 μm), the maximum Knudsen force occurs at 600 Pa while it declines as the gap size is increased to 50 μm. The main impact of gap size on the Knudsen force could be noticed in the pressure distribution. As shown in **Figure 13a**, the pressure gradient hardly reach to the cold arm. This confirms that the pressure gradient is considerably significant on the exerted force.

4. Conclusions

In this study, a DSMC technique is used to investigate rarefied gas inside the low-pressure micro gas sensor. This research has dedicated on the impact of pressure in the flow structure and force generation mechanism. In order to simulate the defined model, Boltzmann equations as governing equations of the present problem are introduced and DSMC method as accessible and robust approach is then offered. The two main key factors are flow patterns and temperature distribution. In this work, these main parameters are compared in various pressures with different temperature of hot and cold arm. Moreover, inclusive physical details on the appliance of Knudsen force production as well as flow structure inside the micro gas actuator are offered. Our findings display that the performance of micro gas sensor highly relies on the temperature difference between hot and cold arms, and the maximum force occurs in specific pressure value for all different temperature difference. On the other side, the effect of gap size is considerable different. Obtained results show that the maximum force occurs in lower pressure as the size of gap is increased. It is also observed that the value of Knudsen force significantly declines when the gap size rises. According to our findings, application of the Knudsen force for the measurement of the gas pressure is a reliable technique and this micro gas actuator could be develop for possible detection of the gas component.

Conflict of interest

There is no conflict of interest in this paper.

Author details

Mostafa Barzegar Gerdroodbary
Department of Mechanical Engineering, Babol Noshirvani University of Technology, Babol, Iran

*Address all correspondence to: mbarzegarg@yahoo.com

IntechOpen

© 2019 The Author(s). Licensee IntechOpen. This chapter is distributed under the terms of the Creative Commons Attribution License (http://creativecommons.org/licenses/by/3.0), which permits unrestricted use, distribution, and reproduction in any medium, provided the original work is properly cited. CC BY

References

[1] Wu CH, Kang D, Chen PH, Tai YC. MEMS thermal flow sensors. Sensors and Actuators A: Physical. 2016;**241**:135-144

[2] Vigne S, Alava T, Videlier H, Mahieu R, Tassetti CM, Duraffourg L, et al. Gas analysis using a MEMS linear time-of-flight mass spectrometer. International Journal of Mass Spectrometry. 2017;**422**:170-176

[3] Mirzaei M, Poozesh A. Simulation of fluid flow in a body-fitted grid system using the lattice Boltzmann method. Physical Review E. 2013;**87**(6):063312

[4] Verma VK, Yadava RD. Stochastic resonance in MEMS capacitive sensors. Sensors and Actuators B: Chemical. 2016;**235**:583-602

[5] Grzebyk T, Górecka-Drzazga A. MEMS type ionization vacuum sensor. Sensors and Actuators A: Physical. 2016;**246**:148-155

[6] Gerdroodbary MB, Ganji DD, Taeibi-Rahni M, Pruiti B, Moradi R. Development of Knudsen thermal force for mass analysis of CH4/He gas mixture. International Journal of Modern Physics C. 2019;**30**(01):1-16

[7] Sarabi S, Bogy DB. Effect of functional end-groups on lubricant reflow in heat-assisted magnetic recording (hamr). Tribology Letters. 2017;**65**(1):15

[8] Mahyari A, Barzegar Gerdroodbary M, Mosavat M, Ganji DD. Detection of ammonia gas by Knudsen thermal force in micro gas actuator. Case Studies in Thermal Engineering. 2018;**12**:276-284

[9] Barzegar Gerdroodbary M, Ganji DD, Moradi R, Abdollahi A. Application of Knudsen thermal force for detection of CO2 in low-pressure micro gas sensor. Fluid Dynamics. 2018;**53**(6):795-806

[10] Gerdroodbary MB, Ganji DD, Taeibi-Rahni M, Vakilipour S, Moradi R. Application of direct simulation Monte Carlo for development of micro gas sensor. Bulgarian Chemical Communications. 2018;**50**(2):298-305

[11] Gerdroodbary MB, Ganji DD, Taeibi-Rahni M, Vakilipour S. Effect of Knudsen thermal force on the performance of low-pressure micro gas sensor. The European Physical Journal Plus. 2017;**132**(7):315

[12] Gerdroodbary MB, Ganji DD, Taeibi-Rahni M, Vakilipour S. Effect of geometrical parameters on radiometric force in low-pressure MEMS gas actuator. Microsystem Technologies. 2018;**24**(5):2189-2198

[13] Gerdroodbary MB, Anazadehsayed A, Hassanvand A, Moradi R. Calibration of low-pressure MEMS gas sensor for detection of hydrogen gas. International Journal of Hydrogen Energy. 2018;**43**(11):5770-5782

[14] Gerdroodbary MB, Mosavat M, Ganji DD, Taeibi-Rahni M, Moradi R. Application of molecular force for mass analysis of krypton/xenon mixture in low-pressure MEMS gas sensor. Vacuum. 2018;**150**:207-215

[15] Gerdroodbary MB, Ganji DD, Shiryanpour I, Moradi R. Mass analysis of CH_4/SO_2 gas mixture by low-pressure MEMS gas sensor. Journal of Natural Gas Science and Engineering. 2018;**53**:317-328

[16] Hassanvand A, Gerdroodbary MB, Moradi R, Amini Y. Application of Knudsen thermal force for detection of inert gases. Results in Physics. 2018;**9**:351-358

[17] Ketsdever A, Gimelshein N, Gimelshein S, Selden N. Radiometric phenomena: From the 19th to the 21st century. Vacuum. 2012;**86**(11):1644-1662

[18] Crookes W. On attraction and repulsion resulting from radiation. Philosophical Transactions of the Royal society of London. 1874;**164**:501-527

[19] Strongrich AD, O'Neill WJ, Cofer AG, Alexeenko AA. Experimental measurements and numerical simulations of the Knudsen force on a non-uniformly heated beam. Vacuum. 2014;**109**:405-416

[20] Strongrich A, Alexeenko A. Microstructure actuation and gas sensing by the Knudsen thermal force. Applied Physics Letters. 2015;**107**:193508

[21] Strongrich AD, Pikus AJ, Sebastiao IB, Peroulis D, Alexeenko AA. Low-pressure gas sensor exploiting the knudsen thermal force: Dsmc modeling and experimental validation. In: 2016 IEEE 29th International Conference on Micro Electro Mechanical Systems (MEMS) (IEEE, 2016). pp. 828-831

[22] Passian A, Warmack RJ, Ferrell TL, Thundat T. Thermal transpiration at the microscale: A Crookes cantilever. Physical Review Letters. 2003;**90**(12):124503

[23] Passian A, Wig A, Meriaudeau F, Ferrell TL, Thundat T. Knudsen forces on microcantilevers. Journal of Applied Physics. 2002;**92**(10):6326-6333

[24] Passian A, Warmack RJ, Wig A, Farahi RH, Meriaudeau F, Ferrell TL, et al. Observation of Knudsen effect with microcantilevers. Ultramicroscopy. 2003;**97**(1):401-406

[25] Lereu AL, Passian A, Warmack RJ, Ferrell TL, Thundat T. Effect of thermal variations on the Knudsen forces in the transitional regime. Applied Physics Letters. 2004;**84**(6):1013-1015

[26] Sista SV, Bhattacharya E. Knudsen force based MEMS structures. Journal of Micromechanics and Microengineering. 2014;**24**:045003

[27] Kaajakari V, Lal A. Thermokinetic actuation for batch assembly of microscale hinged structures. Journal of Microelectromechanical Systems. 2003;**12**:425-432

[28] Aoki K, Sone Y, Yano T. Numerical analysis of a flow induced in a rarefied gas between noncoaxial circular cylinders with different temperatures for the entire range of the Knudsen number. Physics of Fluids A: Fluid Dynamics. 1989;**1**(2):409-419

[29] Zhu T, Ye W. Origin of Knudsen forces on heated microbeams. Physical Review E. 2010;**82**:036308

[30] McNamara S, Gianchandani YB. On-chip vacuum generated by a micromachined Knudsen pump. Journal of Microelectromechanical Systems. 2005;**14**:741

[31] Sarabi S, Bogy DB. Effect of viscoelasticity on lubricant behavior under heat-assisted magnetic recording conditions. Tribology Letters. 2018;**66**(1):33

[32] Sarabi MS, Bogy DB. Simulation of the performance of various PFPE lubricants under heat assisted magnetic recording conditions. Tribology Letters. 2014;**56**(2):293-304

[33] Sheikholeslami M, Gerdroodbary MB, Moradi R, Shafee A, Li Z. Application of neural network for estimation of heat transfer treatment of Al_2O_3-H_2O nanofluid through a channel. Computer Methods in Applied Mechanics and Engineering. 2019;**344**:1-12

[34] Fallah K, Gerdroodbary MB, Ghaderi A, Alinejad J. The influence of micro air jets on mixing augmentation of fuel in cavity flameholder at supersonic flow. Aerospace Science and Technology. 2018;**76**:187-193

[35] Gerdroodbary MB, Imani M, Ganji DD. Investigation of film cooling on nose cone by a forward facing array of micro-jets in hypersonic flow. International Communications in Heat and Mass Transfer. 2015;**64**:42-49

[36] Moradi R, Mosavat M, Barzegar Gerdroodbary M, Abdollahi A, Amini Y. The influence of coolant jet direction on heat reduction on the nose cone with Aerodome at supersonic flow. Acta Astronautica. 2018;**151**:487-493

[37] Gerdroodbary MB, Imani M, Ganji DD. Heat reduction using conterflowing jet for a nose cone with Aerodisk in hypersonic flow. Aerospace Science and Technology. 2014;**39**:652-665

[38] Hassanvand A, Barzegar Gerdroodbary M, Fallah K, Moradi R. Effect of dual micro fuel jets on mixing performance of hydrogen in cavity flameholder at supersonic flow. International Journal of Hydrogen Energy. 2018;**43**(20):9829-9837

[39] Barzegar Gerdroodbary M, Younes Amini DD, Ganji MRT. The flow feature of transverse hydrogen jet in presence of micro air jets in supersonic flow. Advances in Space Research. 2017;**59**:1330-1340

[40] Gerdroodbary MB, Sheikholeslami M, Valiallah Mousavi S, Anazadehsayed A, Moradi R. The influence of non-uniform magnetic field on heat transfer intensification of ferrofluid inside a T-junction. Chemical Engineering and Processing-Process Intensification. 2018;**123**:58-66

[41] Vo DD, Moradi R, Gerdroodbary MB, Ganji DD. Measurement of low-pressure Knudsen force with deflection approximation for gas detection. Results in Physics. 2019;**30**(1):1-16

[42] Epstein PS. Theorie des radiometers. Zeitschrift für Physik. 1929;**54**:537-563

[43] Einstein A. Zur theorie der radiometrerkrafte. Zeitschrift für Physik. 1924;**27**:1-5

[44] Schuster A. On the nature of the force producing the motion of a body exposed to rays of heat and light. Proceedings. Royal Society of London. 1875;**24**:391-392

[45] Brüche E, Littwin W. Experimental contributions to the radiometer question. Zeitschrift für Physik. 1928;**52**:318-335

[46] Scandurra M, Iacopetti F, Colona P. Gas kinetic forces on thin plates in the presence of thermal gradients. Physical Review E. 2007;**75**:026308

[47] Selden N, Ngalande C, Gimelshein N, Gimelshein S, Ketsdever A. Origins of radiometric forces on a circular vane with a temperature gradient. Journal of Fluid Mechanics. 2009;**634**:419-431

[48] Bird GA. Molecular Gas Dynamics and the Direct Simulation of Gas Flows. Oxford: Clarendon Press; 1994

[49] OpenFOAM: The Open Source CFD Toolbox, User Guide, Version 1.6. 2009

Chapter 3

Optical Gas Sensors Using Terahertz Waves in the Layered Media

Borwen You and Ja-Yu Lu

Abstract

Terahertz (THz) wave propagation in the layered media is presented based on the waveguide and artificial-material configurations to sense the gas molecules. The single dielectric layer with a cylindrical conformation works as a pipe waveguide in the wave frequency of 0.1–1 THz. For a long-distance propagation over 10 cm of the pipe, resonant modes are characterized from the transmission power dips. The pipe-waveguide resonator works for a THz refractive-index sensor when the resonance frequency is monitored to sense vapor molecules inside the pipe core. Besides of the waveguide configuration, a multilayer microporous polymer structure (MPS) is considered an artificial material to transmit THz waves for sensing gaseous molecules. The MPS is not only transparent to THz waves but also enhances the detection resolution of THz absorption for the vapor molecules. The porous structure provides a large hydrophilic surface area and numerous micropores to adsorb or fill vapors, thereby leading to greatly enhanced wave-analyte interaction with an apparent THz signal change. Different concentrations of toxic methanol adulterated in alcoholic aqueous solutions are thus identified in their vapor phases by using the MPS-based THz sensor.

Keywords: terahertz wave, optical sensor, waveguide, terahertz spectroscopy, polymers, multilayers, and fiber optics sensor

1. Introduction

Gas sensing for pollutant monitoring and leaky molecules detection is important when the environmental issues on breath health are revealed. Various gas sensors based on different principles are presented, such as the gas chromatography-mass spectroscopy [1–3], electrochemical [4], and optical sensors. For the electrochemical sensors [5, 6], the high sensitivity is requested from the high operation temperature, which is risky for explosive gas detection due to the high-power consumption at electrodes. The optical sensing scheme can solve the unsafe problem because of the room-temperature operation without electric contact [7–9]. THz radiation, which lies between the infrared ray (IR) and microwave regions, can strongly perturb polar gas molecules with the energy level transitions of rotation or vibration. The absorption strength of gas molecules in the THz frequency range is typically on the same order of magnitude as the IR region, and is $\sim 10^3$–10^6 stronger than that in the microwave region [10]. The low photon energy of the THz wave is

IntechOpen

relatively safer than that of IR wave and has the stronger interaction response than that in the microwave region [11–13].

THz gas sensing methods have been demonstrated based on two main styles. The first style is normally illuminating THz radiation directly on the gaseous analytes and acquiring their spectral response for the sensing purposes. For example, the strong absorption lines at specific frequencies (i.e., fingerprint spectra) or the pulse power decay within one certain THz spectral width have been applied to analyze the gaseous analytes [14]. Such the sensing performance are presented from the photo-mixing [15], heterodyne detection [3, 16], and chirped-pulse THz spectroscopy [12]. Such the spectroscopic systems successfully analyze the gas mixtures of more than 30 chemicals [3] and distinguish gases that possess similar compositions. This recognition scheme provides high selectivity based on the rotational/vibrational transition of gas molecules. Nevertheless, the THz spectroscopic system should be equipped with a long gas cell [3, 12, 14], a cryo/sorbent pre-concentration system, and a heating apparatus [3, 16] to improve the sensing limit from the ppm concentration to the ppb level. The overall configuration is complicated, bulky, expensive, and consumes high power. Although the quantum cascade laser is presented as a compact THz laser source for gas sensing applications to simplify THz wave generation [17]. However, the THz laser source should be operated in the low-temperature condition and is limited for practical applications.

The other method of THz gas sensing is to use the THz resonance field in the photonic or periodic structures [18, 19]. For example, one- and two-dimensional photonic structures respectively based on the silicon slabs [18] and pillar arrays [19] have been validated for the non-specific gas sensing in the THz frequency range. The proposed photonic structures have high-quality factors on THz field resonance and are sensitive to slight changes of refractive index. The demonstrated detection limit for hydrogen gas is about 6% concentration change [18]. The approved minimum detectable amount of oxygen or argon is ~1 μmol [19]. Although the resonator-type THz gas sensor is relatively compact, portable, and consumes low power, its short interaction length inside the chip essentially leads to the limited sensitivity and poor selectivity.

In this chapter, THz gas sensors with sufficiently long interaction lengths are presented based on THz wave propagation along the dielectric layers. The layered media specifically perform the enhancement of THz resonance and absorption in the dielectric waveguides and porous structures, respectively. The interaction between THz wave and gas analytes thus becomes efficient. The presented waveguide sensor contributes the detection of THz refractive index variation based on the resonator principle of Fabry-Pérot (FP) etalon, and the porous structures detect vapor molecules based on the response of molecular dipole moment for THz wave absorption.

2. Gas sensors based on THz refractive-index detection

2.1 Pipe-waveguide resonator

One dielectric layer bent to be a cylindrical structure can be used as one hollow core waveguide to guide THz waves. Those dielectric pipes or tubing used for THz pipe waveguides are available from the hydroelectric materials and demonstrated in the literatures [20]. In the study, a 30 cm-long glass pipe is used to load 0.05 cm^3 liquid analytes to evaporate and fill the pipe core. When THz waves input and pass through the glass-pipe core, the vapor molecules interact with the THz wave for the sensing purpose.

The cylindrical layer acts as a FP etalon, and THz waves satisfying the FP resonance condition enables field resonance inside the cylindrical layer, which becomes leaky to form multiple transmission dips. Based on the FP criteria, the resonant wavelength of THz waves in the cylindrical layer is defined as, $\lambda_m = 2d\sqrt{n_{cld}^2 - n_{cor}^2}/\mathrm{m}$, where λ_m, d, m, n_{cld}, and n_{cor} are, respectively, the m^{th}-order resonant wavelengths, thicknesses of a cylindrical layer, orders of the resonant modes, and effective waveguide refractive indices of cylindrical layer and the pipe core [21]. **Figure 1** shows the transmission spectrum of a blank glass pipe, where the spectral dips with low power represent the FP resonant waves along the glass layer. The measured resonant frequencies are approximate to the calculated results via finite-difference time-domain (FDTD) method. The cross section of the glass-pipe sensor is shown in the inset of **Figure 1**, where the inner core diameter D_{in} and the thickness of pipe-wall are 5.57 and 1.17 mm, respectively. The refractive indices of the air-core and glass used in simulation are 1 and 2.6 [17], respectively. There are five spectral dips of the glass-pipe waveguide in the transmission spectrum, 0.2–0.5 THz (**Figure 1**), which are 0.201, 0.266, 0.326, 0.392 and 0.452 THz frequencies. According to resonance condition of FP etalon, the resonant dip frequency changes with n_{cor}, and thus various vapors can be identified in the hollow core by detecting the spectral shifts of the resonant dips.

THz resonant fields inside the cylindrical layer must be sufficiently evanescent toward the air core to make the pipe-waveguide resonator sensitive to the vapor molecules. Interaction between the THz resonant field and the vapor molecules is therefore enhanced, consequently resulting in the sensitive detection. Based on the investigation of THz dielectric pipe waveguides, the high order resonance waves have strong evanescent field inside the pipe core [22]. That is, the resonance dips at the high frequency range have stronger core field than those at the low frequency range. The resonant dip at 0.452 THz as shown in **Figure 1** is thus suitable to probe vapors within the glass pipe core because of the powerful resonant field to interact vapor molecules.

2.2 Vapor sensing principle and results

To approve the sensing principle of a pipe waveguide sensor, the vapor molecules of the water, hydrochloric acid (HCl), acetone and ammonia liquids are used

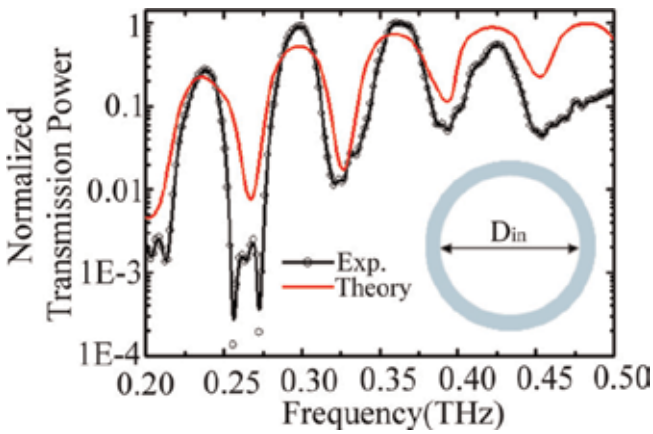

Figure 1.
Transmission spectra of a glass-pipe waveguide: (inset) the cross section of a glass-pipe-waveguide sensor (reprinted from Opt. Express 20, 5858-5866 (2012). © 2012 OSA.

as the standard analytes. The sensing results show that the spectral dip of 0.452 THz obviously shifts toward the high frequency range when various vapors fill in the pipe core (**Figure 2a**). The spectral dip position is shifted to 0.461, 0.465 and 0.477 THz, respectively, for the HCl, acetone and ammonia vapors. Based on the measured spectral dips and FDTD calculation method (**Figure 2b**), the related effective refractive indices of the pipe core ($n_{eff.core}$) are obtained as shown in **Figure 2c**. The core indices of the glass pipe are 1.016, 1.035 and 1.102 for the vapors of HCl, acetone and ammonia, respectively (**Figure 2c**).

The dip-frequency-shift only occurs at the resonance dip of 0.452 THz and the other resonance dips in the low-frequency range do not exhibit any spectral shift for sensing the vapors, which is different from the calculated results in **Figure 2b**. The zero spectral-shift for the low-frequency-dips comes from the low strength of leaky resonance field at the pipe core. It is too weak to sense the presence of vapor molecules. This performance implies that the resonant fields for detecting vapors in the pipe core require high transmission power to identify slight core-index variation for the low densities of vapors. This low sensitivity phenomenon without any significant spectral shift is straightforward correlated to all the anti-resonant fields, i.e., the spectral peaks at the frequency lower than 0.52 THz.

Figure 2c shows the relation between the spectral dip frequencies and the $n_{eff.core}$ values for different vapors inside the pipe core. The dip frequencies increase with the $n_{eff.core}$ values. The increment effect of $n_{eff.core}$ arises from the various vapor pressures of the volatile liquids, which are generated from the 0.05 cm^3 liquid volume. High vapor pressure represents large amounts of vapor molecules inside the pipe core. Therefore, the vapor pressures of volatile liquids are approximately proportional to the quantities of vapor molecules in the sealed pipe core. The high density of the vapor molecules in the pipe core results in the large $n_{eff.core}$, and the resonant dip of 0.452 THz has an apparent blueshift.

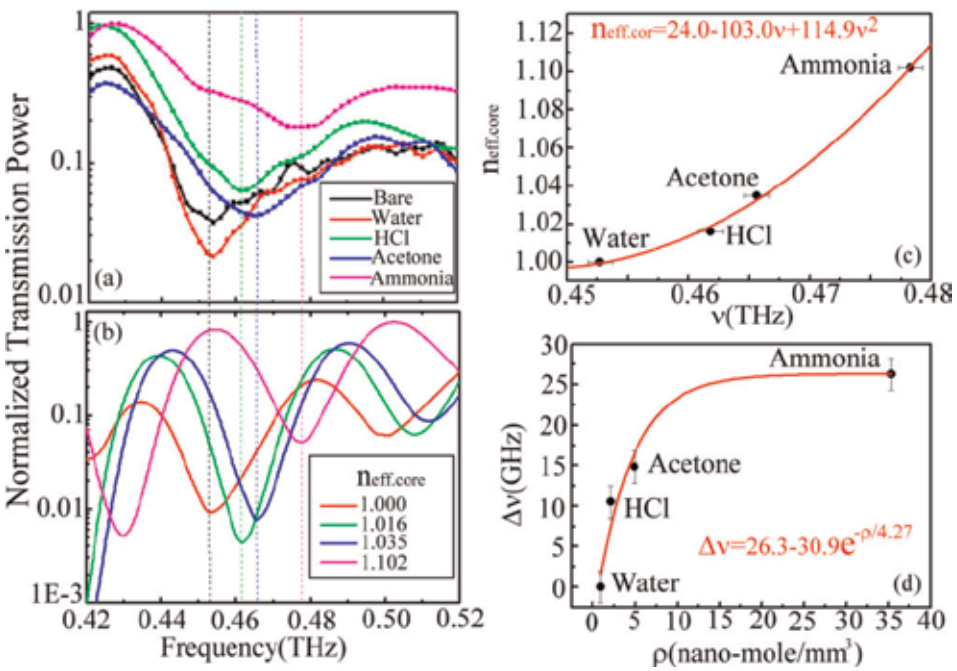

Figure 2.
The spectral dip shift of (a) sensing results and (b) FDTD calculation for different vapors. (c) Relation between $n_{eff.cor}$ *and ν for different vapors. (d) Relation between spectral dip shift and the estimated vapor densities (reprinted from Opt. Express 20, 5858-5866 (2012). © 2012 OSA).*

The $n_{eff.cor}$ value versus the resonance frequency can be fit by curve of $n_{eff.cor} = 24 - 103\nu + 114.9\nu^2$ (**Figure 2c**). The slight index variation could thus be estimated via this fitting cure to identify the molecules in the pipe core. However, the water analyte in the pipe core cannot contribute any spectral shift because the density of water vapor is quite low. The sensing result is reasonable because the vapor pressures of water, HCl, acetone and ammonia at normal atmosphere and room temperature are, respectively, around 17 [23], 38 [24], 202 [24] and 308 [23] mm-Hg.

For qualitative analysis, the vapor molecules discussed in this work are assumed as the ideal gases and their densities in the enclosed pipe would be calculated based on the ideal gas law. **Figure 2d** illustrates the relation of molecular density (ρ) and spectral dip shift ($\Delta\nu$), which can be fit as $\Delta\nu = 26.3 - e^{-\rho/2.7}$. **Figure 2d** illustrates that the blueshift relative to 0.452 THz frequency gradually saturates when the vapor density is over 10 nano-mole/mm^3. The saturation response eventually reduces the sensitivity of the pipe sensor. Based on the spectral resolution of 4 GHz and the fitting curve in **Figure 2d**, the minimum detectable molecular quantity would be around 7.8 μmole, corresponding to a molecular density of 1.6 nano-mole/mm^3.

3. Gas sensors based on THz absorption detection

3.1 Microporous polymer structures (MPSs)

Besides of the single cylindrical layer, multiple layers of MPS can be used as a THz gas sensor. The sensing mechanism of THz wave is monitored from THz absorption of gas molecules, different from the refractive-index detection of the pipe-waveguide resonator. A MPS gas sensor is integrated from multiple layers of polyethylene terephthalate (PET) mesh (SEFAR PET1000, SEFAR AG, Switzerland). To collect and seal the gaseous analytes, MPS is assembled with one microfluidic chamber, which is made of Teflon material. As shown in **Figure 3a** and **b**, a PET mesh is flexible and consists of periodical square holes. PET mesh layers are stacked and fixed by a rectangular acrylic holder to form a MPS structure. There are large numbers of micropores (i.e., square air holes) in one MPS and the micropores are random inside the composite.

Figure 3c shows the schematic diagram of the THz gas sensor based on a MPS device and a microfluidic chamber. The MPS sensor is compact and low loss for THz waves, different from the bulky gas chambers. A flexible plastic tubing to the fluidic

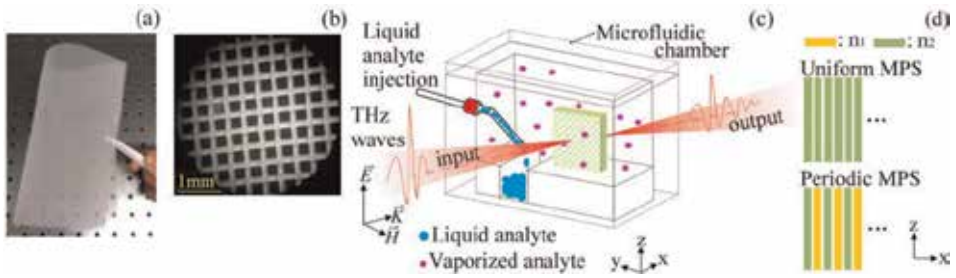

Figure 3.
(a) Macroscopic and (b) microscopic photographs of a PET mesh. (c) The scheme of a MPS volatile gas sensor. (d) Uniform and periodic configurations of the MPSs in the x-z *plane (reprinted from Opt. Express 25, 5651-5661 (2017). © 2017 OSA).*

channel is externally connected with the sample chamber for easy control of the liquid analyte and its vapor. The inner volume of the chamber is larger than the MPS dimension and sealed to easily achieve the saturated pressure of vapor analyte. The inner chamber has a width of 21 mm (x-axis), a length of 60 mm (y-axis), and a height of 45 mm (z-axis). One fluidic channel (18 mm long in x-axis, 5 mm wide in y-axis, and 3 mm deep in z-axis) is machined at the bottom of the Teflon chamber for loading the liquid analytes that are injected via the external tubing. The liquid analytes evaporate, becoming vapors, and diffuse into the MPS. In the volatile gas sensing experiment, the sample loading and sensing processes are performed at room temperature and normal atmosphere without enforcing pump or additional heating process.

To study the sensing performance dependent on the MPS dimensions, four kinds of PET meshes with different thicknesses and square micropore sizes are stacked into two MPS configurations, which are the uniform and periodic structures (**Figure 3d**). The micropores of each PET meshes in a MPS were not precisely aligned with each other when the PET layers are randomly placed layer by layer for both uniform and periodic MPSs. The periodic MPS is constructed by alternately stacking two kinds of PET meshes that have different micropore sizes. In the other way, the uniform MPS is made by stacking only one kind of PET mesh. Different micropore sizes of PET meshes represent different porosities or different effective refractive indices (e.g., n_1 and n_2 in **Figure 1d**). To investigate the pore size effect for the vapor sensitivity, large- and small-pore MPSs are prepared in both the uniform and periodic structures using the four kinds of PET meshes.

In the geometric designs, large-pore periodic MPS is composed by the PET meshes with 90 and 249 μm pore widths, denoted as *Periodic-90-249 MPS*. *Periodic-45-133 MPS* represents the small-pore periodic MPS, possessing 45 and 133 μm pore widths of the PET meshes. Similarly, the small- and large-pore uniform MPSs are denoted as *Uniform-45* and *Uniform-90 MPSs*, respectively. Their pore widths of the composed PET meshes are 45 and 90 μm, respectively. The specifications of the applied MPS devices are list in **Table 1**, including the pore width, mesh thickness, stacking layer number, device thickness, and effective porosity.

MPS No.	Pore width (μm)	PET mesh thickness (μm)	Layer number	MPS thickness (mm)	Effective porosity (%)
Periodic-90-249	249	200	23	3.46	40.5
	90	50			
Periodic-45-133	133	100	6	0.45	37.2
	45	50	34	2.55	
			46	3.45	
Uniform-90	90	100	23	2.3	30.1
Uniform-45	45	50	6	0.3	29.6
			12	0.6	
			34	1.7	

Reprinted from Opt. Express 25, 5651-5661 (2017). © 2017 OSA.

Table 1.
MPS specification.

3.2 Sensing principle

The effective absorption coefficients and refractive indices of MPS micropores are observed in the sensing process to distinguish different types and concentrations of volatile gases. The transmitted power spectra of the microporous structure with and without vapor analytes are defined as follows,

$$P_{v+p}(\omega) = P_0(\omega)e^{-2\alpha_{v+p}(\omega)L}, \tag{1}$$

$$P_p(\omega) = P_0(\omega)e^{-2\alpha_p(\omega)L}. \tag{2}$$

The subscripts p and $v + p$ in the Eqs. (1) and (2) represent the sample chamber without and with vapor analytes, respectively. $P_0(\omega)$, $\alpha(\omega)$, and L mean the power of input THz wave, effect absorption coefficients of micropores, and thickness of the multilayer-stacked device, respectively. Based on the effective medium concept, the effective absorption coefficient of MPS that is defused with vapor analytes can be written as,

$$\alpha_{v+p} = \alpha_v f + \alpha_{PET}(1-f). \tag{3}$$

For the blank structure, the effective absorption coefficient is defined as,

$$\alpha_p = \alpha_{air} f + \alpha_{PET}(1-f). \tag{4}$$

In Eqs. (3) and (4), the factors of f, α_v, α_{air}, and α_{PET} indicate the air filling ratio of micropore volume, the absorption coefficients of vapor analyte, air, and PET material, respectively. α_{v+p} and α_v in Eqs. (1) and (2) are substituted by Eqs. (3) and (4). The absorption coefficient variation $(\alpha_v - \alpha_{air})$ is consequently shown as,

$$\alpha_v - \alpha_{air} = \left[\ln\left(P_p/P_{v+p}\right)\right]/(2fL). \tag{5}$$

The value of $(\alpha_v - \alpha_{air})$ approximates to α_v because the THz wave absorption of air is as small as 10^{-5} cm^{-1} [25]. Thus, the absorption coefficient of vapor (α_v) can be obtained in the approximate condition. The effective medium concept to express the absorption coefficients of the micropore in Eqs. (4) and (5) represents the absorption value within the unit pore space/volume. We thus denote α_{eff} as the vapor absorption coefficient instead of α_v to emphasize the critical assumption of effective medium idea (Eq. (6)).

$$\alpha_{eff} = \left[\ln\left(P_p/P_{v+p}\right)\right]/(2fL). \tag{6}$$

Furthermore, the phase difference for the unit pore volume with and without vapors in the MPS can be defined as $(\Delta\phi/V_{pore})$, where $\Delta\phi = \phi_{v+p} - \phi_p$ and V_{pore} are the phase difference for MPS with-without vapors and the total pore volume, respectively. The phase difference $\Delta\phi$ and the total volume of MPS, V_{pore}, can be individually estimated from Eqs. (7) and (8),

$$\Delta\phi = (\omega/c)\cdot\Delta n\cdot L, \tag{7}$$

$$V_{pore} = A_{beam}\cdot f\cdot L. \tag{8}$$

Δn, ω, c, and A_{beam} are the refractive index variation, angular frequency, light speed in vacuum and input THz beam size on the MPS structure, respectively. The phase difference for the unit volume of micropore is thus presented as,

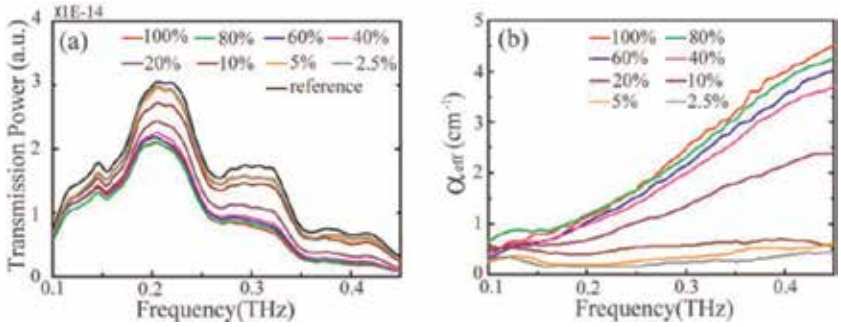

Figure 4.
(a) Power transmission spectra and (b) the corresponding effective absorption coefficient spectra within the unit volume of micropore for various aqueous acetone concentrations (reprinted from Opt. Express 23, 2048-2057 (2015). © 2015 OSA).

$$\Delta\phi/V_{pore} = (\omega/c)\cdot\frac{\Delta n}{(A_{beam}\cdot f)}. \tag{9}$$

Based on Eq. (9), we consider the effective refractive index variation of the unit pore volume, Δn_{eff}, correlating to the macroscopic version of refractive index variation, Δn, as

$$\Delta n_{eff} = \frac{\Delta n}{(A_{beam}\cdot f)}. \tag{10}$$

The macroscopic variation of refractive index (Δn) can be obtained from Eq. (9) as,

$$\Delta n = \frac{c}{\omega}\cdot A_{beam}\cdot f\cdot\frac{\Delta\phi}{A_{beam}\cdot f\cdot L} = \frac{c\cdot\Delta\phi}{\omega\cdot L}. \tag{11}$$

Eq. (10) is then substituted by Eq. (11) and re-written as,

$$\Delta n_{eff} = \frac{c\cdot\Delta\phi}{A_{beam}\cdot f\cdot L\cdot\omega}. \tag{12}$$

The effective refractive index variation within the unit volume of micropore (Δn_{eff}) can eventually be extracted from the phase information of the measured THz waveforms ($\Delta\phi$) and the pore volume that is radiated by the THz-wave beam spot. That is, $V_{pore} = A_{beam}\,L\,f$. Based on the sensing principle as shown in Eqs. (1)–(12), the detected THz fields within the unit pore volume of micropore are measured and compared with and without vapors infiltration in the scheme (**Figure 3c**). Because of the transparent property of PET material in THz frequency, the scattering loss of surface roughness along the propagation axis can be excluded.

3.3 Volatile gas sensing abilities

The *Periodic-90-249 MPS* device was used to study the volatile gas sensing abilities of MPS and observed for the α_{eff} response under different amounts of acetone vapor exposure. **Figure 4a** illustrates THz power transmission spectra of the *Periodic-90-249 MPS* before and after exposure to different concentrations of acetone vapor. The THz spectra are apparently identified for acetone aqueous

solutions with concentrations from 2.5 to 100%. In the sensing scheme (**Figure 3a**), all the acetone aqueous solutions naturally evaporate until the vapor pressure is saturated in the chamber. According to the Raoult's law [26], the aqueous acetone concentration is approximately proportional to the vapor pressure. That is, the large concentration of acetone aqueous solution generates a large acetone vapor pressure. The increased amount of acetone vapor results in power reduction in the THz frequency range of 0.1–0.45 THz (**Figure 4a**).

Figure 4b presents the α_{eff} spectra under different concentrations of acetone vapor exposure, which is extracted from the parameters of spectral transmittance, MPS thickness of 3.46 mm, and the micropore filling ratio, 40.5% (Eq. (6)). The absorption coefficient increases with THz frequency and vapor molecular density. Based on the ideal gas formula and vapor pressures of acetone aqueous solutions, the vapor densities of acetone (ρ) can be obtained. The vapor pressures for different concentrations of acetone solutions are estimated based on the experimental database in [27] and not by using Raoult's law.

THz time-domain spectroscopy (THz-TDS) was used to integrate MPS devices to observe the sensing performance of 0.10–0.45 THz waves. **Figure 4b** shows the extracted α_{eff} values obviously achieve the largest distinction at 0.4 THz. Above 0.4 THz frequency, the signal-to-noise ratio is too low for the vapor sensing. Therefore, we apply the 0.4 THz wave to probe α_{eff} and Δn_{eff} that are responded from the vapor molecules in the MPS devices. Based on the spectroscopic curves of α_{eff} in **Figures 4b** and **5a** and **b** illustrate the sensing results of 0.4 THz wave to detect different concentrations of acetone vapors with and without using the MPS inside the chamber, respectively.

The α_{eff} and Δn_{eff} values of THz wave apparently rise within an acetone vapor density (ρ) of 6 nmol/mm^3 and become saturated while ρ is about 6–14 nmol/mm^3. This trace trends between α_{eff} and Δn_{eff} versus ρ are consistent. It implies that the increased acetone vapor molecules not only significantly absorb the THz wave (represented by α_{eff}) but also introduce considerable phase retardation in the THz electric field oscillation (represented by Δn_{eff}). The high ρ value certainly makes the infiltration of vapor molecules into the micropores and increases the molecular adsorption capacity of the hydrophilic surface [28]. The acetone vapor molecules, confined in the micropores and adsorbed on the pore surface of MPSs, consequently cause the increment of α_{eff} and Δn_{eff}.

The α_{eff} responsivity in **Figure 5a** can be fit by the Langmuir adsorption isotherm with a high R^2 value (>97%). The Langmuir fitting indicates that the monolayer adsorption of acetone vapor molecules on the hydrophilic microporous surface is

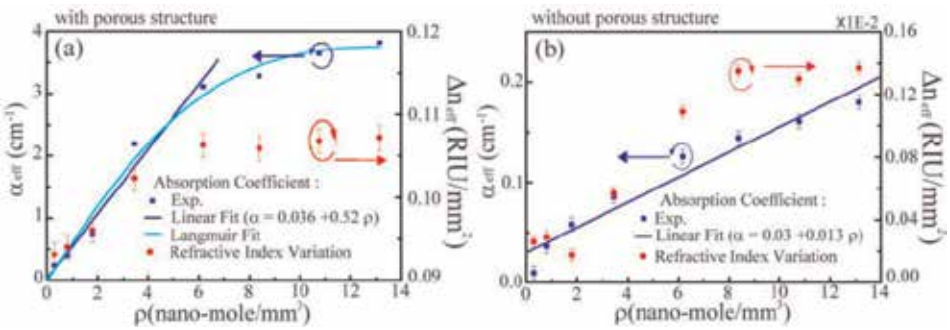

Figure 5.
Detecting the effective absorption coefficients (blue square dot) and refractive index variation (red circular dot) at 0.4 THz for various acetone vapor densities (a) with and (b) without the Periodic-90-249 MPS. *The blue and cyan curves indicate the mathematical fit of the proportional relationship and the Langmuir adsorption isotherm, respectively (reprinted from Opt. Express 23, 2048-2057 (2015). © 2015 OSA).*

mainly caused by physisorption. For the molecular density of <6 nmol/mm^3, the proportional response of the 0.4 THz wave absorption versus the acetone vapor density can be linearly fit as $\alpha = 0.036 + 0.52\rho$ and considered the sensitive region of the sensor, which is denoted by the blue line in **Figure 5a**. The lowest detected concentration of acetone vapor is 291 pmol/mm^3, which is indicated as the first data point of **Figure 5a** and corresponding to 17 ppm. From the slope of the linear fitting curve and α_{eff} inaccuracy (about 0.01–0.02 cm^{-1}), the minimum detectable concentration change of acetone vapor is <108 pmol/mm^3, which is equivalent to 6.29 ppm. Therefore, MPS are particularly advantageous for minute vapor sensing with a detection limit of low ppm level.

Figure 5b shows the sensing results for different ρ values inside the blank chamber without MPS. For the same ρ, the α_{eff} and Δn_{eff} values inside the blank chamber are smaller than those measured with the MPS. The air-filling ratio (f) quals 100% when we obtain α_{eff} and Δn_{eff} for the blank chamber and based on Eqs. (6) and (10). The MPS enhances the THz absorption about 20 times higher than that in the blank chamber (**Figure 5a** and **b**). In addition, the Δn_{eff} in MPS is two orders of magnitude larger than that in the blank chamber for the same ρ. Both α_{eff} and Δn_{eff} slowly increase with vapor density and without the saturation effect for the blank chamber sensing, which is contrast to the MPS condition.

For an acetone liquid concentration of 100% (~13 nmol/mm^3 vapor molecules), the absorption coefficient at 0.4 THz is ~0.18 cm^{-1} in **Figure 5b**, which is on the same order and reasonably agreed with the published value of 0.45 cm^{-1} in [29]. According to the slope of the linear fitting curve in **Figure 5b** and the system uncertainty of α_{eff}, the minimum detectable molecular density variation of acetone vapor is ~0.558 nmol/mm^3, which equals 32.37 ppm. This result reveals that the sensitivity of volatile gas detection by the MPS is higher than that by a traditional THz-TDS system. Given that the MPS can congregate volatile vapors inside the micropores and adsorb on the hydrophilic surface, the interaction strength between THz radiation and polar gas molecules can be enhanced via the adsorbent medium to significantly increase the absorption and index variations.

The sensing ability of MPS is additionally approved to detect other volatile organic compounds (VOCs), including methanol, ethanol, and ammonia. For the three vapors, both the 0.4 THz α_{eff} and Δn_{eff} increase with vapor densities (**Figure 6**). The trends are approximate to the sensing result of acetone vapor (**Figure 5**), but the saturation responses of α_{eff} and Δn_{eff} are different. The *Periodic-90-249 MPS* exhibits obvious differences of α_{eff} and Δn_{eff} among the three VOCs

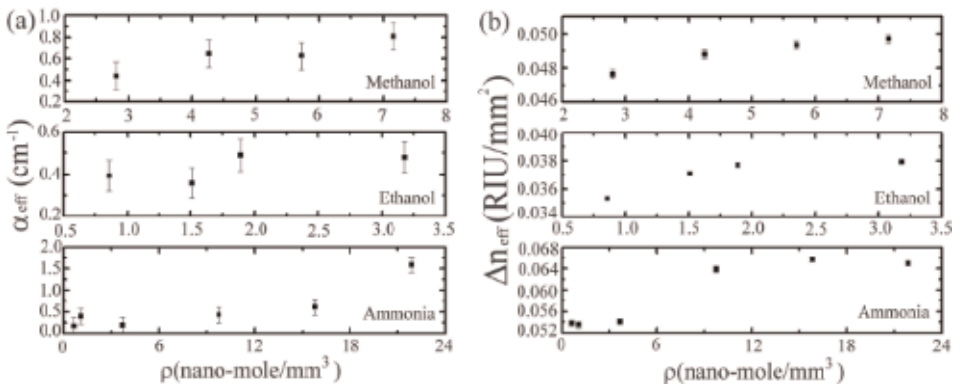

Figure 6.
Detecting (a) effective absorption coefficients and (b) refractive index variations at 0.4 THz for different densities of methanol, ethanol, and ammonia vapors by the Periodic-90-249 MPS *(reprinted from Opt. Express 23, 2048-2057 (2015). © 2015 OSA).*

(**Figure 6**), which are responded from the enhanced adsorption and infiltration of vapors in the micropores. In this sensing configuration of MPS, capillary condensation of vapors does not occur in the micron-sized pores for all vapor species [30, 31].

The 0.4 THz α_{eff} values for different concentrations of acetone, methanol, ethanol, and ammonia vapor exposures are summarized in **Figure 7a**. The magnitude order from the largest to smallest α_{eff} values is ketone, alcohol and ammonia. The linear fitting curves, denoted by the dashed lines in **Figure 7a**, represent the molecular responses of the MPS microporous to the vapor analyte. The sensing ability of MPS is significant to identify the three VOC classes. Each type of vapor has a distinct α_{eff} curve that can be used to distinguish from other vapors. THz radiation can strongly perturb the dipole moment of a VOC, and predominantly induce molecular motion to increase the THz absorption coefficients. Based on the investigation in **Figure 7b**, the magenta columns present magnitudes of the dipole moments of the four polar vapors in the following order: ketone > alcohol > ammonia [32]. The order of molecular dipole moment is approximate to the magnitude sequence of the THz absorption coefficients (**Figure 7a**). The THz interaction strength of acetone vapor is higher than those of the other vapors. Methanol and ethanol vapors belong to alcoholic VOCs and have similar THz absorption coefficients in the MPS. The sensitivities of MPS for detecting the four vapors can be evaluated when considering the linear fitting slopes and the system inaccuracies of α_{eff}. The detection limit (i.e., detectable molecular densities) of acetone, methanol, ethanol, and ammonia vapors using the *Periodic-90-249 MPS* sensor are 0.125, 1.71, 1.62, and 3.35 nmol/mm^3, respectively, which are denoted by the blue columns in **Figure 7b**. The sensing scheme of MPS device not only recognizes minute concentration changes of VOC with picomolar sensitivity but also exhibits excellent discrimination for different polar VOCs.

3.4 Geometry-dependent sensitivity: micropore size effect

To study the micropore size effect of MPS on the detection sensitivity, the pore number of the MPSs to interact a THz beam is fixed and only the pore width is changed. In **Table 1**, the micropore number of the 23-layered *Periodic-90-249 MPS* is consistent with that of the 6-layered *Periodic-45-133 MPS*, but the pore width of the former device is two times larger than the latter device. These two MPSs are compared to observe the pore-size-dependent sensitivity performance. Similarly,

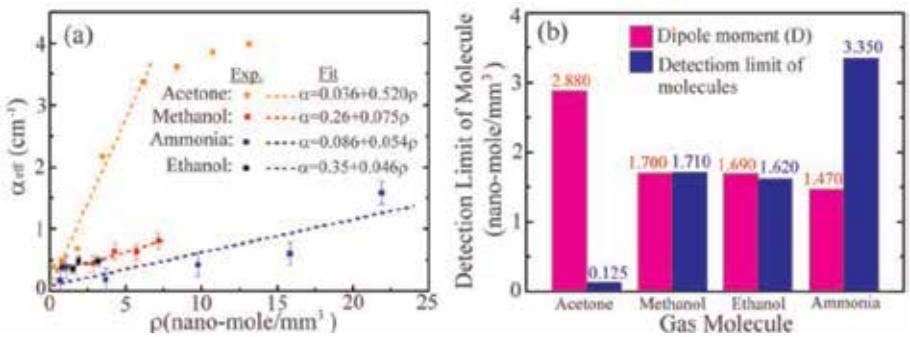

Figure 7.
(a) Detecting the effective absorption coefficients at 0.4 THz under different vapor densities. (b) Investigation of dipole moments and detection limits of the molecular densities (reprinted from Opt. Express 23, 2048-2057 (2015). © 2015 OSA).

the 23-layered *Uniform-90 MPS* and 6-layered *Uniform-45 MPS* devices, having an identical pore number but different pore sizes, are also prepared for this test purpose.

Here is the operation detail to observe the sensitivity dependent on the micropore size effect. The micropore amounts within the THz beam spot for the periodic and uniform MPSs are fixed, and the micropore sizes of both structures are changed to compare their sensitivities in terms of α_{eff} and Δn_{eff}. Regarding the periodic MPS configuration, the small-pore structure (*Periodic-45-133*, average porosity ~37.2%), composed of 6-layered meshes and corresponding to a 0.45 mm thickness, has ~1900 micropores covered by the THz beam. To maintain the same pore quantity in *Periodic-90-249 MPS* (average porosity ~40.5%) under the same THz beam spot, the large-pore mesh of *Periodic-90-249* should be stacked up to 23 layers, corresponding to 3.46 mm thickness. For the MPS uniform configuration, the micropore number covered by the THz beam spot in the 6-layered *Uniform-45 MPS* (porosity ~29.6% and thickness ~0.3 mm) is around 3600. To keep the identical micropore number in the *Uniform-90 MPS* under the same THz beam spot, the *Uniform-90* mesh (i.e., a mesh with the large micropores) with 30.1% porosity should be stacked by 23 layers, corresponding to a 2.3 mm thickness.

The sensitivity of different MPS can be measured by the exposure of the MPS to different VOC amounts, and the THz linear responses in effective absorption and refractive index variation are related to the molecular dipole moment of the VOC (**Figure 7**). In this study, acetone vapor molecule is thus applied as the standard VOC to calibrate the sensitivity performance of MPS because its high dipole moment (~2.88 Debye [33]) is easily perturbed by THz waves. That is, obvious THz electromagnetic attenuation or dispersion can be performed from the acetone vapor molecules. Different amounts of acetone vapor are prepared from different volume concentrations of acetone aqueous solutions, including 2.5, 5, 10, 20, 40, 60, 80, and 100%. All the acetone aqueous solutions are individually loaded inside the microfluidic chamber to naturally evaporate into vapor phase under ambient atmosphere/room temperature until the saturated vapor pressures are approached. The vapor pressure inside the chamber is approximately proportional to the aqueous acetone concentration, following the experiment design in **Figures 4**–**7**.

Figure 8a and **b** present the α_{eff} and Δn_{eff}, respectively, detected by the *Periodic-45-133* and *Periodic-90-249 MPSs*. In **Figure 8a**, the absorption coefficients in the large (*Periodic-90-249*)—and small (*Periodic-45-133*)-pore MPSs both proportionally increase within a molecular density of about 6 nmol/mm^3 and become saturated at high vapor density. The trace trends of refractive-index variations (Δn_{eff}) shown

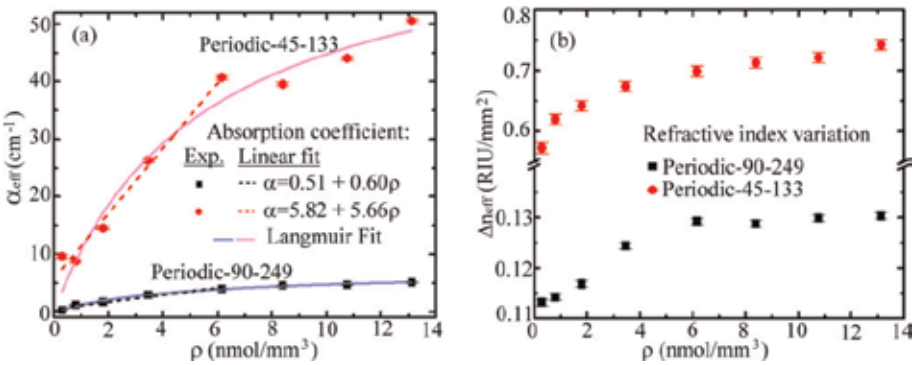

Figure 8.
Detecting (a) effective absorption coefficients and (b) refractive index variations at 0.4 THz within the unit pore volume by the Periodic-45-133 *and* Periodic-90-249 MPSs *(reprinted from Opt. Express 25, 5651-5661 (2017). © 2017 OSA).*

in **Figure 8b** are similar to those of the absorption coefficients (α_{eff}) (**Figure 8a**), except that the saturation phenomenon of Δn_{eff} for the small-pore structure, *Periodic-45-133* MPS, occurs at a much lower vapor density (~2 nmol/mm^3) compared with that of the large-pore structure, *Periodic-90-249* MPS (~6 nmol/mm^3). The comparison results in **Figure 8** show that the α_{eff} and Δn_{eff} of *Periodic-45-133 MPS* for all vapor densities are much larger than those of *Periodic-90-249* MPS. For example, the absorption coefficients of *Periodic-90-249* and *Periodic-45-133 MPSs* (**Figure 8a**) at the vapor molecular density of 13 nmol/mm^3 are around 4 and 50 cm^{-1}, respectively. Further shrinking the micropore volume under a certain vapor density exposure is able to increase the molecular occupied densities, which are confined in the micropore and adsorbed on the pore surface to increase THz wave absorption and phase retardation. The enhancement in α_{eff} and Δn_{eff} of *Periodic-45-133 MPS* is attributed to its small pore size, whereas its pore quantity is identical to that of *Periodic-90-249 MPS*.

The Langmuir adsorption isotherms in **Figure 8a** mean the physisorption of acetone monolayer both occurs on the large and small micropore surfaces of MPS. For the molecular density, <6 nmol/mm^3 (~350 ppm), the THz responsivity of the proportional relation between α_{eff} and ρ in **Figure 8a** are linearly fitted and can be regarded as the sensitive region of the MPS vapor sensor. The α_{eff} of *Periodic-45-133 MPS* increases more rapidly than that of *Periodic-90-249 MPS* within the sensitive region (ρ < 350 ppm). The minimum detectable concentration changes of acetone vapor for the *Periodic-90-249* and *Periodic-45-133 MPS* sensors determined from the system deviation and responsivity slope in **Figure 8** are estimated as less as 108 and 54 pmol/mm^3, corresponding to 6.29 and 3.11 ppm, respectively. The detection limit of *Periodic-45-133 MPS* is two times higher than that of *Periodic-90-249 MPS*, thereby indicating that a decrease in micropore volume (such as half of the pore width) obviously raises the detection sensitivity of the MPS gas sensor.

Figure 9a and **b** show the vapor sensing results of *Uniform-90* and *Uniform-45 MPSs*, respectively. The detected α_{eff} and Δn_{eff} both have linear responsivity versus the vapor density and become saturated at a high vapor density, approximate to the trace trends of the periodic MPSs as shown in **Figure 8**. However, the saturation vapor density of the two uniform MPSs is about 4 nmol/mm^3 (i.e., 200 ppm), and lower than that of the periodic MPSs, which is about 6 nmol/mm^3 or 350 ppm. The THz absorption coefficient curves of *Uniform-90* and *Uniform-45 MPSs* are also well fitted by Langmuir adsorption isotherms with high R^2 values (**Figure 9a**), respectively. According to the slopes of the linear fitting curves in the sensitive region

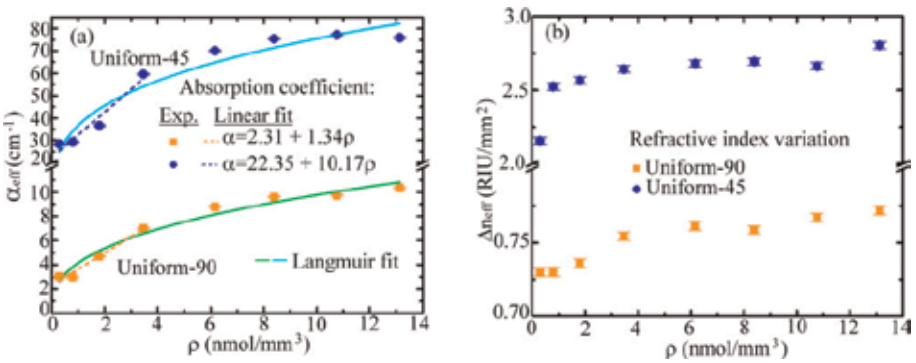

Figure 9.
Detecting (a) effective absorption coefficients and (b) refractive index variations at 0.4 THz within the unit pore volume by the Uniform-45 *and* Uniform-90 MPSs *(reprinted from Opt. Express 25, 5651-5661 (2017). © 2017 OSA).*

(i.e., $\rho < 200$ ppm) and the measurement inaccuracy of the THz absorption coefficient, the minimum detectable concentration changes of acetone vapor using *Uniform-90* and *Uniform-45 MPS* gas sensors are <46 and 31 pmol/mm^3, corresponding to 2.68 and 1.83 ppm, respectively.

The detection sensitivity of *Uniform-45 MPS* is apparently higher than that of *Uniform-90 MPS*, consistent to the comparison result between *Periodic-90-249* and *Periodic-45-133 MPSs*. The performance emphasizes again that half of the pore width, whether periodic or uniform configuration, facilitates the infiltration and adsorption of acetone vapor in the micropores and on the pore surface, leading to an enhanced vapor-field interaction to increase the sensitivity. In addition, the two uniform MPSs in **Figure 9** have obviously higher α_{eff} and Δn_{eff} than those of the periodic MPSs in **Figure 8** under the same vapor density exposure. For example, the largest THz absorption coefficient of *Uniform-45 MPS* is around 80 cm^{-1} and evidently larger than 50 cm^{-1} of *Periodic-45-133 MPS* based on the same 6-layered MPS thickness. The responsivity of linear fitting slopes in **Figures 8** and **9** presents that the two sensing parameters, α_{eff} and Δn_{eff}, of uniform MPSs are increased more rapidly within a narrower sensitive region compared with those of periodic MPSs. It means only fewer amounts of vapor molecules that infiltrate the uniform MPSs can drastically increase the THz absorption coefficient and refractive index variation until the desired chamber saturation is achieved. The average pore width of *Uniform-90/-45 MPS* is smaller than that of *Periodic-90-249/-45-133 MPS* under the similar MPS thickness (i.e., the same stacked layer number of the PET microporous mesh). Therefore, the simple uniform MPS is particularly advantageous for minute vapor sensing with a detection limit of even lower ppm level compared with the periodic MPS.

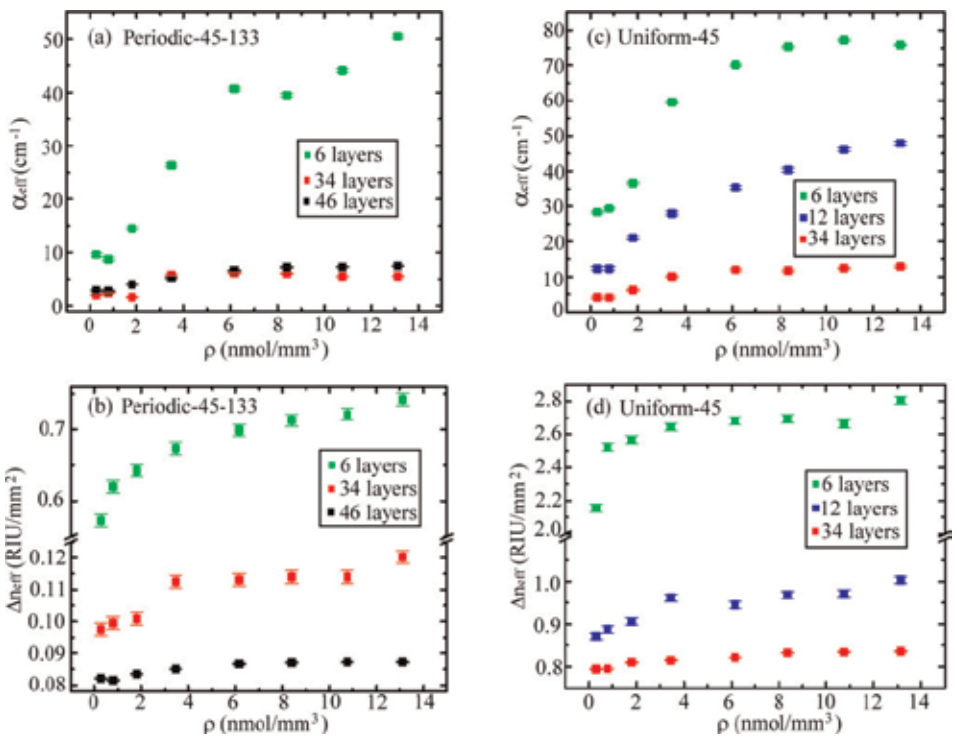

Figure 10.
Detecting (a, c) effective absorption coefficients and (b, d) refractive index variations within unit pore volume by Periodic-45-133 *and* Uniform-45 MPSs *with different thicknesses (reprinted from Opt. Express 25, 5651-5661 (2017). © 2017 OSA).*

3.5 Geometry-dependent sensitivity: micropore number effect

The pore number effect on MPS sensitivity is studied by changing the stacking layer numbers of *Periodic-45-133* and *Uniform-45 MPSs*. As shown in **Table 1**, three different layer numbers of MPSs with identical pore size are prepared for sensitivity comparison in both the *Periodic-45-133* and *Uniform-45 MPSs*. **Figure 10** shows α_{eff} and Δn_{eff} for *Periodic-45-133* and *Uniform-45 MPSs*, which are the small-pore MPSs, respectively, with periodic and uniform configurations. Each type of MPS possesses three kinds of thicknesses formed by stacking different layer numbers of PET mesh. The α_{eff} and Δn_{eff} of *Periodic-45-133 MPS* for 6-layered thickness are evidently larger than those of 34- and 46-layered thicknesses under all vapor densities (**Figure 10a** and **b**). For the response of *Uniform-45 MPS*, both α_{eff} and Δn_{eff} are increased with decreasing device thickness from 34 layers to 12 and 6 layers (**Figure 10c** and **d**). The highest sensitivities for the periodic and uniform MPSs occur in their thinnest conditions (i.e., 6-layered structure). The experiment in this case indicates that the small pore numbers also increase THz wave responses in α_{eff} and Δn_{eff} of the micropores, thereby enhancing the vapor detection sensitivity.

Under a constant amount of vapor exposure, increasing pore quantity or size is equivalent to expanding the pore volume of the microporous structure. The vapor density, congregated within the micropore and adsorbed on the hydrophilic surface, is thus diluted and eventually decreases the measured values in α_{eff} and Δn_{eff}. **Figure 10** also shows that 6-layered *Uniform-45 MPS* requires less acetone vapor amounts to saturate the responsivities of α_{eff} and Δn_{eff} because of its less micropore volume/number, comparing to those of 12- or 34-layered *Uniform-45 MPS*. The vapor saturation density of 6-layered *Uniform-45 MPS* occurs at around 4 nmol/mm^3 (i.e., 200 ppm), indicating the dynamic range of linear responsivity is sufficiently wide for minute vapor detection.

3.6 Sensing applications

The micropore size dependent sensitivity of the four types of MPSs is summarized in **Table 2**, where the sensitivity corresponds to the slope of linear fit. The blank chamber represents the vapor sensing performance of the microfluidic chamber without the MPS. It is THz vapor sensing in the free space measured by traditional THz-TDS. The *Uniform-45 MPS* with a 6-layered thickness has the highest sensitivity, down to 1 ppm-level acetone vapor molecule. Such the sensitivity is more excellent than that of the 23-layered *Periodic-90-249 MPS* and much higher than that of blank chamber.

MPS No.	Layer number	Error bar at 0.4 THz (cm^{-1})	Sensitivity (cm^{-1}/nmol mm^{-3})	Detection limit (ppm)
Periodic-90-249	23	0.065	0.60	6.288
Periodic-45-133	6	0.303	5.66	3.105
Uniform-90	23	0.062	1.34	2.683
Uniform-45	6	0.320	10.17	1.825
Blank chamber	0	0.007	0.013	32.37

Reprinted from Opt. Express 25, 5651-5661 (2017). © 2017 OSA.

Table 2.
Sensing performance of MPS for acetone vapor detection.

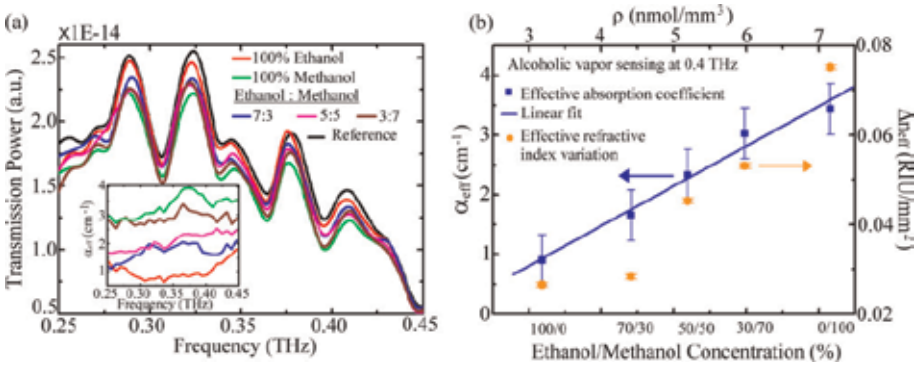

Figure 11.
(a) THz-wave transmission spectrum for sensing toxic methanol adulterated in alcoholic solutions: (inset) detecting THz absorption coefficient spectra by the 6-layered Unifrom-45 *MPS. (b) Detecting absorption coefficient and refractive index variation versus different concentrations of adulterated alcoholic aqueous solutions at 0.4 THz (reprinted from Opt. Express 25, 5651-5661 (2017). © 2017 OSA).*

The 6-layered *Uniform-45 MPS* can thus be used for identifying toxic methanol adulterated in alcoholic solutions. Adulterated alcoholic solutions are prepared by mixing different volume ratios of methanol with ethanol, including 1:0, 7:3, 5:5, 3:7, and 0:1 (ethanol/methanol). The adulterated alcoholic solution is injected into the microfluidic channel of the sealed microfluidic chamber, as shown in **Figure 3c**, and becomes the vapor molecules via natural evaporation to be detected by THz waves. **Figure 11a** illustrates the THz transmission spectrum of *Uniform-45 MPS* exposed to the vaporized mixtures, which are generated from various concentrations of adulterated alcoholic solutions. THz transmission power apparently decreases in the frequency range of 0.25–0.45 THz as the volume ratio of methanol increases. The THz absorption coefficient spectra for the different concentrations of adulterated alcoholic vapors can be estimated and shown in the inset of **Figure 11a**. The measured THz absorption coefficients for each concentration of alcoholic vapor are almost constant in the frequency range of 0.25–0.45 THz. The relatively high absorption coefficients are resulted from the increment of the adulterated methanol concentration. The refractive index variation before and after exposure to different concentrations of alcoholic vapors can also be calculated. **Figure 11b** plots the relations of the α_{eff} and Δn_{eff} at 0.4 THz against different concentrations of alcoholic aqueous solutions. The α_{eff} and Δn_{eff} increase with the methanol concentration adulterated in the alcoholic solution. The proportional relation of α_{eff} and ρ is linearly fitted as $\alpha_{eff} = 1.2 + 0.67\rho$. The sensing result of **Figure 11** reveals that the colorless and high THz-absorbed alcoholic aqueous solutions with different concentrations of toxic methanol adulteration can be easily distinguished using the MPS gas sensor composed of 6-layered *Uniform-45 MPS*.

4. Conclusions

Optical gas sensors are experimentally demonstrated using the THz refractive indices and THz absorption coefficients when THz waves propagating through the dielectric-layer media are monitored in a spectroscopic system (THz-TDS). The cylindrical layer is applied from a glass dielectric pipe to be the waveguide resonator. Based on the FP criteria and FDTD simulation, the THz frequency of pipe-waveguide resonance field is approximately proportional to the refractive index of the pipe core. The experimental results present that only the high-order

resonant modes are sensitive to the refractive-index variation due to the high evanescent power toward the pipe core. Different analytes with different vapor pressures, such as water, HCl, acetone and ammonia, are thus identified by a pipe-waveguide resonator. To further improve the detection sensitivity and selectivity, the MPS structures are applied as 1 THz artificial material to adsorb vapor molecules. THz absorption coefficients of the unit volume are defined based on the effective medium concept and demonstrated to identify various vapor molecules in the investigation. The molecular dipole moment dominates THz absorption in the unit volume of micropore when several analytes, such as the acetone, methanol, ethanol and ammonia, are test in one MPS sensor. The sensing performance based on the MPS geometry is studied for the sensitivity and the possible detection limit. For the acetone molecule, the 6-layered *Uniform-45 MPS* sensor has the high sensitivity and the detection limit is potentially down to 1.8 ppm. The 6-layered *Uniform-45 MPS* sensor is eventually applied for one sensing application to distinct methanol and ethanol vapor molecules from various liquid mixtures. The MPS sensing scheme is therefore applicable to realize one optical gas sensor.

Acknowledgements

This work was supported by grants-in-aid for scientific research from the Ministry of Science and Technology of Taiwan (MOST 107-2221-E-006-183-MY3) and Japan Society for the Promotion of Science (JSPS, KAKENHI, JP16K17525).

Author details

Borwen You[1] and Ja-Yu Lu[2*]

1 Department of Applied Physics, Faculty of Pure and Applied Sciences, University of Tsukuba, Tsukuba, Ibaraki, Japan

2 Department of Photonics, National Cheng Kung University, Tainan, Taiwan

*Address all correspondence to: jayu@mail.ncku.edu.tw

IntechOpen

© 2019 The Author(s). Licensee IntechOpen. This chapter is distributed under the terms of the Creative Commons Attribution License (http://creativecommons.org/licenses/by/3.0), which permits unrestricted use, distribution, and reproduction in any medium, provided the original work is properly cited.

References

[1] Spanel P, Smith D. Selected ion flow tube: A technique for quantitative trace gas analysis of air and breath. Medical & Biological Engineering & Computing. 1996;**34**:409

[2] Phillips M, Herrera J, Krishnan S, Zain M, Greenberg J, Cataneo RN. Variation in volatile organic compounds in the breath of normal humans. Journal of Chromatography B. 1999;**729**:75

[3] Fosnight AM, Moran BL, Medvedev IR. Chemical analysis of exhaled human breath using a terahertz spectroscopic approach. Applied Physics Letters. 2013; **103**:133703

[4] Kanan SM, El-Kadri OM, Abu-Yousef IA, Kanan MC. Semiconducting metal oxide based sensors for selective gas pollutant detection. Sensors-Basel. 2009;**9**:8158-8196

[5] Wang L, Kalyanasundaram K, Stanacevic M, Goum P. Nanosensor device for breath acetone detection. Sensor Letters. 2010;**8**:1-4

[6] Chang SJ, Hsueh TJ, Chen IC, Hsieh SF, Chang SP, Hsu CL, et al. Highly sensitive ZnO nanowire acetone vapor sensor with Au adsorption. IEEE Transactions on Nanotechnology. 2008; **7**:754-759

[7] Chu R, Guan C, Bo Y, Shi J, Zhu Z, Li P, et al. All-optical graphene-oxide humidity sensor based on a side-polished symmetrical twin-core fiber Michelson interferometer. Sensors and Actuators B: Chemical. 2019;**284**: 623-627

[8] Romanovskii OA, Sadovnikov SA, Kharchenko OV, Yakovlev SV. Development of near/mid IR differential absorption OPO lidar system for sensing of atmospheric gases. Optics and Laser Technology. 2019;**116**: 43-47

[9] Kanawade R, Kumar A, Pawar D, Vairagi K, Late D, Sarkar S, et al. Negative axicon tip-based fiber optic interferometer cavity sensor for volatile gas sensing. Optics Express. 2019;**27**: 7277-7290

[10] Mittleman D. Sensing with Terahertz Radiation. Heidelberg, Berlin: Springer-Verlag; 2003. pp. 39-115

[11] Mittleman DM, Jacobsen RH, Neelamani R, Baraniuk RG, Nuss MC. Gas sensing using terahertz time domain spectroscopy. Applied Physics B: Lasers and Optics. 1998;**67**:379-390

[12] Gerecht E, Douglass KO, Plusquellic DF. Chirped-pulse terahertz spectroscopy for broadband trace gas sensing. Optics Express. 2011;**19**: 8973-8984

[13] Lin H, Withayachumnankul W, Fischer BM, Mickan SP and Abbott D. Gas recognition with terahertz time-domain spectroscopy and spectral catalog: a preliminary study. In: Proceedings SPIE 2008; Terahertz Photonics; 68400X. DOI: 10.1117/ 12.760558

[14] Melinger JS, Yang Y, Mandehgar M, Grischkowsky D. THz detection of small molecule vapors in the atmospheric transmission windows. Optics Express. 2012;**20**:6788-6807

[15] Bigourd D, Cuisset A, Hindle F, Matton S, Bocquet R, Mouret G, et al. Multiple component analysis of cigarette smoke using THz spectroscopy, comparison with standard chemical analytical methods. Applied Physics B: Lasers and Optics. 2007;**86**: 579-586

[16] Neese CF, Medvedev IR, Plummer GM, Frank AJ, Ball CD, De Lucia FC. Compact submillimeter/terahertz gas

sensor with efficient gas collection, preconcentration, and ppt sensitivity. IEEE Sensors Journal. 2012;**12**:2565

[17] Consolino L, Bartalini S, Beere HE, Ritchie DA, Vitiello MS, De Natale P. THz QCL-based cryogen-free spectrometer for in situ trace gas sensing. Sensors-Basel. 2013;**13**: 3331-3340

[18] Chen T, Han Z, Liu J, Hong Z. Terahertz gas sensing based on a simple one-dimensional photonic crystal cavity with high-quality factors. Applied Optics. 2014;**53**:3454-3458

[19] Benz A, Deutsch C, Brandstetter M, Andrews AM, Klang P, Detz H, et al. Terahertz active photonic crystals for condensed gas sensing. Sensors-Basel. 2011;**11**:6003

[20] Lai CH, Hsueh YC, Chen HW, Huang YJ, Chang HC, Sun CK. Low-index terahertz pipe waveguides. Optics Letters. 2009;**34**:3457

[21] Litchinitser NM, Abeeluck AK, Headley C, Eggleton BJ. Antiresonant reflecting photonic crystal optical waveguides. Optics Letters. 2002;**27**: 1592-1594

[22] You B, Lu JY, Yu CP, Liu TA, Peng JL. Terahertz refractive index sensors using dielectric pipe waveguides. Optics Express. 2012;**20**: 5858-5866

[23] Dean JA. Lange's Handbook of Chemistry. McGraw-Hill Professional; 1999. Chapter 5

[24] Washburn EW. International Critical Tables of Numerical Data, Physics, Chemistry and Technology. Vol. IV. Knovel; 2003

[25] Yang Y, Shutler A, Grischkowsky D. Measurement of the transmission of the atmosphere from 0.2 to 2 THz. Optics Express. 2011;**19**:8830-8838

[26] Petrucci RH. General Chemistry: Principles and Modern Applications. Pearson Prentice Hall; 2007

[27] Beare WG, McVicar GA, Ferguson JB. The determination of vapor and liquid compositions in binary systems. The Journal of Physical Chemistry. 1929; **34**:1310-1318

[28] Zhang J, Grischkowsky D. Terahertz time-domain spectroscopy study of silica aerogels and adsorbed molecular vapors. The Journal of Physical Chemistry. B. 2004;**108**:18590-18600

[29] Shi W, Ding YJ. Fingerprinting molecules based on direct measurement of absorption spectrum by frequency-tuning monochromatic THz source. Laser Physics Letters. 2004;**1**:560-564

[30] Xu P, Yu H, Li X. Functionalized mesoporous silica for microgravimetric sensing of trace chemical vapors. Analytical Chemistry. 2011;**83**: 3448-3454

[31] Xie Z, Cao K, Zhao Y, Bai L, Gu L, Xu H, et al. An optical nose chip based on mesoporous colloidal photonic crystal beads. Advanced Materials. 2014;**26**:2413-2418

[32] Nelson RD, Lide DR and Maryott AA. Selected values of electric dipole moments for molecules in the gas phase. U. S. National Bureau of Standards NSRDS-NBS; 1967. 10

[33] Dorosh O, Kisiel Z. Electric dipole moments of acetone and of acetic acid measured in supersonic expansion. Acta Physica Polonica A. 2007;**112**:S95-S104

Chapter 4

A Review on Preparation of ZnO Nanorods and Their Use in Ethanol Vapors Sensing

Musarrat Jabeen, R. Vasant Kumar and Nisar Ali

Abstract

The devices of polycrystalline film have small sensitivity that can be overthrown by using high aspect ratio of 1D nanostructures, such as ZnO nanostructures. Sensors based on 1D nanostructures show very quick response time and high sensitivity for their high impact factor. The purpose of this article is to provide a comparison of different methods and the quality of the sensors thus produced. Currently, metal oxide 1D nanoarchitectures like ZnO have great attraction due to their applications in sensors. Metal oxide nanostructures have high aspect ratio, with small consumption of power and low weight, however, keeping excellent chemical and thermal dependability. Different techniques have been adopted to fabricate metal oxide one-dimensional nanostructures like hydrothermal, electrospinning, sol-gel, ultrasonic irradiation, anodization, solid state chemical reaction, molten-salt, thermal evaporation, carbothermal reduction, aerosol, vapor-phase transport, chemical vapor deposition, RF sputtering, gas-phase-assisted nanocarving, molecular beam epitaxy, dry plasma etching, and UV lithography. The sensitivity depends upon the materials; synthesis technique and morphology of the sensor performance toward a particular gas have different range of success. This article estimates the efficiency of ZnO 1D nanoarchitectures, gas sensors. Finally, in this review, we had mentioned the future directions of investigations in this field.

Keywords: ethanol, gas sensing, epitaxy, anodization, ZnO, nanostructures

1. Introduction

The semiconductor metal oxides play the role of an encouraging contester for gas sensing employment. As a result, they have greater sensitivity for target gases due to easy synthesis techniques, being cheaper, and great compatibility with other techniques [1]. Nowadays, nanoarchitectures are being designed from SnO_2, In_2O_3, ZnO, WO_3, TiO_2, CdO, TeO_2, MoO_3, CuO, and Fe_2O_3 with various dimensions and configurations. It was explored that surface morphology plays an important role in sensing applications [2, 3]. Semiconductor metal oxide nanostructures have various compositions and morphologies such as single crystals, one dimensional, and thin or thick film form due to utilization of interest and facility of synthesis techniques [4]. Recently, 1D nanoarchitectors have much attraction

for sensing due to their aspect ratio beside their thermal and chemical stabilities at various working situations [5, 6].

In nanotechnology and nanoscience, advancement in synthesis techniques for manufacturing 1D nanostructures has been an important target [7]. Various techniques have been adopted to fabricate 1D nanostructures for gas detection applications. These fabrication methods are sol-gel [7], ultrasonic irradiation [8], solid-state chemical reaction [9], electrospinning [10], molecular beam epitaxy [11], hydrothermal [12], thermal evaporation [13], molten-salt [14], anodization [15], RF sputtering [16], vapor-phase transport [17] chemical vapor deposition [18], carbothermal reduction [19], nanocarving [20], dry plasma etching [21], aerosol [22], and UV lithography. Various kinds of nanostructures can be fabricated with different morphologies that are directed by fabricating techniques and treatments.

Nanostructures grown by these techniques contain the shape of nanowires [19], nanobelts [16], nanotubes [15], nanoneedles [23], nanorods [5], nanofibers [12], nanoribbons [24], nanowhiskers [25], urchins [26], nanopushpins [27], fiber-mats [22], hierarchical dendrites [17], nanocarving [20], and lamellar [28]. The modifications in surface morphology result in sensing of various kinds of oxidizing and reducing gases like CO, NH_3, NO_2, H_2, O_2, H_2S, LPG, xylene, propane, toluene, triethylamine, methanol, and acetone.

The sensitivity of a one-dimensional nanostructure sensor can increase with the improvement in surface morphology and bulk characteristics. These improvements can be made by doping with other elements or decorating nanoparticles on the surface of nanostructures. Sensors using such kinds of surface morphology and bulk characteristic improvements indicate significantly greater response as compared to that of unrestricted sensors.

The current article shows a detailed discussion of the contemporary investigation of the vigorous developments and adopting techniques for designing 1D SMO sensors. The sensor synthesize with nanostructures shows high sensitivity. This article's exemplary supposition investigates the 1D ZnO nanostructure sensor for ethanol detection process. Finally, conclusions explain the possible future evolution in 1D zinc oxide nanostructures for ethanol sensing.

2. Synthesis of ZnO nanostructures

The growth of ZnO nanostructures can be categories as follows: (a) wet chemical method, (b) solid-state synthesis, and (c) vapor-phase process. Wet chemical process consists of hydrothermal and ultrasonic irradiation growth in solution. However, ZnO nanostructures can be fabricated by solid-state route either through the solid-state chemical reaction or through the carbothermal reduction. The chemical vapor deposition process, molecular beam epitaxy (MBE), thermal evaporation, RF sputtering, vapor-phase transport, and aerosol are included in vapor-phase route. The processing particulars for synthesis of ZnO 1D nanostructure are illustrated in **Table 1**.

2.1 Wet chemical process for the growth of one-dimensional nanostructures

2.1.1 Hydrothermal process

Liwei Wang has synthesized ZnO NRs with hydrothermal technique in greater quantity (about 85%), in $Zn(OH)_4^{2-}$ solution and the presence of cetyltrimethylammonium bromide. CTAB act as a structure director, in the absence of any calcination technique [29].

Processing route	Synthesis technique	Starting material	Synthesis temperature (°C)	Morphology	Diameter of ZnO nanostructure	Length of ZnO nanostructure	Reference
Wet process route	Low-temperature process in autoclave	$(Zn(NO_3)_2{\cdot}6H_2O)$, NaOH, CTAB	90°C for 15 h	ZnO nanorods	90–200 nm	1.7–2.1 μm	[29]
	Hydrothermal process	CuO co-doped ZnO	Room tem.	CuO-ZnO NRs			[30]
	Hydrothermal	$ZnCl_2$ in NH_4OH	400 for 3 h	ZnO capsules			[31]
	Wet chemical technique	Ag/Ag_2O_3/ZnO NRs	Low tem. NRs	300 nm NRs	300 nm		[32]
	Wet chemical low-temperature process	1.0239 g $ZnCl_2$ (7.50 mmol), 3.006 g NaOH (75.00 mmol), 25 mL deionized water	90°C 3 h, 80°C for 12 h °C	Flower-like ZnO nanorods	200–500 nm	1.0–1.5 μm	[32]
	Two-step solution growth	$ZnCO_3$, CO_2-ethanol, KOH		ZnO NRs	150 nm	4 μm	[33]
	Solution growth technique Hydrothermal technique	$LiNbO_3$ Zinc nitrate, hexamethylenetriamine, and polyethylenimine in deionized water	95°C 80°C for 12 h	Nanorods	45 nm	1 μm	[34]
		$ZnAc_2{\cdot}2H_2O$, poly(ethylene glycol) 3 g of NaOH	120°C for 12 h. Dried 60°C for 4 h	Ag-ZnO NRs, nigger-brown	—	—	[31]
		$Zn(NO_3)_2.6H_2O$ $C_6H_{12}N_4$	80°C	Nanorods	30–50 nm	1.2 μm	[35]
		10 ml $Zn(Ac)_2.2H_2O$ in 0.1 M methanol, 20 ml NaOH in 0.5 M methanol, DI water ($K_2SnO_3{\cdot}3H_2O$, 95%), 0.75 g of urea	150°C for 24 h for ZnO NRs and for $ZnSnO_3$ 3 h at 170°C	ZnO NRs	2.8 nm, 2.5 nm	26 and 22 nm	[36]
		$Zn(NO_3)_2{\cdot}6H_2O$ $C_6H_{12}N_4$	80°C deposition time was 16 h	ZnO NRs	30–50 nm	—	[37]
		20 mM $Zn(NO_3)_2$ 20 mM hexamethylenetetramine	90°C for 100 min, dried for 12 h at 60°C and annealed 1 h at 500°C	Well-dispersed ZnO nanorods	290–330 nm	3.2–3.4 μm	[38]

Processing route	Synthesis technique	Starting material	Synthesis temperature (°C)	Morphology	Diameter of ZnO nanostructure	Length of ZnO nanostructure	Reference
	Sol-gel	$Zn(CH_3COO)_2{\cdot}2H_2O$	95°C 50 ml autoclave	Nanorods	51 and 33 nm	262, 748, and 470nm	[39]
		$Zn(CH_3COO)_2$, $2H_2O$ 2-propanol $C_4H_{11}NO_2$, zinc acetate dehydrate, $(CH_2)_6N_4$	75°C for 30 min	Hexagonal NRs	60–70 nm	-	[40]
	One-step solvothermal method	20 mM $Zn(NO_3)_2$ and 20 mM HMTA	90°C for 100 min	Nanorods	220 nm	—	[41]
	Hydrothermal synthesis	$Zn(NO_3)_2.6H_2O$ sodium hydroxide deionized water CTAB	120°C for 12h	ZnO nanorods	80–150 nm	—	[42]
	Ultrasonic irradiation in aqueous solution	Alumina substrate, $Zn(NO_3)_2{\cdot}6H_2O$, $(CH_2)_6N_4$	—	Nanorod (vertically aligned)	50 nm	500 nm	[11]
	DC magnetron sputtering	ZnO (0, 1, 10, and 25 at. wt%) ZnO, MoO_3, Au-IDE, acetone	Annealing in ambient air for 1 h at 773 K	Nanostructures	—	—	[43]
		Metallic zinc foil and formamide solution	55°C	Hexagonal-shaped ZnO nanorods	400 nm	2 μm	[44]
		ITO glass, 7 Ω/sq., CBD (CBD condition: 95°C, 3 h),170 nm thick seed layer	400°C for 1 h	ZnO nanorods	55 nm	1.5 μm	[45]
	Solution method	$Zn(NO_3)$ $6H_2O$ (10 mM), ($C_6H_{12}N_4$,10 mM), $CoSO_4{\cdot}7H_2O$, 0–0.5 mM	90°C for 15–30 min	ZnO nanorods	100–300 nm	1–3 μm	[46]
		$Zn(NO_3)_2(H_2O)_6$, NH_3	80°C for 3 h	ZnO nanocrystals	—	—	[47]
	Microwave irradiation	Zinc acetate dihydrate, NaOH	Dried at 60°C Calcined 600°C, 2 h	ZnO flower-like	200–300 nm	1.5 μm	[48]
		$(CH_3COOH)_2{\cdot}2H_2O$, HMTA, CTAB	120°C for 12 h in autoclave	Hexagonal ZnO nanosheets	17 nm	90 nm	[49]

Processing route	Synthesis technique	Starting material	Synthesis temperature (°C)	Morphology	Diameter of ZnO nanostructure	Length of ZnO nanostructure	Reference
	Seeding by RF-sputtering, thermolysis-assisted aqu. sol. tech.	0.01 mol $C_6H_{12}N_4$, in 400 ml DI water	85°C	ZnO nanorods	8–160 nm thick seed layer	—	[30]
	Solvothermal	$Zn(CH_3COO)_2{\cdot}2H_2O$, methanol, KOH	70°C. 3–5 days	NRs	15 nm	50–120 nm	[50]
Solid-state technique							
Vapor-phase technique	Carbothermal reduction	0.3 g Zn powder and 0.6 g active carbon	900°C at a rate of 25°C/min for 2 h	Nest-like ZnO	—	—	[51]
	Continuous two-step vapor growth	$(CH_3)_4Sn$, DI water, IPA, PDMS substrate	900°C	NWs	50–80 nm thick	Several micrometers	[52]
		ZnO powder	600°C	NRs	Average diameter 400 nm, 550 nm	11.8 μm, 6.5, and 3.5 μm	[53]

Table 1.
Details of different growth techniques of ZnO 1D nanoarchitectures.

Semiconductor metal-doped transition nanomaterials have a number of applications. The hydrothermal growth technique is cost-effective and environment-friendly. The nanostructures of CuO doped with ZnO synthesized at room temperature by hydrothermal technique need great efforts. The properties of CuO doped with ZnO nanorods were measured by various spectroscopy techniques, and sensing was executed by I-V analysis. Aqueous ammonia was used as analytic gas as reported by M. Rahman et al. CuO nanorods doped with ZnO sensor show good stability, sensitivity, and reproducibility. Sensor based on signal/noise ratio has sensitivity of 1.549 ± 0.10 μA cm^{-2} Mm^{-1}. Sensor applications depend on the transition metal coated with ZnO nanomaterial [30].

ZnO nanoparticles were synthesized hydrothermally from urea and zinc chloride and characterized by various spectroscopic techniques. The ZnO NPs range in size from 180 to 130 nm with hexagonal structure. The photocatalyst analysis of ZnO nanoparticles was determined with the degradation of methylene blue. ZnO nanostructures were possessed by high photocatalyst value as compared to TiO_2-UV100. Moreover, the sensing characteristics of the detector were determined with methanol by I-V process at room temperature. It was investigated that sensor shows sensitivity in the range of 0.9554 μA cm^{-2} mM^{-1} at room temperature [39].

ZnO nanocapsules have been synthesized hydrothermally. The structural morphology and characteristics were analyzed with the help of different spectroscopy techniques. The sensing was measured with I-V method by using chloroform as the detecting gas. Sensor shows high sensitivity, small detection limit, and high linear dynamic limit with fine linearity in a small response time. Moreover, the photocatalytic response was calculated with the degradation of acridine orange [31].

Nanoparticles of ZnO-CeO_2 were grown by hydrothermal process. These nanostructures were used for the construction of sensor and photocatalyst by elimination of environmental pollution. These NOs have diameter approximately from 50 ± 10 nm. The composition of NPs was measured by EDS spectroscopy, and UV-visible spectrum investigates the optical characteristics. The photocatalytic degradation of acridine orange and methylene blue dyes has been carried out using ZnO-CeO_2 NPs. The critical routine of ZnO-CeO_2 NPs for ethanol detector shows high sensitivity and small detection limit in shorter time [46].

The nanostructures of ZnO-CeO_2 were grown by hydrothermal technique. These nanostructures have extended shaped CeO_2 NPs having diameters of 40–90 nm. Photocatalytic activity of CeO_2 co-doped ZnO structure was measured with degradation of acridine orange and methylene blue. Sensor fabricated by ZnO-CeO_2 nanostructures shows high sensitivity in 10 s. The chemical sensor used ethanol as the sensing gas using I-V procedure [50].

ZnO NR sensor for ammonia detection has been synthesized by wet chemical technique at cost-effective low temperature. The as-synthesized sensor exhibited high sensitivity of 5.538 mA cm^{-2} mM^{-1}, in small detection range of 0.11 mM, with linear-dynamic limit from 0.5 mM, having high linearity of 0.7102 in 10.0 s response time. In addition, sensor performs good for the degradation of acridine-orange, methylene-blue, and amido black. Spectroscopy analysis exhibited that ZnO NRs have wurtzite crystalline structure with diameter of 58.61 nm [50].

The calcined AgO co-doped ZnO NPs were synthesized by hydrothermal process using alkaline medium as reducing agent. The as-prepared NPs were analyzed by different spectroscopy techniques. Sensor was fabricated on a microchip for methanol sensing that exhibited high response. Careful observation exhibits that microchip sensors have high value of sensitivity, reliability, small volume reproducibility with ease of integration, high stability, and good response. The calibration graph is linear over methanol concentration. The sensitivity was measured at 3 at signal-to-

noise ratio having the value of 7.917 Ma cm^{-2} mmol L^{-2} with a detection range of 71 ± 0.5 μmol L^{-1} [45].

A reliable technique for detecting dissolved acetone by doped nanomaterials was investigated by Mohammed M. Rahman et al. ZnO NRs co-doped with Co_3O_4 were fabricated by solvothermal process. The as-fabricated NRs were characterized for different spectroscopic techniques. NRs were calcined at 400°C that shows excellent semiconductor nanomaterial for sensing acetone with silver electrodes. The detector exhibits high sensitivity, reproducibility, and stability. The calibration graph is linear and exhibits high sensitivity and small detection range in large concentration of acetone [40].

Here, we investigate hydrothermal growth of $Ag/Ag_2O_3/ZnO$ NRs that exhibit high crystalline structure. The characterization confirms that composite NRs have 300 nm cross-section areas. The composite NRs have absorption edge at 375 nm that exhibited that they are optically active. The sensor shows high sensitivity and small detection range. Hence, NRs can be used as redox mediator for efficient phenylhydrazine detector [33].

Good-quality crystalline ZnO NPs were prepared by hydrothermal process using aqueous solution of zinc chloride and ammonium hydroxide. Nanoparticles have wurtzite geometry with an approximate size of 50 ± 60 nm. The composition quality of the as-prepared NPs exhibited 1:1 stoichiometry of Zn and O_2, which was confirmed from spectroscopy analysis. The optical characterization of ZnO NPs exhibits that they are used as photocatalyst for the degradation of acridine-orange and for the detection of acetone. The constructed sensor shows high sensitivity of 0.14065 μA cm^{-2} mM^{-1} and small detection range in 10 s [32].

ZnO NRs in vertical direction were synthesized on flexible polyimide films by a thermolysis-assisted chemical solution method [42].

ZnO nanorod arrays with various aspect ratios and characteristics relevant to tailored defect are prepared and used to synthesize gas sensors. The ZnO gas sensors are of three different types synthesized by sol-gel process and successive aqueous chemical growth (ACG). According to Shi et al. and Vayssieres et al., ACG solutions used in the current research work are two types: Zn salt/KOH and Zn salt/HMTA [41].

An accomplished photochemical method was used for the synthesis of Ag NPs decorated on ZnO nanorods for investigation of gas sensing. ZnO NRs decorated with Ag increased long-term stability and response time [54].

NRs with and without Co doping were synthesized in 10 mM solution of zinc nitrate hexahydrate $Zn(NO_3)\cdot 6H_2O$, hexamethylenetetramine, and 0.5 mM cobalt sulfate hydrate ($CoSO_4\cdot 7H_2O$) in water at 90°C for 15–30 min. The sensor showed high response and sensitivity as NRs fabricated by electrodeposition process [44].

To fabricate ZnO nanorods by solvothermal technique, prepare a 1.12 M solution of zinc acetate dihydrate in methanol (40 mL) under vigorous stirring at 70°C. Particularly, at 70°C, add 21.33 mL solution of KOH (21.33 mL) dropwise in methanol. After 2 h of vigorous stirring of the mixture, transfer it to 100 mL autoclaves, which were allowed to react at 70°C for 3–5 days and then cooled down naturally. Harvest the resultant product [35].

1D ZnO NRs were grown on ITO-coated glass (AUO Co., Ltd.). The ITO glass has 7 Ω/sq. resistance in sequential chemical bath deposition. A seeding layer was deposited with a thickness of 170 nm at 25°C by the process of dip coating in the first step and then followed by the process of CBD at 95°C for 3 h with the synthesis of ZnO nanorods in 0.05 M precursor solution of ZnO. The ZnO samples were thermally treated at 400°C for 1 h in an electric furnace after deposition. Ethanol of analytical grade and deionized water with 2.61 μs/cm and pH 6.7 were used in the experiment [49].

ZnO nanorods were prepared from HMT solution on p-Si substrate using oxidation furnace at 1000°C for drying 30 min following 2 h wet oxidation process. The seed layer for ZnO nanocrystal was prepared with zinc acetate dihydrate ($Zn(CH_3COO)_2{\cdot}2H_2O$) in 2-propanol by sol-gel process. Then, 3 ml diethanolamine ($C_4H_{11}NO_2$) was added dropwise to clear the solution and aged for 24 h. The samples were spin coated and annealed at 450°C for 1 h. A 50 ml solution in deionized water (~18.2 MΩ cm) of zinc acetate dihydrate and $(CH_2)_6N_4$ in 1:3 mass ratio was prepared. Then, the substrate was placed into the nucleation solution at 75°C for 30 min [36].

ZnO NRs were fabricated from $ZnCO_3$ fibers that were formed in a solution of CO_2-ethanol, by consecutive treatment in KOH solution. The ZnO NRs were single crystal with a diameter of 150 nm and length of 4 μm. It was observed that ethanol sensing was done at 250°C [48].

ZnO nanorods having a flower-like shape were fabricated at 90°C by the hydrothermal process in the absence of any surfactant, organic solvent, or toxic regent. In a particular growth, solution A was formed by dissolving 7.50 mmol $ZnCl_2$ in 25 mL deionized water under stirring. Adopting the similar technique, 75.00 mmol NaOH was dissolved in 25 ml deionized water consequence in solution B. Finally, solution A was added into B dropwise under stirring. The resultant solution was placed at 90°C for 3 h, harvesting the white precipitate rinsed with deionized water and drying them in vacuum for 12 h at 80°C [38].

ZnO nanorods were fabricated by dissolving 2.97 g $Zn(NO_3)_2{\cdot}6H_2O$ and 4.00 g NaOH (molar ratio of Zn^{2+}/OH^- by1:10) in 200 ml DI water. Consequently, 5.00 g CTAB was added under vigorous stirring for 1 h. The solution was shifted to a Teflon-lined steel autoclave and kept at 120°C for 12 h and then allowed to cool down naturally. Then, white precipitates were collected, washed, and dried overnight at 60°C. At a pressure of 6.0 MPa, ZnO NRs were used to design a sensor. The pellets were 3.0 mm thick and have an area of 5.3 cm^2. On the surface of pellets, electrodes of 2.0 cm^2 were deposited by silver paste [47].

A 20 mM nutrient solution of $Zn(NO_3)_2$ and hexamethylenetetramine (HMTA) was prepared. The used precursors are such a kind that dissolved in necessary solvents. After dissolving $Zn(NO_3)_2$ and HMTA precursor solutions, the beaker was covered. Then, it was put in an oven for 100 min at 90°C. After cooling down naturally, the white precipitates were collected by centrifuging and rinsed and dried at 60°C for 12 h. Calcinations were done for 1 h at 500°C in the presence of air. The samples prepared with 0, 10, 20, 30, 40, and 50 vol% ethanol solvent were numbered a0, a10, a20, a30, a40, and a50, respectively [55].

To fabricate one-dimensional multifaceted ZnO nanostructures, a new strategy has been introduced that consists of two-phase solution process. Through these techniques, nanowires, nanorod arrays (NAs), nanotubes, nanorod hollow spheres (NHSs), nanoribbons, and nanonetworks were grown at low temperature without any catalysts, templates, or precursors [53].

ZnO nanostructures with different morphologies have been grown from zinc foil (1×1 cm^2) and substrates were cleaned by ultrasonication process in ethanol. The substrates were suspended vertically to the bottom of a vial in formamide solution 3 ml of 15%. The vial with substrate was sealed and put inside an oven with fixed temperature at 55°C. The samples were washed thoroughly with ethanol and dried. Time-dependent experiments estimate the illumination transformation process as well as reaction time of ZnO nanodisks from NRs [43].

Filtered cathodic vacuum arc (FCVA) mechanism was introduced to deposit ZnO layer on the surface of alumina substrates decorated with gold IDTs. The substrates were loaded in the holder with varied temperature heater. After completion of deposition, the substrate was carried out for analysis from the chamber.

The ZnO seeding layer will act as nucleation site for the fabrication of ZnO NRs from hydrothermal process. An equimolar growth solution of zinc nitrate hexahydrate ($Zn(NO_3)_2.6H_2O$) and $C_6H_{12}N_4$ was prepared. The transducers were washed ultrasonically in acetone and dried in nitrogen atmosphere. Then, the transducer was kept inverted on Teflon holder and attached to a glass rod before inserting into the reaction bottle. The bottle was placed in an oven for 16 h at 80°C. Finally, the substrate was washed thoroughly to remove impurities and dried in N_2 stream at a flow of 200 sccm [51].

A solution of 1 mM zinc acetate dihydrate ($Zn(CH_3COOH)_2{\cdot}2H_2O$),

0.5 mM hexamethylenetetramine, and 0.05 g cetyltrimethylammonium bromide (CTAB) in 40 mL deionized water was prepared after vigorously stirring for 1 h. Then, the mixture was transferred in autoclave and placed under heat treatment for 12 h at 120°C. After centrifugation, the white precipitates were harvested, rinsed with ethanol and deionized water. Finally, the product was dried in air atmosphere at 60°C [52].

2.2 Sol-gel process

2.2.1 Preparation of seed layer and ZnO nanorod arrays

The ZnO nanorod array was fabricated by dissolving 10 ml $Zn(Ac)_2{\cdot}2H_2O$ in 0.1 M methanol and 20 ml NaOH in 0.5 M methanol solution. After filtration, the solution was transferred to a 50 ml autoclave and heat treated for 24 h at 150°C. The precipitates were collected and washed. For hydrothermal growth of $ZnSnO_3$ nanorods, 0.06 g of ZnO nanorods was dissolved by ultrasonication (Power, 500 mW) in 32 ml of water-alcohol (38 vol% alcohol) mixture. Then, 0.115 g of potassium stannate trihydrate ($K_2SnO_3{\cdot}3H_2O$, 95%) and 0.75 g of urea were transferred to the above mixture. After vigorous stirring for 5–10 min, the solvent was shifted into a 50 ml autoclave and heated for 3 h at 170°C. A white product was obtained and rinsed with distilled water [34].

2.3 Solid-state processing route (microwave irradiation)

A 0.1 M solution of zinc acetate dehydrates was prepared and vigorously stirred for 10 min. To obtain 0, 2, 5, and 10 wt% samaria, a suitable quantity of samarium nitrate was added during magnetically stirring. Then, guanidinium carbonate (0.1 M) solution was dropped to the mixture. Consequently, 10 min latter, 4 M solution of NaOH also was added dropwise to attain a clear solution with pH 12. Lastly, the microwave irradiation (with 75% power) was exposed to the mixture for 2 min. For irradiation, a microwave oven was used with a power of 800 W (Concave Reflex Systems (C.R.S.), KOR-63A5). The white precipitates were separated, rinsed, dried under vacuum at 60°C, and calcined for 2 h at 600°C in air [56].

Interdigital electrodes (IDTs) were placed on the upper surface of alumina substrate (96%), with line/space of 30 μm. Actually, such kind of line-printing is not feasible with thick film method. By a laser printer of gold film, the interdigital electrodes were printed [57].

A 20 mM nutrient solution (equal molar solution) of $Zn(NO_3)_2$ and HMTA in distilled water was prepared, and 4:1 volume ratio of the anhydrous ethanol was added. Precursors were formulated by dispersing in their relative solvents. The container with precursors was put in an oven for 100 min at 90°C. After cooling, the white sludge was collected and cleaned using centrifuge and rinsing water. Finally, the sludge was dried for 12 h at 60°C and annealed in air for 1 h at 500°C [58].

2.4 Vapor-phase route (pulsed laser deposition)

ZnO nanorods were grown onto the long-period gratings (LPGs), followed by a two-step process. They contain pulsed laser deposition (Zn layer onto optical fiber), followed by the growth of ZnO nanostructures in aqueous solution. Zinc precursor layer was deposited by a laser beam (248 nm KrF excimer) that was focused on target (Zn target with 99.9% purity) to produce fluence (1.3 J/cm^2). The evaporated material was deposited on the optical fibers located at 6 cm apart from the target. According to identical conditions, the deposition on substrate has resulted in Zn layer nearly 40 mm thick, when exposed with 2000 laser pulses [59].

2.5 RF sputtering

A seeding of ZnO was sputtered (5 nm) on the recommended area of CMOS devices and illustrated with metal shadow mask. The as-prepared substrate was dipped in 25 mM equimolar solution of zinc nitrate hexahydrate ($Zn(NO_3)_2{\cdot}6H_2O$) and hexamethylenetetramine and was maintained for 2 h at 90°C. The device was removed from the nutrient solution after ZnO NWs' growth washed with deionized water and dried. This process is suitable for simultaneously growing ZnO NWs on microhotplate and provides an economic process for thin film level growth as well [60].

By RF sputtering process, deposit a layer of 50 nm on the glass substrate. Wash the substrate with standard process and keep the substrate in its holder. The NRs of ZnO:Ti were grown onto the ZnO sputtered by reactive evaporation with hot-wire resistance in a furnace. After the growth of ZnO:Ti NRs, the Pt electrodes were deposited by photolithography and liftoff technique on the substrate. For better ohmic contact, anneal the samples in an Ar ambient atmosphere for 15 min at 350°C [61].

Prepare nanostructured thin film with pure ZnO (25 at. wt%) and MoO_3 for gas response. Deposit it on the surface of as-prepared alumina sensor chips by sputtering and annealing process. The sensor chips containing Au-IDE and thin film Pt-heater structures were comprehended by means of DC magnetron sputtering, plasma etching, and UV-lithography. Gold wires (diameter of 50 μm) were made to contact for sensor testing body that mounted on TO-8 header by microwelding method [62].

2.6 Carbothermal reduction

In a particular growth mechanism, 0.3 g zinc powder and 0.6 g effective carbon were adequately mixed in an agate mortar. The mixture was transferred into an alumina boat and kept in a horizontal muffle furnace at 900°C with 25°C/min for 2 h under normal pressure. Finally, the yellowish product formed and massed in the boat [63].

Carbothermal reduction technique can be used to synthesize ZnO NWs from graphite and ZnO powder in horizontal muffle furnace. At the downstream, the Si wafer sputtered with a 30°A Au coating. A rotary pump was used to evacuate the quartz tube at approximately 10^{-2} Torr, and Ar gas was introduced at 100 sccm. The temperature was increased to 900°C, and O_2 gas was introduced with 2 sccm for 30 min. After the growth of single crystalline ZnO NWs, an SnO_2 shell layer was deposited, and the temperature of the furnace cooled from 900 to 700°C. Tetramethyltin ($(CH_3)_4Sn$, 99.999%, UP Chemical Co., Ltd.) was kept in the quartz tube at 0.5 sccm of Ar as carrier gas and introduced with 2 sccm oxygen for 10 min [64].

2.7 Surface acoustic wave

The ZnO nanorod sensor was designed on Y-cut $LiNbO_3$ substrate for ethanol sensing. The performance of SAW is excellent due to electromechanical coupling coefficient ($k2$ = 4.5%) offered by $LiNbO_3$ and small attenuation at high temperature. The interdigital transducers (IDTs) have a gap of 12 mm delay line, and each contains 50 pairs of electrodes. The width and the spacing inside the adjacent IDT electrodes are adjusted 15 μm. The IDT electrodes have length of 3 mm. The propagation of SAW elongated in x-direction of the crystal as IDTs is oriented on the surface of wafer.

Deposit a photoresistive layer by spin coated process and decorate it with window covering delay line for the construction of sensor. ZnO layer (100 nm) was sputtered with ZnO ceramic target by DC sputtering (conditions for sputtering, pressure = 2.7 Pa, in the presence of 80% argon and 20% oxygen) and the current required was 0.25 A DC. Acetone removed the photoresist layer leaving behind seed layer of ZnO. The devices were suspended with ZnO seed layer inverted in the solution of zinc nitrate, hexamethylenetriamine, and polyethylenimine. The bottle was incubated for 4 h at 95°C. The substrates were taken off from the solution, washed, and dried at room temperature [65].

3. Characterization

The characterization was done by using various spectroscopic techniques such as X-ray diffraction, scanning electron microscopy, and transmission electron microscopy for structural and morphological analysis.

3.1 X-ray diffraction

X-ray diffraction was done by a diffractometer of Rigaku D/max-2500 with Cu Kα radiation (λ = 0.15418 nm) and 2θ range from 20 to 80°, which confirm the hexagonal wurtzite structure of ZnO (JCPDS card no. 36-1451), the peaks are in agreement in Bragg reflections and no impurity peaks were observed [29].

3.2 Scanning electron microscopy

Surface morphology was done by Shimadzu SS-550 with a voltage of 15 kV. The ZnO rod-like nanostructure affirms from SEM images. High magnification revealed that ZnO nanorods have a length from 1.7 to 2.1 μm and diameter in the range of 90–200 nm.

3.3 Transmission electron microscopy

Transmission electron microscopy (Philips FEI Tecnai 20ST) at an accelerating voltage of 200 kV investigates the detailed structure of ZnO NRs [29].

The orientation of ZnO NRs was examined by X-ray diffractometer (Rigaku D/MAX B) utilizing Cu Kα radiation for post- and preannealing. The operating voltage and current were 40 kV and 40 mA, respectively. The measurement was conducted from 20 to 60° in the 2θ range with scanning rate 5°/min. Field emission scanning ELECTRON microscope (FESEM, JEOL JSM-7000F) was utilized to observe the morphology of grown ZnO nanorods. For sensitivity measurement, an ambient environment was controlled inside a chamber by flowing synthetic air.

The resistance was recorded by a Keithley 2400 SourceMeter (Keithley Instruments, Inc.) [42].

The top view of the ZnO NRs and cross-section morphologies were investigated by high resolution scanning electron microscopy (HR-SEM, S4200, HITACHI) and field emission (FE-SEM, XL-40FEG, PHILIPS). The crystal pattern of the NRs was revealed by X-ray powder diffraction (Rigaku MultiFlex) with a scanning step of 0.01° and scan speed of 4°/min. Fluorescence Spectrometer (MFS230) were used to determine the photoluminescent spectra of ZnO NRs at 325 nm excitation. The gas detection properties were investigated by measuring the resistance variation of the sensor in ambient air condition and ethanol mixed environment at 300°C [41].

A transmission electron microscopy (TEM: JEM-200CX, 160 kV, and HR-TEM: JEOL-2010F, 200 kV) was used to visualize the morphology of the grown Ag-ZnO NRs. 0.1 g of Ag-ZnO nanorod was ultrasonically suspended in ethanol 10 mL solution for TEM investigations. Then one drop of this solution is put on a copper grid with thin coating of carbon that evaporated at room temperature in air. An EDX analyzer (EDX: INCA OXFORD) was connected to the JEOL-2010F HR-TEM for in situ investigation of the configuration of the fabricated Ag-ZnO NRs. The elemental composition of Ag-ZnO NRs was further investigated by X-ray photoelectron spectrometer (XPS, PHI 5000C ESCA System, Perkin Elmer) with Mg Kα (λ = 1253.6 eV). The data investigation was done by RBD Auger Scan 3.21 software. Differential scanning calorimetry (DSC) analysis was carried out on a STA409PC thermal analyzer (Netzsch, Germany) with 10°C/min heating rate in air. The phase analysis of NRs was identified with powder X-ray diffraction analysis using a D/max 2550 V diffractometer with Cu Kα radiation (λ = 1.54056 Å) (Rigaku, Tokyo, Japan). One typical sensor containing Ag-ZnO NRs was further visualized by scanning electron microscopy (SEM: JSM-6700F, 10 kV) after working for 100 days [54].

The surface morphology visualization of the final product was investigated with a field-emission scanning electron microscopy (FESEM, JEOL JSM-6500F). The electrodeposited NRs have cross-sectional SEM image with 100–300 nm diameter and 1–2 μm in length. TEM low magnification image confirmed that ZnO NRs are well aligned in nature. Selected area electron diffraction (SAED) indicates that NRs are single crystalline ZnO with wurtzite structure. Energy dispersive analysis confirms the presence of Zn, O, Co, and Cu elements [44].

The crystal pattern of the ZnO NRs was revealed with X-ray diffraction (XRD, D8 Advance Bruker) with incident monochromatized radiation Cu Kα (λ = 1.5418 Å). XRD pattern was measured with a scanning step of 0.02°/s from 20° to 80° (2θ). Scanning electron microscopy (SEM, JSM-6301F) recorded the sizes of the samples and surface morphologies. SEM was operated at 20 KeV and transmission electron microscopy (TEM) investigation was done by H-800 transmission electron microscope that operated at 200 kV. The photoluminescence (PL) analysis was recorded at 325 nm (20 mW) by excitation with a laser emitter He-Cd at room temperature. The gas detection was determined by a China sensitivity instrument HW-30A. The gas response was evaluated by Ra/Rg, where Ra is the resistance in ambient air and Rg is the resistance in tested gas atmosphere [35].

Scanning electron microscopy (SEM, Holland Philips XL30) evaluates the surface morphology and crystalline size of Sm_2O_3-loaded ZnO samples. The EDX analysis evaluates the elemental composition of the synthesized samples. The crystalline pattern is recorded by the X-ray powder diffraction (XRD, Holland Philips) with Xpert diffractometer (CoKα = 1.7889 Å). The CHEMBET 3000 instrument was employed to record the specific surface areas (SSA) of the fabricated samples defaced at 330°C for 1 h utilizing Brunauer-Emmett-Teller (BET) technique. Diffuse reflectance UV-vis analysis for band gap evaluation was evaluated by an Avantes Avaspec-2048-TEC (using $BaSO_4$ as a reference) [56].

The morphology of ZnO NR surface was evaluated by scanning electron microscopy (SEM, FEI Nova Nano). X-ray diffraction (XRD) recorded the crystalline pattern and chemical composition of the seed layer as well as NRs deposited on the substrate. XRD was done by Bruker D8 Discover microdiffractometer equipped with a GADDS (general area detector diffraction system). The XRD was filtered with a graphite monochromator in the parallel mode (175 mm collimator with 0.5 mm pinholes) that operated with a potential of 40 kV and a current of 40 mA. Data were recorded using Cu Kα radiation (λ = 1.54178 Å) at room temperature. The electrical characterization like conductivity of the sensor was measured with a multimeter (Keithley 2001) with various concentrations of ethanol in synthetic air. The information in real time was collected by data acquisition card attached to the computer with LabVIEW software. The gas mixture was supplied at the rate of 200 sccm and sensing done at a temperature range of 25–330°C [57].

The crystalline size and morphology of ZnO NWs were evaluated with field-emission scanning electron microscopy (FESEM, JEOL 6340F, operated at 5 kV). NW length and diameter were recorded with high-resolution SEM images. The phase analysis was explored with X-ray diffraction (XRD, Philips PW1730 diffractometer) with Cu Kα radiation [60].

Field-emission scanning electron microscopy (FESEM, JEOL model JSM-6700 F) was employed to evaluate the cross-sectional images and morphology of ZnO NRs. The NRs are distributed over the selected area uniformly and have hexagonal wurtzite structure with average length of 1.5 μm and diameter is about 55 nm. The crystalline pattern was recorded by X-ray diffraction using Cu Kα radiation. The electrical impedance spectroscopy (EIS) was done by Hioki LCR meter (model: 3532-50). EIS has AC signal amplitude of 50 mV with the frequency range from 42 Hz to 1 MHz. A two-electrode method was applied to determine the response of the ZnO NR sensor (working electrode) and counterelectrode as ITO was employed with a thin coating of Au [49].

The characterization such as X-ray powder diffraction (XRD, D/MAX2500, and Cu Kα radiation), scanning electron microscopy (SEM, JEOL JSM6700F), and transmission electron microscopy (TEM, JEOL 2010) determines the crystal pattern and surface analysis. The growth technique of the sensors based on the products has been described elsewhere [11, 12]. Briefly, the products were dispersed in ethanol, and a drop was spun on a ceramic tube between Pt electrodes to form a thin film (about tens of nanometers). A resistance heater in the ceramic tube was used to control the temperature. The sensitivity is defined as S = Ra/Rg, where Ra is the sensor resistance in air and Rg is the resistance in the target-air mixed gas [34].

Crystal pattern of the annealed ZnO NRs was characterized by X-ray diffractometer (XRD, DX-2700) using Cu Kα radiation (λ = 0.15418 nm) with 2θ range from 20 to 80°. The morphology, dimension, and surface details of the NRs were explored by scanning electron microscopy (FEI Quanta 200) that operated at 20 kV. The photoluminescence spectrum (PL, PE LS55 spectrophotometer) was recorded with 325 nm excitation from Xe lamp at room temperature. The sensing was done using a sensitivity instrument WS-30A (Wei Sheng Electronics Co. Ltd., China) with gas detection chamber of 30 L [58].

The effective limit of the sensor was found to be typically high (190–1530 ppm ethanol in air), for both kind of modified and unmodified NRs, with a saturation tendency beyond 1530 ppm ethanol (in air) [36].

X-ray diffraction (XRD, D8 Advance Bruker) analysis was conducted to calculate the crystal pattern with Cu Kα1 radiation (λ = 0.15406 nm) that operated at 40 kV. Field-emission scanning electron microscopy (FESEM, JEOL JSM-6700F) was performed to explore the surface morphology of the samples operating at a voltage of 5 kV. Transmission electron microscopy (TEM) pattern and selected area electron

diffraction (SAED) analysis were obtained by JEOL JEM-2010 microscope that was operating at an accelerating voltage of 200 kV. Photoluminescence (PL) spectrum was determined by Hitachi F-7000 FL Spectrophotometer with 325 nm excitation range at room temperature from Xe lamp. X-ray photoelectron spectrometry (XPS) was done by using Al Kα ($h\nu$ = 1486.6 eV) with X-ray beams as the excitation source. Binding energies were calibrated relative to the C1s peak at 284.6 eV. The specific surface areas were measured via the Brunauer-Emmett-Teller (BET) method using an N2 adsorption at 77 K after treating the samples at 100°C and 10^{-4} Pa for 2 h using a Tristar-3000 apparatus [38].

4. Ethanol sensor performance characteristics

The different electrophysical properties exhibited by semiconductor metal oxides lie in the range from insulators to various band gap materials [20]. The conductivity of semiconducting materials like ZnO normally deviates from stoichiometry [27]. In the measurement of conductivity, vacancies of interstitial ions play an essential part. Sensors of semiconductor metal oxide work as a result of adsorption of gas on the sensing surface that cause in the variation of electrical resistance of ZnO. Due to charge concentration, semiconducting materials are categorized in n-type (like ZnO, TiO_2, WOx, MoO_3, TiO_2, CdO, and SnO_2) and p-type (such as NiO, TeO_2, and CuO) materials. The species of target gas can also be categorized into two types, oxidizing and reducing gases: oxidizing gas (electron acceptors) like NO_2 and O_2 and reducing gas (electron donors) such as CO, H_2, HCHO, H_2S, and C_2H_5OH. On the exposure of reducing gas on an n-type material surface, it chemisorbed and excess electrons are transferred to the surface of material. As a consequence, the material's resistivity reduced. The adverse effect is investigated in p-type materials. Such type of electrical adaptation was employed for gas sensing.

The important parameters of a sensor are sensitivity, recovery time, operating temperature, response time, and sensing smallest range as described in literature. Everywhere in the literature, sensitivity (S) of a sensor was illustrated in various ways consisting of S = Ra/Rg, S = Rg/Ra, S = ΔR/Rg and S = ΔR/Ra, where Ra is the sensor resistance in ambient air, Rg is the sensor resistance in the target gas, and ΔR = |Ra − Rg| [28, 66]. The investigation shows that sensitivity values are described as introduces by the author. The formula for measurement of sensitivity is also specifying. Response time can be stated as the time needed for a sensor to attain the original baseline 90% of the final response of the signal-like resistance on flow of required gas. The sensor recovery time can be stated as the time required returning 90% of the final signal on removal of target gas.

5. Design of gas sensor with 1D nanostructures

In the designing of nanogas sensors, 1D nanoarchitectures are used that contain metal oxide semiconductors in the structure of nanowires, nanotubes, nanorods, nanobelts, nanowhiskers, nanofibers, nanoneedles, nanoribbons, nanopushpins, fiber-mats, lamellar, urchin, and in the form of hierarchical dendrites. In all these structures, nanowires, nanotubes, nanofibers, and nanorods are rod-form nanoarchitectures with a diameter ranging from 1 nm to 200 nm. Nanowires and nanorods have aspect ratios from 2 to 20 and more than 20 [67]. Anyhow, the aspect ratio of nanofibers is greater than that of nanowires. Primarily, nanotubes are hollow nanorods with a determined thickness of walls. The interpretation of nanoarchitectures like nanowhiskers [25], fiber-mats [22], nanoribbons [24],

nanobelts [16], urchin [26], nanoneedles [23], lamellar [28], nanopushpins [27], and hierarchical dendrites [17] can be established in the appropriate literatures. It is essential to indicate that the difference among various nanoarchitectures is not forever understandable and is mostly conditions used alternately from one to another reference.

To design sensor, nanoarchitectures are arranged in various forms. Normally, nanostructures are arranged in electrode attachment technique. Generally, adjustment of nanostructures is divided into three forms such as: (a) single arrangement of nanostructures, (b) aligned, and (c) random adjustment. It has been investigated that in the detection of different gases like hydrogen single adjustment of nanofiber was used by researchers [68–70]. Due to various aspect ratios, the nanostructures may be in the form of nanowires or nanorods [5].

An in-situ lift-out method has been investigated by Lupan et al. to detect hydrogen gas for preparing single ZnO nanorod sensor. An electropolished tungsten wire is joined to a single ZnO nanorod, which is connected to external electrodes. In the way Lupan et al. [71, 72] and Hwang I-S [64] has also designed single tripod and tetrapod sensors with the help of in-situ lift-out process by FIB. For nano-/microsensors depending upon nanostructures from semiconductor metal oxides, their process gained a 90% progress rate.

Liao et al. fabricate a gas sensor for ethanol detection in which zinc oxide nanorod arrays were used inside an indium thin film and silicon substrate [71, 72]. Ohmic contact is provided by an indium film, and for electrode, copper sheet was used. Arbitrary separated nanostructured sensors have alterations such as (a) distribution of nanostructures randomly in the film shape, (b) arbitrary separation of nanostructures' drop on the circumference of a tube, and (c) random distribution of nanostructures pressed in tablet shape. Flat interdigitated substrate was used by Wan et al. where arbitrary distribution of zinc oxide nanowires were dissolved by ultrasonication in ethanol and then spin coated on silicon interdigitated substrate. Occasionally, fabrication and attachment of nanowires with substrate are integrated with the device construction [73–75].

The tube-shaped sensors are modification of film-shaped arbitrary distributed nanostructured sensors; hence, the smooth surface is the form to a tube. Such kind of sensor has a ceramic tube-type substrate. Normally, Al_2O_3 is used as tube material and the surface is coated with one-dimensional gas sensing materials. Different types of one-dimensional gas sensing materials having various morphologies may be used on the surface of the tube. Hao et al. [26] designed a tube-shape sensor for H_2S sensing.

To design tablet-shaped sensors, randomly separated nanostructures can be used. Ethanol sensing was done by such detectors as reported by Zhou et al. [47]. At 6 MPa pressure, ZnO nanorods were grown in pellets form with thickness of 5.3 cm^2 areas and dimension of 3 mm. Electrodes were made from silver paste at the back and front surface of the ZnO pellets.

5.1 Gas detection from nanostructural materials

Nowadays, due to fine crystallinity, high aspect ratio and charge detection capability of one-dimensional nanostructure materials have become intensified for gas detection applications.

Various routes have been adopted for the synthesis of 1D nanostructures for gas detectors. The cost, yield, quality of the materials, and complexity differ for various processes. The metal oxides TiO_2, ZnO, WOx, SnO_2, CdO, In_2O_3, CuO, Fe_2O_3, $AgVO_3$, TeO_2, and MoO_3 have been studied for various required gases with

different sensitivity. Here, we discuss ZnO 1D nanostructures in terms of their fabrication, characterization, and sensitivity for sensing ethanol.

6. Performance of ethanol sensors

The ZnO NRs were then used to construct a gas sensor for ethanol sensing at various working temperature from 200 to 340°C. The as-prepared ZnO nanorod gas sensor exhibited a high, reversible, and fast response to ethanol, indicating its potential application as a gas sensor to detect ethanol. It is obvious that with the increase of ethanol concentration the response increases [29].

Flexible ZnO nanorod sensors were examined to monitor ethanol gas by varying the working temperature from 300°C to by changing the ethanol concentration in a range from 100 to 10 ppm in synthetic air. The sensitivity of a gas sensor is not influenced by the thickness of the seed layer, which presents that density of the charge carrier of ZnO NR is responsible for gas detection properties. The dimension of NRs plays an essential part in evaluating the sensitivities. A flexible ZnO nanorod sensor can detect 100 ppm of ethanol gas with a sensitivity of 3.11 at 300°C [42].

Due to large aspect ratio, the response of ZnO NRs to ethanol gas is better than that of the ZnO seed layer sensor. There are more free electrons taking part in the sensing processes with adsorbed oxygen species for the NRs grown with Zn salt/KOH solution. Therefore, a better sensitivity of the NRs grown with Zn salt/KOH solution to ethanol gas is mainly a result of the more free carriers originating from oxygen vacancies in sensor materials. The Schottky or ohmic contact shows that Au has more work function than ZnO. Hence, the sensor exhibiting the Schottky contact has a better response to ethanol gas than possessing an ohmic behavior. In conclusion, the free electrons are an important parameter for increasing the sensor response beside large aspect ratio [41].

The response of ZnO NRs decorated with photochemical Ag NP sensor to 50 ppm ethanol is almost three times as high as that of those made from pure-ZnO NRs. The electronic sensitization of noble metal doping like Ag is comfortable to grow stable oxide (Ag_2O) at operating temperature (280°C) in air. The adsorbed O_2 on the surface of Ag_2O extracts electron from ZnO and produces a depletion layer. After exposing to some target gases, Ag_2O reduced to Ag and eventually gives ZnO. Hence, due to increase in charge carrier, the sensitivity of the sensor enhanced. The responses of the sensors have no apparent degradation after being exposed to ethanol of 30 ppm for 100 days [54].

The doped ZnO sensors show increased sensitivity as compared to undoped conditions. It is shown that the sensitivity was highly affected by both Co doping and its concentration. The sensor response has been boosted by a factor of 1.6 and 1.8 for 1.85 at.% Co (Sg = 10.9) in comparison with 0.76 at.% (Sg = 6.7) and by undoped conditions (Sg = 6) in ZnO NRs, respectively, for 50 ppm C_2H_5OH [44].

The response of gas sensor based on n-type semiconductor ZnO nanorods exposed to various concentrations of the ethanol vapors at 400°C has been investigated. It showed a considerably high response even at low concentration of 5 ppm ethanol. Their response and recovery times were less than 10 and 30 s, respectively. In addition, the sensors were still sensitive to 5 ppm ethanol, even after exposure to 300 ppm ethanol. The reversible cycles of the response curve indicate a stable and repeatable operation of gas sensing. The much higher sensitivity may be due to the large effective surface areas. The results revealed that ZnO NRs show excellent response and stability. The higher response may be due to greater surface area [35].

The resistance of the sensor significantly enhanced in air at the small temperature of 200°C, due to samaria contents. A 10 times further increase in the resistance of ZS-10 consisting of 10 wt% Sm_2O_3 is investigated.

At the small temperature of 200°C, the sensor resistance in air significantly increases with samaria contents. A 10 times more increase in the resistance of ZS-10 consisting of 10 wt% Sm_2O_3 is investigated. At greater value of temperatures from 250 to 350°C, the ZS-5 and ZS-10 have the same resistances, yet greater than those of ZS-2 and Z. The main work of samaria is perhaps placed on the ZnO surface, averting direct interaction with ZnO nanoparticles that as a result enhanced the Schottky barrier. The analysis of ZnO by 10 wt% Sm_2O_3 is perhaps liable for the greater resistance explored for this sample. These investigations are explained with DRS UV-vis. The sensitivity of the Sm_2O_3-ZnO sensor was observed in the presence of 500 ppm of CO, toluene, and ethanol and 1.0 vol% of methane at a temperature of 200–400°C in air for Sm_2O_3. A significant increase in the ethanol response was investigated at different temperatures due to 5 wt% doping of Sm_2O_3-ZnO, although a smaller one toward toluene, methane, and CO. A 60 times greater response was observed to ethanol with 5 wt% Sm_2O_3-ZnO as compared to that of pure ZnO sensor [56].

A rapid and repeatable detection was observed toward ethanol vapors at normal temperature and 330°C. At an operating temperature between 280 and 310°C, the sensor has excellent response with a detection time to 500 ppm ethanol and in a time from 16 s to 120 s. High sensitivity, fast recovery, and response time have been explored at this temperature limit. The results investigate that the constructed sensor is a potential candidate for industrial applications and promising for commercialization [57].

The research explores the ZnO growth environment that explains the properties related to opto-geometry of the random ZnO nanorods over layer and the spectral response is dominating over the long time grating device. The response of ethanol toward ZnO-overlaid LPGs was confirmed under various fabrication conditions and also their spectral response correlating with available simulation models [59].

The sensor resistance enhanced with the flow of ethanol on the surface of the sensor. The sensor response time (which is defined as the 90% of the full response) is small and changes from 200 to 125 s as the concentrations enhanced from 809 to 4563 ppm, and it was investigated that the recovery time is approximately 10 min [60].

The result presents that high sensing characteristic has been established by ZnO-based sensor in the ethanol concentration (1–99.5%). The conduction process depends upon internal resistance of the nanorods for small value of ethanol concentration (a semicircle at high frequency). The charge transfer resistance interior the grain boundaries shows a straight line at small frequency region. I-V characteristics determine the sensitivity of ZnO sensor. ZnO NR arrays have potential to fabricate a chemical sensor with small power consumption and high sensitivity [49].

The recovery time response and response were established in the range of 15 and 5 s for 95% of total recovery and response, respectively. The porous structure of the sensing material is responsible to this phenomenon. The molecules diffused easily into and out of the sensing materials than did the dense structures [65].

The response enhanced from 7 to 9 with increase in temperature from 160 to 300°C. Hence, it enhanced drastically when temperature attains a value of more than 300°C. The value of the response varies from 9 to 24 as the temperature changes from 300 to 340°C and then attains the maximum value of 34 at a temperature of 370°C [58].

The SAW sensor for ethanol detection constructed from ZnO nanorods exhibits a frequency of 24 kHz at 270°C to 2300 ppm ethanol response, which is an improvement of 9 kHz of the sensor without nanorods [65].

It was investigated that a large surface energy and greater amount of O_2 vacancies' concentration exist in the NA and NHS surface that increased the ethanol detection characteristics at small temperature [53].

The conductivity of Ti-ZnO sensor was greater than that of the pure ZnO NRs by a factor of 80.7 that is 1.86%. The ethanol gas sensing response of the ZnO:Ti NR sensor has a linear relationship with temperature. The responses were found at 27.5, 66.7, 117.1, 183.5, 276.5, and 389.5% with 10, 50, 100, 250, 500, and 1000 ppm ethanol concentration, respectively. It was investigated that the responses of ZnO:Ti NR sensor are greater than those of the ZnO NRs at 1000 ppm ethanol concentration by about 5.1 [61].

It was demonstrated that they exhibited good performance for detecting ethanol vapor even at 380 and 250°C [48].

It is confirmed from the experimental results that there is no noticeable degradation of the sensor response after the flow of 50 ppm ethanol for consecutive 60 days at the operating temperature [63].

The response to 10 ppm NO_2 became negligibly small (2.3) compared to that at 200 and 300°C (66.3 and 12.4). This shows that with enhancing temperature at 400°C the capability of C_2H_5OH sensing increases. The selective detection was investigated with ZnO NWs by 200 ppm C_2H_5OH as compared to that with ZnO-SnO_2 core shell NWs only at a limit of 1/7 [64].

The research results show that from a temperature of 300°C the gas response increases abruptly till it attains the maximum value of 400°C. Then, the response decreases rapidly to a temperature limit of 400–430°C. The smaller value of working temperatures (300–400°C), 400°C, was investigated as the OOT for the ZnO NR sensor with 200 ppm ethanol response was observed to have a value of 193.7 [38].

The addition of detection layers in ZnO shows greater value of sensitivity with greater stability/reproducibility to ethanol, and comparatively small response and recovery time relative to the pure layer of MoO_3. Ethanol sensing increased with the impurity (Gethanol/Gair). The 25% ZnO in the presence of MoO_3 layer as impurity for 500 ppm ethanol attains a level of 171 under nonhumid air. Its response under humid air is 117 (75% r.H. at 21°C). This response is 6 times greater than that for the pure MoO_3 layer [62].

The sample has approximate response and recovery time of 3 and 4 min, respectively. As regard the detection characteristics of other ZnO nanoarchitectures working at greater temperatures, the ZnO NR sensors have high response and recovery time when operated at room temperature [47].

Author details

Musarrat Jabeen[1*], R. Vasant Kumar[2] and Nisar Ali[3]

1 Department of Physics, Government Degree College for Women, Haveli Lakha, Pakistan

2 Department of Material Science and Metallurgy, University of Cambridge, UK

3 Department of Physics Government Post Graduate, Jahanzeb College, Saidu Sharif Swat, Pakistan

*Address all correspondence to: musarrat97@yahoo.com; musarrat.physics@gmail.com

IntechOpen

© 2020 The Author(s). Licensee IntechOpen. This chapter is distributed under the terms of the Creative Commons Attribution License (http://creativecommons.org/licenses/by/3.0), which permits unrestricted use, distribution, and reproduction in any medium, provided the original work is properly cited.

References

[1] Kolmakov A, Moskovits M. Chemical sensing and catalysis by one-dimensional metal-oxide nanostructures. Annual Review of Materials Research. 2004;**34**:151-180

[2] Pearton SJ, Ren F, Wang Y-L, Chu BH, Chen KH, Chang CY, et al. Recent advances in wide bandgap semiconductor biological and gas sensors. Progress in Materials Science. 2010;**55**:1-59

[3] Wang C, Chu X, Wu M. Detection of H_2S down to ppb levels at room temperature using sensors based on ZnO nanorods. Sensors & Actuators, B: Chemical. 2006;**113**:320-323

[4] Min Y, Tuller HL, Palzer S, Wöllenstein J, Böttner H. Gas response of reactively sputtered ZnO films on Si-based micro-array. Sensors & Actuators, B: Chemical. 2003;**93**: 435-441

[5] Yang Z, Li L-M, Wan Q, Liu Q-H, Wang T-H. High-performance ethanol sensing based on an aligned assembly of ZnO nanorods. Sensors & Actuators, B: Chemical. 2008;**135**:57-60

[6] Wan Q, Li QH, Chen YJ, Wang TH, He XL, Li JP, et al. Fabrication and ethanol sensing characteristics of ZnO nanowire gas sensors. Applied Physics Letters. 2004;**84**:3654-3656

[7] Lu X, Yin L. Porous indium oxide nanorods: Synthesis, characterization and gas sensing properties. Journal of Materials Science and Technology. 2011; **27**:680-684

[8] Oh E, Choi H-Y, Jung S-H, Cho S, Kim JC, Lee K-H, et al. High-performance NO_2 gas sensor based on ZnO nanorod grown by ultrasonic irradiation. Sensors & Actuators, B: Chemical. 2009;**141**:239-243

[9] Cao Y, Hu P, Pan W, Huang Y, Jia D. Methanal and xylene sensors based on ZnO nanoparticles and nanorods prepared by room-temperature solid-state chemical reaction. Sensors & Actuators, B: Chemical. 2008;**134**: 462-466. Sensors. 2012;**12**:7253

[10] Lupan O, Chai G, Chow L. Novel hydrogen gas sensor based on single ZnO nanorod. Microelectronic Engineering. 2008;**85**:2220-2225

[11] Wang HT, Kang BS, Ren F, Tien LC, Sadik PW, Norton DP, et al. Hydrogen-selective sensing at room temperature with ZnO nanorods. Applied Physics Letters. 2005;**86**:243503

[12] Qi Q, Zhang T, Liu L, Zheng X. Synthesis and toluene sensing properties of SnO_2 nanofibers. Sensors and Actuators B. 2009;**137**:471-475

[13] Wan Q, Lin CL, Yu XB, Wang TH. Room-temperature hydrogen storage characteristics of ZnO nanowires. Applied Physics Letters. 2004;**84**: 124-126

[14] Wang D, Chu X, Gong M. Gas-sensing properties of sensors based on single-crystalline SnO_2 nanorods prepared by a simple molten-salt method. Sensors & Actuators, B: Chemical. 2006;**117**:183-187

[15] Hu A, Cheng C, Li X, Jiang J, Ding R, Zhu J, et al. Two novel hierarchical homogeneous nanoarchitectures of TiO_2 nanorods branched and P25-coated TiO_2 nanotube arrays and their photocurrent performances. Nanoscale Research Letters. 2011;**6**:2-6

[16] Sadek AZ, Choopun S, Wlodarski W, Ippolito SJ, Kalantar-zadeh K. Characterization of ZnO nanobelt-based gas sensor for H_2, NO_2,

and hydrocarbon sensing. IEEE Sensors Journal. 2007;**7**:919-924

[17] Zhang N, Yu K, Li Q, Zhu ZQ, Wan Q. Room-temperature high-sensitivity H_2S gas sensor based on dendritic ZnO nanostructures with macroscale in appearance. Journal of Applied Physics. 2008;**103**:104305

[18] Kim SS, Park JY, Choi S-W, Kim HS, Na HG, Yang JC, et al. Significant enhancement of the sensing characteristics of In_2O_3 nanowires by functionalization with Pt nanoparticles. Nanotechnology. 2010;**21**:415502

[19] Huang MH, Wu Y, Feick H, Tran N, Weber E, Yang P. Catalytic growth of zinc oxide nanowires by vapor transport. Advanced Materials. 2001;**13**: 113-116

[20] Carney CM, Yoo S, Akbar SA. TiO_2-SnO_2 nanostructures and their H_2 sensing behavior. Sensors & Actuators, B: Chemical. 2005;**108**:29-33

[21] Francioso L, Taurino AM, Forleo A, Siciliano P. TiO_2 nanowires array fabrication and gas sensing properties. Sensors & Actuators, B: Chemical. 2008; **130**:70-76

[22] Baratto C, Sberveglieri G, Onischuk A, Caruso B, di Stasio S. Low temperature selective NO_2 sensors by nanostructured fibres of ZnO. Sensors & Actuators, B: Chemical. 2004;**100**: 261-265

[23] Qurashi A, El-Maghraby EM, Yamazaki T, Kikuta T. Catalyst supported growth of In_2O_3 nanostructures and their hydrogen gas sensing properties. Sensors & Actuators, B: Chemical. 2010;**147**:48-54

[24] Ying Z, Wan Q, Song ZT, Feng SL. SnO_2 nanowhiskers and their ethanol sensing characteristics. Nanotechnology. 2004;**15**:1682-1684

[25] Kong X, Li Y. High sensitivity of CuO modified SnO_2 nanoribbons to H_2S at room temperature. Sensors & Actuators, B: Chemical. 2005;**105**:449-453

[26] Hao Q, Li L, Yin X, Liu S, Li Q, Wang T. Anomalous conductivity-type transition sensing behaviors of n-type porous α-Fe_2O_3 nanostructures toward H2S. Materials Science and Engineering B. 2011;**176**:600-605

[27] Qurashi A, Yamazaki T, El-Maghraby EM, Kikuta T. Fabrication and gas sensing properties of In_2O_3 nanopushpins. Applied Physics Letters. 2009;**95**:153109

[28] Imawan C, Solzbacher F, Steffes H, Obermeier E. Gas-sensing characteristics of modified-MoO_3 thin films using Ti-overlayers for NH_3 gas sensors. Sensors & Actuators, B: Chemical. 2000;**64**:193-197

[29] Wang L, Kang Y, Liu X, Zhang S, Huang W, Wang S. ZnO nanorod gas sensor for ethanol detection. Sensors and Actuators B: Chemical. 2012;**162**(1): 237-243. ISSN 0925-4005

[30] Rahman MM, Jamal A, Khan SB, Faisal M. CuO Codoped ZnO based nanostructured materials for sensitive chemical sensor applications. ACS Applied Materials & Interfaces. 2011; **3**(4):1346-1351

[31] Faisal M, Khan SB, Rahman MM, Jamal A, Asiri AM, Abdullah MM. Synthesis, characterizations, photocatalytic and sensing studies of ZnO nanocapsules. Applied Surface Science. 2011;**258**:672-677

[32] Asiri AM, Khan SB, Rahman MM, Al-Sehemi AG, Al-Sayari SA, Al-Assiri MS. Green material: Ecological importance of imperative and sensitive chemi-sensor based on Ag/Ag_2O_3/ZnO composite nanorods. Nanoscale Research Letters. 2013;**8**:380

[33] Rahman MM, Khan SB, Asiri AM, Alamry KA, Khan AAP, Khan A, et al. Acetone sensor based on solvothermally prepared ZnO doped with Co_3O_4 nanorods. Microchimica Acta. 2013;**180**: 675-685

[34] Men H, Gao P, Zhou B, Chen Y, Zhu C, Xiao G, et al. Fast synthesis of ultra-thin $ZnSnO_3$ nanorods with high ethanol sensing properties. Chemical Communications. 2010;**46**(40): 7581-7583

[35] Li Y-J, Li K-M, Wang C-Y, Kuo C-I, Chen L-J. Low-temperature electrodeposited Co-doped ZnO nanorods with enhanced ethanol and CO sensing properties. Sensors and Actuators B: Chemical. 2012;**161**(1): 734-739. ISSN 0925-4005

[36] Lee Y-M, Huang C-M, Chen H-W, Yang H-W. Low temperature solution-processed ZnO nanorod arrays with application to liquid ethanol sensors. Sensors and Actuators A: Physical. 2013; **189**:307-312. ISSN 0924-4247

[37] An G, Sun Z, Zhang Y, Ding K, Xie Y, Tao R, et al. CO_2 mediated synthesis of ZnO nanorods and their application in sensing ethanol vapor. Journal of Nanoscience and Nanotechnology. 2011;**11**(2):1252-1258

[38] Zhang L, Yin Y. Large-scale synthesis of flower-like ZnO nanorods via a wet-chemical route and the defect-enhanced ethanol-sensing properties. Sensors and Actuators B: Chemical. 2013;**183**:110-116. ISSN 0925-4005

[39] Faisal M, Khan SB, Rahman MM, Jamal A, Abdullah MM. Fabrication of ZnO nanoparticles based sensitive methanol sensor and efficient photocatalyst. Applied Surface Science. 2012;**258**:7515-7522

[40] Rahman MM, Khan SB, Asiri AM. Smart methanol sensor based on silver oxide-doped zinc oxide nanoparticles deposited on microchips. Microchimica Acta. 2014;**181**:553-563

[41] Ahn H, Park J-H, Kim S-B, Jee SH, Yoon YS, Kim D-J. Vertically aligned ZnO Nanorod sensor on flexible substrate for ethanol gas monitoring. Electrochemical and Solid-State Letters. 2010;**13**(11):J125-J128

[42] Khan SB, Faisal M, Rahman MM, Jamal A. Low-temperature growth of ZnO nanoparticles. Photocatalyst and Acetone Sensors, Talanta. 2011;**85**: 943-949

[43] Israr-Qadir S, Jamil-Rana O, Nur M, Willander LA, Larsson PO. Holtz fabrication of ZnO nanodisks from structural transformation of ZnO nanorods through natural oxidation and their emission characteristics. Ceramics International. 2014;**40**:2435-2439

[44] Xiang Q, Meng G, Zhang Y, Xu J, Xu P, Pan Q, et al. Ag nanoparticle embedded-ZnO nanorods synthesized via a photochemical method and its gas-sensing properties. Sensors and Actuators B: Chemical. 2010;**143**(2): 635-640. ISSN 0925-4005

[45] Faisal M, Khan SB, Rahman MM, Ismail AA, Asiri AM, Al-Sayari SA. Development of efficient chemi-sensor and photo-catalyst based on wet-chemically prepared ZnO nanorods for environmental remediation. Journal of the Taiwan Institute of Chemical Engineers. 2014;**45**:2733-2741

[46] Faisal M, Khan SB, Rahman MM, Jamal A, Asiri AM, Abdullah MM. Smart chemical sensor and active photo-catalyst for environmental pollutants. Chemical Engineering Journal. 2011;**173**: 178-184

[47] Zhou X, Li J, Ma M, Xue Q. Effect of ethanol gas on the electrical properties of ZnO nanorods. Physica E: Low-dimensional Systems and Nanostructures. 2011;**43**(5):1056-1060. ISSN 1386-9477

[48] Roy S, Banerjee N, Sarkar CK, Bhattacharyya P. Development of an ethanol sensor based on CBD grown ZnO nanorods. Solid-State Electronics. 2013;**87**:43-50. ISSN 0038-110

[49] Chen J, Li J, Li J, Xiao G, Yang X. Large-scale syntheses of uniform ZnO nanorods and ethanol gas sensors application. Journal of Alloys and Compounds. 2011;**509**(3):740-743. ISSN 0925-8388

[50] Faisal M, Khan SB, Rahman MM, Jamal A, Akhtar K, Abdullah MM. Role of ZnO-CeO_2 nanostructures as a photocatalyst and chemi-sensor. Journal of Materials Science & Technology. 2011;**27**:594-600

[51] Ahmad MZ, Sadek AZ, Latham K, Kita J, Moos R, Wlodarski W. Chemically synthesized one-dimensional zinc oxide nanorods for ethanol sensing. In: IMCS 2012—The 14th International Meeting on Chemical Sensors.

[52] Guo W, Fu M, Zhai C, Wang Z. Hydrothermal synthesis and gas-sensing properties of ultrathin hexagonal ZnO nanosheets. Ceramics International. 2014;**40**:2295-2298

[53] Bao D, Gao P, Wang L, Wang Y, Chen Y, Chen G, et al. ZnO nanorod arrays and hollow spheres through a facile room-temperature solution route and their enhanced ethanol gas-sensing properties. ChemPlusChem. 2013;**78**:1266-1272

[54] Chang CM, Hon MH, Leu IC. Preparation of ZnO nanorod arrays with tailored defect-related characterisitcs and their effect on the ethanol gas sensing performance. Sensors and Actuators B: Chemical. 2010;**151**(1): 15-20. ISSN: 0925-4005

[55] Yin M, Liu M, Liu S. Diameter regulated ZnO nanorod synthesis and its application in gas sensor optimization. Journal of Alloys and Compounds. 2014; **586**:436-440. ISSN 0925-8388

[56] Bagheri M, Hamedani NF, Mahjoub AR, Khodadadi AA, Mortazavi Y. Highly sensitive and selective ethanol sensor based on Sm_2O_3-loaded flower-like ZnO nanostructure. Sensors and Actuators B: Chemical. 2014; **191**:283-290. ISSN 0925-4005

[57] Ahmad MZ, Sadek AZ, Latham K, Kita J, Moos R, Wlodarski W. Chemically synthesized one-dimensional zinc oxide nanorods for ethanol sensing. Sensors and Actuators B: Chemical. 2013;**187**:295-300. ISSN 0925-4005

[58] Yin M, Liu M, Liu S. Development of an alcohol sensor based on ZnO nanorods synthesized using a scalable solvothermal method. Sensors and Actuators B: Chemical. 2013;**185**: 735-742. ISSN 0925-400

[59] Konstantaki M, Klini A, Anglos D, Pissadakis S. An ethanol vapor detection probe based on a ZnO nanorod coated optical fiber long period grating. Optics Express. 2012;**20**:8472-8484

[60] Santra S, Guha PK, Ali SZ, Hiralal P, Unalan HE, Covington JA, et al. ZnO nanowires grown on SOI CMOS substrate for ethanol sensing. Sensors and Actuators B: Chemical. 2010; **146**(2):559-565. ISSN 0925-400

[61] Hsu C-L, Gao Y-D, Chen Y-S, Hsueh T-J. Vertical Ti doped ZnO nanorods based on ethanol gas sensor prepared on glass by furnace system with hotwire assistance. Sensors and Actuators B: Chemical. 2014;**192**(1): 550-557. ISSN 0925-4005

[62] Illyaskutty N, Kohler H, Trautmann T, Schwotzer M, Pillai VPM. Enhanced ethanol sensing response from nanostructured MoO_3: ZnO thin films and their mechanism of sensing. Journal of Materials Chemistry C. 2013; **1**:3976-3984

[63] Qin N, Wang X, Xiang Q, Xu J. A biomimetic nest-like ZnO: Controllable

synthesis and enhanced ethanol response. Sensors and Actuators B: Chemical. 2014;**191**:770-778. ISSN 0925-4005

[64] Hwang I-S, Kim S-J, Choi J-K, Choi J, Ji H, Kim G-T, et al. Synthesis and gas sensing characteristics of highly crystalline ZnO–SnO2 core–shell nanowires. Sensors and Actuators B: Chemical. 2010;**148**(2):595-600. ISSN 0925-4005

[65] Giffney TJ, Ng YH, Aw KC. A surface acoustic wave ethanol sensor with zinc oxide nanorods. Smart Materials Research. 2012;Article ID 210748, 4 p. DOI: 10.1155/2012/210748

[66] Huang J, Wan Q. Gas sensors based on semiconducting metal oxide one-dimensional nanostructures. Sensors. 2009;**9**:9903-9924

[67] Mai L, Xu L, Gao Q, Han C, Hu B, Pi Y. Single β-$AgVO_3$ nanowire H_2S sensor. Nano Letters. 2010;**10**: 2604-2608

[68] Mai LQ, Hu B, Hu T, Chen W, Gu ED. Electrical property of Mo-doped VO_2 nanowire array film by melting-quenching sol-gel method. The Journal of Physical Chemistry. B. 2006;**110**: 19083-19086

[69] Tsuji M, Hashimoto M, Nishizawa Y, Tsuji T. Synthesis of gold nanorods and nanowires by a microwave-polyol method. Materials Letters. 2004;**58**:2326-2330

[70] Hu P, Du G, Zhou W, Cui J, Lin J, Liu H, et al. Enhancement of ethanol vapor sensing of TiO_2 nanobelts by surface engineering. Journal of the American Chemical Society. 2010;**2**: 3263-3269

[71] Lupan O, Emelchenko GA, Ursaki VV, Chai G, Redkin AN, Gruzintsev AN, et al. Synthesis and characterization of ZnO nanowires for nanosensor applications. Materials Research Bulletin. 2010;**45**:1026-1032

[72] Lupan O, Chow L, Chai G. A single ZnO tetrapod-based sensor. Sensors & Actuators, B: Chemical. 2009;**141**: 511-517

[73] Varghese OK, Gong D, Paulose M, Ong KG, Grimes CA. Hydrogen sensing using titania nanotubes. Sensors & Actuators, B: Chemical. 2003;**93**: 338-344

[74] Liao L, Lu HB, Li JC, He H, Wang DF, Fu DJ, et al. Size dependence of gas sensitivity of ZnO nanorods. The Journal of Physical Chemistry. 2007;**111**: 1900-1903

[75] Choi Y-J, Hwang I-S, Park J-G, Choi KJ, Park J-H, Lee J-H. Novel fabrication of an SnO_2 nanowire gas sensor with high sensitivity. Nanotechnology. 2008;**19**:095508

Chapter 5

Design and Growth of Metal Oxide Film as Liquefied Petroleum Gas Sensors

Rakesh Kumar Sonker, Saroj Radheyshyam Shabajeet, Rahul Johari and Balchandra Yadav

Abstract

Nowadays innovations in synthesis methods for metal oxide-based nanomaterials such as nanostructured and both physical and chemical route techniques have been adopted by various researchers around the world. The investigation has been focusing on various deposition parameters for fabricating nanostructured metal oxide. Gas sensors that use metal oxide materials are broadly utilized in industry to monitor combustion processes. While they are economical to powerful in high temperature environments, many of these instruments are not selective towards the species of interest when placed in a stream composed of multiple gases. Research on nanostructured metal oxide materials has generated great interest in scientific community. Metal oxide is a chemically stable, harmless, biocompatible, inexpensive material with very high dielectric constant and interesting photocatalytic activities. It is a wide-gap semiconductor and depending on its chemical composition, it shows a large range of electrical conductivity. Synthesis strategies regarding nanocomposites of metal oxide with other inorganic and organic materials sensing activities has been reviewed. The measure response of metal oxide film-based sensor highat low concentration of LPG.

Keywords: metal oxide, thin film, deposition technique, LPG sensor

1. Introduction

Liquefied petroleum gas (LPG) is the composition of hydrocarbons mainly propane and butane. The lower explosive limit (LEL) as specified by National Institute for Occupational Safety and Health (NIOSH) and Occupational Safety and Health Administration (OSHA) standards for chemical hazards is 21,000 ppm (2.1% by volume in air) for propane and 19,000 ppm (1.9% by volume in air) for butane. The permissible exposure limit (PEL) for LPG as specified by NIOSH and OSHA standards is 1000 ppm [1]. LPG is mostly used as fuel for vehicles and as cooking gas for household applications. Exact observing of leakages of LPG even at low concentrations can be useful to avoid accidental explosions [2, 3]. Sensors have turned into an indispensable piece of the cutting-edge human progress attributable to its significance, where metal oxides have played a major role as reliable sensor materials. Nanoparticle do research presents broad scope for the growth of novel solutions in the field of healthcare, cosmetics, optics and electronics. Varying their sub-atomic and nuclear states results in surprising results, which may not be conceivable by utilizing the materials in their unique states. A few metal oxides

such as TiO_2, SnO_2, ZnO, WO_3 and Cr_2O_3, etc., are shown in semiconducting nature of materials. The electrical properties of these oxides are sensitive to the oxygen partial pressure since it changes in the concentration of electrons or electron holes in the oxides. This article manages the properties and utilizations of titanium oxide nanoparticles. Titanium oxide (TiO_2) is accessible as nanocrystals or nanodots having a high surface area.

Titanium oxide (TiO_2) nanoparticle is a non-broke down material which does not break up itself when degrades organic contaminant and kills germs. It has a lasting effect on killing germs and degrading organic contaminants. TiO_2 nanoparticle is broadly used as ultra violet-resistant nanomaterials and in the field of produce chemical fiber, plastics, printing ink, coating, self-cleaning glass, self-cleaning ceramic objects, antibacterial material, air purification, cosmetics, sunscreen cream, natural white moisture protection cream, moistening refresher, vanishing cream, skin protecting cream, foods packing material, coating for paper-making industry: used for civilizing the pliability and opacity of the paper and used for producing titanium, ferrotitanium alloy, carbide alloy, etc., in the metallurgical industry, astronautics industry, conducting material, gas sensor, and moisture sensor. TiO_2 also famous such as titania is the obviously occurring oxide of titanium. Titania is an inventive material used broadly in industry, research and environmental cleaning. Titania occurs in several crystalline forms; the most significant of which are anatase and rutile. Uncontaminated TiO_2 does not occur in nature but is derived from ilmenite or leucoxene ores. It is additionally eagerly mined in one of the most perfect structures, rutile shoreline sand. These minerals are the real crude materials utilized in the generation of titanium dioxide pigment. The initial step is to filter the mineral and is for the most part a refinement step. Either the sulfate process, which uses sulfuric acid as a removal agent or the chloride process, which uses chlorine, may achieve this. After filtration the powders may be treated to enhance their performance as pigments.

Therefore, metal oxide nanomaterials play imperative role in the recent development of science due to its small size and large surface area [4]. In this chapter several synthesis methods to prepare ceramic nanoparticles, characterization techniques and different properties of gas/humidity sensors are described. The role of water vapor has been studied in the environment with respect to human life. For the measurement of humidity, conventional approaches and modern methods using solid state devices are described. Nanomaterials can be metals, stoneware, polymeric materials, or composite materials. Their significant characteristic is a very small feature size in the range of 1–100 nm. At the nanomaterial level, some material properties are influenced by the laws of nuclear material science, instead of carrying on as conventional mass materials do.

1.1 Lattice structure of TiO_2

The three forms of titanium dioxide structure materials can exist: rutile, anatase and brookite shown in **Figure 1**.

The basic structural features of anatase and rutile materials have been assessed, as the brookite structure is not used regularly for exploratory examinations. Together, the crystal structures of rutile and anatase are found in the widespread octahedron. In rutile, the bending is slightly orthorhombic in which the unit cell extends beyond a cubic form. In anatase, the distortion of the cubic lattice is more significant and, therefore, the resulting symmetry is smaller than the orthorhombic one. **Figure 2** shows a structural drawing of rutile and anatase bulk materials. The lengths of the connections and the angles between the atoms are shown, showing the elongated cubic form [5].

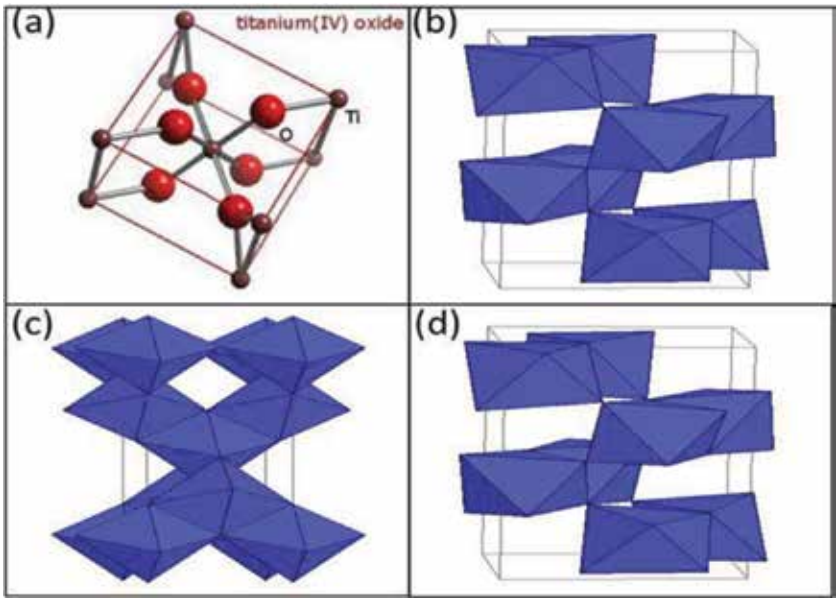

Figure 1.
(a) Unit cell of the crystalline structure of TiO_2 and crystal structure of (b) rutile (tetragonal) TiO_2, (c) anatase (tetragonal) TiO_2, and (d) brookite (orthorhombic) TiO_2.

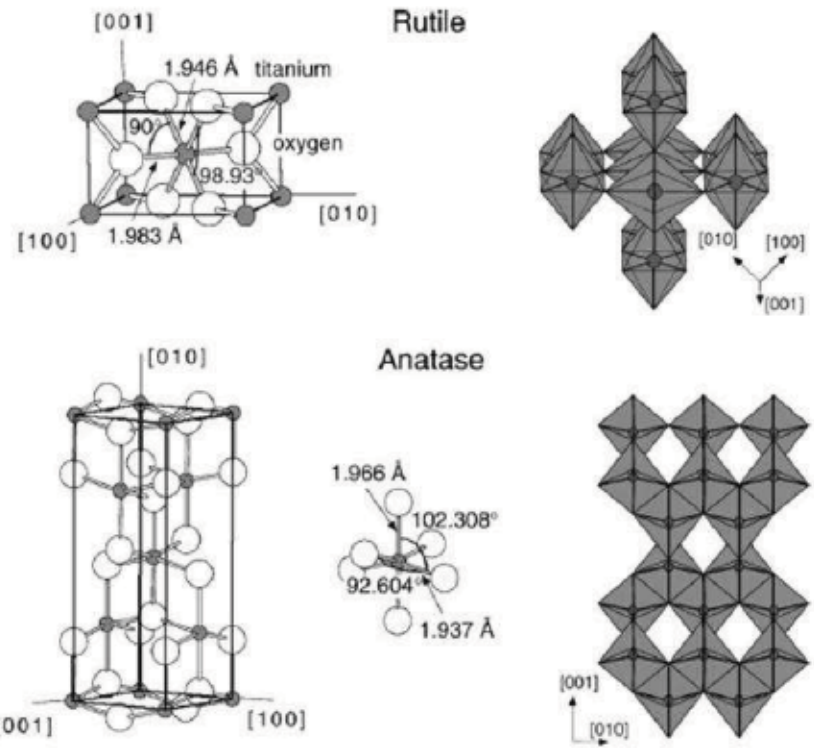

Figure 2.
The structure of rutile and anatase titanium dioxide.

The crystal structure of TiO_2 nanoparticles depend great extent on the arrangement technique. The tiny TiO_2 nanoparticle (<50 nm) anatase appeared to be steadier and more changed in to rutile phase at >973K. The change arrangement

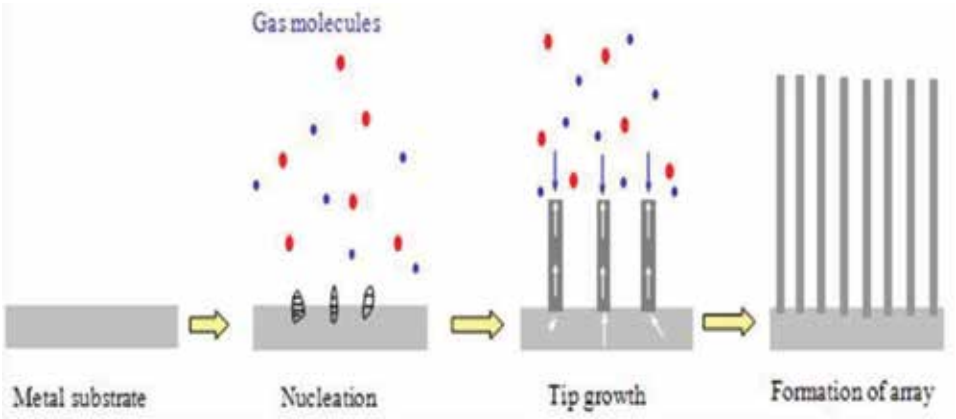

Figure 3.
The schematic diagram of growth of nanoparticles.

and thermodynamic stage steadiness relied upon the underlying molecule sizes of anatase appeared in **Figure 3**. In the temperature range 973–1073 K only one phase change from anatase to rutile occurred. Both sizes of anatase and rutile particles increased with increasing temperature, but the growth rate was different. Rutile had a much higher growth rate than anatase. The rate of development of the anatase has been stabilized at 800°C. The rutile particles, after nucleation, have grown rapidly, where the size of the anatase particles has remained virtually unchanged with the decrease of the initial particle size, the temperature of start the diminished transition [6]. The diminished warm steadiness in better nanoparticles was fundamentally because of the lessened enactment vitality as a size related surface enthalpy and stress vitality expanded.

1.2 Properties of TiO_2

The chemical composition of Ti and O in TiO_2 is as given in **Table 1**.

1.2.1 Key properties

The summarized **Table 2** shows the physical and mechanical properties of sintered titania, while the optical properties of titania are provided in **Table 3**.

1.2.2 Photo catalytic properties

Titania used a photosensitizer for photovoltaic cells and when used as an solid state coating electrode in photo-electrolysis cells, can improve the efficiency of electrolytic splitting of water into hydrogen and oxygen.

In 1972, Fujishima and Honda discovered the photocatalytic water division in TiO_2 electrodes. This incident developed the foundations of a new era inheterogeneity. photo-catalysis. Titania is a promising photocatalyst chemical. Two different crystal

Element	Content (%)
Titanium	59.93
Oxygen	40.55

Table 1.
Chemical composition.

Density	4 g cm^{-3}
Porosity	0%
Compressive strength	680 MPa
Poisson's ratio	0.27
Shear modulus	90 GPa
Modulus of elasticity	230 GPa
Resistivity (25°C)	10^{12} ohm cm
Resistivity (700°C)	2.5×10^{4} ohm cm
Dielectric constant (1 MHz)	4
Thermal expansion (RT-1000°C)	9×10^{-6}
Melting point (°C)	1843°C
Boiling point (°C)	2972°C

Table 2.
Typical physical and mechanical properties of titania.

Phase	Refractive index	Density (g cm^{-3})	Crystal structure
Anatase	2.49	3.84	Tetragonal
Rutile	2.903	4.26	Tetragonal
Brookite		4.123	Orthorhombic

Table 3.
Titania optical properties.

structures of TiO_2, rutile and anatase, are normally used in photo-catalysis activity. Photo-catalysis is a photon energy (from the UV in sunlight) used to the medium (catalyst) to support chemical reaction to continue. TiO_2 is a semiconductor in which, the valence band is filled with electrons. Since the band gap of TiO_2 is 3.20 eV and can use only UV light below 400 nm, numerous efforts have been made to sensitize larger band gap semiconductors or to use slight band gap semiconductors that can absorb visible light. Photon or UV light which is below the wavelength of violet (400 nm) has a high destructive energy. When the photon is familiarized to titania, it becomes unstable thus the electron escapes. This electron can break chemical bond since it has a high energy. This reaction can be very useful to decompose organic material, impurities and bacteria in the air.

1.3 Synthesis methods of nanomaterials

Synthesis methods play very important part of research to control the size and surface area of nanomaterials. There is numerous synthesis methods, some of them are described below:

- Hydrothermal synthesis
- Sol-gel method
- Aerosol methods
- Low temperature combustion methods

1.3.1 Hydrothermal synthesis

The hydrothermal synthesis is a process which uses single heterogeneous phase reactions in aqueous medium at higher temperature and pressure to crystallize and produce ceramic materials hydrated directly from the solutions [7]. This synthesis offers a low temperature direct route to the oxide powder with a small size distribution that prevents the passage of calcination. The hydrothermal reaction mechanism monitors a liquid nucleation model. Normally, in the hydrothermal process temperature falls between the boiling point of the water and the critical temperature (T_c = 374°C), while the pressure is higher than 100 kPa. The product is washed with deionized water to remove ions from the solvent and other impurities. After drying in the air, very well dispersed ceramic nanoparticles are obtained.

1.3.2 Sol-gel method

First, a solution of the appropriate precursors (metal salts of organic metal compounds) is formed, followed by conversion into homogeneous oxide (gel) after hydrolysis and condensation [8]. The drying and subsequent calcination of the gel produce an oxide product. Usually, for the preparation of multicomponent oxides, the alkoxides are mixed in alcohol. The components for which alkoxides are not available are introduced as salts, such as acetates. The hydrolysis is carried out at a controlled temperature, pH and alkoxide concentration, addition of water and alcohol.

1.3.3 Aerosol method

This method is also defined as a gas phase method. It is considered to be convenient and convenient in the large-scale industrial production of multicomponent materials [9]. Aerosols are suspensions of small solid or liquid particles in a gas. There are two ways of preparing ultrafine particles by aerosol processes. The first concerns the generation of a supersaturated vapor from a reagent followed by a homogeneous nucleation (conversion of gas into particles). The second concerns the generation of liquid droplets, which are subjected to a heat treatment in solid particles (conversion of liquid into particles). The latter is used to prepare multicomponent materials.

Spray drying and spray pyrolysis are the most common methods for converting liquid into solid. A metal precursor (sol) solution is produced, followed by drop atomization, which are conducted to an oven. Therefore, spray drying can be a suitable process for consolidating the nanoparticles into submicronic spherical granules that can be compacted into microscopic shapes.

1.3.4 Low temperature combustion method

The low-temperature combustion synthesis technique (LCS, for its acronym in English) has proven to be an innovative, extremely easy path, which saves time and saves energy for the synthesis of ultrafine powders [10–13]. This is based on the gelling and subsequent combustion of an aqueous solution containing salts of the desired metals and some organic fuels, which provides a voluminous and fluffy product with a large surface area. As starting materials, oxidizing metals salts, such as metal nitrates and a combination agent (fuel), such as citric acid, polycyclic acid or urea are used. Citrate acid is used more widely, since it does not function only as a reducing/fueling agent, but also as a chelating agent.

1.4 Introduction to gas sensor

1.4.1 Gas sensor technology

A gas sensor is a device that produces an electrical signal in response to a chemical interaction with the vapors because the information obtained from this process is advantageous. Gas sensors have generated extensive applications in both domestic and industrial environments. However, despite its value, there are many difficulties in making a reliable sensor before it can be used safely. Ideally, gas sensors should exhibit a high sensitivity to steam that are designed to detect. Furthermore, the sensor should produce only an electrical response when exposed to the gas of interest. The sensors must also have stable and reproducible electrical signals to reduce the time required for calibration. There are other practical concerns, such as minimizing size, weight and energy consumption, as well as the ability to position the sensor close to where measurements are to be made.

According to the definition of gas sensor, provided by the International Union of Pure and Applied Chemistry (IUPAC), "a chemical sensor is a device that transforms chemical information, ranging from the concentration of a specific component of the sample to the analysis of the composition total, in an analytically useful signal. The above chemical information can derive from a chemical reaction of the analyte or from a physical property of the system under examination" [14]. Normally, chemical sensors consist of two main parts, a receiver and a transducer. A sensor is an instrument that responds to a physical stimulus (such as heat, light, sound, pressure, magnetism or movement). Collects and measures data related to some properties of a phenomenon, object or material. Sensors are an important part for any measurement and automation application. The sensor is responsible for converting a certain type of physical phenomenon into an amount that can be measured by a data acquisition system (DAQ). The receiver transforms the chemical information into a form of energy, which can be measured by the transducer. The transducer converts this energy into a useful analytical signal, typically electric. Chemical sensors are classified in different ways. One of the classifications uses the operating principle of the receiver [14].Using this principle, one can distinguish between.

1. Physical sensors,

2. Chemical sensors, and

3. Biochemical sensors.

In physical sensors a chemical reaction does not take place in the receiver and the signal is the result of a physical process, such as mass, absorbance, refractive index, temperature or conductivity change. Chemical sensors are based on chemical reactions between the analyte molecules and the receptor. Biochemical sensors are a subclass of chemical sensors, in which the reaction is biochemical. Typical examples of such sensors are microbial potentiometric sensors or immune sensors. It is not always possible to discriminate between physical and chemical sensors. A good example is a gas sensor, in which the signal is the result of gas adsorption.

Gas loss is a major concern in residential, commercial and gas transportation vehicles. One of the precautionary measures to avoid the danger associated with gas leaks is to install a gas leak detector in vulnerable locations. The purpose of this document is to present the design of an automatic economic alarm system, capable of detecting liquefied petroleum gas leaks in different locations. In particular, the

designed alarm system has a high sensitivity, especially for butane, which is also sold individually bottled as fuel for cooking and camping. The proposed system is designed to meet UK occupational health and safety standards. Test results are proven for a USB powered gas leak detection system and provide early warning signals in less severe conditions and trigger an acute alarm in case of emergency to protect users. Liquefied petroleum gas (LPG) is commonly used in homes for central heating, hot water, gas ovens, kitchens and mobile heaters for recreational activities such as boats, caravans and grills. This energy source is mainly composed of propane and butane, which are highly flammable chemical compounds. LPG leaks can occur, though rarely, in a home, commercial facility, or gasoline vehicle. Loss of this gas can be dangerous as it increases the risk of fire or explosion. The victims of this danger are still common news in the media. Since LPG as such has no odor, gas/refinery companies add an odor, such as ethanediol, thiophene or mercaptan, so that most people can detect losses [15]. However, it is possible that some people with reduced sense of smell cannot rely on this intrinsic safety mechanism. In such cases, a gas leak detector becomes vital and helps protect people against the dangers of gas leaks. Several research papers on gas leak detection techniques have been published [16–24]. In [16] a home wireless security gas leakage system [16] was proposed in which the alarm device provides mobility within the house's premises. Detection of losses and identification of their position is the most important task of pipeline operators in the gas industry. Flow monitoring and methods based on linear parameter variation models (LPV) are widely used in the gas industry to detect gas leaks. Both methods continuously measure pressure at different sections of the tube, usually at the ends [17–22]. However, the disadvantage of these techniques is that they rely heavily on the noise of pressure/temperature measurements. The reliability problems of gas leak detectors were addressed in [23]. The gas leak sounds generated by the cracks in the tubes were analyzed in [24] to locate the leak.

Use of nanotechnology in engineering materials for sensor applications may improve the working detection limit of gas sensors to lower temperatures. This will be achieved predominantly by alterations of the space charge layers for each grain and enhancing other electronic properties of the material. The science of nanomaterials deals with new phenomena and new sensor devices that exploit these phenomena are being built. Sensitivity may increase due to better conduction properties, detection limits may be lower and very small amounts of samples may be analyzed, direct detection is possible without the use of labels and some reagents may be removed [25].

Inorganic nanomaterials with controllable sizes and shapes have a wide range of unique physical, chemical, electrical, surface and optical properties. Nanometric sensors are essential for many interesting developments in nanotechnology research. Several "bottom-up" techniques widely reported in parallel offer the potential for the integration of high-density nanosensors beyond the capacity of conventional technologies with a small fraction of the current manufacturing cost. The field of nanosensors requires the identification of several self-organized nanostructures with structural characteristics and special physical properties to have devices with the appropriate integration of the circuit [26].

The large surface-to-volume ratio of nanomaterials can be used as an advantage for the development of the gas sensor. The large surface to volume ratio of nanocrystalline structures increases the opportunity for this surface reaction. This in turn will increase the sensitivity of the gas sensor. Engineering materials with selective chemistry to modify and manipulate the structure is the key to the improvement in gas sensor sensitivity and selectivity. Nanomaterials have been highlighted for gas sensor applications due to their enhanced abilities over their conventional entering material counterparts. The surface of nanomaterials can comprise much of the actual material making them ideal for gas sensors. Ability

to synthesize one dimensional nanostructure with extremely high aspect ratios makes them attractive in gas sensor fabrication as well. The space charge layer control of nanostructures makes them particularly interesting since conduction can change drastically with expansion and contraction of the layer in the presence of different gases. Despite these observations at the nano-scale, many of the mechanisms responsible for conduction at the nano-scale are still poorly understood. The oxygen vacancies also need to not be "pinned" to any impurities and need as little resistance as possible at the grain boundaries when the appropriate reducing gas is present. Second, increasing the number of surface sites for gas interaction will help achieve this goal; so that even low concentrations of gas can be detected at room temperature. The use of nanomaterials is important because of their high surface/volume ratio. This can be increased by changing the nanoparticle shape from spherical to unidimensional, creating hollow tubes or tubes. The third modification that can be made to the sensor material is the modification of the space-loading layer. This is done to obtain the maximum signal change in the presence of the target gas. Modification of the space charge layer can be done by: (1) reducing the size of the crystallite, (2) changing the chemistry of the defects within the space charge layer and the surface of the material, and (3) changes in the charge layer space. The shape of the particle may play a factor. Another interesting aspect of nanomaterials that make them a candidate for room temperature gas sensor applications is the fact that changes in the band gap have been reported at extremely small sizes. The possibility to modify this band gap may be another way to improve room temperature gas sensing by changing the potential barrier energy required for charged species to conduct. Another enhanced feature of nanocrystallites is their conduction of electrons from the surface reaction. These conduction electrons have to overcome a potential barrier induced by the space charge layer. The magnitude of this space charge layer is dependent on the crystallite size (D) as well as the space-charge layer thickness (L). It has been shown that when $D < 2\,L$, the sensitivity of a gas sensor is enhanced drastically. This $D < 2\,L$ limit can be reached when employing nanostructures.

1.4.2 Importance of a gas sensor

Gas sensors are very important in the industrial sector and in other areas. Although there are many difficulties in solving these problems, gas sensors still have several specific functions in theworld. For example, hydrogen sensors are needed in the rocket propulsion industry because the dispersion of the hydrogenpropellant presents significant safety risks. In addition, theautomotive industry routinely monitors the air/fuel ratio invehicles with oxygen sensors that use an electrochemical cell containing TiO_2 that conducts oxygen ions at high temperatures. The automotive industry is also interested in NOx sensors because nitrogen oxides are formed when the fuel is burned at high temperatures. Nitrogen oxides are a unique hazard because they can travel long distances from their emission source and generate ozone, pollution and particles away from the actual source of contamination. Carbon dioxide sensors are an example of devices that have found multiple uses; they are required for indoor air quality operations and for food storage and processing incubators. In addition, hydrocarbon sensors are required to monitor aeronautical and automotive discharges, leak detection and fire detection. Hydrocarbons are also a precursor of tropospheric ozone, and it is known that some types of hydrocarbons are toxic. Clearly, there are many requirements for accurate and reliable sensors in the environment:

- The material should sensitive in lower explosive limit (LEL) for explosive gases.
- The material should have high sensitivity over a wide range of humidity and temperature.
- It should quickly respond to any fast changes in the ambient.
- The sensor material should have rapid response to the variation of gas concentration and good reproducibility of the electrical signal.
- The sensitivity should be independent of the ambient temperature.
- The material should not react with any chemical contaminants present in the application ambient.
- It should show stable characteristics for a long time.
- It should be less portable.
- The construction of the sensor should preferably be simple using IC technology and of low cost.
- The device should be operated by a battery.

1.4.3 Gas sensing method

1.4.3.1 Properties of LPG

The LPG gas consists of isobutene, propane, methane, etc. In 1910, LPG [27], first produced by Dr. Walter Snelling of the United States Department of Mines, studied gasoline to understand why it evaporated so quickly and found that the gases that evaporated were propane, butane and other light hydrocarbons. Both LPG and natural gas respect the environment and are easily detectable. These gases are usually stored in pressurized steel cylinders in liquid form and vaporized at normal temperatures. By comparing air with LPG, it is heavier that it flows through the ground and even installs at low points that make it difficult to disperse. LPG is a blend of commercial butane and commercial propane with saturated and unsaturated hydrocarbons. Due to the versatile nature of LPG, it is used for many requirements such as domestic fuel, industrial fuel, automotive fuel, heating, lighting, etc. And the demand for LPG increases exponentially every day. Gas leaks caused by fatal hell have become a serious problem in homes and other areas where domestic gas is handled and used. Gas leaks cause several accidents that result in financial losses, as well as human injuries and/or losses. The LP gas property is shown in **Table 4**. The explosion occurs when the following three conditions are satisfied:

Gas	Formula	%LEL	%UEL	Ignition temperature	Flash point in (°C)
Propane	C_3H_8	2.2	9.5	470	97
Butane	C_4H_{10}	1.8	8.4	365	152

Table 4.
Properties of LPG.

- The concentration of gas is between LEL.
- A sufficient amount of oxygen exists.
- There is a source of ignition [28].

1.4.3.2 Liquid petroleum gas sensor

Coal gas and liquefied petroleum gas (LPG) are combustible gases. They are potentially dangerous because explosions may occur when accidental or accidental spills occur. Therefore, detecting it in household appliances is very important for safety. One of the most common types of domestic energy source is propane, which contains liquefied gas. Although safety issues are considered by the company, gas leaks have become a very common incident that can cause damage to human lives and property. The system has two main devices: the gas detector and the centralized alarm unit. Alarms are missing during cooking, which requires the equipment to detect LPG.

There may be more than one detector in the systems, which can be identified separately in the system. The centralized alarm unit detects alarms sent by the detectors and releases the alarm. It has an indication of which detector has released the notice. The alarm unit has AC power and has a battery backup to solve power problems. The components of the device were chosen taking into account the energy consumption and the time intervals were calculated in relation to the current consumption of each component. Liquefied petroleum gas is a flammable mixture of hydrocarbon gas used as fuel in heating appliances and vehicles. The varieties of LPG bought and sold include mixtures that are mainly propane (C_3H_8), mainly butane (C_4H_{10}) and, more commonly, include propane and butane, depending on the application [29].

Unlike natural gas, LPG is heavier than air, unlike natural gas, so it will flow through floors and will tend to settle in lower locations such as basements. There are two main dangers of this [29].

1. Possible explosion if mixture of LPG & air is right & if there is an ignition source.
2. Suffocation due to LPG displacing air, causing a decrease in oxygen concentration.

1.4.3.3 Basic principle of solid state gas sensors

The basic principle of solid state gas sensors is schematically illustrated in **Figure 4**. Solid state gas sensors are based on adsorption/desorption or chemical reactions of target gases on the surface or grain boundaries of sensing material and lead to physical changes like in temperature, mass, conductivity, refractive index, etc.

Although the basic principle behind solid state sensors seem to be similar, multitude of sensor technologies have been developed. Conducting polymers are under the category of resistive sensors and its conductance changes with the interaction of sensing gas molecules. Although polymer sensors are operated at room temperature but drift in their response with time and sensitivity to ambient conditions are of major concern. The semiconductor metal oxide gas sensors are in the form of thin ceramics or films and operate at high temperatures. The resistance of these sensors changes in the presence of sensitive gas (oxidant or reducer). However, the energy consumption of these sensors is high and could be reduced to some extent by using MEM-based structures. The surface plasmon resonance (SPR) technique was also used for gas detection, based on the principle that when a target gas interacts with a

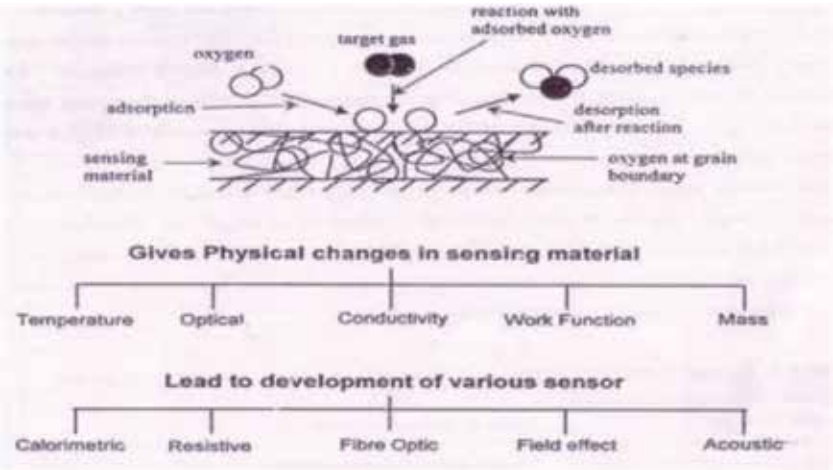

Figure 4.
General principle of solid state gas sensors.

Physical changes	Type of sensor devices
Conductivity	Semiconducting metal oxide conducting polymer.
Optical	Fibre optic, thin film: SPR, reflection interferometry, adsorption, fluorescence.
Work function	Field effect device: diode, capacitor, transistor, Kelvin probe.
Heat generation	Pt-wire, thermopile, thin film resistor.
Dielectric permittivity	Capacitor.
Mass	Quartz crystal microbalance. Surface acoustic wave.

Table 5.
Various types of solid state sensors and the respective physical changes.

metal film, the optical property (refractive index) changes. The change of the refractive index before and after the interaction of the chemical species with a metal layer gives the concentration of the target gas. The main disadvantage of SPR is complicated optics and the system is not easy to use. The problem of selectivity is another critical problem. The gas sensors based on the field effect transistors depend on the change in the working function of the metal gate with the interaction of the target gas. However, the design is complicated, and the characteristics are very sensitive to environmental conditions. **Table 5** lists several types of solid-state gas sensors and the respective expected physical variations due to the interaction of the target gas.

1.5 Sensor parameters

It is very much important to understand the sensing parameters of a good sensor. These are defined as:

- Sensing response,
- Operating temperature,
- Response time and
- Recovery time

There are some of the salient parameters that are associated with measurement of response characteristics of a gas sensor.

c. Sensing response:

The response (S) of a gas sensor to a target gas at a given temperature T is determined from the measured value of resistance of the sensing element (SnO_2 thin film) in the absence (Ra) and presence of the sensing gas (R_g). The sensor response S is defined as:

$$S = \frac{R_g - R_a}{R_a} \tag{1}$$

where $R_g > > R_a$ for oxidizing gases, and therefore to a good approximation

$$S \approx \frac{R_g}{R_a} \tag{2}$$

a. Response time (T_{res}):

The response time is defined as the time taken by the sensor to acquire 90% of its maximum resistance value in the presence of target oxidizing gas.

b. Recovery time (T_{rec}):

The recovery time is defined as time taken by the sensor to reacquire about 10% higher value of its initial resistance in the presence of atmospheric air.

The typical variation in the response (S) of a gas sensor with temperature for a specific concentration of target gas is shown in **Figure 5**. A maximum in the response (S_{max}) at a certain critical temperature (T_{opt}) is referred to as the operating temperature of the sensor.

Response (t_{res}) and recovery (t_{rec}) time characterization of a typical sensor are shown in **Figure 6** which gives a clear picture about the increase in resistance value as soon as any oxidizing gas comes in contact with n-type semiconducting sensing layer. The sample regains its original resistance value (R_a) as soon as the sensing gas is expelled out from its vicinity.

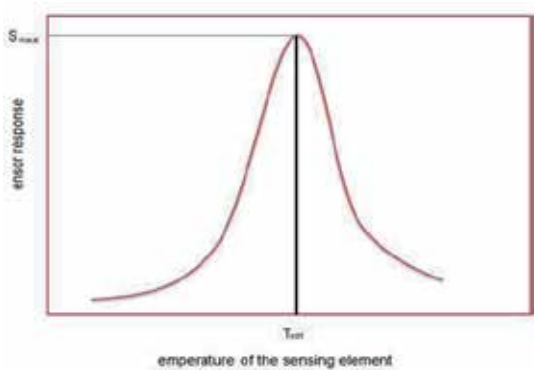

Figure 5.
Variation of sensor response with temperature for a typical sensor.

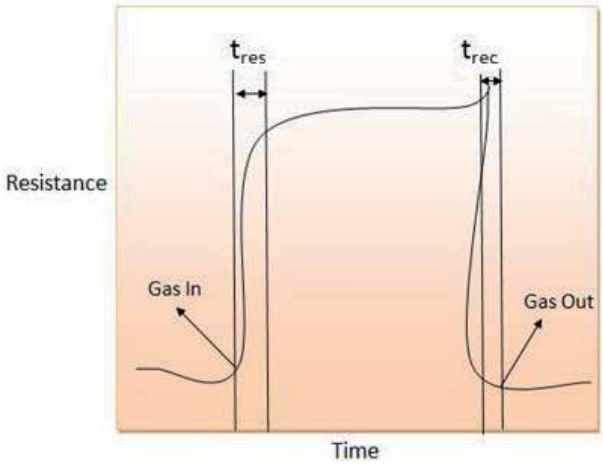

Figure 6.
Sensor response as a function of time, defining response time and recovery time of a typical sensor in response to an oxidizing gas.

The gas sensing mechanism of LPG sensor is a surface-controlled phenomenon, i.e., it is based on the surface area of the thin film. Initially, oxygen from the atmosphere gets adsorbed on the surface of the film and pick up electrons from its conduction band. In the present investigation, an exertion has been built up LPG detection with metal oxide (TiO_2) thin film arranged by the chemical route method which recognizes a leakage of LPG at operable RT. The surface mechanism of thin film-based sensor is governed by surface reaction. The change in resistance of thin film sensor in the presence of LPG molecule is prescribed by the oxygen species on the surface. However, the LPG sensing reaction mechanism is given [30]. The oxygen atoms were adsorbed the surface of metal oxide thin film when subjected to air. Various ionic species such as O_2, O_2^-, O^- or O^{2-} available on the surface of film plays a important task in the detection of gases. Oxygen captures the electron from the conduction band of metal film and is adsorbed on the surface as O^- ions, which are given as below:

$$O_2(gas) \leftrightarrow O_2(ads) \text{ (Thin Film Surface)} \quad (3)$$

$$O2(gas) + e^- \leftrightarrow O_2^- \text{ (Thin Film Surface)} \quad (4)$$

The adsorption of O_2^- ions on the nanostructured TiO_2 surface is vital to enhance the receptor function of the sensor, and, hence, its sensing response. The stabilization of surface resistance (R_a) results into the equilibrium of chemisorption process (state of saturation). **Figure 7** shows the sensor stabilization characteristic of metal oxide through different steps: (a) the conduction electrons are thermally excited in thin film (b) the electron donation by thin film to the oxygen, (c) physisorbed of oxygen atoms on the surface of metal oxide. The curve (d) of **Figure 7** shows the stabilization value of sensor resistance with time. When metal oxide film was exposed to LPG, it responds with the chemisorbed oxygen and a surface charge layer would be framed. The electron transfer from the conduction band to the chemisorbed oxygen results in the decrease in electron concentration at the film surface. As a consequence, an increase in the resistance of the film was observed before exposure to LPG. When the LPG reacts with the surface oxygen ions then the combustion products such as water depart and a potential barrier to charge transport would be developed, i.e., this mechanism involves the displacement of

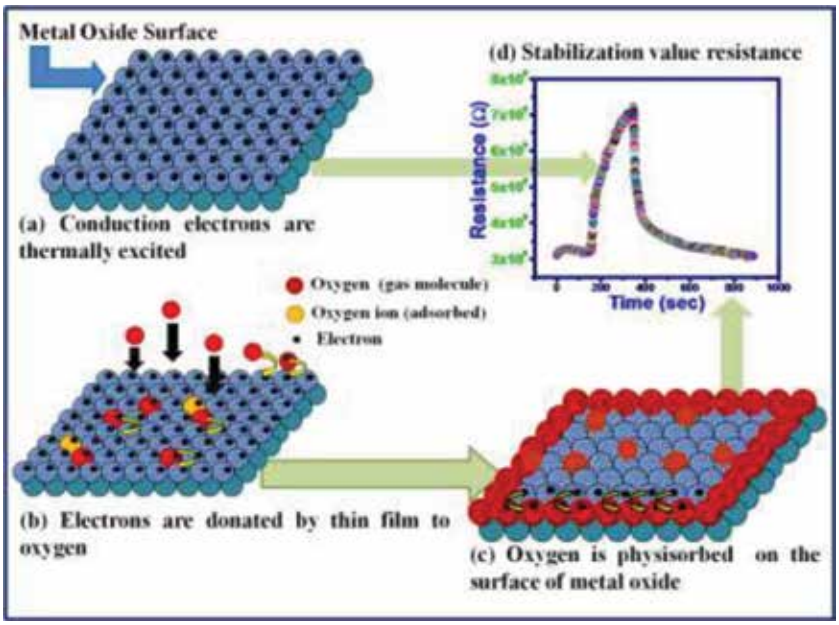

Figure 7.
Proposed model of sensing stabilization of metal oxide thin film.

adsorbed oxygen species by formation of water. The overall reaction of LPG with the chemisorbed oxygen may takes place as shown below [31]:

$$C_nH_{2n+2} + O_2^- \rightarrow C_nH_{2n}O + H_2O + e^- \quad (5)$$

where, C_nH_{2n+2} represent the various hydrocarbons. Due to the release of electrons, the resistance of the sensitive film decreases dramatically at first due to rapid absorption, after which it slowly decreases and eventually becomes saturated. When the flow of LPG stops for the study of the recovery characteristics, the oxygen molecules in the air will be absorbed on the surface of the film and the capture of electrons through the process indicated in the equations will increase the resistance of the sensor. Because the detection mechanism is based on the reaction of the chemisorption that occur on the surface of the film, the increase in the specific area of the sensitive material leads to multiple sites for the adsorption of the target gas. The function of the receiver is a capacity of the sensitive surface to receive the target gas that is directly related to the surface capacity of the adsorbed O_2^- ions. In the present sensor at room temperature when the complex $C_nH_{2n+2} - O + H_2O$ produced throughout Eq. (5), the delivered water vapor being lighter than gas stimulated to the highest point of chamber was released out from the chamber by rotary vacuum, greater the capacity of the surface to receive the target gas, the greater the change in the resistance of the sensor and, therefore, the improvement of the sensory response of the sensor.

1.6 Requirements of a gas sensor

LPG is a combustible gas and it is widely used as a fuel for domestic heating and industrial use. Although it is one of the extensively used gases, it is hazardous. Hence, it is crucial to detect it in its early stages of the leakage and to perform the active suppression. For designing a robust gas sensor, the sensor material should possess following qualities given as under:

- The material should sensitive in lower explosive limit (LEL) for explosive gases.
- The material should have high sensitivity over a wide range of humidity and temperature.
- It should quickly respond to any fast changes in the ambient.
- The sensor material should have rapid response to the variation of gas concentration and good reproducibility of the electrical signal.
- The sensitivity should be independent of the ambient temperature.
- The material should not react with any chemical contaminants present in the application ambient.
- It should show stable characteristics for a long time.
- It should be less portable.
- The construction of the sensor should preferably be simple using IC technology and of low cost.
- The device should be operated by a battery.

2. Conclusions

Nanostructured semiconducting materials are the most promising materials for study of sensors because of their much surface to volume ratio. We have been interested in carrying out our investigations with a new material that possess good sensitivity for the LPG concentration at the LEL level, with properties that are stable over time and thermal cycling after exposure to the various species likely to be present in the ambient. Titania show very good surface reactivity and they have temperature dependent surface morphology. In this chapter, thorough experimental investigation was carried out in order to develop electrical type LPG sensor using thin films of nanosized Titania with some other additives material.

Acknowledgements

Dr. R.K. Sonker acknowledges the financial support provided by the SERB-National Post-Doctoral Fellow, under the DST funded project, government of India (File No. PDF/2016/002827).

Conflict of interest

The authors declare that there is no conflict of interests regarding the publication of this paper.

Author details

Rakesh Kumar Sonker[1*], Saroj Radheyshyam Shabajeet[2], Rahul Johari[3] and Balchandra Yadav[2]

1 Department of Physics and Astrophysics, University of Delhi, Delhi, India

2 Nanomaterials and Sensor Research Laboratory, Department of Applied Physics, Babasaheb Bhimrao Ambedkar University, Lucknow, UP, India

3 Department of Applied Sciences and Humanities, Jamia Millia Islamia, New Delhi, India

*Address all correspondence to: rakesh.sonker81@gmail.com

IntechOpen

© 2019 The Author(s). Licensee IntechOpen. This chapter is distributed under the terms of the Creative Commons Attribution License (http://creativecommons.org/licenses/by/3.0), which permits unrestricted use, distribution, and reproduction in any medium, provided the original work is properly cited. CC BY

References

[1] Available from: https://www.osha.gov/dts/chemicalsampling/data/CH_249630.html. [Accessed: 13 February 2017]

[2] Available from: https://www.findlayrv.com/learn--lp-gas-101

[3] Sivapunniyam A, Wiromrat N, Myint MTZ, Dutta J. High-performance liquefied petroleum gas sensing based on nanostructures of zinc oxide and zinc stannate. Sensors and Actuators B: Chemical. 2011;**157**:232-239

[4] Page K, Proffen T, Terrones H, Terrones M, Lee L, Yang Y, et al. Direct observation of the structure of gold nanoparticles by total scattering powder neutron diffraction. Chemical Physics Letters. 2004;**393**:385-388

[5] De Matteis V, Cascione M, Brunetti V, Toma CC, Rinaldi R. Toxicity assessment of anatase and rutile titanium dioxide nanoparticles: The role of degradation in different pH conditions and light exposure. Toxicology In Vitro. 2016;**37**:201-210

[6] Chen X, Mao SS. Chemical Reviews. 2007;**107**:453-460

[7] Somiya S, Roy R. Hydrothermal synthesis of fine oxide powders, Bulletin of Materials Science, Vol. 23, 6, 12 (2000) 453-460

[8] Nathand M, Parkinson BA. A simple sol-gel synthesis of superconducting MgB_2 nanowires. Advanced Materials. 2006;**18**:1865-1868

[9] Laughlin JB, Sarquis JL, Jones VM, Cox JA. Using sol-gel chemistry to synthesize a material with properties suited for chemical sensing. Journal of Chemical Education. 2000;77:77-79

[10] Salma I, Maenhaut W, Zaray G. Comparative study of elemental mass size distributions in urban atmospheric aerosol. Aerosol Science. 2002;**33**:339-356

[11] Wang Z, Weng W, Ji D, Shen G, Du P, Han G. Synthesis and properties of SDC powders and ceramics for low temperature SOFC by stearic acid process. Journal of Electro ceramics. 2008;**21**:698-701

[12] Patil KC, Aruna ST, Mimani T. Combustion synthesis: An update. Current Opinion in Solid State and Materials Science. 2002;**6**:507-512

[13] Sasikumar S, Vijayaraghavan R. Low temperature synthesis of nanocrystalline hydroxyapatite from egg shells by combustion method. Trends in Biomaterials and Artificial Organs. 2006;**19**(2):70-73

[14] Hulnnicki A, Clab S, Ingman F. Pure and Applied Chemistry. 1991;**63**:1247

[15] National Institute of Health. 2004. What you need to know about natural gas detectors. Available from: http://www.nidcd.nih.gov/health/smelltaste/gas dtctr.asp [Accessed: 12 March 2011]

[16] Fraiwan L, Lweesy K, Bani-Salma A, Mani N. A wireless home safety gas leakage detection system. In: Proceedings of 1st Middle East Conference on Biomedical Engineering; 2011. pp. 11-14

[17] Johansson A, Birk W, Medvedev A. Model-based gas leakage detection and isolation in a pressurized system via Laguerre spectrum analysis. In: Proceedings of IEEE International Conference on Control Applications; 1998. pp. 212-216

[18] Lopes dos Santos P, Azevedo-Perdicoúlis TP, Ramos JA, Jank G, Martins de Carvalho JL, Milhinhos J. Gas pipelines LPV modelling and identification for leakage detection. In: Proceedings of American Control Conference; 2010. pp. 1211-1216

[19] Lopes dos Santos P, Azevedo-Perdicoúlis TP, Ramos JA, Martins de Carvalho JL, Jank G, Milhinhos J. An LPV modelling and identification approach to leakage detection in high pressure natural gas transportation networks. IEEE Transactions on Control Systems Technology. 2011;**19**(1):77-92

[20] Zeng Z, Xuan L, Sun Y, Udpa L, Udpa S. Probability of detection model for gas transmission pipeline inspection. Research in Nondestructive Evaluation. 2004;**15**(3):99-110

[21] Zeng Z, Udpa L, Udpa S. Robust design of a natural gas transmission pipeline inspection tool using the Taguchi method. Research in Nondestructive Evaluation. 2006;**17**(1):17-28

[22] Chengjun D, Ximao L, Ping D. Development on gas leak detection and location system based on wireless sensor networks. In: Proceedings of 3rd International Conference on Measuring Technology and Mechatronics Automation; 2011. pp. 1067-1070

[23] Nasaruddin NMB, Elamvazuthi I, Hanif NHHBM. Overcoming gas detector fault alarm due to moisture. In: Proceedings of IEEE Student Conference on Research and Development; 2009. pp. 426-429

[24] Nakano S, Goto Y, Yokosawa K, Tsukada K. Hydrogen gas detection system prototype with wireless sensor networks. In: Proceedings of IEEE Conference on Sensors; 2005. pp. 1-4

[25] Erol A, Okur S, Comba B, Mermer O, Arikan MC. Humidity sensing sensing properties of ZnO nanoparticles synthesized by sol-gel process. Sensors and Actuators B. 2010;**145**:174-180

[26] Available from: http://edugreen.teri.res.in/explore/n_renew/lpg.htm.

[27] What is Gas Leak Detection Gas Monitors. UK Europe; 2012

[28] Liquefied petroleum gas. Encyclopedia; 2016

[29] LPG is a flammable mixture of hydrocarbon gases. Encyclopedia; 2016

[30] Sonker RK, Yadav B. Chemical route deposited SnO_2, SnO_2-Pt and SnO_2-Pd thin films for LPG detection. Advanced Science Letters. 2014;**20**:1023-1027

[31] Sonker RK, Singh M, Kumar U, Yadav BC. MWCNT doped ZnO nanocomposite thin film as LPG sensing. Journal of Inorganic and Organometallic Polymers. 2016;**26**:1434-1440

Chapter 6

Synthesis of Metal Oxide Semiconductor Nanostructures for Gas Sensors

Nazar Abbas Shah, Majeed Gul, Murrawat Abbas and Muhammad Amin

Abstract

Zinc oxide (ZnO) is a unique and important metal oxide semiconductor for its valuable and huge applications with wide band gap (3.37 eV) and most promising candidate for gas sensor due to its high surface-to-volume ratio, good biocompatibility, stability, and high electron mobility. Due these properties, metal oxide shows good crystallinity, higher carrier mobility, and good chemical and thermal stability at moderately high temperatures. In this chapter nanostructures have been investigated, main focus being their synthesis and sensing mechanism of different toxic chemicals, synthesized by thermal evaporation through vapor transport method using vapor-liquid-solid (VLS) mechanism. The doped ZnO nanobelts showed significant enhanced sensing properties at room temperature, indicating that doping is very much effective in improving the methane CH_4 sensing of ZnO nanostructures. ZnO nanowires showed a remarkable sensing response toward acetone and CH_4 gas.

Keywords: metal oxide, semiconductor material, Mg doping, nanobelts, structural and morphological properties, band gap, gas sensing

1. Introduction

From the last decade, nanotechnology has established a bridge among all the fields of science and technology. Low-dimensional materials and structures have exceptional properties that make them able to play a critical role in the rapid progress of field science. With these excellent properties, 1-D metal oxide semiconductors (MOS) have become the backbone of research in all fields of natural sciences.

Nanotechnology deals with structures and materials of very small dimensions. Nanotechnology is the foundation and exploitation of nanomaterial with structural features in between those of atoms and their bulk material. The properties of the materials at nanoscale are extensively different from those of bulk materials. The high surface reactivity with the surrounding surface improves significantly. When the size of materials is in the nanoscale, the surface-area-to-volume-ratio (L/D) becomes large that makes the nanomaterial ideally an appropriate candidate for many types of sensing applications. That is why nanomaterial has opened up possibilities for new pioneering functional devices and technologies. Nanostructures have at least one dimension less than 100 nm. Crystal structures are much stable at nanoscale [1].

Reduction of an object size results in large surface to volume ratio hence the surface turn out to more vital and that large surface to volume ratio greatly affected the chemical, electrical and optical properties of nanomaterials. Quantum effects owing to size confinement in nanostructures occurs, when the typical size of the object is equivalent to the crucial length (range 1–10 nm) of the equivalent physical properties' screening length, then the mean free path of electrons; 0-D quantum dots, 1-D quantum dots, and 2-D quantum well are the characteristic structure forms.

Low power consumptions, best crystallinity, and high integration density 1-D with high aspect ratio are shown by the 1-D nanostructures. The nanostructure materials show high sensitivity to surface chemical reactions, with increased surface-to-volume ratio and a Debye length matching with small size. Tunable band gap is enabled by size confinement [2]. In the recent past, various synthesis methods, such as vapor phase method, electrochemical method, liquid phase methods, and solution-gel methods, were used. Out of these growth techniques, vapor transport method, using vapor-liquid-solid (VLS) growth mechanism or VS growth, is one of the finest growth techniques used for the growth of metal oxide semiconductor nanostructures. It is a cost-effective easy method used to create many single-crystalline 1-D nanostructures [3–11].

Smart and functional materials are based on metal oxides [10]. Synthesis and fabrication of devices based on metal oxide semiconductor have become more important recently, because the tuning of physical properties of these metal oxides is so easy. Among these MOS, ZnO is a material that has strong piezoelectric and optical properties on the bases of its wide band gap, stability at high temperature, large surface-to-volume ratio, and high excitonic binding energy. They are used in solar cells, photocatalysis, and antibacterial active material. Therefore research work has been carried out on ZnO nanostructures. Metal oxide materials possess electrical, chemical, and physical properties that are highly sensitive to the changes in a chemical environment, through a variety of detection principles based on ionic, conducting, photoconducting, piezoelectronic, pyroelectronic, and luminescence properties [12–21].

Doping is another technique utilized to improve ultraviolet (UV) sensing properties of metal oxides, where the dopant atoms are believed to act as activators for surface reactions. In MOS, the electrical, optical, and chemical properties can be changed by adding the doping materials or by creating oxygen defects which results in large concentration of carriers, mobility, and electrical resistivity. So doping offers another avenue for expanding their sensing capability [12].

Up to now, various metal oxides' 1-D nanostructures (SnO_2 nanowhiskers, In_2O_3 nanowires, ZnO nanorods, WO_3 nanowires, TiO_2 nanowires etc.) have been fabricated into film-type nanosensors by means of thermal evaporation or vapor transport method. The most widely studied substances are SnO_2 and ZnO nanowires [13]. In this research work, 1-D n-ZnO nanostructures (nanowires, nanorods, nanobelts with needle-like ends, and typical nanobelts) were grown by using vapor transport method using VLS mechanism on n-type Au-coated silicon substrate Si (100). The electrical and optical properties of ZnO nanostructures were investigated using different characterization techniques [14–37].

2. Important properties of metal oxide semiconductors

As work done in this chapter mainly deals with ZnO semiconductor, structural properties of ZnO material are presented below.

2.1 Structural properties of ZnO

ZnO is a key technological and prominent material. One of the important properties of ZnO is that it has a wide band gap that makes it suitable for optoelectronic applications of short wavelength. ZnO has high excitonic binding energy (60 meV) at room temperature by ensuring efficient excitonic emission. It has been noted that disordered nanoparticles and thin films at room temperature have ultraviolet (UV) luminescence. In addition, due to the unavailability of centrosymmetry in wurtzite structures that combines with large electromechanical coupling which result in strong piezoelectric and pyroelectric properties and make ZnO a prominent material in the use of mechanical actuators and piezoelectric sensors. As a versatile functional material, ZnO has a different group of growth morphologies, such as nanocombs, nanowires, nanobelts, nanosprings, etc. These ZnO nanostructures are easily obtained, even on cheap substrates such as glass. As work done in this thesis mainly deals with ZnO semiconductor, structural properties of this material are presented below.

2.2 Crystal and surface structure of ZnO

At normal temperature and pressure, ZnO crystallizes in wurtzite (B4 type) structure, as shown in **Figure 1**. It is a hexagonal lattice, belonging to the space group P63mc with lattice parameters a = 0.3296 nm and c = 0.52065 nm. The tetrahedral coordination in ZnO is responsible for noncentral symmetric structure and consequently results in piezoelectricity and pyroelectricity. Another important characteristic of ZnO is polar surfaces. The most common polar surface is the basal plane. The oppositely charged ions produced positively charged Zn^{+} (0001) and negatively charged O^{-} ($000\bar{1}$) surfaces, which result in a normal dipole moment and spontaneous polarization along the c-axis as well as variance in surface energy. The two most commonly observed facets for ZnO are ($2\bar{1}\bar{1}0$) and ($01\bar{1}0$) which are nonpolar surfaces and have lower energy than the (0001) facets [14, 15]. ZnO has varied properties, covering all of its physical, chemical, or material properties.

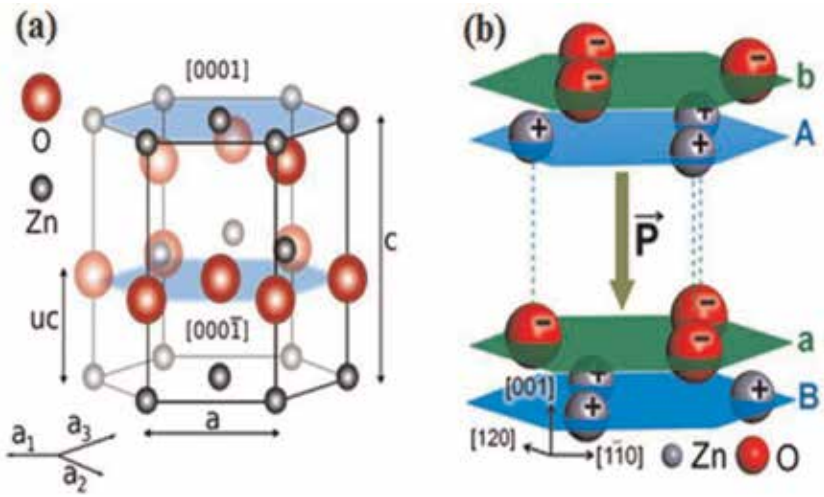

Figure 1.
(a) Crystal structure of hexagonal wurtzite ZnO, ZnO unit cell, including the tetrahedral coordination between Zn and its neighboring O. (b) ZnO has a noncentro-symmetric crystal structure that is made up of alternate layers of positive and negative ions, leading to spontaneous polarization.

ZnO is a well-suited II–VI wide bandgap semiconductor, which is naturally found in three forms: cubic zinc blend, hexagonal wurtzite, and cubic rock salt which is not as common as other [16]. The most common phase of ZnO is hexagonal wurtzite, whose space group is C6v or P63mc, which can be found mainly in ambient condition [17].

In **Figure 1(a)** is a crystal structure of ZnO which is a combination of alternating planes with tetrahedral coordination of Zn^{+2} and O^{-2} ions along the c-axis. Due to the presence of polar surfaces, ZnO crystal becomes spontaneously polarized in two type of planes, i.e., tetrahedrally coordinated O^{-2} and Zn^{+2} ions stacked alternately along the c-axis.

2.3 Gas sensing properties

In recent times due to environmental pollution and other chemical hazards, the needs for the development of a trusted chemical sensor have been significantly increased. For sensing of trace vapor of chemicals, different types of sensors, for example, potentiometric, fiber optics, amperometric, and biological sensors, are used, but ZnO nanostructure-based sensor has its own importance owing to its stability, high sensitivity, selectivity, as well as wide operating temperature range and flexibility in processing during device fabrication [18–24].

High surface area, well organized molecular structure, and single crystalline make ZnO nanostructures unique and prominent candidates for gas sensing application. Gas attachment sensing mechanism, such as O^{-}, O_2, H^{+}, and OH^{-} contact as analytes that result in change in the electrical conductivity of the charges, is mainly dependent on the redox reaction. This process can only be activated by activation energy because the classic metal oxide semiconductor sensors only operate at a temperature higher than 200°C. Because of the significant changes in optoelectronic properties at nanoscale, the problem of power consumption might be tackled, and the sensor with low energy consumption can operate even at room temperature. On exposing the surface of sensor to air, attachment of O or O_2 takes place. Due to these attachments of O or O_2 on the nanostructure surface, formation of space charge region with high resistivity takes place. Due to high aspect ratio (L/T), the nanobelt nanostructure surface give rise to a high resistance in the normal state; this is due to the thin thickness of nanobelt nanostructures that offer a significant amount of surface acceptor states. The removal of chemisorbed oxygen from nanostructure surface by chemical reaction on the surface of nanostructures results in the improvement of conductance of nanostructures in chemical environment as shown in **Figure 2**.

2.4 Gas sensors based on metal oxide semiconductor nanostructures

It is important to note that two main types of semiconducting metal oxides exist which are used in chemiresistive sensors. The first one is n-type semiconductors (conductance increases, when redox reaction takes place on the surface of nanostructures, e.g., TiO_2, ZnO, and SnO_2) whose majority carriers are electrons. The second type of metal oxides used is p-type semiconductors (conductance decreases, when redox reaction takes place on the surface of nanostructures, e.g., NiO and CuO) whose majority carriers are holes. The majority of semiconducting metal oxides used in chemiresistive sensors are n-type because electrons are spontaneously produced via oxygen vacancies at the operating temperature of the sensors during the synthesis process. A typical metal oxide gas sensor can be described as an interactive material which interacts with the environment and generates a

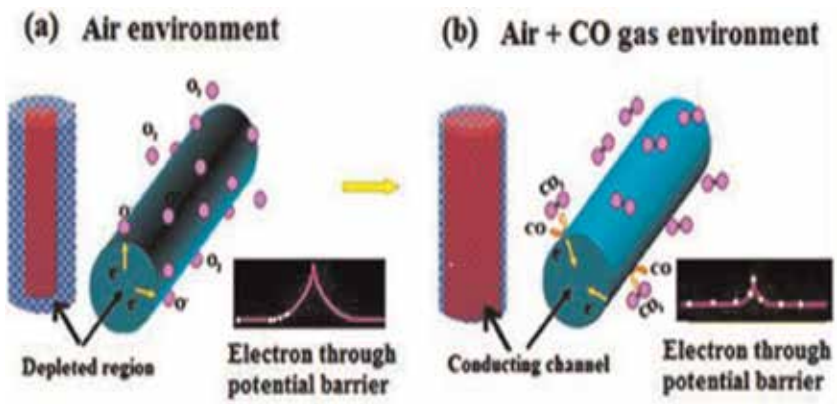

Figure 2.
Schematic illustration of toxic chemical sensing process. (a) Adsorption of oxygen at surface of nanowires in air and creation of potential barrier and depletion region. (b) Modulation of potential barrier and depletion region after reaction of carbon monoxide (CO) at surface of n-type semiconductor.

response (as receptor) plus a device which reads the response and converts it into an interpretable and quantifiable term (as transducer).

2.4.1 Sensing mechanism of metal oxide semiconductor gas sensors

It is necessary to understand the sensing mechanism of the chemiresistive gas sensors for the subsequent chapters in this thesis. Since sensing mechanism of metal oxide semiconductor is mainly based on band theory, band theory can be applied to the gas sensor to explain the sensing mechanism. On interaction of the analytes (undetected) with the surface of nanostructures, these analytes react with attached oxygen ions on the surface of nanostructures; a change in the carrier concentrations of the material occurs. Due to the change in carrier concentrations of the material, the electrical resistivity of the materials changes. Decrease in resistivity (increase in conductivity) occurs for n-type metal oxide semiconductor on interaction of reducing gas [25]. So the sensing mechanism of oxide semiconductor is mainly based on the principle of modification in electrical properties (resistivity/conductivity) as a consequence of chemical reaction between gas molecules and the reactive oxygen ions on the surface of MOS nanostructure material. The sensing mechanism can be divided into three sections: (a) adsorption of oxygen at surface, (b) detection of gases by a reaction with adsorbed oxygen, and (c) change in resistance due to charge transfer at the surface.

2.4.2 Adsorption of oxygen at surface

Interactions of oxygen with the surface of a metal oxide semiconductor are of utmost importance in gas sensing mechanism. Oxygen is a strong electron acceptor on the surface of a metal oxide. Since the majority of sensors operate in an air at ambient temperature, therefore the concentration of oxygen on the surface is directly related to the sensor electrical properties. The conversion to O_2^- or O^- at prominent temperatures is useful in gas sensing mechanism, as only a monolayer of oxygen ions are present with these strongly chemisorbed species [26, 27]. Different forms of oxygen ions may be ionosorbed on the surface of metal oxide semiconductor nanostructures [28]. At low temperature ranges (150–200°C), molecules in the form of neutral O_2 or charged O^- are adsorbed. At higher temperatures ranges above 200°C, atomic form of oxygen as O^- ions is adsorbed [29]. It is observed that

the reaction kinetics increase with increase in temperature. Sensors based on resistivity/conductivity properties (resistive sensors) work better at temperature of 300°C or above to react with ionosorbed oxygen at the surface. At temperature T < 200°C, the following reactions take place at the surface of sensor (for physisorption):

$$\begin{aligned} &E < (0.4\ eV) \\ &O_2(gas) \rightarrow O_2(ads) \end{aligned} \quad (1)$$

$$O_2(ads) + e \rightarrow O_2^-(ads) \quad (2)$$

At temperature T > 200–400°C, the following reaction takes place at the surface of sensor (for chemisorptions):

$$\begin{aligned} &E > (0.4\ eV) \\ &O_2^-(ads) + e \rightarrow 2O^-(ads) \end{aligned} \quad (3)$$

Adsorption energy of oxygen on metals lies in the range of 4–6 eV. Extracted carriers originate from donor sites of the metal oxide surface in the material [30]. Intrinsic oxygen vacancies and other impurity defects give rise to donor sites and surface-trapped electrons. As a result of this, ionosorbed oxygen produces a depletion layer on the surface. A buildup charge is created on the surface of metal oxide semiconductors due to different events of adsorption, and this leads to upward band bending for n-type semiconductors [31].

2.5 Classification of nanomaterials

Over decades, the capability of varying surface morphologies and the structure of MOS with near atomic scale have led to further idealization of semiconductor structures: quantum wells, wires, and dots. These variations at nanoscale of metal oxide semiconductors have led to different concentrations and densities of electronic states. On the bases of their fundamental dimensions (x, y, and z) in space, nanostructures can be classified into 0-D (zero-dimensional), 1-D (one-dimensional), 2-D (two-dimensional), and 3-D (three-dimensional). 0-D nanostructures are quantum dots or nanoparticles; 1-D nanostructures are nanorods, nanowires, nanobelts, and nanotubes; 2-D nanostructures refer to nanosheets, nanowalls, and nanoplates; and 3-D nanostructures refer to nanoflowers and other complex structures such as nanotetrapods [32–34]. Quantum effects dominate most of the properties of the nanomaterials. There is a great difference between density of states of the nanomaterials and those of the bulk materials. The density of states which describe the electronic states versus energy in the band diagram of the 0-D, 1-D, 2-D, and bulk materials are shown in **Figure 3**.

2.6 Synthesis of ZnO nanostructures

Different methods are used for synthesis of ZnO nanostructures.

2.6.1 Vapor transport synthesis

Vapor transport process is one of the most common and cost-effective method used to synthesize ZnO nanostructures. In this process, ZnO vapors are transported usually by Argon (Ar) gas. Zinc (Zn) and oxygen (O) vapors can be generated by

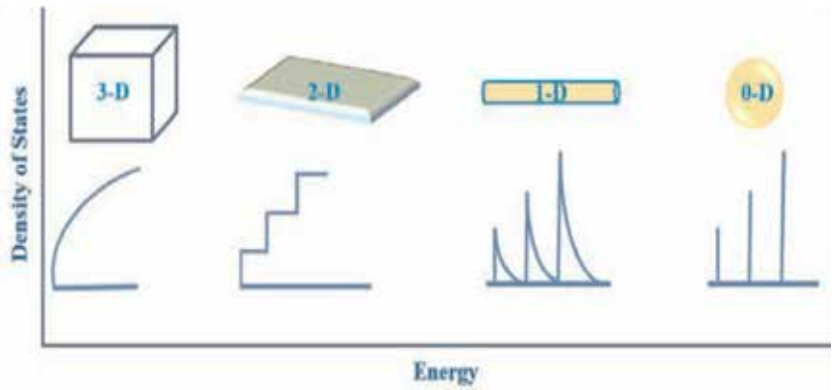

Figure 3.
The electron density of states in bulk metal oxide semiconductor and in that of quantum well (2-D), in quantum wire (1-D), and in quantum dot (0-D) nanomaterials.

different ways. Decomposition of ZnO is a direct and simple method; however due to high melting point of ZnO, it requires high temperature (~1975°C) [35]. To reduce the melting point of ZnO, graphite (C) powder is mixed with the same ratio with ZnO as a source material. At about 800–1000°C temperature, graphite reduces the melting point of ZnO to form Zn and CO/CO_2 vapors. Zn and CO/CO_2 later react and result in ZnO nanostructures. The advantage of this method is that the existence of graphite significantly reduces the decomposition temperature of ZnO, i.e., graphite acts as a catalyst. On the bases of difference on nanostructure formation mechanisms, the vapor transport process can be divided into the following:

i. Catalyst-free vapor-solid (VS) mechanism

ii. Catalyst-assisted vapor-liquid-solid (VLS) mechanism

A rich variety of nanostructures, such as nanorods, nanowires, nanobelts, and other complex structures, can be synthesized by utilizing vapor-solid mechanism. In this mechanism, the nanostructures are produced by condensing directly from vapor phase. This mechanism is not so capable to provide best control on the geometry, alignment, and precise location of ZnO nanostructures.

Vapor-liquid-solid mechanism is a catalyst-assisted mechanism which is used for controlled growth of oxide semiconductor nanostructures. So nanowires, nanorods, and nanobelts have been achieved by VLS mechanism [36]. In this mechanism metals such as Au, Cu, Co, Sn, etc. are used as catalyst materials [37]. Alloy droplets are formed at high temperature as a result of the reaction between catalyst film and the substrate surface interface. In the growth of 1-D oxide nanostructures, the liquid droplet plays the role of nucleation sites for the precursor's vapors [38]. The vapors of the precursor are transported through carrier gases (usually noble gases are used as carrier gas) toward the substrate placed in the furnace tube during the growth of oxide semiconductor. During this process some materials are evaporated. The selection of catalyst is mainly based on its high surface tension and its high accommodation coefficient. These properties directly link with the supersaturation of the droplet with the source material vapors. The high Gibbs free energy carried by the precursor's vapors enables it to diffuse into the alloy droplet in order to minimize its energy.

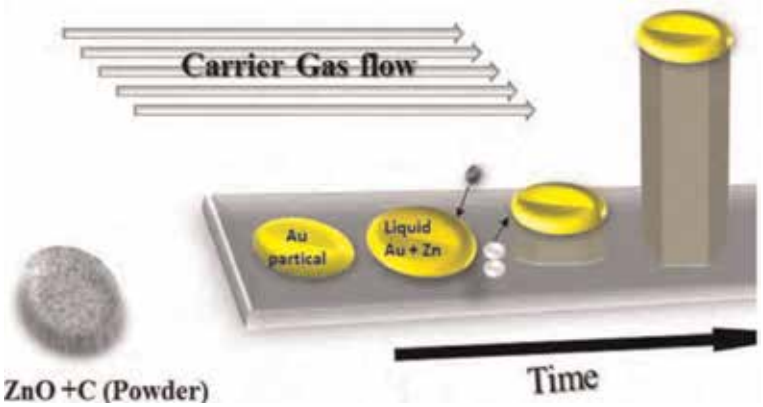

Figure 4.
Schematic illustration of VLS mechanism for ZnO nanorod catalyst droplets at the tip of nanorods.

The supersaturation of liquid droplet (that acts as nucleation's site) with the source material vapors results in crystal structures of source material at the liquid-solid interface on the substrate, consequently forming one-dimensional nanostructure as shown in **Figure 4**.

2.6.2 Other synthesis methods

Despite the growth of 1-D oxide semiconductor nanostructures such as ZnO, GaN, and nanowires, the vapor transport process is the most dominant and cost-effective synthesis method; other growth methods such as electrochemical deposition (ECD), sol-gel, polymer assisted growth, etc. have been developed so far in parallel [39]. The possibility of forming ZnO nanostructures even at low temperature may be provided by these methods.

2.7 Catalyst effect on the growth of metal oxide semiconductors

Thickness of the catalyst layer coated on the substrate plays a vital role in the growth of MOS nanostructure materials by reducing the activation energy of the reaction without taking part in the chemical reaction.

In supersaturation state catalyst droplet acts as a sink for source material in vapor-liquid-solid mechanism. The supersaturation level of droplet becomes smaller than the surrounding atmosphere's supersaturation level, when supersaturation of catalyst occurs. This difference creates a driving force, which drives the precursor vapors into the droplet, and growth of 1-D structures takes place in energetically favored crystallographic directions.

In vapor-solid mechanism, various types of substances are used as catalyst for the growth of 1-D nanostructures. The size and morphology of nanostructures can be controlled by using various types and thicknesses of catalysts. The finest catalyst has ideal rough surface whose sticking coefficient for the impinging of precursor material's atom from vapor phase is almost 1 [39].

2.8 Effect of gold catalyst on growth

Owing to its high surface tension, high accommodation coefficient, and high sticking power, gold (Au) is generally used as a catalyst in the synthesis of 1-D oxide nanostructure. Growth of 1-D oxide nanostructures with high crystallinity, density,

and long controlled diameter can be obtained by using Au as a catalyst. Growth of 1-D nanostructures has been reported by Borchers et al. with high density using Au catalyst [40]. ZnO nanowires can be grown through VLS mechanism by adding the catalyst substance which provides the nucleation sites for the growth of nanowires. The formation of these nuclei takes place through internal chemical reaction. This is considered to be a self-catalytic VLS growth. During the growth process, the reaction at low temperature can be fastening for vapor generation by adding some external materials in the source material. ZnO powder has a melting point of 1975° C, so pure ZnO does not sublimate at 900–1100°C. So for this purpose carbon powder is mixed with ZnO power with equal mass ratio that gives rise to the formation of Zn or Zn suboxide vapors at 1000°C [41], i.e.,

$$ZnO + C \rightarrow Zn + CO \tag{4}$$

$$ZnO + CO \rightarrow Zn + CO_2 \tag{5}$$

$$ZnO + (1 - x)\,CO \rightarrow ZnO_x + (1 - x)CO_2 \tag{6}$$

Various forms of ZnO nanostructures grow even at lower temperature because Zn or Zn suboxides act as nucleation sites for ZnO nanostructures. Other parameters like vacuum conditions, carrier gases, and catalysts are not essential in this condition. So the temperature is the only parameter that plays a vital role in the formation of various kinds of ZnO nanostructures. The formation of CO takes place by the direct reaction between graphite (C) and ZnO or O_2 depending upon the reaction condition (tube condition).

The formations of suboxides take place in open quartz tube due to the partially oxidized Zn vapor or droplet by the addition of graphite (C) at low melting temperature. Due to the high reactive power of suboxides as compared to ZnO, the deposition of zinc at the tips of grown nanostructures may increase during the synthesis process [42]. It is the main advantage of self-catalytic growth that impurity-free growth can be obtained as compared to catalyst-assisted growth of VLS.

2.9 Temperature effect on the growth of 1-D nanostructures

Temperature plays a crucial role in the growth of 1-D oxide nanostructures by thermal evaporation method through vapor-liquid-solid mechanism.

The thermodynamic phenomena like stability, dissociation adsorption, surface diffusion, and solubility of certain phases can be directly affected by temperature.

There are three types of ZnO fast growth direction from the structure point of view, namely, $<2\bar{1}\bar{1}0>$, $<01\bar{1}0>$, and $\pm$ [0001], as shown in **Figure 5**. ZnO consists of various structures due to the polar surface activities of different growth facets. Every crystal has a unique crystal plane with different kinetic parameters, which are to be considered under controlled growth conditions.

The tetrahedral coordination of ZnO is shown, which has noncentral symmetry and piezoelectric effect [43, 44]. [0001] is the fastest growing direction which is along the c-axis because its activation temperature is lower than other two directions. Due to activation, energy growth of nanorods with smaller lengths and diameters takes place at lower temperature, but when temperature increases, length and diameter of nanowires increase because the energy of this fast-growing direction [0001] increases. At the higher temperatures, nanobelts with further increase in temperature facets $<2\bar{1}\bar{1}0>$ and $<0\bar{1}\bar{1}0>$ get high activation energies to grow nanosheets.

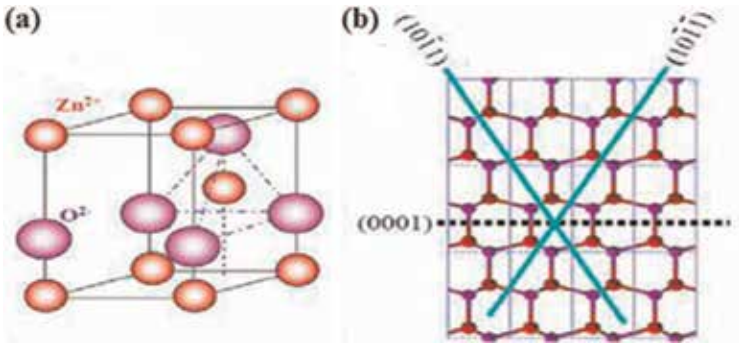

Figure 5.
(a) Wurtzite structure. (b) Growth direction model of ZnO.

2.10 Doping of nanostructures

Doping of the nanowires and nanorods through in situ or post processing techniques will provide a far more favorable approach to modulate their electrical, optical, and piezoelectric properties. Most metal dopant ions result in the increase of density of the conduction carriers by occupying the lattice sites in the ZnO crystal. The complete picture of the crystal can be changed by changing the doping level. The controlled modification of morphological features as well as enhancement of electrical and optical properties can be achieved by introducing dopant element in metal oxide semiconductor [45]. The electrical as well as optical properties of MOS can be tuned by adding the foreign elements or by the alternation of oxygen stoichiometry. By making these changes, one can get an increase in carrier's concentration, electrical resistivity, and mobility [45]. Doped nanostructure-based sensors are fully capable of sensing different harmful gases, with good stability, selectivity, and sensitivity. Out of many other methods, doping is considered to be one of the best methods for enhancement of gas sensing properties of ZnO nanostructures at room temperature. Doped ZnO nanostructures were used in the past by many researchers for the detection of harmful gases in the environment. For example, the gas sensing properties of Sn-doped ZnO nanostructures were investigated by S.C. Navel and I.S. Mulla using the thermal evaporation method. The results show good response to different gases for pure Sn-doped nanostructures, in temperature range of 275°C to 300°C. They proved that the sensitivity toward UV sensing can be increased by the doping of Sn material [46].

3. Experimental procedure

Experimental process comprises the following steps:

1. Preparation of substrate for growth

2. Coating of Au catalyst in ultrahigh vacuum (UHV) chamber on Si substrate

3. Preparation of nanostructure samples by vapor transport method through VLS mechanism

4. Fabrication of sensor for toxic gas sensing applications

3.1 Preparation of substrate for growth

By using the diamond cutter, Si substrates were cut in suitable sizes and shapes. In order to avoid the contamination, the substrates were cleaned before the deposition of catalyst, as oily layer and dust particles may stick to the surface of the substrates. For the cleaning purpose, the acetone was poured into a beaker, and the beaker was filled up to half level. The substrates were put into the acetone-filled beaker to completely immerse in them. The acetone-filled beaker was placed in ultrasonic bath at room temperature for 30 min. Si (100) substrates were then put into ethanol and deionized water for decontamination purpose for 30 min.

3.2 Deposition of Au catalyst on Si substrate in UHV chamber

For the growth of 1-D ZnO nanostructures, n-type silicon substrates Si (100) were used through the following steps:

1. Si substrates were cleaned in isopropyl alcohol (IPA), acetone, and deionized water (DI) by sonication to remove the contaminations in ultrasonic bath for 30 min at room temperature.

2. Sample substrates were loaded in the ultrahigh vacuum chamber for deposition of thin film of gold under vacuum of 10^{-7} Torr.

3. In nm, a thin layer of gold catalyst was deposited on Si (100) substrates for the growth of ZnO nanostructures.

4. Around 200 nm of thin layer of gold catalyst was deposited on Si (100) and glass substrates for preparation of sensor.

5. The samples were taken out from UHV chamber and used for growth process of ZnO nanostructures.

3.3 Preparation of samples by vapor transport method through VLS mechanism

The growth was performed by thermal evaporation in a temperature-controlled horizontal tube furnace by vapor transport process through VLS mechanism. An equimolar mixture (mixed in a ball mill for 2 h with 250 rpm) of ZnO (purity 99.99%) and graphite (purity 99.9%) was placed in a ceramic boat (88 mm of length) with a mass ratio1:1 (measured by physical balance). This boat containing the source material (mixture of ZnO + C) was placed at the center of quartz tube (length 100 cm and diameter 3.5 cm). Tube furnace was set at a temperature of 850, 900, 950, and 1030°C for the four different experiments. Catalyst-coated substrates of 4 nm labeled as S1, S2, S3, and S4 were placed at the downstream of the source material at a distance of 18 cm (S1, 850°C), 12 cm (S2, 900°C), 9 cm (S3, 950°C), and 6 cm (S4, 1030°C), respectively. Furnace temperature was raised at the rate of 10°C per minute. At the start Ar gas (99.99%) was introduced at a rate of 50 standard cubic centimeter per minute (sccm) to flush out the residual present in the tube. Brass rod fitted in the rubber cork was inserted in the quartz tube to connect it to argon (Ar) gas source through a plastic pipe of 5 mm diameter. Argon gas was used as a carrier for transport of vapors from source material to gold-coated substrates. The other end of quartz tube was kept opened. The temperature of the furnace was increased from room temperature to 850°C (S1), 900°C (S2), 950°C

(S3), and 1030°C (S4) in four different experiments. When the temperature of the furnace reached the set temperature, the dwell or growth time was noted for 45 min. After 45 min the furnace program was "OFF," and the temperature started decrease gradually. When the temperature decreased to 650°C, the Ar gas flow was switched "OFF." Furnace was then cooled to room temperature after the reaction.

Doping of Mg was carried out, and for that purpose 0.05 g and 0.08 g of magnesium acetate [$Mg(CH_3COO)_2{\cdot}4H_2O$] (purity 99.99%) was added in 1 g of source material (ZnO + C). Mg-doped ZnO nanostructures were synthesized by thermal evaporation in a temperature-controlled horizontal furnace on an Au-coated Si (100) substrate. Vapor transport method has been used for the synthesis of Mg-doped ZnO nanostructures which was done in a temperature-controlled tube furnace. The temperature, growth time, and gas flow rate were 900°C, 45 min, and 50 sccm, respectively.

3.4 Sensor fabrication

The synthesized ZnO nanostructures were used for UV as well as for chemical sensing applications. ZnO nanostructures were annealed by heating it in digital

Samples	Source material	Catalyst used	Catalyst thickness (nm)	Synthesis temperature (°C)	Gas flow rate (sccm)	Growth time (min)
S1	ZnO + C	Au	4	850	50	45
S2				900		
S3				950		
S4				1030		

Table 1.
Sample details (synthesis temperature, gas flow rate, growth time).

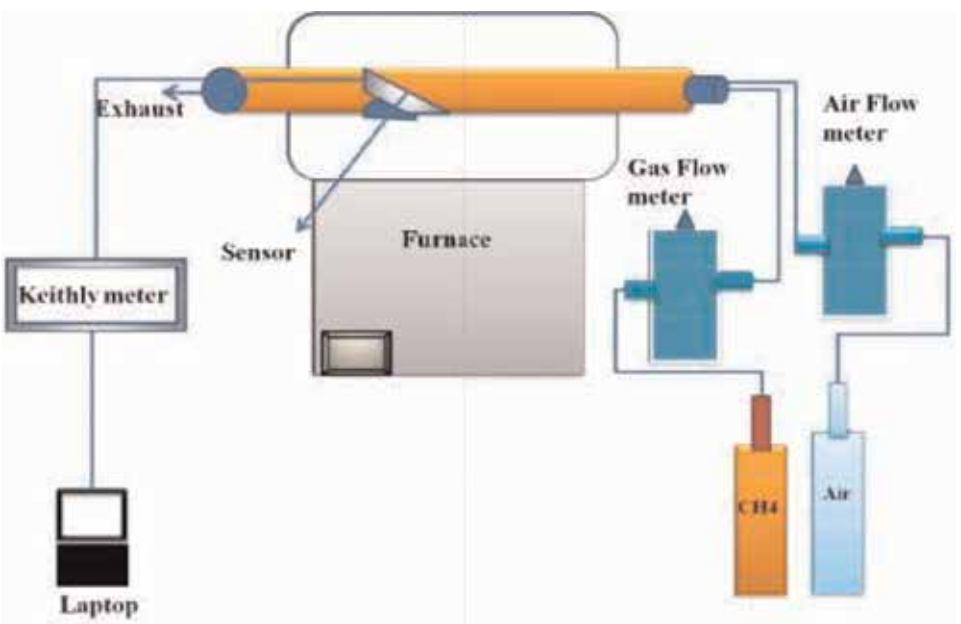

Figure 6.
Schematic illustration of chemical sensing experimental setup.

furnace at 400°C for 2 h. The annealing process was usually done for attachment of oxygen on the surface of ZnO nanostructures. The nanostructures were scratched with the help of blades, and the gaps or cuts on gold-coated quartz substrate were filled with the scratched nanostructures as shown in **Figure 6**. A small drop of methanol was dropped on the nanostructures with the help of 5 cc disposable syringe so that a thick paste was formed. The sensor was then placed under IR (infrared) light for 10 min for the purposes of sticking material on the quartz substrate. The experimental setup for chemical sensing is shown in **Figure 6**.

4. Morphological properties of ZnO nanostructures

Morphology, size, and shape of the synthesized ZnO nanostructures were characterized by using scanning electron microscopy (SEM) characterization technique. The four samples were synthesized at different temperatures with the same flow rate of 50 sccm of Ar (argon) gas and with same growth time of 45 min. A total eight samples was prepared in four different experiments; out of eight samples, four samples were optimized. Four experiments were done at different temperatures, i.e., 850, 900, 950, and 1030°C. The catalyst used was 4 nm thin layer of gold coated on n-type Si (100) substrate.

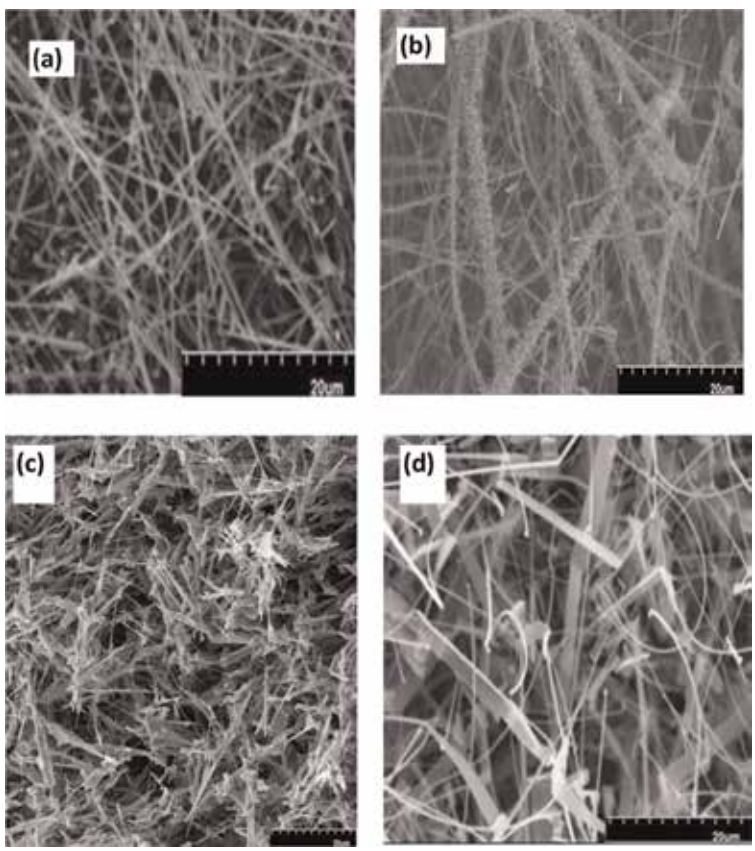

Figure 7.
SEM images of different morphologies of ZnO nanostructures at different synthesized temperatures. (a) SEM images of nanowires grown at 850°C. (b) SEM images of nanorods grown at 900°C. (c) SEM images of nanobelts with needle-like ends grown at 950°C. (d) SEM images of nanobelts grown at 1030°C.

4.1 Sample S1

In the first experiment, ZnO nanowires with various dimensions were obtained. **Figure 7(a)** shows the SEM micrograph of the ZnO nanostructures of sample S1, consisting of randomly oriented ZnO nanowires. These nanowires were grown at a temperature of 850°C on a thin layer of pure gold-coated Si (100) substrate. The nanowires intertwine with each other and distribute on the whole substrate surface randomly. The average diameter and the average length are 0.95 ± 0.11 μm and 35.59 ± 9.90 μm, respectively.

4.2 Sample S2

In the second experiment, ZnO nanorods of different dimensions were obtained. **Figure 7(b)** shows the SEM micrograph of complex ZnO nanorods of sample S2. These complex nanorods were grown at temperature of 900°C on a thin layer of gold-coated Si (100) substrate. The average diameter and the average length of S2 SEM images are 12.66 ± 3.72 μm and 319.48 ± 93.50 μm, respectively.

4.3 Sample S3

In the third experiment, ZnO nanobelts with needle-like ends were obtained. **Figure 7(c)** shows the SEM micrograph of ZnO nanobelts of sample S3 with needle-like ends. These nanobelts were obtained with different dimensions at temperature of 950°C grown on 4 nm Au-coated thin layer of Si substrate. The average width, average length, and average thickness of tips are 1.39 ± 0.44 μm, 10.34 ± 2.71 μm, and 0.38 ± 0.086 μm, respectively.

4.4 Sample S4

Figure 7 shows the SEM micrograph of ZnO nanobelts of the fourth experiment which was grown at 1030°C on gold-coated Si substrate. The average length of 2.67 ± 0.42 μm, average width of 0.33 ± 0.03 μm, and the average thickness of 0.09 ± 0.01 μm of nanobelts were obtained.

The scanning electron micrographs clearly showed that the morphologies tuned from nanowires and nanorods to nanobelts due to change in temperature. High temperature and supersaturation conditions lead to the formation of nanobelts with needle-like ends and typical nanobelts.

The possible reason for this tune in morphologies is attributed to supersaturation, growth rate, and quick availability of ZnO polar surfaces for growth [46]. Overall, the supersaturation conditions are different at different temperatures which eventually change the morphology.

4.5 Energy diffraction X-ray (EDX) analysis

EDX spectroscopy analytic technique was used for the chemical composition analysis of the synthesized ZnO nanostructures. **Figure 8** shows the typical EDX spectrum of the sample S1 (ZnO nanowires). Only the Zn, O, and Au peaks were observed. The observation of Au peak may suggest that the growth is catalyst-assisted [47–52]. The approximate atomic ratio was found to be 58:32. These ratios show nonstoichiometry, i.e., crystal defects of grown nanostructures during the growth process. Deviation from the stoichiometry is large due to carbothermal reaction and oxygen-deficient environment (Ar gas) during the growth process. Most of the oxygen is used in the formation of CO_2, i.e.,

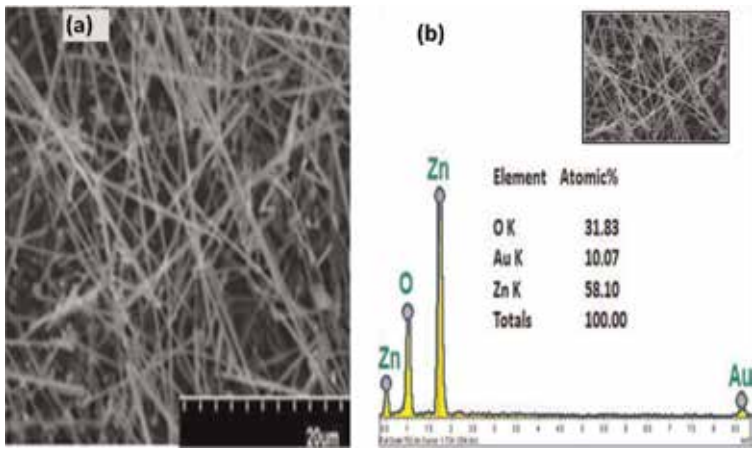

Figure 8.
(a) SEM images of ZnO nanowires and (b) EDX image of the corresponding ZnO nanowires grown at 900°C.

$$ZnO + C \rightarrow Zn + CO \tag{7}$$

$$ZnO + CO \rightarrow Zn + CO_2 \tag{8}$$

4.6 Synthesis of Mg-doped ZnO nanostructures

The whole process of Mg-doped ZnO nanowires could be explained in two steps:

In the first step, a thin layer (4 nm) of Au film was coated on Si (100) substrate in UHV chamber by ion sputtering technique. Cleaning of Si (100) substrates was carried out by sonicating in acetone, ethanol, and deionized water for 30 min. Si (100) substrates were then coated with SiO_2 for 2 h at temperature of 1050°C for insulation purpose. The quartz tube was cleaned first with chromosulfuric acid (cleaning agent) to remove the permanent residue, then the deionized water was used to wash the tube, and last ethanol was used to clean the tube.

In the second step, the Mg-doped ZnO nanostructures were grown by vapor transport method through VLS mechanism in a temperature-controlled digital horizontal furnace as shown in the schematic illustration. In the first experiment, doping of sample S1 (nanowires) was carried out. A mixture of ZnO (purity 99.9%), magnesium acetate [$Mg(CH_3COO)_2{\cdot}4H_2O$] (purity 99.99%), and graphite powders (carbon) with mass ratio in gram (weighted by physical balance) of 1:1:0.05 was used as the source materials. The source material was placed at the center of quartz tube of length 100 cm and diameter 3.5 cm in a ceramic boat of 88 mm length. Sample S1 substrate was placed on a second ceramic boat at the downstream at a distance of 18 cm away from the source materials in the quartz tube. The temperature of the furnace was maintained at 850°C.

At the start Ar gas was introduced at the rate of 50 sccm to flush out the residual present in the tube. As the temperature reached 850°C, the dwell time was noted for 45 min. After 45 min the furnace program was "OFF," and the temperature started to decrease gradually. When the temperature decreased to 650°C, the Ar gas flow was switch "OFF." Furnace was then cooled down to room temperature after the reaction. In the second experiment, Mg doping of sample S2 (ZnO nanorods) was carried out. The same condition and parameters were used for doping of S2, except

the magnesium acetate [$Mg(CH_3COO)_2{\cdot}4H_2O$] weight was 0.08 g, and the sample distance from the source material was 12 cm.

The collected Mg-doped ZnO nanostructure sample characterization was carried out for crystallinity, morphology and elemental composition, and optical properties. Optical and gas sensing response of the respective Mg-doped ZnO nanostructures was carried out by measuring respective resistances by two probe methods using a multimeter (Keithly 2100).

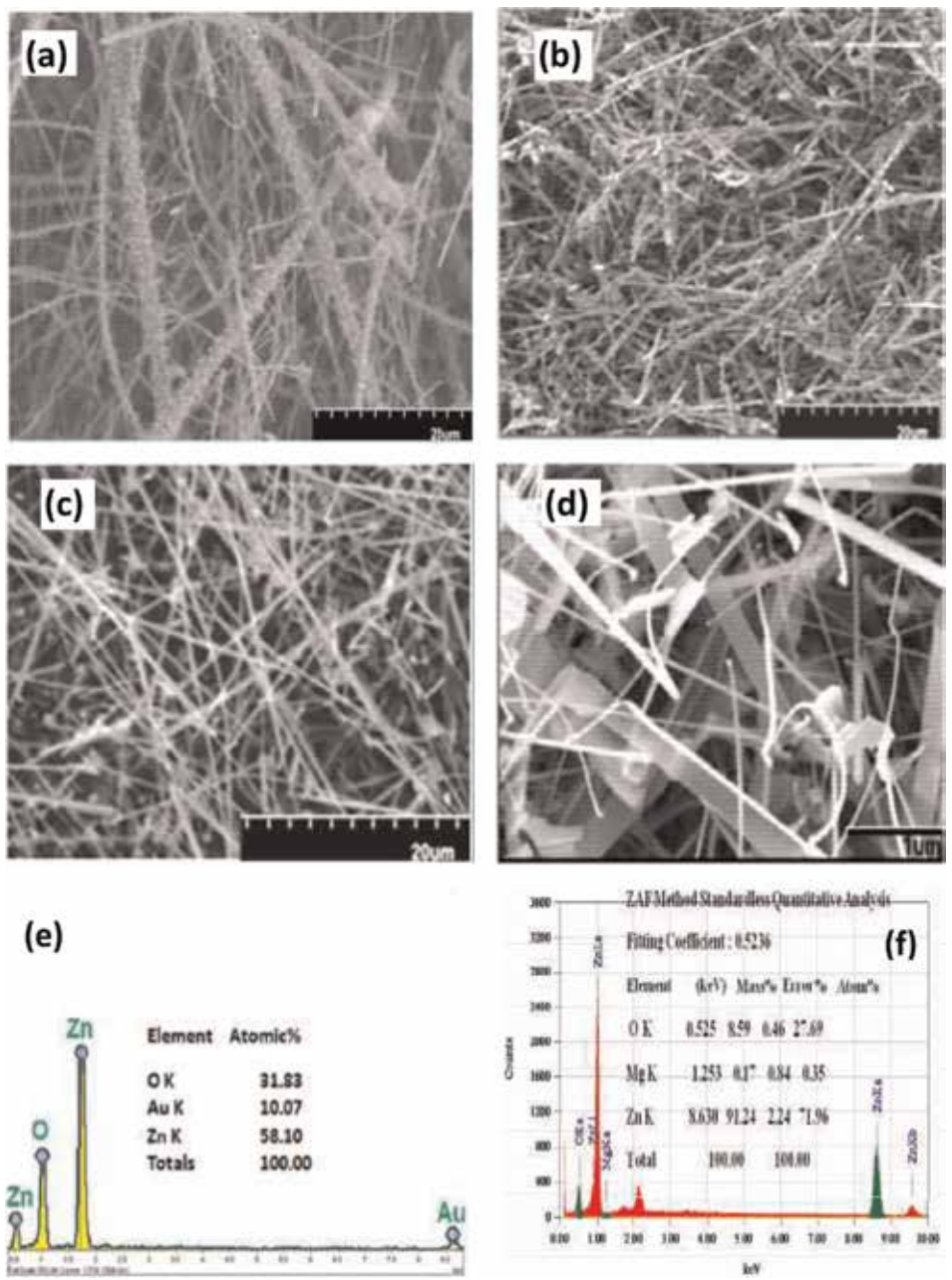

Figure 9.
(a) SEM image of undoped ZnO nanorods (S2). (b) SEM images of Mg-doped ZnO nanobelts. (c) SEM image of undoped ZnO nanowires (S1). (d) SEM images of Mg-doped ZnO nanobelts. (e) and (f) show EDX analysis of undoped and Mg-doped ZnO nanowires and nanobelts, respectively.

4.7 Morphology analysis

Mg-doped ZnO nanostructure morphology was probed by means of SEM. **Figure 9(a)** shows the SEM image of undoped ZnO nanorods (S2) with average diameter and length of 12.66 ± 3.72 μm and 319.48 ± 93.50 μm, respectively. **Figure 9(b)** shows SEM images of Mg-doped (0.05 g) ZnO nanobelts. The average thickness of 1.88 ± 0.70 μm, average width of 4.7 ± 1.04 μm, and average length of 72.03 ± 18.84 μm of the Mg-doped ZnO nanobelts were measured. **Figure 9(c)** shows the SEM image of undoped typical ZnO nanowires (S1) with different dimensions, having average diameter and average length of 0.95 ± 0.11 μm and 35.59 ± 9.90 μm, respectively. **Figure 9(d)** shows the respective EDX analysis spectrum of the undoped ZnO nanowires (S1). The EDX spectra show the attachment of O (oxygen) and Zn (zinc) in the ratio O/Zn which was found to be 32:58, respectively. These composition analyses clearly showed that no impurity peak was observed, showing the purity of ZnO nanostructures. The aspect ratio of undoped and doped ZnO nanorods and nanobelts was found to be 25 and 51, respectively. **Figure 9(e)** shows the Mg-doped (0.08 g) ZnO nanobelts having average thickness of 0.05 ± 0.009 μm, average width of 0.28 ± 0.02 μm, and average length of 2.93 ± 0.87 μm. The corresponding elemental compositions of the synthesized ZnO nanobelts were confirmed by EDX spectroscopy. **Figure 9(f)** shows the corresponding EDX analysis of the doped ZnO nanobelts, showing the presence of oxygen, magnesium, and zinc in the ratio O/Mg/Zn which was found to be 28:0.35:72 respectively. EDX analysis confirmed that the compositions of the products are Mg-doped ZnO without impurity. The aspect ratio of undoped ZnO nanowires and Mg-doped ZnO nanobelts was found to be 37 and 38, respectively. The possible reason for the formation of thin and transparent nanobelts is due to the morphology tuning from nanorods and nanowires to nanobelts by Mg doping, because doping of definite elements plays a key role in the alteration of the dimensions of nanostructures [52–58]. Growth rates and polar surfaces can provoke the asymmetric growth. Formation of nanobelts was explained as continuous process of 1-D branching and subsequent 2-D interspace filling.

Polar surfaces of wurtzite crystals of oxide semiconductors can induce asymmetric growth which leads to the diverse nanostructures, e.g., nanocombs, nanobrushes, needle-like belts/rods, etc. [59].

4.8 CH_4 gas sensing response

The first step was the preparation of CH_4 gas sensor. In the fabrication of CH_4 gas sensor, a thick layer (200 nm) of Au was coated by ion sputtering technique on Si (100) wafers. A small amount of ZnO nanostructures was put on a pair of interdigitated electrodes on Si substrates having a gap of 55 μm. A small drop of methanol was dropped on the nanomaterials so that a thick paste was formed. The annealing of sensors was carried out in an open furnace tube for 2 h at 400°C before performing the gas sensing experiments, for the purpose of attachment of oxygen on the surface of sensors. The sensing experiment was performed at 200°C with 5-min cycles of dry air and 400 ppm CH_4 gas concentration. The sensing response ($S = Ra/Rg$) of the device was measured by resistance change upon exposure to air (Ra) and CH_4 gas (Rg). **Figure 10(a)** and **(b)** shows the sensitivity response of CH4 (methane gas) at 200°C for undoped ZnO nanowires and for Mg-doped ZnO nanobelts, respectively. Research papers showed that the sensitivity of the resistive sensors is highly affected by the Mg doping. The sensors were tested in a temperature range of 50–200°C for 400 ppm of CH_4 gas. Sensors show some response magnitude from 100°C temperature. Undoped ZnO nanowire sensors get its optimal point at 200°C

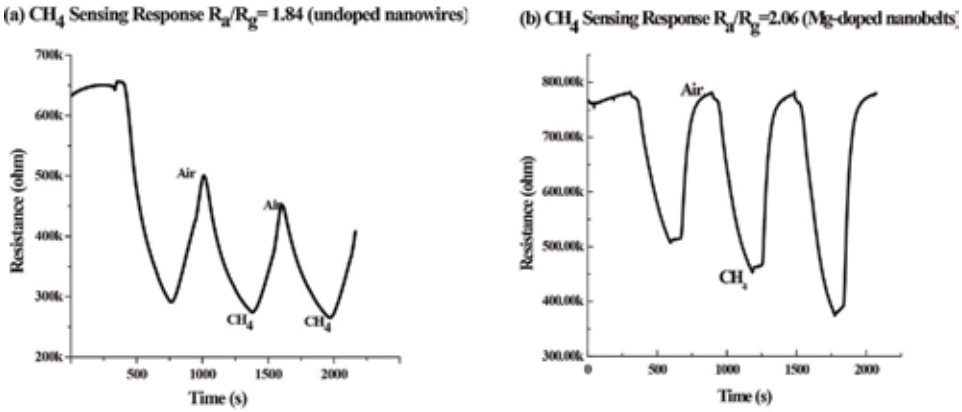

Figure 10.
(a) CH_4 gas sensing response of undoped ZnO nanowires (S1). (b) CH_4 gas sensing response of Mg-doped ZnO nanobelts.

with response magnitude of 1.84. Doped ZnO nanobelts also get its optimal operating point at 200°C. Its response magnitude was obtained at 2.06. The best sensing signal response of CH_4 was found at 200°C. The sensing response at 50, 100, and 150°C (not shown) was comparatively negligible. The sensing response of undoped ZnO nanowires and Mg-doped ZnO nanobelts was found to be 1.84 and 2.06 at 200° C for the same concentration, respectively. The enhanced sensitivity response was observed for the ZnO nanostructures as shown in **Figure 10(b)**. Large amount of oxygen molecules and atoms are adsorbed on Mg-doped ZnO nanobelts due to large surface area (i.e., large defects are created) due to which interaction chance of CH_4 gas increases as compared to undoped ZnO nanostructures [60, 61]. On exposing the surface of the ZnO nanostructures to air, oxygen is adsorbed at the ZnO nanostructures surface by capturing an electron from conduction band of surface sites of undoped and Mg-doped ZnO nanostructures [62, 63]. Reactive O_2 (oxygen molecules) are chemisorbed or trapped by these ZnO nanostructures from the air, forming active oxygen species O_2^- and O^-; as a result transformation of electrons takes place, due to which a wide space charge is formed that results in a decrease in carrier concentration due to which the resistance of the material is increased.

5. Conclusions

Growth of 1-D ZnO nanostructures was presented in the present chapter. Vapor-liquid-solid mechanism has been employed for the synthesis of ZnO nanostructures. It was found that the morphologies tuned with change in temperature which leads to the formation of nanowires at 850°C, nanorods at 900°C, nanobelts at 950°C, and nanobelts with needle-like ends at 1030°C. The dimensions of the morphologies have been measured by SEM. The length of the structures from 2.93 to 319.48 μm, thickness of the structures from 0.05 to 1.88 μm, and diameter of the structures from 0.95 to 12.66 μm have been obtained successfully. XRD peaks show that the crystallinity and intensity increase with increase in temperature. Doping of magnesium acetate (0.05 g) in ZnO through vapor transport method was successfully achieved. The sensing response of doped ZnO nanostructures for UV light at room temperature and CH_4 gas at 200°C has increased. ZnO nanowires show great selectivity response toward different volatile organic compounds (ethanol, methanol, and acetone). At the same concentration and temperature, the ZnO nanowires show

a huge sensing response to acetone (14), and those of the other solvents are no greater than 8.6.

Acknowledgements

The Higher Education Commission (HEC) of Pakistan is acknowledged for financial support through project No. 9294/NRPU/R&D/HEC/2017. Thanks to Prof. Dr. Syed Zafar Ilyas and Dr. Waqar. A. Syed. The authors would also be thankful to COMSATS University Islamabad for necessary funds for the project.

Conflict of interest

There is no conflict of interest in this chapter.

Author details

Nazar Abbas Shah[1*], Majeed Gul[2], Murrawat Abbas[3] and Muhammad Amin[2]

1 Thin Films Technology Laboratory, Department of Physics, COMSATS University, Islamabad, Pakistan

2 Centre of Excellence in Science and Applied Technologies, Islamabad, Pakistan

3 NUST University, Islamabad, Pakistan

*Address all correspondence to: nabbasqureshi@yahoo.com

IntechOpen

© 2019 The Author(s). Licensee IntechOpen. This chapter is distributed under the terms of the Creative Commons Attribution License (http://creativecommons.org/licenses/by/3.0), which permits unrestricted use, distribution, and reproduction in any medium, provided the original work is properly cited.

References

[1] Roco MC, Mirkin CA, Hersam MC. Nanotechnology research directions for societal needs in 2020: Summary of international study. Journal of Nanoparticle Research. 2011;**13**(3):897

[2] Chen P-C, Shen G, Zhou C. Chemical sensors and electronic noses based on 1-D metal oxide nanostructures. IEEE Transactions on Nanotechnology. 2008; **7**(6):668

[3] Xiong HM et al. Sonochemical synthesis of highly luminescent zinc oxide nanoparticles doped with magnesium (II). Angewandte Chemie International Edition. 2009;**48**(15):2727

[4] Maity R et al. Synthesis and characterization of ZnO nano/microfibers thin films by catalyst free solution route. Physica E: Low-dimensional Systems and Nanostructures. 2005;**25**(4):605

[5] Qi Q et al. Humidity sensing properties of KCl-doped ZnO nanofibers with super-rapid response and recovery. Sensors and Actuators B: Chemical. 2009;**137**(2):649

[6] Ivanov P et al. Development of high sensitivity ethanol gas sensors based on Pt-doped SnO_2 surfaces. Sensors and Actuators B: Chemical. 2004;**99**(2):201

[7] Vander Wal R et al. Metal-oxide nanostructure and gas-sensing performance. Sensors and Actuators B: Chemical. 2009;**138**(1):113

[8] Röck F, Barsan N, Weimar U. Electronic nose: Current status and future trends. Chemical Reviews. 2008; **108**(2):705

[9] Zhou X et al. Humidity detection by nanostructured ZnO: A wireless quartz crystal microbalance investigation. Sensors and Actuators A: Physical. 2007; **135**(1):209

[10] Iwanaga H et al. Growth mechanism of ZnO ribbon crystals from ZnS. Journal of Crystal Growth. 1976;**35**(2):159

[11] Huang J, Wan Q. Gas sensors based on semiconducting metal oxide one-dimensional nanostructures. Sensors. 2009;**9**(12):9903

[12] Lei B et al. Tuning electronic properties of In_2O_3 nanowires by doping control. Applied Physics A. 2004;**79**(3): 439

[13] Kolmakov A, Moskovits M. Chemical sensing and catalysis by one-dimensional metal-oxide nanostructures. Annual Review of Materials Research. 2004;**34**:151

[14] Dulub O, Boatner LA, Diebold U. STM study of the geometric and electronic structure of ZnO (0001)-Zn, (0001)-O, (1010), and (1120) surfaces. Surface Science. 2002;**519**(3):201

[15] Meyer B, Marx D. Publisher's Note: Density-functional study of the structure and stability of ZnO surfaces [Phys. Rev. B 67, 035403 (2003)]. Physical Review B. 2003;**67**(3):039902

[16] Spencer MJ. Gas sensing applications of 1D-nanostructured zinc oxide: Insights from density functional theory calculations. Progress in Materials Science. 2012;**57**(3):437

[17] Bylander E. Surface effects on the low-energy cathodoluminescence of zinc oxide. Journal of Applied Physics. 1978;**49**(3):1188

[18] Kasai PH. Electron spin resonance studies of donors and acceptors in ZnO. Physical Review. 1963;**130**(3):989

[19] Yang X et al. Effect of post-thermal annealing on properties of ZnO thin film grown on c-Al_2O_3 by metal-organic

chemical vapor deposition. Journal of Crystal Growth. 2003;**252**(1):275

[20] Hong H-K et al. Portable electronic nose system with gas sensor array and artificial neural network. Sensors and Actuators B: Chemical. 2000;**66**(1):49

[21] Hsueh T-J et al. Laterally grown ZnO nanowire ethanol gas sensors. Sensors and Actuators B: Chemical. 2007;**126**(2):473

[22] Fine GF et al. Metal oxide semiconductor gas sensors in environmental monitoring. Sensors. 2010;**10**(6):5469

[23] Barsan N, Weimar U. Understanding the fundamental principles of metal oxide based gas sensors; the example of CO sensing with SnO_2 sensors in the presence of humidity. Journal of Physics: Condensed Matter. 2003;**15**(20):R813

[24] Kim H, Sigmund W. Zinc oxide nanowires on carbon nanotubes. Applied Physics Letters. 2002;**81**(11):2085

[25] Sahm T et al. Basics of oxygen and SnO_2 interaction; work function change and conductivity measurements. Sensors and Actuators B: Chemical. 2006;**118**(1):78

[26] Franke ME, Koplin TJ, Simon U. Metal and metal oxide nanoparticles in chemiresistors: Does the nanoscale matter? Small. 2006;**2**(1):36

[27] Yamazoe N, Shimanoe K. Roles of shape and size of component crystals in semiconductor gas sensors I. Response to oxygen. Journal of the Electrochemical Society. 2008;**155**(4):185

[28] Moulson AJ, Herbert JM. Electroceramics: Materials, Properties, Applications. John Wiley & Sons; 2003

[29] Suehiro J et al. Dielectrophoretic fabrication and characterization of a ZnO nanowire-based UV photosensor. Nanotechnology. 2006;**17**(10):2567

[30] Kumar S et al. Mechanism of ultraviolet photoconductivity in zinc oxide nanoneedles. Journal of Physics: Condensed Matter. 2007;**19**(47):472202

[31] Bera A, Basak D. Carrier relaxation through two-electron process during photoconduction in highly UV sensitive quasi-one-dimensional ZnO nanowires. Applied Physics Letters. 2008;**93**(5):053102

[32] Kind H et al. Nanowire ultraviolet photodetectors and optical switches. Advanced Materials. 2002;**14**(2):158

[33] Lupan O, Chow L, Chai G. A single ZnO tetrapod-based sensor. Sensors and Actuators B: Chemical. 2009;**141**(2):511

[34] Liu M, Kitai A, Mascher P. Point defects and luminescence centres in zinc oxide and zinc oxide doped with manganese. Journal of Luminescence. 1992;**54**(1):35

[35] Studenikin S, Golego N, Cocivera M. Fabrication of green and orange photoluminescent, undoped ZnO films using spray pyrolysis. Journal of Applied Physics. 1998;**84**(4):2287

[36] Alivisatos AP. Perspectives on the physical chemistry of semiconductor nanocrystals. The Journal of Physical Chemistry. 1996;**100**(31):13226

[37] Zhang Y et al. Synthesis, characterization, and applications of ZnO nanowires. Journal of Nanomaterials. 2012;**2012**:20

[38] Zhao W et al. Self-assembly of ZnO nanosheets into nanoflowers at room temperature. Materials Research Bulletin. 2008;**43**(11):3171

[39] Liu D et al. Surface functionalization of ZnO nanotetrapods with photoactive and electroactive

organic monolayers. Langmuir. 2008; **24**(9):5052

[40] Kong XY, Wang ZL. Spontaneous polarization-induced nanohelixes, nanosprings, and nanorings of piezoelectric nanobelts. Nano Letters. 2003;**3**(12):1625

[41] Leung Y et al. Zinc oxide ribbon and comb structures: Synthesis and optical properties. Chemical Physics Letters. 2004;**394**(4):452

[42] Yang P et al. Controlled growth of ZnO nanowires and their optical properties. Advanced Functional Materials. 2002;**12**(5):323

[43] Chang P-C et al. ZnO nanowires synthesized by vapor trapping CVD method. Chemistry of Materials. 2004; **16**(24):5133

[44] Wagner R, Ellis W. Vapor-liquid-solid mechanism of single crystal growth. Applied Physics Letters. 1964;**4**(5):89

[45] Li Y, Cheng G, Zhang L. Fabrication of highly ordered ZnO nanowire arrays in anodic alumina membranes. Journal of Materials Research. 2000;**15**(11):2305

[46] Johansson J et al. Growth related aspects of epitaxial nanowires. Nanotechnology. 2006;**17**(11):S355

[47] Borchers C et al. Catalyst–nanostructure interaction and growth of ZnS nanobelts. Nanotechnology. 2006; **17**(4):1067

[48] Wang N, Cai Y, Zhang R. Growth of nanowires. Materials Science and Engineering: R: Reports. 2008;**60**(1):1

[49] Wang ZL. ZnO nanowire and nanobelt platform for nanotechnology. Materials Science and Engineering: R: Reports. 2009;**64**(3):33

[50] Yang R, Ding Y, Wang ZL. Deformation-free single-crystal nanohelixes of polar nanowires. Nano Letters. 2004;**4**(7):1309

[51] Nguyen P et al. Epitaxial directional growth of indium-doped tin oxide nanowire arrays. Nano Letters. 2003; **3**(7):925

[52] Qin Y, Yang R, Wang ZL. Growth of horizonatal ZnO nanowire arrays on any substrate. The Journal of Physical Chemistry C. 2008;**112**(48):18734

[53] Gilliland G. Photoluminescence spectroscopy of crystalline semiconductors. Materials Science and Engineering: R: Reports. 1997;**18**(3):99

[54] Manzoor U, Kim DK. Size control of ZnO nanostructures formed in different temperature zones by varying Ar flow rate with tunable optical properties. Physica E: Low-dimensional Systems and Nanostructures. 2009;**41**(3):500

[55] Brewster MM et al. The growth and optical properties of ZnO nanowalls. The Journal of Physical Chemistry Letters. 2011;**2**(15):1940

[56] Kwak EL et al. Anaplastic lymphoma kinase inhibition in non-small-cell lung cancer. New England Journal of Medicine. 2010;**363**(18):1693

[57] van Dijken A et al. The kinetics of the radiative and nonradiative processes in nanocrystalline ZnO particles upon photoexcitation. The Journal of Physical Chemistry B. 2000;**104**(8):1715

[58] Kang HS et al. Investigation on visible emission control of ZnO thin film. Physica Status Solidi. 2004;**1**(10): 2550

[59] Ahn SE et al. Photoresponse of sol-gel-synthesized ZnO nanorods. Applied Physics Letters. 2004;**84**(24):5022

[60] Manzoor U, Kim DK. Synthesis and enhancement of ultraviolet emission by post-thermal treatment of unique zinc

oxide comb-shaped dendritic nanostructures. Scripta Materialia. 2006;**54**(5):807

[61] Han N et al. Photoluminescence investigation on the gas sensing property of ZnO nanorods prepared by plasma-enhanced CVD method. Sensors and Actuators B: Chemical. 2010;**145**(1): 114

[62] Prades JD et al. The effects of electron-hole separation on the photoconductivity of individual metal oxide nanowires. Nanotechnology. 2008;**19**(46):465501

[63] Fan HJ et al. Vapour-transport-deposition growth of ZnO nanostructures: Switch between c-axial wires and a-axial belts by indium doping. Nanotechnology. 2006;**17**(11): S231

Chapter 7

Gas Sensors Based on Conducting Polymers

Nagy L. Torad and Mohamad M. Ayad

Abstract

Since the discovery of conducting polymers (CPs), their unique properties and tailor-made structures on-demand have shown in the last decade a renaissance and have been widely used in fields of chemistry and materials science. The chemical and thermal stability of CPs under ambient conditions greatly enhances their utilizations as active sensitive layers deposited either by in situ chemical or by electrochemical methodologies over electrodes and electrode arrays for fabricating gas sensor devices, to respond and/or detect particular toxic gases, volatile organic compounds (VOCs), and ions trapping at ambient temperature for environmental remediation and industrial quality control of production. Due to the extent of the literature on CPs, this chapter, after a concise introduction about the development of methods and techniques in fabricating CP nanomaterials, is focused exclusively on the recent advancements in gas sensor devices employing CPs and their nanocomposites. The key issues on nanostructured CPs in the development of state-of-the-art miniaturized sensor devices are carefully discussed. A perspective on next-generation sensor technology from a material point of view is demonstrated, as well. This chapter is expected to be comprehensive and useful to the chemical community interested in CPs-based gas sensor applications.

Keywords: conducting organic polymers, gas sensors, polypyrrole (PPY), polyaniline (PANI), toxic gases, miniaturized sensor devices

1. Introduction

The initial development of conducting polymers (CPs) began in 1977 by the American scientists MacDiarmid and Heeger and their Japanese colleague Shirakawa, as they discovered a highly conductive polyacetylene (PA) via chemical doping with iodine or other ionic dopants which endowed the polymer with metal-like properties, producing copper-colored films with an increased conductivity of 10 orders of magnitude (Noble Laureate in Chemistry in 2000) [1–3]. However, the instability and ease of degradation of PA by oxidative degradation was a big obstacle to find applications such as batteries or electronic devices. Since then, there have been worldwide considerable efforts in synthesizing numerous other CPs similar to those of PA with high doping level over the range from insulator to metal, such as polyphenylene (PP), polypyrrole (PPY), polythiophene (PTH), and polyaniline (PANI) [4–7].

Hitherto, however, studies on CPs have been extensively investigated in both fundamental and practical perspectives; their unique chemical and physical characteristics have been continuously discovered. These fascinating properties are derived from their π-electron conjugation system along the polymer chain, which allow

the formation of delocalized electronic states, resulting in a resonance-stabilized structure of the polymer [8]. Over a wide range of polymer-based materials, CPs are of particular interest due to their unique electrical and optical properties rivaling metals or inorganic semiconductors and still retain the attractive mechanical properties and processing advantages of polymeric materials, known as "synthetic metals" [9]. In addition to a variety of advantages, ease of preparation procedures, controlling the morphology, structural flexibility, light weight, and cost-effectiveness are included. The molecular structures of some of the prominent CPs include PANI, PPY, poly-paraphenylene (PPP), and PTH, which are shown in **Figure 1** (left) in their non-conducting (undoped) states. In the past few decades, CPs have been continuously studied for their tremendous use in electronic and optoelectronic devices. In this context, particular interest has been paid toward utilization of nanostructured CP-based sensors as high-performance signal transducers with enhanced sensing capability relative to their conventional bulk-scale materials, because of their high surface-to-volume ratios and unique electrical and physical properties [10]. In the sense of sensor applications, the distinguishing properties of CPs offer a great potential in efficient sensing systems by virtue of their unique electrical, optical, and mechanical transduction mechanisms [11, 12]. To achieve superior performances in both sensitivity and response time, critical issues include conductivity, morphological design, size control, bioprobes, and surface modification which are very crucial. In terms of conductivity change, oxidation level achieved by chemical and electrochemical doping/dedoping mechanisms could in turn fabricate a sensitive and rapid sensor response to an analyte of interest at room temperature [11, 13]. Recently, special attention has been paid to nanostructured CPs as one of the most substantial achievements in sensor technology because their high surface areas, multidimensional architectures, and easy functionalization with a variety of functional groups enable the sensing of a trace amount of a target species [14]. Further, the signal intensity of the sensor can be enhanced by controlling the shapes because of the one-directional signal pathway of the CP nanostructure.

Typical CPs, such as PPY, PANI, PTH, and poly(3,4-ethylenedioxythiophene) (PEDOT), have been extensively studied in environmental monitoring of various types of target analytes, such as volatile organic compounds (VOCs), gases, heavy metals, and biomolecules [15–17]. On exposure to analyte, their response mechanisms comprise chemical and physical interactions, including oxidation/reduction, swelling, conformational changes, charge transfer, and so on. In terms of charge

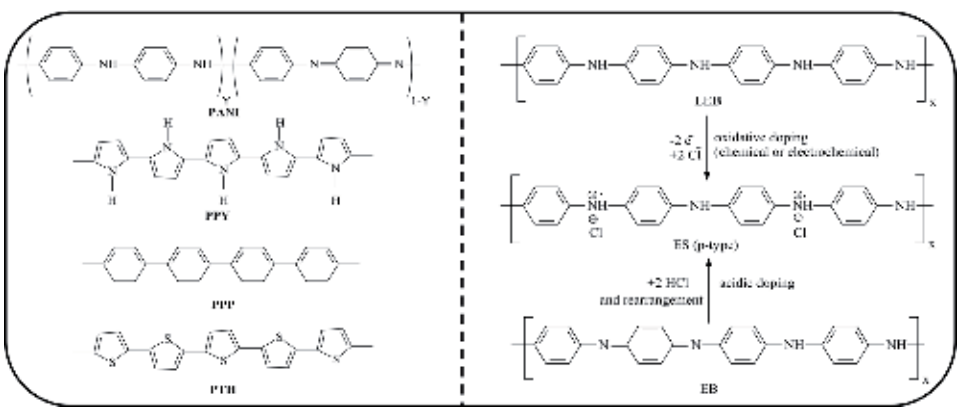

Figure 1.
(Left) Representative of typical molecular structures of CPs and (right) illustration of doping mechanisms of PANI. The terms "LEB and ES" represent the completely reduced form of colorless PANI called "leucoemeraldine base" and the highly conducting emeraldine salt (ES) obtained by chemical reaction with protonic acids whose color is green, and the conductivity is around 15 S·cm^{-1}.

transfer, doping and oxidation levels and conjugation length are key intrinsic factors of CPs in which the delocalization of the π-electron takes place. It is well-known that most of CPs are p-type semiconductors, and thus they feature the emergence of charge carriers (polaron and biopolaron) as oxidative doping proceeds as shown in **Figure 1** (right). Accordingly, these intrinsic factors are very useful for designing the high performance of CP-based sensors.

2. Synthesis of nanostructured conducting polymers

Conducting polymers have traditionally been synthesized either by chemical or electrochemical oxidation routes of the corresponding monomers with acid or peroxide initiators resulting in insulating materials that require a post-doping process [11, 18–20]. In both cases, the overall polymerization process includes the oxidation of monomer, followed by coupling reaction of the charged monomers to produce a polymer chain. Chemical polymerization method is usually applicable for large-scale production of CP powders. In contrast, electrochemical polymerization offers an in situ one-step effective process for producing CP nanomaterials deposited onto the electrode surface as films for a sensor device, which grow along the direction of the electric field to form oriented nanostructures. The morphological structure and thickness of the CP films can be tailored by controlling the electrochemical polymerization conditions, applied potential or current density, and electrolyte. Owing to their electrical conductivity, CPs can grow electrochemically on an electrode surface without addition of oxidizing agents.

Great efforts have been devoted toward the preparation of CP nanomaterials for the fabrication of miniaturized novel flexible sensor platforms that enable portability and high-density arrays because of using small sample amounts, which offer excellent prospects in sensor nanotechnology for advanced detection systems [21]. Recent studies have demonstrated the synthesis of nanostructured CPs with controlled shape and size, which ranged from lithographic techniques to chemical methods [22–33]. Stejskal and coworkers demonstrated synthesizing PANI nanostructures and its derivatives by the chemical oxidative polymerization in water [34–36]. Further, Ayad et al. reported the synthesis of PANI and PPY nanotubes, nanorods, nanoflowers, nanoflakes, and nanocomposites via chemical oxidative polymerization using diluted aqueous camphor sulfonic acid (CSA) and acetic acid solutions as shown in **Figure 2** [37, 38]. Besides, the incorporation of metals/metal oxide NPs, graphene, or carbon nanotubes (CNTs) into nanostructured PANI and PPY has been recently reported as a way of increasing the CP electrochemical and electrocatalytic activities and sensing capabilities [39–42].

Recently, research studies have focused on the development of templating approaches such as hard template, soft template, and template-free synthesis as an aid template in combination with other polymerization methods, like dispersion polymerization, interfacial polymerization, vapor deposition polymerization (VDP), and electrochemical polymerization for the synthesis of well-defined CP

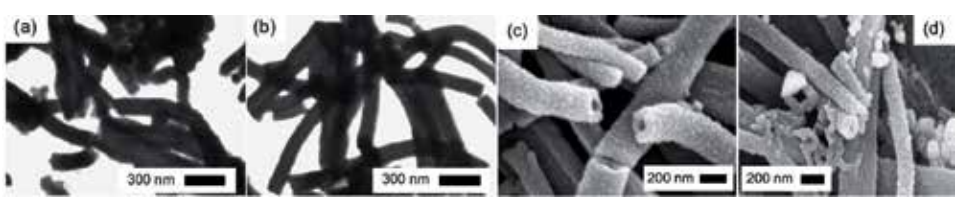

Figure 2.
(a and b) STEM of PANI salt and PANI base prepared with CSA, respectively. (c and d) SEM images of nanotubular PANI and PANI/Ag nanoparticles, respectively, prepared using chemical oxidative polymerization in acetic acid (adapted with permission from Ref. [37, 38] Copyright 2009, Elsevier).

nanomaterials [43–48]. Depending on the monomer properties, whether it interacts electrostatically or chemically bound to the template, different CP micro- and nanostructures can be fabricated retaining the original shape of the porous template itself.

So far, the hard template approach is utilized for the synthesis of one-dimensional (1D) CP nanostructures such as nanotubes, nanorods, and nanofibers which are synthesized using anodic aluminum oxide (AAO) membranes, zeolite channels, mesoporous silica, and track-etched polycarbonate [49, 50]. Depending on the pore length and diameter of the membrane template, size and diameter of CP nanostructures can be precisely controlled because the monomers are absorbed or attached inside the pore walls, followed by chemical oxidative polymerization [51]. In addition, the wall thickness can be tuned by controlling the polymerization time and concentration of monomer. In pioneering studies to Jang et al., they proposed a facile route to synthesize PPY nanotubes with a wall thickness of a few nanometers using AAO membrane template via VDP as signal transducers [52, 53]. Park et al. reported a one-pot synthesis of Ag NPs decorated PEDOT nanotubes with high surface area and enhanced conductivity via VDP method using an AAO template and $Fe(NO_3)_3$ as an oxidant for sensing ammonia gas [54]. Furthermore, combination of electrospinning using electrospun nanofiber templates and VDP methods provided CP nanomaterials with remarkable surface areas and uniform nanostructures [55]. Kwon et al. reported the use of electrospun ultrathin poly(methyl methacrylate) (PMMA) nanofibers as a template to synthesize PEDOT after immersing with ferric chloride solution followed by VDP of EDOT monomer at controlled temperatures and pressures to yield core-shell PEDOT nanofibers [56]. However, this method suffers from the difficulties of removing the template without aggregation of the resulting CPs and is not suitable for commercial applications. Regardless, high-impact nanostructured CP composites can be prepared without removal of template. Furthermore, previous studies reported that the synthesis of different CP nanohybrids, such as metal, metal sulfides, and metal oxides/PPY nanowires, was prepared by the hard template method [57–59].

An alternative strategy known as the soft template approach has been used to effectively fabricate CP nanomaterials using templates such as surfactants, block copolymers, polyelectrolytes, and liquid crystals combined with interfacial polymerization and emulsion/dispersion polymerization [60–62]. Accordingly, 1D CP nanostructures can be tailored by varying the synthetic conditions and produced in large scale [63]. A cationic surfactant, dodecyltrimethylammonium bromide (DTAB), has been utilized to form spherical micelles reinforced with decanol in aqueous solution as a stable microemulsion for the synthesis of monodispersed PPY nanoparticles with a large quantity [64]. However, this technique requires high surfactant concentration, which is problematic in terms of cost and environmental pollution. Jang and coworkers reported the formation of PPY nanotubes and nanoparticles using a reverse micelle system (water-in-oil systems) with a molecular template, sodium bis(2-ethylhexyl) sulfosuccinate (known as AOT), and dispersion polymerization (water-soluble polymers) employing polyvinyl alcohol (PVA) in an aqueous solution, respectively [65–67]. In addition, PANI nanowire network was carefully synthesized using a cationic surfactant, hexadecyltrimethylammonium bromide and oxalic acid in aqueous solution [68]. Further, an anionic oxidant/cationic surfactant complex was used as a template to fabricate clip-like nanostructures of PPY, PANI, and PEDOT [69]. By judiciously changing the combination of surfactants, oxidizing/doping agents, pH, and temperature, infinite nanostructures with desirable morphology could be successfully fabricated. A facile method to synthesize nanostructured core-shell PPY/Ag using sodium dodecyl benzyl sulfonate (SDBS) and CTAB as templates through a redox reaction was proposed [70]. Very recently, Stejskal et al. demonstrated a cotton fabric coating of PPY and PANI nanotubes, colloidal PPY nanotubes/nanorods, and microporous PANI cryogels obtained by the chemical polymerization

of pyrrole in the presence of a structure-directing dye, methyl orange (MO), as a starting template, and poly(*N*-vinypyrrolidone) (PVP), respectively [71–78]. The interaction between starting materials and dye was expected to produce a template, which is further used for the growth of CP nanotubes. After the addition of oxidant, MO itself in its acid form has limited solubility which may serve as a starting template and the growth of nanotubes may proceed beyond the template [79, 80]. Also, the partial solubilization of MO-$FeCl_3$ template in the presence of CTAB was an effective way to fabricate PPY nanotubes having smaller diameter by reactive self-degrade template method [81, 82]. In addition, ionic liquid template-assisted synthesis of PANI/AgCl and PPY/Ag nanocomposites has recently been conducted by the direct oxidation of pyrrole by silver cations from silver bis(trifluoromethanesulfonyl)imide ($AgTf_2N$), using 1-butyl-3-methylimidazolium bis(trifluoromethylsulfonyl)imide ($BMImTf_2N$) as solvent and template [83, 84]. Moreover, dual-template approach involving an AAO template and surfactants was also applied by another research group for fabricating nanotubular PPY [85].

Template-free approach is a quite facile and a straightforward method for producing CP nanomaterials with large quantity without using specific sacrificial templates and post−/pretreatment procedures; however extensive efforts are needed to design building blocks that can spontaneously self-assemble into nanostructures under certain conditions without addition of artificial templates. PANI nanofibers prepared from template-free synthesis have been considered as an interesting sensing material since the pioneering study by Huang et al. [86]. Several types of template-free methods, such as chemical, electrochemical, dispersion, and aqueous/organic interfacial polymerization, resulting in various CP micro−/nanostructures, including nanotubes, nanofibers, hollow nanoparticles, core-shell nanoparticles, and multidimensional nanotubes, were extensively reported [87–96]. In addition, a template-free site-specific electrochemical method was developed for the fabrication of PPY, PANI, and PEDOT nanowires on microelectrode junctions [97, 98]. Moreover, a bottom-up approach was applied for the fabricating of PPY/Ag core-shell nanoparticles with an average core diameter of 36 nm and a shell thickness of 13 nm via a simple one-pot synthesis using a starch [99]. In this process, the OH^- groups of the soluble starch provided nucleation sites for Ag^+ that were readily reduced by the pyrrole monomer. Simultaneously, pyrrole monomers were oxidized to form radical cations that have led to the generation of PPY short chains which are further oxidized by the silver nanoseed active sites to finally produce PPY core-shell nanostructures.

3. Gas sensors based on CPs

Chemical sensor is composed of a sensitive material to a particular analyte (molecular recognition) and a transducer, which transforms the concentrations of an analyte into other detectable physical signals, such as current, absorbance, or mass (**Figure 3**). Depending on signal transduction, gas sensor devices based on CPs have been classified by IUPAC [100]. Sensors based on chemical modulation of electronic, optical, or mechanical transduction mechanisms of CPs will be discussed in detail in light of the gas sensing applications.

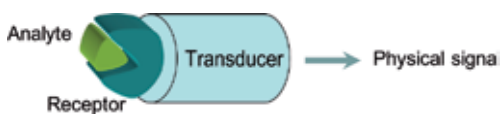

Figure 3.
Illustration of a chemical sensor. (modified and adapted with permission from Ref. [103]. Copyright 2008, MDPI).

3.1 Electrochemical device sensors

Electrochemical devices transform the electrochemical interaction that occurred at analyte-electrode interface into a detectable signal related to the analyte involved in the chemical process. Most of CP sensors rely on electrochemical techniques using amperometric (measurement of current at constant potential) and potentiometric (current measurements during varying potentials). In electrochemical sensor, the charge transport properties of CPs are changed when exposed to an analyte, and the change can be correlated quantitatively to the analyte concentration [101, [102]. In either case, the peak current, as the voltage is scanned, is proportional to the concentration of the target molecule. Based on the electrical transduction modes, electrochemical sensors are classified into the following.

3.1.1 Amperometric sensors

Amperometric gas sensor is a subgroup of electrochemical gas sensing devices that can be utilized for environmental monitoring and clinical analysis of electroactive species, whether in a liquid or a gas phase [102]. The principle of amperometric sensing is to measure the current generated by the redox reaction of an analyte at a working electrode, where the current is subject to Faraday's law and a dynamic reaction, achieving steady-state conditions in the system under an impressed constant voltage on the chemically stable CP-modified electrode [103]. Based on the nature of analyte, when an appropriate potential is applied on the electrode, the analyte molecules are respectively oxidized or reduced on anode or cathode, resulting in a current change. For gas-phase analytes, amperometric sensors are characterized with a gas/liquid/solid boundary and an interfacial transport process that frequently controls the analytical performances and sensor response characteristics. Besides, an inorganic acid is usually used as the supporting electrolyte to provide H^+ ions for ionic conductance in Nafion film. Do et al. fabricated an amperometric NO_2 gas sensor based on PANI/Au/Nafion hybrid nanocomposite using the CV technique at ambient temperature [104]. NO_2 diffusion into a porous PANI was prepared by CV and constant current (CC) methods, resulting in a reduction of mass transfer resistance with increment in cathodic reduction of NO_2 compared to Au/Nafion [105, 106]. Also, the redox response plays a definitive role in the signal transduction of the PANI nanoparticle-based amperometric ammonia gas sensor [107]. The sensor exhibited a sensitivity of 3.04 μA ppm^{-1} with a switching effect for 0 and 100 ppm concentrations. Recent studies have also demonstrated that CNTs enhance the electrocatalytic properties of gases in PANI films associated with the high electron density and conductivity of the polymer and surface reactivity of the composite when used as an amperometric sensor. For example, a 3D nanofibrous structure of WO_3-chitosan-*co*-PANI nanocomposite prepared electrochemically was used for amperometric detection of NO_2 gas in acidic media without interferences using a mineral acid as a supporting electrolyte [108]. The sensor was very highly sensitive enough to low concentrations of NO_2 gas in the range from 100 to 500 ppb, at a pH 2.0 and using 0.25 V *vs* Ag-AgCl. Solid-state amperometric gas sensor based on Nafion/Pt/nanostructured PANI/Au/Al_2O_3 and xerogel Ag/V_2O_5/nanofibrous PANI/Ag hybrids were also investigated for detecting H_2 and NH_3, respectively [109, 110]. The sensitivity and response time for H_2 gas was remarkably promoted by decreasing the Nafion film thickness, and the charge passed for the electrodeposition of Pt and PANI with activity was found to be 338.50 μA ppm^{-1} g^{-1} for measuring 10–10,000 ppm H_2. Upon using xerogel Ag/V_2O_5/nanofibrous PANI/Ag hybrids, the sensor could detect gaseous NH_3 in the range of 0–54 ppm, which would be beneficial for animal confinement husbandry.

3.1.2 Potentiometric sensors

As a subgroup of electrochemical sensors, potentiometric sensors, known as ion-selective or ion-sensitive sensors (ISEs), are utilized for monitoring voltage as a result of specific electrochemical reactions involving a redox reaction for determination of the analyte concentration by measuring accumulation of a charge potential at the working electrode when zero or no current flow arises mainly from shifts in the "dopant" anion equilibrium within the polymer chain (sensing membrane) [111]. Potentiometric sensor technique is very attractive for practical applications, because it provides advantages in the use of small-sized, portable, and low-cost instruments. In the electrochemical cell, the potential (E) arises between two electrodes, defined as the potential difference between the cathodic and anodic potentials typically proportional to the logarithm of the gas analyte concentration which can be estimated from Nernst equation (Eq. (1)).

$$E = E_o + \frac{RT}{nF} lnQ \tag{1}$$

where E_o is the standard electrode potential in volts, R is the universal gas constant (8.314472 J K^{-1} mol^{-1}), T is the absolute temperature in kelvin, F is Faraday's constant (9.648 × 10^4 coulombs mol^{-1}), n is the number of electrons participating in the electrochemical reaction, and Q is the chemical activity of the analytes. In case of physical phenomena, in which apparent redox reactions are not involved, they will generate a potential; however those initial conditions have a non-zero free energy. Therefore, ion concentration gradients across a semipermeable membrane induce a potentiometric response which is the basis of measurements that use ISEs. In pioneering studies by Hyodo et al., they investigated CO, CO_2, and H_2 sensing properties of potentiometric gas sensor by employing noble metals (Ag, Au, Ir, Ru, Rh, Pd, or Pt), loaded metal oxides (Bi_2O_3, CeO_2, In_2O_3, SnO_2, ZnO, or V_2O_5), or carbon black as sensing electrode materials and anion-conducting polymers (ACP) electrolyte in order to improve the selectivity of the resulting chemical sensors [112–117]. The gas sensing mechanism was discussed as the overall potential (sensing electrode potential) arising from the electrochemical reduction of oxygen and CO oxidation balanced with wet synthetic air (57%RH) at 30°C based on the following equations (Eq. (2) and(3)):

$$1/2O_2 + H_2O + 2e^- \rightarrow 2OH^- \tag{2}$$

$$CO + 2OH^- \rightarrow CO_2 + H_2O + 2e^- \tag{3}$$

Among the sensors, Pt-loaded SnO_2 exhibited the most excellent CO selectivity against H_2. On the other hand, Au-loaded In_2O_3 or SnO_2 effectively improved the magnitude of the CO and H_2 responses, resulting in a relatively poor CO selectivity against H_2. However, the selectivity was improved after heat treatment of the Au-loaded In_2O_3 or SnO_2 powder under a reducing atmosphere at 250°C [113, 114]. Based on electrical transduction modes, dynamic processes, such as chemical and diffusion which occurred at the sensor surface under the steady-state condition, result in a thermodynamically accurate signal for potentiometric sensors following Nernst's law of thermodynamics, whereas amperometric sensors relate to Faraday's law (**Table 1**).

3.2 Electrical device sensors

Conductometric gas sensor is an electrical device-based measurement, which measures the signal induced by the change of CP electrical properties as a result

Electrochemical sensor	Sensor signal vs. [gas]	Principle
Amperometric	$E = E_c + k\ln P$	Kinetics (Faraday's law)
Potentiometric	$E = kP$	Thermodynamics (Nernst's law)

Table 1.
Differences between potentiometric and amperometric gas sensor.

of analyte interaction, and no electrochemical reactions take place [100]. Because of their cost-effectiveness and sensitivity, conductometric gas sensors can be used to study the analyte interaction with the sensing materials leading to a resistance change (Eq. (4)). This process causes changes in carrier density or mobility, resulting in a conductivity change (ρ) which is the reciprocal of resistivity (Eq. (5)).

$$\Delta R = \frac{R_o - R_{exposure}}{R_o} \tag{4}$$

$$\rho = \frac{RA}{L} \tag{5}$$

where R_o is the resistance before exposure and R, A, and L are the resistance, sample area, and thickness, respectively. The interaction of CPs with an electron acceptor or donor analyte causes changes in both carrier density and mobility, resulting in an enhanced change in conductivity at the electrode/CP interface, as a result of modulation of the Schottky barrier height (determined by the difference in work function of the intrinsically CP material). When a p-type CP donates electrons to analyte gas molecules, its hole conductivity increases, whereas electron-accepting CPs result in a decrease in conductivity. At the electrode/CP interface, a space charge region is created, and the effective resistance greatly depends on the bias voltage applied during the measurement [118]. Accordingly, there are two different types of conductometric sensor-based CPs.

3.2.1 Polymer-absorption sensors (chemiresistors)

Chemiresistors are the most common type of sensors which can measure the change in the resistance of an electrically active sensitive material on exposure of a target gas analyte or a medium [119]. In addition to their small-sized low-power devices, chemiresistors exhibited good sensitivity and are amenable for online monitoring of various toxic chemicals. Compared with standard electrochemical sensors, chemiresistors do not require liquid electrolyte to work properly. The measured electrical resistance change as the output is attributed to absorption/adsorption of gas analytes into the sensitive material (**Figure 4**). It is a known fact that the conductivity of an identical CP material varies according to the method of preparation and the thickness of the film [120], which has a considerable influence over the surface morphology. In addition, the CP/insulating substrate (oxides such as glass, quartz, sapphire) interface is another aspect which may contribute to the overall conductivity. As a result, the degree of hydration alters the surface conductivity of the substrate because of the interfering water vapors when chemiresistors are operated at room temperature [121]. Making such a substrate surface rather hydrophobic before depositing CP material may mitigate this problem [121].

In the mid-1990s, Agbor et al. demonstrated the deposition of PANI thin films by various techniques (evaporation, spinning, and the Langmuir–Blodgett) as chemiresistor gas sensor of NO_x, H_2S, SO_2, CO, and CH_4 [122]. All types of deposited PANI/EB were sensitive to NO_x, H_2S gas down to 4.0 ppm, whereas only spun

and evaporated PANI/EB dissolved in NMP were responsive to SO_2. Then after, recent studies investigated the design of flexible room temperature chemiresistive NH_3 [123–126], and CO_2 [127] gas sensor based on nanostructured PPY and PANI was synthesized via an in situ chemical polymerization with an aid of dual templates, MO and CTAB. This work represented competitive results for pure, metal-free, and flexible CP sensors operated at room temperature for monitoring NH_3 sensor in workplaces and air pollution with a fast response time and a high selectivity. Bartlett and coworkers have used poly-5-caboxyindole, PPY, and PANI and their derivatives formed by electrochemical polymerization as sensors for alcohols, ether, and other organic vapors; however it showed a low sensitivity [128–130] and an incomplete desorption of the gas molecules [128]. Of the four polymers investigated, poly-5-caboxyindole was the most stable and represented a reproducible behavior. A chemiresistive type H_2 gas sensor based on PANI and PANI/CNT composite at room temperature has been developed by Srivastava et al. [131]. The sensor response showed a higher response after doping of CNT using IDE-type sensor due to a significant interaction between H_2- and CNT-doped PANI composites. In an interesting study by Xue et al., they fabricated a miniaturized chemiresistor gas sensor to next-generation high-performance sensors based on oriented single crystal PPY nanotube (SCPNT) arrays with an ultrathin wall thickness prepared with a combination of cold-wall VDP and template-assisted synthesis using AAO template. A SCPNT chemiresistor sensor exhibited a superior sensing capability to NH_3 gas at a low detection limit down to 0.05 ppb at room temperature, surpassing commercially metal oxide-based sensors [132]. The ultrahigh sensor sensitivity originating from not only higher crystal orientation but also hollow structure and high surface area of the nanotubes allowed the easy diffusion of gas molecules, since the thickness of the SCPNT walls is only about 10 nm scale. An innovative flexible chemiresistor NH_3 gas sensor was fabricated by an in situ chemical oxidative polymerization of PANI with multiwalled CNTs [133] and S, N-doped graphene quantum dots (S, N:GQDs) [134, 135]. A significant increase in the gas sensing performance with improved sensor response/recovery characteristics could be realized at trace-level detection under ambient conditions. The response of S, N:GQDs/PANI composite toward NH_3 gas was five times higher than pure PANI, because the S, N:GQDs cavities facilitated large interaction sites for NH_3 via π-electron networks. Also, the enhancement in PANI/MWCNTs performance was attributed to the physisorption/chemisorption of NH_3 gas due to the synergetic cooperation between acid–base doping/dedoping effect of PANI and the electron transfer between NH_3 molecules and CNT or GQDs. Once NH_3 has adsorbed onto the surface of PANI, it reacted with amine (N-H) groups of PANI forming NH_4^+, resulting in the localization of PANI polarons, and thus increased the sensor resistance.

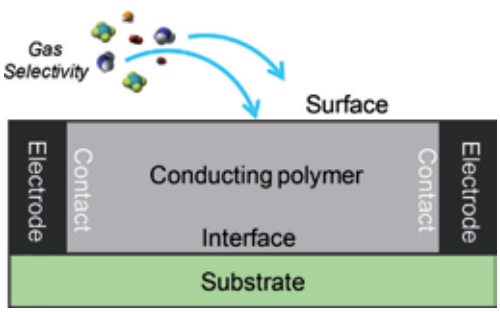

Figure 4.
Schematic illustration of the chemiresistor sensor principle based on chemically sensitive CPs for selective detection of chemical sensing materials.

For maximizing the renewable energy recovery, Xue and coworkers designed a flexible hierarchical PANI/CNT nanocomposite film-based electronic gas sensor for a real-time monitoring of NH_3 in anaerobic digestion from 200 ppb to 50 ppm at room temperature [136]. The sensor exhibited a fast response/recovery time with excellent selectivity to NH_3 compared to other VOCs, such as methanol, ethanol, acetone, dichloromethane, isopropyl alcohol, ethylene glycol, and pyridine due to the high surface area of nanocomposite films. An in situ synthesis of SnO_2-rGO)-PANI (SGP) nanocomposite via surfactant-free precursor at low temperature was investigated for enhanced performance of NH_3 gas sensor [137]. From XPS, the well-defined p-n hetero junction existed in the hybridized SGP nanocomposite dramatically enhanced the sensing activity, selectivity, and chemical stability, in comparison of pure SnO_2 and SnO_2-rGO hybrid. In addition, Ye et al. reported the rGO/Poly (3-hexylthiophene) (rGO/P3HT) composite film prepared by spray process for constructing the resistive NH_3 sensor [138]. The composite film sensor exhibited better sensing properties and reversibility than pure rGO, as a result of π-π interaction between rGO and P3HT. Moreover, Sharma and coworkers demonstrated the synthesis of Al-SnO_2-PANI, MWCNT-PANI, and MWCNT-PEDOT-polystyrene sulfonic acid (PSS) nanofibers via electrospinning technique for H_2 and NH_3 gas sensing application [139, 140]. On exposure to 1000 ppm of H_2 gas, the Al-SnO_2-PANI nanofiber composite showed fast response/recovery at 48°C [139]. MWCNT-PEDOT-PSS was found to be more effective than MWCNT-PANI composite in terms of sensitivity and repeatability for NH_3 gas [140]. However, the sensor presented a major challenge of complete recovery of chemisorbed NH_3 from CNT; the research group proposed a trial experiment for sensor complete recovery within a short time (20 min) using a combination of heat and DC electric field.

Besides, various metals and/or metal oxides were also introduced to further enhance the response/recovery kinetics of the sensing materials. Chemiresistor gas sensing behavior of NH_3 based on nanostructured PPY/SnO_2 [141], PPY/ZnO [142–144], PPY/Zn_2SnO_4 [145], PPY/Ag-TiO_2 [146], PPY/silicon nanowires (PPY/SNWs) [147], PANI/SnO_2 [148], PANI/ZnO [149], PANI/In_2O_3 [150], PANI/TiO_2 [151], PANI/flower-like WO_3 [152], PANI/SnO_2/rGO [153], PANI-TiO_2-Au [154], and Ag-AgCl/PPY [155] has recently been studied so far. The CP/metal oxide nanocomposite thin films exhibited an outstanding response time of 2 S for NH_3 at very low concentration of 50 ppb in air with respect to methanol and ethanol vapors [156]. Thin films of Cu/PANI have also been examined as a sensor toward different gases, such as NH_3, CO, CO_2, NO, and CH_4 at room temperature [157]. Incorporation of Cu nanoparticles improved the response and the recovery times, in addition to its excellent selectivity toward NH_3 due to doping and dedoping processes of PANI. Composite of Pd-PANI-rGO [158] has been recently synthesized to fabricate a highly sensitive and selective chemiresistive H_2 gas sensor. In addition to high surface area of the PANI-GO composite, the fast spillover effect and hydrogen dissociation over Pd significantly enhanced the sensing performance. Other studies by Xu and coworkers employing films of SnO_2-ZnO/PANI [159] and SnO_2/PANI [160] hybrids as NO_2 gas sensors prepared by the solvothermal hot-press (SHP) process were demonstrated. The later sensors exhibited much high affinity and selectivity to a low concentration of NO_2 gas at 140°C caused by the formation of p-n junction. For porous SnO_2-ZnO/PANI, a high selective sensor responded to a low NO_2 concentration at 180°C, due to the porous nature of SnO_2 and high ZnO content (20 wt.%). Mane et al. investigated chemiresistive NO_2 gas sensors based on DBSA-doped PPY/WO_3 and CSA-doped PPY/NiO nanocomposites at room temperature [161, 162]. The sensor can successfully detect NO_2 gas at a concentration as low as 5 ppm. The enhanced gas sensing properties would be assigned to the formation of random nano p-n junctions distributed over the polymer surface film

and activity of dopants. Moreover, Mondal and coworkers [163] reported a green chemical route synthesis of P3TH/CdSe (QDs) nanocomposites as a chemiresistive $CHCl_3$ gas sensor at concentrations range of 100–1200 ppm at room temperature. On illumination of the sensor with a monochromatic light of 600 nm, an enhancement of charge transfer in nanocomposites was photo-induced, resulting in an improvement in sensor response and recovery time.

3.3 Optical device sensors

The gas sensors based on optical transductions are described as change in absorbance and luminescence as a result of gas analytes, interaction with a sensitive material [164]. For signal generation, optical parameters such as refractive index and reflectivity have been used. Optical gas sensors have been recently utilized for multi-analyte array-based gas sensing, due to low cost, miniaturized optoelectronic light sources, and efficient detectors [164]. Based on the signal generated due to intrinsic properties of sensing material, optical sensors are classified as absorption and luminescence.

3.3.1 UV–vis and infrared sensors

The UV–visible and near infrared (NIR) spectra can reflect the electron configurations of CPs. After doping process, the spectral absorbance of CP film is changed with an appearance of new bands due to the formation of polarons and bipolarons [165]. Thus, the interaction of gas analytes at CP film interfaces can be detected by the change in spectra of UV–vis or NIR. When an ultrathin film of CP was deposited on a glass, an optic sensor can be fabricated to record the corresponding spectrum (absorbance or transmittance) by using conventional spectrometers [166]. However, colorimetry is limited in sensitivity to an individual analyte and not useful for in situ applications [167]. For IR sensors, they can only monitor specific analytes of nonlinear molecules; in addition, the measurements are influenced by humidified environment [167]. So far, UV–vis–NIR spectrophotometer has been used to study the sensing characteristics of PANI to a variety of VOCs [168]. Tavoli and Alizadeh designed an optical NH_3 gas sensor based on nanostructure PPY doped with eriochrome cyanine R (ECR) thin film as a dopant for optical selectivity of NH_3 gas using UV–vis spectroscopy with a fast response time (50 s) and a high sensitivity in the concentration range of 15–260 μg L^{-1} [169]. The sensor showed a low detection limit of 5 μg L^{-1} and a good reproducibility.

3.3.2 Fiber-optic devices

Fiber-optic sensors are a class of optical sensors that use optical fibers to detect chemical analytes. Light is generated by a light source and is sent through an optical fiber, then reflects the absorption property of the CP surface when it returns through the optical fiber, and finally is captured by a photo detector [170]. Sensors based on fiber optics used the light guiding properties of the optical fibers to carry the light into and from the CP active layer [171]. However, this type of optical sensor has some drawback concerning the complication of associated electronics and software, cost-effectiveness, concentration limitation, short lifetime due to photobleaching, and limited ability to transmit light through optical fiber over long distances [167, 172]. A fiber-optic device based on PANI was used to detect HCl, NH_3, hydrazine (H_4N_2), and dimethyl methylphosphonate (DMMP, a nerve agent, sarin stimulant) [173]. Muthusamy and coworkers developed gas sensors

based on PPY and PPY/Prussian blue (PPY-PB) nanocomposite coating on fiber optic to monitor NH_3, acetone, and ethanol gases at room temperature [174]. The PPY-PB nanocomposite-based fiber-optic sensor exhibited an enhanced sensitivity for ethanol than pure PPY nanoparticles, and spectral intensity increases linearly with increasing the concentrations of gas. Very recently, Mohammed et al. fabricated an etched-tapered single-mode fiber (SMF) coated with a high surface area PANI/graphite nanofiber (GNF) nanocomposite as optical sensor for NH_3 gas at room temperature in the visible wavelength range [175]. The sensor exhibited a good response time, sensitivity, and reproducibility for NH_3, compared with pure PANI-coated SMF. Furthermore, an optical microfiber sensor was designed by drop coating of PANI doped with dioctyl sodium sulfosuccinate onto a microfiber resonator as a sensor for alcohols [176]. The sensor output spectrum showed red shift in wavelength upon response to various alcohols at different concentrations, due to the increase in dihedral angle and average band gap (lower energy) of PANI fiber. In a recent study by Kim and coworkers reported the application of fiber-optic reflectance sensors (FORS) coated with PPY film for sensing VOCs up to 1 ppm under atmospheric conditions [177]. The variation in the reflected light intensity was caused by the formation of polaron-bipolaron and film swelling when interacted with VOCs.

3.3.3 Surface plasmon resonance (SPR)

Surface plasmon resonance is another class of optical sensors which referred to excitation of surface plasmon-based optical sensor for chemical sensing utilizing light. SPR optical sensor is a thin film refractometer sensing device which measures the changes in refractive index that occurred at the surface of a plasmon-supported metal film. On excitation by the monochromatic light, a change in the refractive index of a dielectric material gives rise to a change in propagation constant of the surface plasmon (prism coupled, i.e., attenuated total reflectance (ATR), waveguide coupled, and grating coupled) [178, 179]. The propagation constant of a radiation alters the characteristics of light wave coupled to the surface plasmon, e.g., coupling angle, coupling wavelength, and intensity phase [180]. After exposing to analytes, the minimum in the reflectance curve can be shifted, indicating the presence of analyte. The sensitivity of this type of sensors is high, but the detecting procedures are complicated. A SPR device was explored by Agbor and coworkers using PANI thin films to detect NO_2 and H_2S gases, resulting in an increase in reflectivity and resonance angle [180].

3.4 Mass-sensitive device sensors

Mass-sensitive devices transform the mass change at a specially modified surface into a change of a property of the piezoelectric material. Surface acoustic wave (SAW) and the quartz crystal microbalance (QCM) techniques are the main categories of piezoelectric gas sensing devices [181]. SAW and QCM are the simplest piezoelectric devices with a selective coating deposited on the surface to serve as an adsorptive surface capable of measuring an extremely small mass change at room temperatures [182]. Interestingly, SAW and QCM sensors are very promising and are widely accepted as smart transducers for their miniaturized design, possibility of wireless integration, high thermal stability, inertness, and room temperature operation. In addition, they can be easily combined with a variety of recognition sensitive layers for sensing applications ranging from small gas molecules to large biomolecules or even whole cell structures.

3.4.1 Surface acoustic wave

Surface acoustic wave resonators represent one of the most prominent acoustic devices for their exceptionally high frequency from several hundred MHz to GHz, which can record remarkably diminutive frequency shifts resulting from exceptionally small mass loadings making them potentially suitable in mass sensing applications [183]. Clearly, SAW resonator is a sensitive layer coated on the gap between a transmitter (an input) and a receptor (an output) interdigital transducers (IDTs) coating on the top of the piezoelectric crystal to design a SAW gas sensor [184]. An input radio-frequency voltage is applied across the transmitter IDTs, inducing deformations in the piezoelectric crystal that give rise to an acoustic wave, traversing the gap between two IDTs. When it reaches the receptor IDTs, the mechanical energy was converted back to radio-frequency voltage. The adsorption/desorption of gas on the CP film on the gap modulates the wave propagation characters, and a frequency shift can be recorded between the input and output voltages. In the sense of applications, a SAW sensor based on fibrous PANI nanocomposites layers prepared by chemical oxidative polymerization of aniline in the presence of finely divided metal oxides deposited on ZnO/64° YX $LiNbO_3$ SAW transducer to detect H_2, NO_2, NO, CO_2 and CO gases [185–188]. The designed SAW sensor exhibited improved sensitivity and repeatability of the gas molecules in ppm level at room temperature. Attractive studies utilized PPY nanocomposite-based SAW gas sensors deposited onto 128° YX-$LiNbO_3$ substrate via Langmuir-Blodgett (LB) method due to high sensitivity and low cost. The LB PPY nanocomposite-based SAW exhibited excellent selectivity toward low NH_3 concentration of 20 ppm, with respect to other interfering gases, such as CO, CH_4, H_2, and O_2, at room ambient temperature [189–191]. By merging with electrical conductivity gas response, the sensing mechanism for gas detection has been investigated as elastic loading. Very recently, SAW integrated with PPY and PPY/TiO_2 films has been utilized for NO_2 and H_2S detection at room temperature by the self-assembly method [192]. Upon exposure to NO_2, the SAW sensors coated with PPY film showed a negative frequency shift (ΔF) tendency, in contrast to PPY/TiO_2 that exhibited a faster sensor response and a higher sensitivity. Besides, the selectivity was greatly improved by addition of TiO_2 to PPY.

3.4.2 Quartz crystal microbalance

The advantage of conceptual simplicity, relative ease of modification, chemical inertness of the substrates, ruggedness, low cost, and ready availability of piezoelectric transducers have encouraged the development of QCM technique in various sensor applications. In addition, the sensitivity of piezoelectric transducers is based on the mass per unit area, suggesting miniaturization without losses in their sensitivity. The associated electronics are fairly simple, and frequency measurements are very precise (<1 part in 10^7) [193]. As illustrated in **Figure 5**, a QCM sensor consists of a quartz disk coated with metal electrodes on both sides (usually Pt or Au). When a voltage is applied to the quartz crystal plate, it can oscillate at a specific frequency, and the relation between frequency change (ΔF) of the oscillating crystal and the mass change (Δm) on the quartz surface was described by Sauerbrey empirical derivation (Eq. (6)) [195]. The change of ΔF (Hz) in the area of the electrode (A cm^{-2}) in terms of the mass increment, Δm (g cm^{-2}), loaded onto the crystal surface under a fundamental resonant frequency F_0 can be estimated from Eq. (1), where N, F_0, ρ, μ, and A are the harmonic overtone, the fundamental resonance frequency, the crystal density (2.649 g cm^{-3}), the elastic modulus of the quartz crystal (2.947×10^{11} g cm^{-1} s^{-2}), and the surface area, respectively.

$$\Delta F = \frac{2NF_0^2}{\sqrt{\rho\mu}}\frac{\Delta m}{A} \tag{6}$$

During the past few decades, the relationship between frequency shift and mass change, which was initially described by Sauerbrey, has been extensively applied for chemical sensing [182]. The ΔF, which is proportional to a mass adsorbed and/or sorbed on sensitive layers of distinct morphologies coated over the QCM electrode, is constantly monitored to identify and quantify the target analyte at the ng level (ng cm^{-2}) [182].

The interaction between target molecules and sensitive coating layers (known as "guest-host interaction") plays an important role in the sensing mechanism. Such a guest-host interaction is considered as an adsorption process involving enrichment of guest species at the interface of a certain adsorbent, such as CP nanomaterials (**Figure 5**). In terms of high sensitivity and selectivity, the fabrication of CP nanomaterials is an important step toward the development of efficient advanced detection sensors. Since 1964, a QCM sensor had been implemented by King into a gas chromatography system for the detection of hydrocarbons [196]. Then after, QCM sensor device has been successfully applied as a sensitive tool to sense mass interfacial [197] and polymer film properties [198–201]. Accordingly, ΔF was investigated in terms of rigid mass changes, based on the Sauerbrey equation. The QCM technique has been used in the fields of gas sensing application including gas mixture analysis [202], discrimination of aromatic optical isomers [203], and VOC vapors detection [204, 205]. In the early trials, Gomes et al. [206] have used uncoated quartz crystals with gold electrodes to detect and quantify volatile amines, such as *iso*-propylamine, *n*-butylamine, *s*-butylamine, and *tert*-butylamine; however this method suffers from low sensitivity. Attention has been paid to the development of efficient QCM sensors which rely greatly on the utilization of CPs as sensitive coatings. Thin film-coated QCM sensors were pioneered by Ayad et al. [207–212]. For example, a QCM technique concomitant with sensitive layers of CPs, PANI in the form of ES, and EB prepared by the in situ chemical oxidative polymerization was explored to detect and quantify varieties of VOCs in air, such as chlorinated aliphatic hydrocarbons, like CCl_4, $CHCl_3$, CH_2Cl_2, and $ClCH_2$-CH_2Cl; aliphatic alcohols, like CH_3OH, C_2H_5OH, C_3H_7OH, and C_4H_9OH; and aliphatic amines including CH_3NH_2, $(CH_3)NH$, $(CH_3)_3N$, and $(CH_3CH_2)_3N$ [213–217]. The adsorption mechanism was discussed as a kind hydrogen bonding or a dipole/dipole interaction formed between the imine and amine sites of PANI with chemical vapor. The difference in adsorption affinity was attributed to the differences in their chemical structure and strength of the electrostatic interactions. Interestingly, the PANI adsorption kinetics (Eq. (7)) [217] and diffusion of chemical vapor were carefully discussed, in terms of diffusion coefficient (D) using Fick's second equation (Eq. (8)), which has been reviewed by Crank [218].

$$\frac{\Delta F_t}{\Delta F_\infty} = 1 - e^{-kt} \tag{7}$$

$$\frac{\Delta F_t}{\Delta F_\infty} = 4\sqrt{\frac{D}{\pi}}\frac{t^{1/2}}{L} \tag{8}$$

$$\Delta F_t = F_{polymer} - F_t \; and \; \Delta F_\infty = F_{polymer} - F_\infty \tag{9}$$

where k is the pseudo-first-order rate constant for vapor uptake. ΔF_t and ΔF_∞ (Hz) are the frequency changes due to the adsorption uptake of the vapor into the polymer film at any time t and at the steady-state, respectively. $F_{polymer}$ is the

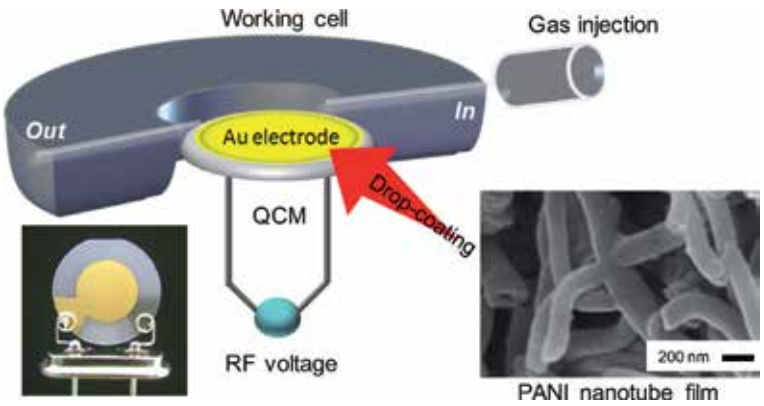

Figure 5.
Schematic representation of the interaction of an analyte with PANI nanotube prepared with CSA coating on a QCM (modified and adapted with permission from Ref. [194]. Copyright 2014, Wiley-VCH Verlag GmbH &Co. KGaA, Weinheim).

frequency of the polymer film estimated from QCM. L (cm) is the film thickness and can be determined by the density of the polymer and mass change, and Δm (g cm^{-2}) is from the Sauerbrey equation (Eq. (4)). The k and D can be calculated from the slope of linear graphs of $\ln(1 - \Delta F_t/\Delta F_\infty)$ against t and $\Delta F_t/\Delta F_\infty$ as a function of $t^{1/2}/L$, respectively.

Li et al. constructed a sensor using water-soluble PANI and PANI-TiO_2 nanocomposite-coated QCM for a selective detection of amine vapors [219, 220]. The nanocomposite exhibited a higher sensing affinity and good selectivity toward $(CH_3)_3N$ and $(CH_3CH_2)_3N$ than other VOCs, such as C_2H_5OH, CH_3-COO-CH_2-CH_3, CH_2O, and CH_3CHO. As the van der Waals absorption is the main interaction between PANI and amine, the sensor responses could be completely recovered after purging N_2 at room temperature. Further, PANI/ES films doped with several dopants, such as HCl and DBSA, and 1,5-naphtalenedisulfonic acid (1,5-NDSA))-coated QCM sensor films have been fabricated to detect BTEX vapors [221]. The ΔF due to adsorption of VOCs is attributed to electrostatic interactions between vapor molecules and dopant in PANI/ES films. Interestingly, PANI-DBSA films were found to be highly sensitive and selective to *p*-xylene compared with toluene and benzene. Further, the adsorption behavior of poly(3-butoxythiophene) (P3BOT) mixed with stearic acid (SA) LB film-coated QCM was studied as a sensing material for series of chemical vapor analytes, such as chlorinated aliphatic hydrocarbons and some short-chain aliphatic alcohols [222]. On exposure to vapor analyte, the frequency of the QCM was changed, due to the dipole/dipole or hydrogen bonding interaction with P3BOT/SA film. Additionally, a control of sensitivity and selectivity of the sensor could be achieved through polymer functionalization with ether group, difference in molecular weight, and structure of the chemical vapors.

Gas sensing properties of the CPs have dramatically improved after incorporation of other nanomaterials such as CNTs, GO, metals, and other nanometal oxides. Very recently, Wang et al. fabricated a gas sensor by using PPY and PPY/TiO_2 coating on QCM electrode for detecting different chemical vapors [223]. As a result, the sensor coated with PPY/TiO_2 was found to exhibit a better sensing performance, long-term stability, and excellent reversibility, as well as acceptable selectivity toward NH_3 in comparison to $(CH_3)_3N$, H_2S, and C_2H_5OH. Based on QCM measurements, researchers could fabricate a PPY/TiO_2 sensor for evaluating shelf-life quality changes of three typical foodstuffs (mango, egg, and fish) during 1-week storage.

Novel low-humidity sensors were investigated by the in situ photopolymerization of PPY/Ag/TiO_2 nanoparticle composite thin film coating on QCM [224]. Room temperature highly sensitive sensors with short response/recovery time for humidity based on GO/SnO_2/PANI and PANI-GO coating on QCM were explored by Zhang et al. [225, 226]. The adsorption process of water molecules on QCM senor was carefully discussed using Langmuir adsorption isotherm model.

3.5 Summary and perspectives

With the development of nanotechnology, CP nanostructures integrated into advanced electronics have pursuit of better sensing systems during the past decade for fabricating miniaturizing state-of-the-art sensor devices, due to their continuously discovered unique chemical and physical characteristics, such as reversible signal transduction processes, low operating temperature, tunable sensitivity, and design flexibility. However, sensing technologies based on CPs still require significant incubation and device development. From the viewpoint of sensing activity, control over CP characteristics is necessary to improve sensitivity, selectivity, and stability to design advanced detection sensors. The desired set of physicochemical properties can be introduced into the CPs through the rational molecular design of specific receptors or judicious functionalization of the CP surface with a molecular recognition, leading to enhanced specificity via covalent attachments and reproducibility in response. Also, for large-scale synthesis, it is important to develop reliable routes to synthesize CP nanostructures and nanocomposites with controlled morphology. Of the exciting synthetic methods, the soft template approach is somewhat advantageous in both large-scale synthesis and size/shape control. Such improvements in their molecular structure and crystallinity and an increase in conjugation length are crucial for increasing room temperature conductivity. Another concern is that CPs are also susceptible to environmental perturbations such as moisture, heat, and light, which may degrade over time, even in dry, oxygen-free environments, and thus much attention must be paid to improving their long-term stability that is considered to be an important factor in pursuing high sensor reliability for an ever-increasing role in online environmental monitoring, industrial safety control, and security. Since the fabrication of nanostructured CPs, response time and sensitivity have experienced impressive improvements with great advances in sensor nanotechnology. However, selectivity is still a challenging task for detecting specific target analyte in a multi-analyte environment which hindered the widespread application of CP-based sensors. Besides, the demand for miniaturization has encouraged for designing portable sensor devices, lower power dissipation, and better device integration. In this sense, nanostructured CPs have considerable potential for fabricating miniaturized multi-sensing arrays by using microcontact printing, surface-directed assembly, site-specific polymerization, inkjet printing, etc. Interestingly, CPs are highly compatible with a flexible substrate, which opens up the possibility of realizing all-polymer electronics. From viewpoint, we believe that nanostructured CPs still have many unexplored potentials and will definitely play an expanding role in future sensor technology for exclusively designing of next-generation sensors involving high sensitivity, high reliability, multi-analyte determination, miniaturization, and structural flexibility due to their fascinating chemical/physical properties that are not available in other materials. Thus, it is anticipated that extensive future research studies into the development of flexible high-performance sensors by utilizing CPs will be expected in the near future.

DOI: http://dx.doi.org/10.5772/intechopen.89888

Author details

Nagy L. Torad[1] and Mohamad M. Ayad[1,2]*

1 Chemistry Department, Faculty of Science, University of Tanta, Tanta, Egypt

2 Institute of Basic and Applied Sciences, Egypt-Japan University of Science and Technology (E-JUST), New Borg El-Arab City, Alexandria, Egypt

*Address all correspondence to: mohamad.ayad@ejust.edu.eg and mohamed.ayad@science.tanta.edu.eg

IntechOpen

© 2019 The Author(s). Licensee IntechOpen. This chapter is distributed under the terms of the Creative Commons Attribution License (http://creativecommons.org/licenses/by/3.0), which permits unrestricted use, distribution, and reproduction in any medium, provided the original work is properly cited.

References

[1] Shirakawa H, Louis EJ, MacDiarmid AG, Chiang CK, Heeger AJ. Synthesis of electrically conducting organic polymers: Halogen derivatives of polyacetylene, (CH)x. Journal of the Chemical Society, Chemical Communications. 1977:579-580

[2] Chiang CK, Fischer CR, Park YW, Heeger AJ, Shirakawa H, Louis EJ, et al. Electrical conductivity in doped polyacetylene. Physical Review Letters. 1977;**39**:1098-1101

[3] Chiang CK, Druy MA, Gau SC, Heeger AJ, Louis EJ, MacDiarmid AG, et al. Synthesis of highly conducting films of derivatives of polyacetylene, (CH)x. American Chemical Society. 1987;**100**:1013-1015

[4] DelamarM,LacazePC,DumousseauJS, Dubois JE. Electrochemical oxidation of benzene and biphenyl in liquid sulfur dioxide: Formation of conductive deposits. Electrochimica Acta. 1982;**27**:61-65

[5] Diaz AF, Kanazawa KK, Gardini GP. Electrochemical polymerization of pyrrole. Journal of the Chemical Society, Chemical Communications. 1979:635-636

[6] Waltman RJ, Bargon J, Diaz AF. Electrochemical studies of some conducting polythiophene films. The Journal of Physical Chemistry. 1983;**87**:1459-1463

[7] Diaz AF, Logan JA. Electroactive polyaniline films. Journal of Electroanalytical Chemistry. 1980;**111**:111-114

[8] MacDiarmid AG. Synthetic metals: A novel role for organic polymers. Synthetic Metals. 2001;**125**:11-22

[9] Ibanez JG, Rinćon ME, Gutierrez-Granados S, Chahma M, Jaramillo-Quintero OA, Frontana-Uribe BA. Conducting polymers in the fields of energy, environmental remediation, and chemical-chiral sensors. Chemical Reviews. 2018;**118**:4731-4816

[10] Jang J. Conducting polymer nanomaterials and their applications. Advances in Polymer Science. 2006;**199**:189-260

[11] Yoon H, Jang J. Conducting-polymer nanomaterials for high performance sensor applications: Issues and challenges. Advanced Functional Materials. 2009;**19**:1567-1576

[12] Janata J, Josowicz M. Conducting polymers in electronic chemical sensors. Nature Materials. 2003;**2**:19

[13] Li C, Bai H, Shi G. Conducting polymer nanomaterials: Electrosynthesis and applications. Chemical Society Reviews. 2009;**38**:2397-2409

[14] Kwon OS, Song HS, Park TH, Jang J. Conducting nanomaterial sensor using natural receptors. Chemical Reviews. 2019;**119**:36-93

[15] Li D, Huang J, Kaner RB. Polyaniline nanofibers: A unique polymer nanostructure for versatile applications. Accounts of Chemical Research. 2008;**42**:135-145

[16] Kaushik A, Kumar R, Arya SK, Nair M, Malhotra BD, Bhansali S. Organic-inorganic hybrid nanocomposite-based gas sensors for environmental monitoring. Chemical Reviews. 2015;**115**:4571-4606

[17] Hatchett DW, Josowicz M. Composites of intrinsically conducting polymers as sensing Nanomaterials. Chemical Reviews. 2008;**108**:746-769

[18] Ćiric-Marjanović G. Recent advances in polyaniline research:

Polymerization mechanisms, structural aspects, properties and applications. Synthetic Metals. 2013;**177**:1-47

[19] Ayad MM, Zaki EA. Synthesis and characterization of polyaniline films using Fenton reagent. Journal of Applied Polymer Science. 2008;**110**:3410-3419

[20] Xia Y, Wiesinger J, MacDiarmid AG, Epstein AJ. Camphorsulfonic acid fully doped polyaniline emeraldine salt: Conformations in different solvents studied by an ultraviolet/visible/near-infrared spectroscopic method. Chemistry of Materials. 1995;**7**:443-445

[21] Baker CO, Huang X, Nelson W, Kaner RB. Polyaniline nanofibers: Broadening applications for conducting polymers. Chemical Society Reviews. 2017;**46**:1510-1525

[22] Sen T, Mishra S, Shimpi NG. Synthesis and sensing applications of polyaniline nanocomposites: A review. RSC Advances. 2016;**6**:42196-42222

[23] Ayad MM, Amer WA, Zaghlol S, Minisy IM, Bober P, Stejskal J. Polypyrrole-coated cotton textile as adsorbent of methylene blue dye. Chemical Papers. 2018;**72**:1605-1618

[24] Ayad MM, Amer WA, Zaghlol S, Maráková N, Stejskal J. Polypyrrole-coated cotton fabric decorated with silver nanoparticles for the catalytic removal of *p*-nitrophenol from water. Cellulose. 2018;**25**:7393-7407

[25] Ayad MM, Zaghlol S. Nanostructured crosslinked polyaniline with high surface area: Synthesis, characterization and adsorption for organic dye. Chemical Engineering Journal. 2012;**204-206**:79-86

[26] Stejskal J, Sapurina I, Trchova M. Polyaniline nanostructures and the role of aniline oligomers in their formation. Progress in Polymer Science. 2010;**35**:1420-1481

[27] Ayad MM, Salahuddin NA, Fayed A, Bastakoti BP, Suzuki N, Yamauchi Y. Chemical design of a smart chitosan-polypyrrole-magnetite nanocomposite toward efficient water treatment. Physical Chemistry Chemical Physics. 2014;**16**:21812-21819

[28] Ayda MM, Amer WA, Kotp MG, Minisy IM, Rehaba AF, Kopecký D, et al. Synthesis of silver-anchored polyaniline–chitosan magnetic nanocomposite: A smart system for catalysis. RSC Advances. 2017;**7**:18553-18560

[29] Ayad MM, Amer WA, Kotp MG. Magnetic polyaniline-chitosan nanocomposite decorated with palladium nanoparticles for enhanced catalytic reduction of 4-nitrophenol. Molecular Catalysis. 2017;**439**:72-80

[30] Minisy IM, Salahuddin NA, Ayad MM. Chitosan/polyaniline hybrid for the removal of cationic and anionic dyes from aqueous solutions. Journal of Applied Polymer Science. 2019;**136**:47056. DOI: 10.1002/APP.47056

[31] Amer WA, Al-saida B, Ayad MM. Rational design of a polypyrrole-based competent bifunctional magnetic nanocatalyst. RSC Advances. 2019;**9**:18245-18255

[32] Virji S, Huang J, Kaner RB, Weiller BH. Polyaniline nanofiber gas sensors: Examination of response mechanisms. Nano Letters. 2004;**4**:491-496

[33] Zhang L, Wan M. Self-assembly of polyaniline-from nanotubes to hollow microspheres. Advanced Functional Materials. 2003;**13**:815-820

[34] Trchová M, Šeděnková I, Konyushenko EN, Stejskal J, Holler P,

Ćirić-Marjanović G. Evolution of polyaniline nanotubes: The oxidation of aniline in water. The Journal of Physical Chemistry. B. 2006;**110**:9461-9468

[35] Janošević A, Ćirić-Marjanović G, Marjanović B, Holler P, Trchová M, Stejskal J. Synthesis and characterization of conducting′ polyaniline 5-sulfosalicylate nanotubes. Nanotechnology. 2008;**19**:135606

[36] Ćiric-Marjanović G, Trchová M, Stejskal J. The chemical oxidative polymerization of aniline in water: Raman spectroscopy. Journal of Raman Specroscopy. 2008;**39**:1375-1387

[37] Ayad MM, Prastomo N, Matsuda A. Synthesis and characterization of polyaniline-camphorsulphonic acid nanotube film. Materials Letters. 2010;**64**:379-382

[38] Ayad MM, Prastomo N, Matsuda A, Stejskal J. Sensing of silver ions by nanotubular polyaniline film deposited on quartz-crystal in a microbalance. Synthetic Metals. 2010;**160**:42-46

[39] Prastomo N, Ayad MM, Kawamura G, Matsuda A. Synthesis and characterization of polyaniline nanofiber/TiO_2 nanoparticles hybrids. Journal of the Ceramic Society of Japan. 2011;**119**:342-345

[40] Wang G, Morrin A, Li M, Liu N, Luo X. Nanomaterial-doped conducting polymers for electrochemical sensors and biosensors. Journal of Materials Chemistry B. 2018;**6**:4173-4190

[41] Moozarm P, Woi N, Meng P, Alias Y. Hydrogen peroxide sensor: Uniformly decorated silver nanoparticles on polypyrrole for wide detection range. Applied Surface Science. 2015;**357**:1565-1572

[42] Ghanbari K. Fabrication of silver nanoparticles-polypyrrole composite modified electrode for electrocatalytic oxidation of hydrazine. Synthetic Metals. 2014;**195**:234-240

[43] Yoon H. Current trends in sensors based on conducting polymer nanomaterials. Nanomaterials. 2013;**3**:524-549

[44] Jackowska K, Biegunski AT, Tagowska M. Hard template synthesis of conducting polymers: A route to achieve nanostructures. Journal of Solid State Electrochemistry. 2008;**12**:437-443

[45] Zhang F, Nyberg T, Inganas O. Conducting polymer nanowires and nanodots made with soft lithography. Nano Letters. 2002;**2**:1373-1377

[46] Wu Q-F, He K-X, Mi H-Y, Zhang X-G. Electrochemical capacitance of polypyrrole nanowire prepared by using cetyltrimethylammonium bromide (CTAB) as soft template. Materials Chemistry and Physics. 2007;**101**:367-371

[47] Huang J, Kaner RB. Nanofiber formation in the chemical polymerization of aniline: A mechanistic study. Angewandte Chemie. 2004;**116**:5941-5945

[48] Jang J, Oh JH, Stucky GD. Fabrication of ultrafine conducting polymer and graphite nanoparticles. Angewandte Chemie, International Edition. 2002;**41**:4016-4019

[49] Martin J, Maiz J, Sacristan J, Mijangos C. Tailored polymer-based nanorods and nanotubes by "template synthesis": From preparation to applications. Polymer. 2012;**53**:1149-1166

[50] Zhang F, Liu X, Pan C, Zhu J. Nano-porous anodic aluminium oxide membranes with 6-19 nm pore diameters formed by a low-potential anodizing process. Nanotechnology. 2007;**18**:345302

[51] Xiong S, Wang Q, Xia H. Preparation of polyaniline nanotubes array based on anodic aluminum oxide template. Materials Research Bulletin. 2004;**39**:1569-1580

[52] Jang J, Ko S, Kim Y. Advanced Functional Materials. 2006;**16**:754-759

[53] Jang J, Oh J. A facile synthesis of polypyrrole nanotubes using a template mediated vapor deposition polymerization and the conversion to carbon nanotubes. Chemical Communications. 2004:882-883

[54] Park E, Kwon OS, Park SJ, Lee JS, You S, Jang J. One-pot synthesis of silver nanoparticles decorated poly (3, 4-ethylenedioxythiophene) nanotubes for chemical sensor application. Journal of Materials Chemistry. 2012;**22**:1521-1526

[55] Greiner A, Wendorff JH. Electrospinning: A fascinating method for the preparation of ultrathin fibres. Angewandte Chemie, International Edition. 2007;**46**:5670-5703

[56] Kwon OS, Park SJ, Park HW, Kim T, Kang M, Jang J, et al. Kinetically controlled formation of multidimensional poly (3,4-ethylenedioxythiophene) nanostructures in vapor-deposition polymerization. Chemistry of Materials. 2012;**24**:4088-4092

[57] Guo Y, Tang Q, Liu H, Zhang Y, Li Y, Hu W, et al. Light-controlled organic/inorganic P-N junction nanowires. Journal of the American Chemical Society. 2008;**130**:9198-9199

[58] Gence L, Faniel S, Gustin C, Melinte S, Bayot V, Callegari V, et al. Structural and electrical characterization of hybrid metal-polypyrrole nanowires. Physical Review B: Condensed Matter and Materials Physics. 2007;**76**:115415

[59] Liu R, Lee SB. MnO_2/poly(3,4-ethylenedioxythiophene) coaxial nanowires by one-step coelectrodeposition for electrochemical energy storage. Journal of the American Chemical Society. 2008;**130**:2942-2943

[60] Salabat A, Mirhoseini F, Arjomandzadegan M, Jiryaei E. A novel methodology for fabrication of Ag-polypyrrole core-shell nanosphere using microemulsion system and evaluation of its antibacterial application. New Journal of Chemistry. 2017;**41**:12892-12900

[61] Huang L, Wang Z, Wang H, Cheng X, Mitra A, Yan Y. Polyaniline nanowires by electropolymerization from liquid crystalline phases. Journal of Materials Chemistry. 2002;**12**:388-391

[62] Choi SJ, Park SM. Electrochemical growth of nanosized conducting polymer wires on gold using molecular templates. Advanced Materials. 2000;**12**:1547-1549

[63] Yoon H, Chang M, Jang J. Formation of 1D poly(3,4-ethylenedioxythiophene) nanomaterials in reverse microemulsions and their application to chemical sensors. Advanced Functional Materials. 2007;**17**:431-436

[64] Jang J, Yoon H. Multigram-scale fabrication of monodisperse conducting polymer and magnetic carbon nanoparticles. Small. 2005;**1**:1195-1199

[65] Jang J, Yoon H. Facile fabrication of polypyrrole nanotubes using reverse microemulsion polymerization. Chemical Communications. 2003:720-721

[66] Jang J, Yoon H. Formation mechanism of conducting polypyrrole nanotubes in reverse micelle systems. Langmuir. 2005;**21**:11484-11489

[67] Hong JY, Yoon H, Jang J. Kinetic study of the formation of polypyrrole

nanoparticles in water-soluble polymer/metal cation systems: A light-scattering analysis. Small. 2010;**6**:679-686

[68] Zhong WB, Deng JY, Yang YS, Yang WT. Synthesis of large-area three-dimensional polyaniline nanowire networks using a "soft template". Macromolecular Rapid Communications. 2005;**26**:395-400

[69] Liu Z, Zhang XY, Poyraz S, Surwade SP, Manohar SK. Oxidative template for conducting polymer nanoclips. Journal of the American Chemical Society. 2010;**132**:13158-13159

[70] Zhao B, Nan Z. Formation of self-assembled nanofiber-like Ag@ PPy core/shell structures induced by SDBS. Materials Science and Engineering C. 2012;**32**:1971-1975

[71] Li Y, Bober P, Trchová M, Stejskal J. Polypyrrole prepared in the presence of methyl orange and ethyl orange: Nanotubes versus globules in conductivity enhancement. Journal of Materials Chemistry C. 2017;**5**:4236-4245

[72] Bober P, Stejskal J, Šeděnková I, Trchová M, Martinková L, Marek J. The deposition of globular polypyrrole and polypyrrole nanotubes on cotton textile. Applied Surface Science. 2015;**356**:737-741

[73] Kopecká J, Kopecký D, Vrňata M, Fitl P, Stejskal J, Trchová M, et al. Polypyrrole nanotubes: Mechanism of formation. RSC Advances. 2014;**4**:1551-1558

[74] Varga M, Kopecká J, Morávková Z, Křivka I, Trchová M, Stejskal J, et al. Effect of oxidant on electronic transport in polypyrrole nanotubes synthesized in the presence of methyl orange. Journal of Polymer Science Part B: Polymer Physics. 2015;**53**:1147-1159

[75] Škodová J, Kopecký D, Vrňata M, Varga M, Prokeš J, Cieslar M, et al. Polypyrrole-silver composites prepared by the reduction of silver ions with polypyrrole nanotubes. Polymer Chemistry. 2013;**4**:3610-3616

[76] Stejskal J, Trchová M, Bober P, Morávková Z, Kopecký D, Vrňata M, et al. Polypyrrole salts and bases: Superior conductivity of nanotubes and their stability towards the loss of conductivity by deprotonation. RSC Advances. 2016;**6**:88382-88391

[77] Humpolíček P, Radaszkiewicz KA, Capáková Z, Pacherník J, Bober P, Kašpárková V, et al. Polyaniline cryogels: Biocompatibility of novel conducting macroporous material. Scientific Reports. 2018;**8**:135. DOI: 10.1038/s41598-017-18290-1

[78] Li Y, Bober P, Apaydin DH, Syrový T, Saricifci NS, Hromádková J, et al. Colloids of polypyrrole nanotubes/nanorods: A promising conducting ink. Synthetic Metals. 2016;**221**:67-74

[79] Dai T, Lu Y. Water-soluble methyl orange fibrils as versatile templates for the fabrication of Conducting polymer microtubules. Macromolecular Rapid Communications. 2007;**28**:629-633

[80] Stejskal J, Sapurina I, Trchová M, Konyushenko EN, Holler P. The genesis of polyaniline nanotubes. Polymer. 2006;**47**:8253-8262

[81] Upadhyay J, Kumar A. Structural, thermal and dielectric studies of polypyrrole nanotubes synthesized by reactive self-degrade template method. Materials Science and Engineering B. 2013;**178**:982-989

[82] Upadhyay J, Kumar A. Investigation of structural, thermal and dielectric properties of polypyrrole nanotubes tailoring with silver nanoparticles.

Composites Science and Technology. 2014;**97**:55-62

[83] Zhang Q, Liu F, Li L, Pan G, Shang S. Magnetic ionic liquid-assisted synthesis of polyaniline/AgCl nanocomposites by interface polymerization. Journal of Nanoparticle Research. 2011;**13**:415-421

[84] Oliveira LVF, Camilo FF. Facile synthesis of silver-polypyrrole nanocomposites: Use of ionic liquid as solvent and template. Synthetic Metals. 2019;**247**:219-227

[85] Lee KJ, Min SH, Oh H, Jang J. Fabrication of polymer nanotubes containing nanoparticles and inside functionalization. Chemical Communications. 2011;**47**:9447-9449

[86] Huang J, Virji S, Weiller BH, Kaner RB. Polyaniline nanofibers: Facile synthesis and chemical sensors. Journal of the American Chemical Society. 2003;**125**:314-315

[87] Tran HD, D'Arcy JM, Wang Y, Beltramo PJ, Strong VA, Kaner RB. The oxidation of aniline to produce "polyaniline": A process yielding many different nanoscale structures. Journal of Materials Chemistry. 2011;**21**:3534-3550

[88] Ding H, Shen J, Wan M, Chen Z. Formation mechanism of polyaniline nanotubes by a simplified template-free method. Macromolecular Chemistry and Physics. 2008;**209**:864-871

[89] Martin CR. Nanomaterials: A membrane-based synthetic approach. Science. 1994;**266**:1961-1966

[90] Wan M. A template-free method towards conducting polymer nanostructures. Advanced Materials. 2008;**20**:2926-2932

[91] Wan M, Huang J, Shen Y. Microtubes of conducting polymers. Synthetic Metals. 1999;**101**:708-711

[92] Tang Q, Wu J, Sun X, Li Q, Lin J. Shape and size control of oriented polyaniline microstructure by a self-assembly method. Langmuir. 2009;**25**:5253-5257

[93] Liu H, Kameoka J, Czaplewski DA, Craighead H. Polymeric nanowire chemical sensor. Nano Letters. 2004;**4**:671-675

[94] Du JM, Zhang JL, Han BX, Liu ZM, Wan MX. Polyaniline microtubes synthesized via supercritical CO_2 and aqueous interfacial polymerization. Synthetic Metals. 2005;**155**:523-526

[95] Wan MX. Some issues related to polyaniline micro−/nanostructures. Macromolecular Rapid Communications. 2009;**30**:963-975

[96] Zhang LJ, Wan MX. Chiral polyaniline nanotubes synthesized via a self-assembly process. Thin Solid Films. 2005;**477**:24-31

[97] Wang J, Chan S, Carlson RR, Luo Y, Ge GL, Ries RS, et al. Electrochemically fabricated polyaniline nanoframework electrode junctions that function as resistive sensors. Nano Letters. 2004;**4**:1693-1697

[98] Alam MM, Wang J, Guo YY, Lee SP, Tseng HR. Electrolyte-gated transistors based on conducting polymer nanowire junction arrays. The Journal of Physical Chemistry. B. 2005;**109**:12777-12784

[99] Chang M, Kim T, Park HW, Kang M, Reichmanis E, Yoon H. Imparting chemical stability in nanoparticulate silver via a conjugated polymer casing approach. ACS Applied Materials & Interfaces. 2012;**4**:4357-4365

[100] Adam H, Stanisław G, Folke I. Chemical sensors definitions and classification. Pure and Applied Chemistry. 1991;**63**:1274-1250

[101] Tierney MJ, Kim HOL. Electrochemical gas sensor with extremely fast response times. Analytical Chemistry. 1993;**65**:3435-3440

[102] Stetter JR, Li J. Amperometric gas sensors–A review. Chemical Reviews. 2008;**108**:352-366

[103] Rahman MA, Kumar P, Park D-S, Shim Y-B. Electrochemical sensors based on organic conjugated polymers. Sensors. 2008;**8**:118-141

[104] Do J-S, Chang W-B. Amperometric nitrogen dioxide gas sensor: Preparation of PAn/Au/SPE and sensing behavior. Sensors and Actuators B: Chemical. 2001;**72**:101-107

[105] Do J-S, Shieh R-Y. Electrochemical nitrogen dioxide gas sensor based on solid polymeric electrolyte. Sensors and Actuators B: Chemical. 1996;**37**:19-26

[106] Do J-S, Chang W-B. Amperometric nitrogen dioxide gas sensor based on PAn/Au/Nafion®prepared by constant current and cyclic voltammetry methods. Sensors and Actuators B: Chemical. 2004;**101**:97-106

[107] Morrin A, Smyth M, Killard AJ, Ngamna O, Wallace GG, Moulton SE, CrowleyK.SensorComprisingConducting Polymer Materials, European Patent Office. 2007. EP2004840A1

[108] Tiwari A, Gong S. Electrochemical synthesis of chitosan-copolyaniline/ WO3. nH_2O composite electrode for amperometric detection of NO_2 gas. Electroanalysis. 2008;**20**:1775-1781

[109] Do J-S, Chen Y-Y, Tsai M-L. Planar solid-state amperometric hydrogen gas sensor based on Nafion®/ Pt/nano-structured polyaniline/ Au/Al_2O_3 electrode. International Journal of Hydrogen Energy. 2018;**43**:14848-14858

[110] Santos MC, Hamdan OHC, Valverde SA, Guerra EM, Bianchi RF. Synthesis and characterization of V_2O_5/ PANI thin films for application in amperometric ammonia gas sensors. Organic Electronics. 2019;**65**:116-120

[111] Bakker E, Telting-Diaz M. Electrochemical sensors. Analytical Chemistry. 2002;**74**:2781-2800

[112] Hyodo T, Ishibashi C, Yanagi H, Kaneyasu K, Shimizu Y. Potentiometric hydrogen sensors using an anion-conducting polymer as an electrolyte. Reports of the Faculty of Engineering, Nagasaki University. 2012;**42**:42-47

[113] Hyodo T, Takamori M, Goto T, Ueda T, Shimizu Y. Potentiometric CO sensors using anion-conducting polymer electrolyte: Effects of the kinds of noble metal-loaded metal oxides as sensing-electrode materials on CO-sensing properties. Sensors and Actuators B: Chemical. 2019;**287**:42-52

[114] Hyodo T, Goto T, Ueda T, Kaneyasu K, Shimizu Y. Potentiometric carbon monoxide sensors using an anion-conducting polymer electrolyte and Au-loaded SnO_2 electrodes. Journal of the Electrochemical Society. 2016;**163**:B300-B308

[115] Goto T, Hyodo T, Ueda T, Kamada K, Kaneyasu K, Shimizu Y. CO-sensing properties of potentiometric gas sensors using an anion-conducting polymer electrolyte and Au-loaded metal oxide electrodes. Electrochimica Acta. 2015;**166**:232-243

[116] Hyodo T, Ishibashi C, Matsuo K, Kaneyasu K, Yanagi H, Shimizu Y. CO and CO_2 sensing properties of electrochemical gas sensors using an anion-conducting polymer as an electrolyte. Electrochimica Acta. 2012;**82**:19-25

[117] Goto T, Hyodo T, Kaneyasu K, Yanagi H, Shimizu Y. CO sensing properties of electrochemical gas sensors using an anion-conducting polymer as an electrolyte. ECS Transactions. 2013;**50**:267-272

[118] Hagleitner C, Hierlemann A, Lange D, Kummer A, Kerness N, Brand O, et al. Smart single-chip gas sensor microsystem. Nature. 2001;**414**:293-296

[119] Langea U, Mirsky VM. Chemiresistors based on conducting polymers: A review on measurement techniques. Analytica Chimica Acta. 2011;**687**:105-113

[120] Stussi E, Stella R, De Rossi D. Chemoresistive conducting polymer-based odour sensors: Influence of thickness changes on their sensing properties. Sensors and Actuators B: Chemical. 1997;**43**:180-185

[121] Wang PC, Huang Z, MacDiarmid AG. Critical dependency of the conductivity of polypyrrole and polyaniline films on the hydrophobicity/hydrophilicity of the substrate surface. Synthetic Metals. 1999;**101**:852-853

[122] Agbor NE, Petty MC, Monkman AP. Polyaniline thin films for gas sensing. Sensors and Actuators B: Chemical. 1995;**28**:173-179

[123] Syrový T, Kuberský P, Sapurina I, Pretl S, Bober P, Syrová L, et al. Gravure-printed ammonia sensor based on organic polyaniline colloids. Sensors and Actuators B: Chemical. 2016;**225**:510-516

[124] Rawal I, Kaur A. Synthesis of mesoporous polypyrrole nanowires/nanoparticles for ammonia gas sensing application. Sensors and Actuators A. 2013;**203**:92-102

[125] Patois T, Sanchez J-B, Berger F, Rauch J-Y, Fievet P, Lakard B. Ammonia gas sensors based on polypyrrole films: Influence of electrodeposition parameters. Sensors and Actuators B: Chemical. 2012;**171-172**:431-439

[126] Joshi A, Gangal SA, Gupta SK. Ammonia sensing properties of polypyrrole thin films at room temperature. Sensors and Actuators B: Chemical. 2011;**156**:938-942

[127] Chena X, Wong CKY, Yuan CA, Zhang G. Impact of the functional group on the working range of polyaniline as carbon dioxide sensors. Sensors and Actuators B: Chemical. 2012;**175**:15-21

[128] Bartlett PN, Ling-Chung SK. Conducting polymer gas sensors part III: Results for four different polymers and five different vapours. Sensors and Actuators. 1989; **20**:287-292

[129] Bartlett PN, Archer P, Ling-Chung SK. Conducting polymer gas sensors. Part I: Fabrication and characterisation. Sensors and Actuators. 1989;**19**:125-140

[130] Bartlett PN, Ling-Chung SK. Conducting polymer gas sensors. Part II: Response of polypyrrole to methanol vapour. Sensors and Actuators. 1989;**19**:141-150

[131] Srivastava S, Sharma SS, Agrawal S, Kumar S, Singh M, Vijay YK. Study of chemiresistor type CNT doped polyaniline gas sensor. Synthetic Metals. 2010;**160**:529-534

[132] Xue M, Li F, Chen D, Yang Z, Wang X, Ji J. High-oriented polypyrrole nanotubes for next-generation gas sensor. Advanced Materials. 2016;**28**:8265-8270

[133] Xiang C, Jiang D, Zou Y, Chu H, Qiu S, Zhang H, et al. Ammonia sensor based on polypyrrole-graphene nanocomposite decorated with titania

nanoparticles. Ceramics International. 2015;**41**:6432-6643

[134] Hakimi M, Salehi A, Boroumand FA, Mosleh N. Fabrication of a room temperature ammonia gas sensor based on polyaniline with n-doped graphene quantum dots. IEEE Sensors Journal. 2018;**18**:2245-2252

[135] Gavgania JN, Hasanib A, Nourib M, Mahyari M, Salehi A. Highly sensitive and flexible ammonia sensor based on S and N co-doped graphene quantum dots/polyaniline hybrid at room temperature. Sensors and Actuators B: Chemical. 2016;**229**:239-248

[136] Xue L, Wang W, Guo Y, Liu G, Wan P. Flexible polyaniline/carbon nanotube nanocomposite film-based electronic gas sensors. Sensors and Actuators B. 2107;**244**:47-53

[137] Bera PS, Kundu S, Khan H, Jana S. Polyaniline coated graphene hybridized SnO_2 nanocomposite: Low temperature solution synthesis, structural property and room temperature ammonia gas sensing. Journal of Alloys and Compounds. 2018;**744**:260-270

[138] Ye Z, Jiang Y, Tai H, Yuan Z. The investigation of reduced graphene oxide/P3HT composite films for ammonia detection. Integrated Ferroelectrics. 2014;**154**:73-81

[139] Sharma HJ, Jamkar DV, Kondawar SB. Electrospun nanofibers of conducting polyaniline/Al-SnO_2 composites for hydrogen sensing applications. Procedia Materials Science. 2015;**10**:186-194

[140] Sharma S, Hussain S, Singh S, Islam SS. MWCNT-conducting polymer composite based ammonia gas sensors: A new approach for complete recovery process. Sensors and Actuators B: Chemical. 2014;**194**:213-219

[141] Joulazadeh M, Navarchian AH. Ammonia detection of one-dimensional nano-structured polypyrrole/metal oxide nanocomposites sensors. Synthetic Metals. 2015;**210**:404-411

[142] Jain S, Karmakar N, Shah A, Kothari DC, Mishra S, Shimpi NG. Ammonia detection of 1-D ZnO/polypyrrole nanocomposite: Effect of CSA doping and their structural, chemical, thermal and gas sensing behavior. Applied Surface Science. 2017;**396**:1317-1325

[143] Li Y, Jiao M, Yang M. In-situ grown nanostructured ZnO via a green approach and gas sensing properties of polypyrrole/ZnO nanohybrids. Sensors and Actuators B: Chemical. 2017;**238**:596-604

[144] Chougule MA, Sen S, Patil VB. Polypyrrole-ZnO hybrid sensor: Effect of camphor sulfonic acid doping on physical and gas sensing properties. Synthetic Metals. 2012;**162**:1598-1603

[145] Zhang D, Wu Z, Zong X, Zhang Y. Fabrication of polypyrrole/Zn_2SnO_4 nanofilm for ultrahighly sensitive ammonia sensing application. Sensors and Actuators B: Chemical. 2018;**274**:575-586

[146] Ramesan MT, Santhi V, Bahuleyan BK, Al-Maghrabi A. Structural characterization, material properties and sensor application study of in-situ polymerized polypyrrole/silver doped titanium dioxide nanocomposites. Materials Chemistry and Physics. 2018;**211**:343-354

[147] Qin Y, Cui Z, Zhang T, Liu D. Polypyrrole shell (nanoparticles)-functionalized silicon nanowires array with enhanced NH_3-sensing response. Sensors and Actuators B: Chemical. 2018;**258**:246-254

[148] Khuspe GD, Navale ST, Chougule MA, Patil VB. Ammonia gas

sensing properties of CSA doped PANi-SnO_2 nanohybrid thin films. Synthetic Metals. 2013;**185-186**:1-8

[149] Zhu G, Zhang Q, Xie G, Su Y, Zhao K, Du H, et al. Gas sensors based on polyaniline/zinc oxide hybrid film for ammonia detection at room temperature. Chemical Physics Letters. 2016;**665**:147-152

[150] Tai H, Jiang Y, Xie G, Yu J. Preparation, characterization and comparative NH_3-sensing characteristic studies of PANI/inorganic oxides nanocomposite thin films. Journal of Materials Science and Technology. 2010;**26**:605-613

[151] Tai H, Jiang Y, Xie G, Yu J, Chen X, Ying Z. Influence of polymerization temperature on NH_3 response of PANI/TiO_2 thin film gas sensor. Sensors and Actuators B: Chemical. 2008;**129**:319

[152] Li S, Lin P, Zhao L, Wang C, Liu D, Liu F, et al. The room temperature gas sensor based on polyaniline@flower-like WO_3 nanocomposites and flexible PET substrate for NH_3 detection. Sensors and Actuators B: Chemical. 2018;**259**:505-513

[153] Kulkarni S, Patil P, Mujumdar A, Naik J. Synthesis and evaluation of gas sensing properties of PANI, PANI/SnO_2 and PANI/SnO_2/rGO nanocomposites at room temperature. Inorganic Chemistry Communications. 2018;**96**:90-96

[154] Liu C, Tai H, Zhang P, Ye Z, Su Y, Jiang Y. Enhanced ammonia-sensing properties of PANI-TiO_2-Au ternary self-assembly nanocomposite thin film at room temperature. Sensors and Actuators B: Chemical. 2017;**246**:85-95

[155] Yanga X, Li L, Zhao Y. Ag/AgCl-decorated polypyrrole nanotubes and their sensory properties. Synthetic Metals. 2010;**160**:1822-1825

[156] Gong J, Li Y, Hu Z, Zhou Z, Deng Y. Ultrasensitive NH_3 gas sensor from polyaniline nanograin enchased TiO_2 fibers. Journal of Physical Chemistry C. 2010;**114**:9970-9974

[157] Patil UV, Ramgir NS, Karmakar N, Bhogale A, Debnath AK, Aswal DK, et al. Room temperature ammonia sensor based on copper nanoparticle intercalated polyaniline nanocomposite thin films. Applied Surface Science. 2015;**339**:69-74

[158] Zou Y, Wang Q, Xiang C, Tang C, Chu H, Qiu S, et al. Doping composite of polyaniline and reduced graphene oxide with palladium nanoparticles for room-temperature hydrogen-gas sensing. International Journal of Hydrogen Energy. 2016;**41**:5396-5404

[159] Xu H, Chen X, Zhang J, Wang J, Cao B, Cuid D. NO_2 gas sensing with SnO_2-ZnO/PANI composite thick film fabricated from porous nanosolid. Sensors and Actuators B: Chemical. 2013;**176**:166-173

[160] Xu H, Ju D, Li W, Gong H, Zhang J, Wang J, et al. Low-working-temperature, fast-response-speed NO_2 sensor withnanoporous-SnO_2/polyaniline double-layered film. Sensors and Actuators B: Chemical. 2016;**224**:654-660

[161] Mane AT, Navale ST, Patil VB. Room temperature NO_2 gas sensing properties of DBSA doped PPy-WO_3 hybrid nanocomposite sensor. Organic Electronics. 2015;**19**:15-25

[162] Nalage SR, Navale ST, Mane RS, Naushad M, Stadlar FJ, Patil VB. Preparation of camphor-sulfonic acid doped PPy-NiO hybrid nanocomposite for detection of toxic nitrogen dioxide. Synthetic Metals. 2015;**209**:426-433

[163] Mondal SP, Bera S, Narender G, Ray SK. CdSe quantum dots-poly(3-hexylthiophene) nanocomposite sensors

for selective chloroform vapor detection at room temperature. Applied Physics Letters. 2012;**101**:173108

[164] McDonagh C, Burke CS, MacCraith BD. Optical chemical sensors. Chemical Reviews. 2008;**108**:400-422

[165] Brédas JL, Scott JC, Yakushi K, Street GB. Polarons and bipolarons in polypyrrole: Evolution of the band structure and optical spectrum upon doing. Physical Review B. 1984;**30**:1023-1025

[166] Gallazzi MC, Tassoni L, Bertarelli C, Pioggia G, Francesco FD, Montoneri E. Poly(alkoxy-bithiophenes) sensors for organic vapours. Sensors and Actuators B: Chemical. 2003;**88**:178-189

[167] Ho CK, Itamura MT, Kelley M, Hughes RC. Review of chemical sensors for in-Situ monitoring of volatile contaminants. SAND2001-0643. Albuquerque, New Mexico: Sandia National Laboratories; 2001

[168] Hwang HR, Roh JG, Lee DD, Lim JO, Huh JS. Sensing behavior of the polypyrrole and polyaniline sensor for several volatile organic compounds. Metals and Materials International. 2003;**9**:287-291

[169] Tavoli F, Alizadeh N. Optical ammonia gas sensor based on nanostructure dye-doped polypyrrole. Sensors and Actuators B: Chemical. 2013;**176**:761-767

[170] Bansal L, El-Sherif M. Intrinsic optical-fiber sensor for nerve agent sensing. IEEE Sensors Journal. 2005;**5**:648-655

[171] Dickinson TA, White J, Kauer JS, Walt DR. A chemical-detecting system based on a cross-reactive optical sensor array. Nature. 1996;**382**:697-700

[172] Nagle HT, Gutierrez-Osuna R, Schiffman SS. The how and why of electronic noses. IEEE Spectrum. 1998;**35**:22-31

[173] El-Sherif M, Bansal L, Yuan J. Fiber optic sensors for detection of toxic and biological threats. Sensors. 2007;**7**:3100-3118

[174] Muthusamy S, Charles J, Renganathan B, Sastikumar D. In situ growth of Prussian blue nanocubes on polypyrrole nanoparticles: Facile synthesis, characterization and their application as fiber optic gas sensor. Journal of Materials Science. 2018;**53**:15401-15417

[175] Mohammed HA, Rashid AS, Baker MHA, Anas SBA, Mahdi MA, Yaacob MH. Fabrication and characterizations of a novel etched-tapered single mode optical fiber ammonia sensors integrating PANI/GNF nanocomposite. Sensors and Actuators B: Chemical. 2019;**287**:71-77

[176] Chiam YS, Lim KS, Harun SW, Gan SN, Phang SW. Conducting polymer coated optical microfiber sensor for alcohol detection. Sensors and Actuators A. 2014;**205**:58-62

[177] Qin H, Kulkarni A, Zhang H, Kimb H, Jiang D, Kim T. Polypyrrole thin film fiber optic chemical sensor for detection of VOCs. Sensors and Actuators B: Chemical. 2011;**158**:223-228

[178] Homola J, Yee SS, Gauglitz G. Surface plasmon resonance sensors: Review. Sensors and Actuators B: Chemical. 1999;**54**:3-15

[179] Homola J. Surface plasmon resonance sensors for detection of chemical and biological species. Chemical Reviews. 2008;**108**:462-493

[180] Agbor NE, Cresswell JP, Petty MC, Monkman AP. An optical gas sensor

based on polyaniline Langmuir-Blodgett films. Sensors and Actuators B: Chemical. 1997;**41**:137-141

[181] Chang SM, Muramatsu H, Nakamura C, Miyake J. The principle and applications of piezoelectric crystal sensors. Materials Science and Engineering C: Biomimetic and Supramolecular Systems. 2000;**12**:111-123

[182] Torad NL, Zhang S, Amer WA, Ayad MM, Kim M, Kim J, et al. Advanced nanoporous material-based QCM devices: A new horizon of interfacial mass sensing technology. Advanced Materials Interfaces. 2019;**6**:1900849

[183] Mujahid A, Dickert FL. Surface acoustic wave (SAW) for chemical sensing applications of recognition layers. Sensors. 2017;**17**:2716

[184] Ballantine DS, Wohltjen H. Surface acoustic wave devices for chemical analysis. Analytical Chemistry. 1989;**61**:704A-715A

[185] Shen C-Y, Cheng Y-H, Wang S-H, Kuo S-H, Hsu C-L. A polyaniline/WO_3 nanocomposite layer based surface acoustic wave NO_2 gas sensors. In: ICICIC. 2010. pp. 1220-1222

[186] Sadek AZ, Wlodarski W, Shin K, Kaner RB, Kalantar-Zadeh K. A layered surface acoustic wave gas sensor based on a polyaniline/In_2O_3 nanofibre composite. Nanotechnology. 2006;**17**:4488-4492

[187] Shen CY, Huang HM, Wang SH, Chiu YC. Room temperature detection properties of a surface acoustic wave gas sensor with Cu^{2+}/PANI/SnO_2 nanocomposite thin film to nitric oxide. Applied Mechanics and Materials. 2013;**312**:732-735

[188] Wang B, Zheng L, Zhou L. Surface acoustic wave sensors with graphene/PANI nanocomposites for nitric oxide detection. IOP Conference Series: Earth and Environmental Science. 2017;**100**:012044

[189] Milella E, Penza M. SAW gas detection using Langmuir-Blodgett polypyrrole films. Thin Solid Films. 1998;**329**:694-697

[190] Penza M, Milella E, Anisimkin VI. Monitoring of NH_3 gas by LB polypyrrole-based SAW sensor. Sensors and Actuators B: Chemical. 1998;**47**:218-224

[191] Penza M, Milella E, Anisimkin VI. Gas sensing properties of Langmuir-Blodgett polypyrrole film investigated by surface acoustic waves. IEEE Transactions on Ultrasonics, Ferroelectrics, and Frequency Control. 1998;**45**:1125-1132

[192] Yan XF, Li DM, Hou CC, Wang X, Zhou W, Liu M, et al. Comparison of response towards NO_2 and H_2S of PPy and PPy/TiO_2 as SAW sensitive films. Sensors and Actuators B. 2012;**161**:329-333

[193] Hillier AC, Ward MD. Scanning electrochemical mass sensitivity mapping of the quartz crystal microbalance in liquid media. Analytical Chemistry. 1992;**64**:2539-2554

[194] Tang J, Torad NL, Salunkhe RR, Yoon J-H, Al Hossain MS, Dou SX, et al. Towards vaporized molecular discrimination: A quartz crystal microbalance (QCM) sensor system using cobalt-containing mesoporous graphitic carbon. Chemistry, an Asian Journal. 2014;**9**:3238-3244

[195] Sauerbrey G. Verwendung von Schwingquarzen zur Wägung dünner Schichten und zur Mikrowägung. Zeitschrift für Physik. 1959;**155**:206-222

[196] King WH. Piezoelectric sorption detector. Analytical Chemistry. 1964;**36**:1735-1739

[197] Watts ET, Krim J, Widom A. Experimental observation of interfacial slippage at the boundary of molecularly thin films with gold substrates. Physical Review B. 1990;**41**:3466

[198] Ayad MM, Salahuddin NA, Shenashin MA. Optimum reaction conditions for in situ polyaniline films. Synthetic Metals. 2003;**132**:185-190

[199] Ayad MM, Gemaey AH, Salahuddin NA, Shenashin MA. The kinetics and spectral studies of the in situ polyaniline film formation. Journal of Colloid and Interface Science. 2003;**263**:196-201

[200] Ayad MM. In-situ polypyrrole film formation using ferric nitrate as oxidizing agent. Journal of Materials Science. 2003;**22**:1577-1579

[201] Ayad MM, Rehab AF, El-Hallag IS, Amer WA. Preparation and characterization of polyaniline films in the presence of N-phenyl-1, 4-phenylenediamine. European Polymer Journal. 2007;**43**:2540-2549

[202] Abbas MN, Moustafa GA, Mitrovics J, Gopel W. Multicomponent gas analysis of a mixture of chloroform, octane and toluene using a piezoelectric quartz crystal sensor array. Analytica Chimica Acta. 1999;**393**:67-76

[203] Ide J, Nakamoto T, Moriizumi T. Development of odour-sensing system using an auto-sampling stage. Sensors and Actuators A. 1993;**13**:351-354

[204] Xu X, Cang H, Li C, Zhao ZK, Li H. Quartz crystal microbalance sensor array for the detection of volatile organic compounds. Talanta. 2009;**78**:711-716

[205] Açikbaş Y, Evyapan M, Ceyhan T, ÇaPan R, Bekaroğlu Ö. Characterization and organic vapor sensing properties of Langmuir-Blodgett film using a new three oxygen-linked phthalocyanine incorporating lutetium. Sensors and Actuators B: Chemical. 2009;**135**:426-429

[206] Gomes MTSR, Veríssimo MIS, Oliveira JABP. Detection of volatile amines using a quartz crystal with gold electrodes. Sensors and Actuators B: Chemical. 1999;**57**:261-267

[207] Ayad MM, Torad NL, Minisy IM, Izriq R, Ebeid EM. A wide range sensor of a 3D mesoporous silica coated QCM electrodes for the detection of volatile organic compounds. Journal of Porous Materials. 2019;**26**:1731-1741

[208] Ayad MM, Salahuddin NA, Abu El-Nasr A, Torad NL. Amine-functionalized mesoporous silica KIT-6 as a controlled release drug delivery carrier. Microporous and Mesoporous Materials. 2016;**229**:166-177

[209] Ayad MM, Salahuddin NA, Torad NL, Abu El-Nasr A. pH-responsive sulphonated mesoporous silica: A comparative drug release study. RSC Advances. 2016;**6**:57929-57940

[210] Ayad MM, Minisy IM. Detection and kinetics of methylamine on chitosan film coated quartz crystal microbalance electrode. Progress in Organic Coating. 2016;**100**:76-80

[211] Ayad MM, Salahuddin NA, Minisy IM. Detection of some volatile organic compounds with chitosan-coated quartz crystal microbalance. Designed Monomers and Polymers. 2014;**17**:795-802

[212] Ayad MM, Abu El-Nasr A. Adsorption of cationic dye (methylene blue) from water using polyaniline nanotubes base. Journal of Physical Chemistry C. 2010;**114**:14377-14383

[213] Ayad MM, El-Hefnawey G, Torad NL. Quartz crystal microbalance sensor coated with polyaniline emeraldine base for determination of chlorinated aliphatic hydrocarbons. Sensors and Actuators B: Chemical. 2008;**134**:887-894

[214] Ayad MM, Torad NL. Alcohol vapours sensor based on thin polyaniline salt film and quartz crystal microbalance. Talanta. 2009;**78**:1280-1285

[215] Ayad MM, El-Hefnawey G, Torad NL. A sensor of alcohol vapours based on thin polyaniline base film and quartz crystal microbalance. Journal of Hazardous Materials. 2009;**168**:85-88

[216] Ayad MM, Salahuddin NA, Minisy IM, Amer WA. Chitosan/polyaniline nanofibers coating on the quartz crystal microbalance electrode for gas sensing. Sensors and Actuators B: Chemical. 2014;**202**:144-153

[217] Ayad MM, Torad NL. Quartz crystal microbalance sensor for detection of aliphatic amines vapours. Sensors and Actuators B: Chemical. 2010;**147**:481-487

[218] Crank J. The Mathematics of Diffusion. 2nd ed. Oxford: Clarendon Press; 1975. p. 414

[219] Li G, Zheng J, Ma X, Sun Y, Fu J, Wu G. Development of QCM trimethylamine sensor based on water soluble polyaniline. Sensors. 2007;**7**:2378-2388

[220] Zheng J, Li G, Ma X, Wang Y, Wu G, Cheng Y. Polyaniline-TiO_2 nanocomposite-based trimethylamine QCM sensor and its thermal behavior studies. Sensors and Actuators B: Chemical. 2008;**133**:374-380

[221] Ihdene Z, Mekki A, Mettai B, Mahmoud R, Hamada B, Chehimi MM. Quartz crystal microbalance VOCs sensor based on dip coated polyaniline emeraldine salt thin films. Sensors and Actuators B: Chemical. 2014;**203**:647-654

[222] Xu L, Hu X, Lim YT, Subramanian VS. Organic vapor adsorption behavior of poly(3-butoxythiophene) LB films on quartz crystal microbalance. Thin Solid Films. 2002;**417**:90-94

[223] Cui S, Yang L, Wang J, Wang X. Fabrication of a sensitive gas sensor based on PPy/TiO_2 nanocomposites films by layer-by-layer self-assembly and in food storage. Sensors and Actuators B: Chemical. 2016;**233**:337-346

[224] Su P-G, Chang Y-P. Low-humidity sensor based on a quartz-crystal microbalance coated with polypyrrole/Ag/TiO_2 nanoparticles composite thin films. Sensors and Actuators B: Chemical. 2008;**129**:915-920

[225] Zhang D, Wang D, Zong X, Dong G, Zhang Y. High-performance QCM humidity sensor based on graphene oxide/tin oxide/polyaniline ternary nanocomposite prepared by in-situ oxidative polymerization method. Sensors and Actuators B: Chemical. 2018;**262**:531-541

[226] Zhang D, Wang D, Li P, Zhou X, Zong X, Dong G. Facile fabrication of high-performance QCM humidity sensor based on layer-by-layer self-assembled polyaniline/graphene oxide nanocomposite film. Sensors and Actuators B: Chemical. 2018;**255**:1869-1877

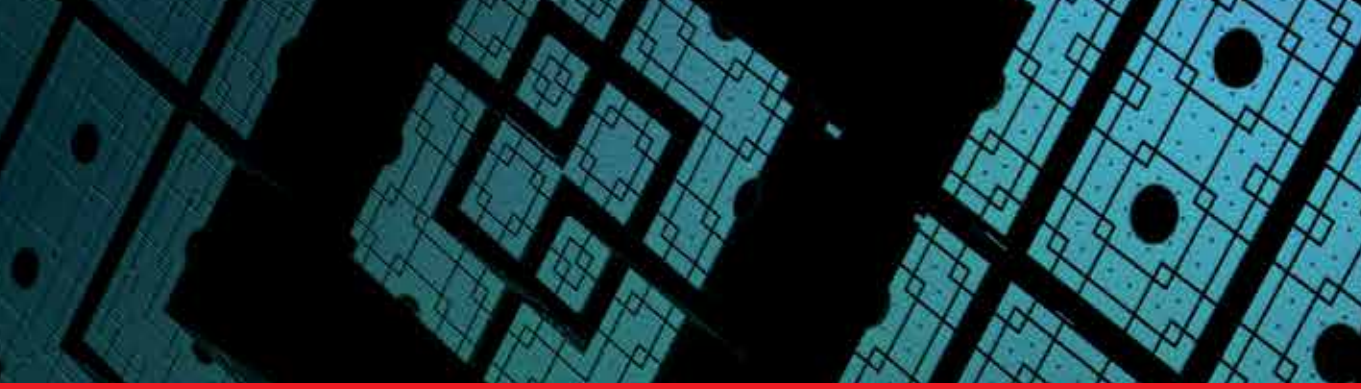

Edited by Sher Bahadar Khan, Abdullah M. Asiri and Kalsoom Akhtar

This book focuses on the applications of nanomaterials in the fabrication of gas sensors. It covers recent developments of different materials used to design gas sensors, such as conducting polymers, semiconductors, as well as layered and nanosized materials. The widespread applications of various gas sensors for the detection of toxic gases are also discussed. The book provides a concise but thorough coverage of nanomaterials applications and utilization in gas sensors. In addition, it overviews recent developments in and the fabrication of gas sensors and their attributes for a broad audience, including beginners, graduate students, and specialists in both academic and industrial sectors.

Published in London, UK
© 2020 IntechOpen
© PIRO4D / pixabay

IntechOpen

ISBN 978-1-83880-501-2